A SEARCH FOR COMPRESSED MASS SPECTRUM SUPERSYMMETRY VIA ELECTROWEAK VECTOR BOSON FUSION PROCESSES IN PROTON-PROTON COLLISIONS AT THE LARGE HADRON COLLIDER

By

Dale Adam Julson

Dissertation
Submitted to the Faculty of the
Graduate School of Vanderbilt University
in partial fulfillment of the requirements
for the degree of

DOCTOR OF PHILOSOPHY
in

Physics

September 30th, 2022

Nashville, Tennessee

Approved:

Alfredo Gurrola, Ph.D.

Paul Sheldon, Ph.D.

Will Johns, Ph.D.

Teruki Kamon, Ph.D.

Sait Umar, Ph.D.

To my family, friends, mentors, and colleagues,
Thank you!

TABLE OF CONTENTS

Page

LIST OF TABLES . . . . **v**

LIST OF FIGURES . . . . **viii**

1 The Standard Model of Particle Physics **1**

- 1.1 History 1
- 1.2 Mathematical Foundation 1
- 1.3 Fermions 2
- 1.4 Bosons 3
- 1.5 ElectroWeak Symmetry Breaking & The Higgs Mechanism 5

2 Physics Beyond the Standard Model & Supersymmetry **9**

- 2.1 Problems of the Standard Model 9
- 2.2 Supersymmetry 9
  - 2.2.1 Cosmological Considerations & Compressed Mass Spectrum Supersymmetry . . . 12
- 2.3 Status of Current SUSY Searches 15

3 The Large Hadron Collider & the Compact Muon Solenoid Detector **22**

- 3.1 The Large Hadron Collider 22
- 3.2 Proton-Proton Collisions 23
- 3.3 The Compact Muon Solenoid Detector 25
  - 3.3.1 Inner Tracking System 27
  - 3.3.2 Electromagnetic Calorimeter 29
  - 3.3.3 Hadronic Calorimeter 30
  - 3.3.4 Superconducting Solenoid Magnet 31
  - 3.3.5 The Muon System 31
- 3.4 Triggering & Data Acquisition 33

4 Particle Identification & Event Reconstruction **36**

- 4.1 Tracking & Vertex Finding 36
- 4.2 Electrons & Photons 37
- 4.3 Muons 39
- 4.4 Jets 42
  - 4.4.1 Pile-Up Jets 42
  - 4.4.2 Jet Energy Corrections 43
- 4.5 Hadronic Taus 46
- 4.6 Missing Transverse Momentum 47
- 4.7 Particle Flow Algorithm 48

5 Analysis Strategy & Sample Production **49**

- 5.1 Vector Boson Fusion Processes 49
- 5.2 Monte Carlo Sample Production 52
- 5.3 Signal Samples 52
  - 5.3.1 Wino-Bino “Virtual W/Z” Scenario 53

5.3.2 Wino-Bino "Stau-Dominated" Scenario 54
5.3.3 Democratic Light Slepton Scenario 54
5.3.4 Higgsino Scenario 54
5.4 Background Samples 55
5.5 Data Samples 56
5.6 Data Corrections 59
5.6.1 L1 Pre-firing (2016 & 2017) 59
5.6.2 EE Noise Veto (2017) 61
5.6.3 HEM Veto (2018) 61

6 Signal Optimization 62

6.1 Central Selection Optimization 62
6.2 VBF Selection Optimization 65

7 Background Estimation 73

7.1 Z+Jets 73
7.2 W+Jets 84
7.3 $t\bar{t}$ 93
7.4 Diboson 102

8 Systematic Uncertainties 109

8.1 Pile-Up (PU) 109
8.2 Jet Energy Resolution (JER) 112
8.3 Jet Energy Scale (JES) 113
8.4 L1-PreFiring 114
8.5 Miscellaneous 115

9 Results 116

9.1 Signal Region Predictions 118
9.1.1 Dimuon Channel (OS & LS) 118
9.1.2 Dielectron Channel (OS & LS) 124
9.1.3 Muon-Electron Channel (OS & LS) 129
9.2 Expected Upper Limits 134
9.2.1 Limits for Individual Channels 135
9.2.2 Limits for Combined Channels 138
9.3 Conclusions & Future Outlook 140

A Appendix A 141

A.1 Mathematical Treatment of the Lorentz Group and the Poincaré Group 141
A.2 Mathematical Treatment of the SuperSymmetric Extension of the Poincaré Group 143
A.3 Mathematical Treatment of Vector Bosons 143
A.4 Background Samples List 146
A.5 Z+jets Full Event Tables 152
A.6 W+jets Full Event Tables 154
A.7 $t\bar{t}$ Full Event Tables 156
A.8 Diboson Full Event Tables 158

References 160

LIST OF TABLES

Table Page

1.1 Fermion content of the SM, showing representations under $SU(3)_C$, $SU(2)_L$, & $U(1)_y$ gauge groups and resulting electric charge Q. Q_L and L_L refer to the left handed quark doublet and left hand lepton doublet respectively. Table adapted from [1]. 3
1.2 Summary of the four fundamental forces. Table adapted from [2]. 4
1.3 Boson content of the SM before electroweak symmetry breaking, showing representations under respective $SU(3)_C$, $SU(2)_L$, & $U(1)_y$ gauge groups and resulting electric charge Q. Table adapted from [1]. 5

2.1 Chiral supermultiplets within the MSSM. Table adapted from [3]. 10
2.2 Gauge supermultiplets within the MSSM. Table adapted from [3]. 11

5.1 Run II MET Primary Datasets 56
5.2 Run II Muon Primary Datasets 57
5.3 Run II Electron Primary Datasets 57
5.4 Run II Tau Primary Datasets 58
5.5 The effects of L1 Pre-firing weights on the event yields in data, MC, and SFs, after the application of central selections and VBF2 selections in Z+jets, 2016. 60
5.6 The effects of L1 Pre-firing weights on the event yields in data, MC, and SFs, after the application of central selections and VBF2 selections in Z+jets, 2017. 60
5.7 The effects of L1 Pre-firing weights on the event yields in data, MC, and SFs, after the application of central selections and VBF2 selections in W+jets, 2016. 60
5.8 The effects of L1 Pre-firing weights on the event yields in data, MC, and SFs, after the application of central selections and VBF2 selections in W+jets, 2017. 60

6.1 Initial Event selections for signal region. Values shown in **bold** will be re-optimized . . . 62
6.2 Final Event selection cuts for the signal region. Values shown in **bold** have been re-optimized, while values shown in **bold red** are the new value (not all values changed after re-optimization). 67
6.3 Event selection criteria for VBF1, VBF2, & VBF3. 67
6.4 Central Selection cuts used in the ee channel when determining VBF optimization. 69
6.5 Resulting R-values from Higgs Combine Tool for 2016 Virtual W/Z scenario showing multiple signal mass points for VBF1 vs VBF2. ee channel OS, LS, & combined results are all shown. 69
6.6 Resulting R-values from Higgs Combine Tool for 2017 Virtual W/Z scenario showing multiple signal mass points for VBF1 vs VBF2. ee channel OS, LS, & combined results are all shown. 69
6.7 Resulting R-values from Higgs Combine Tool for 2018 Virtual W/Z scenario showing multiple signal mass points for VBF1 vs VBF2. ee channel OS, LS, & combined results are all shown. 70
6.8 Central Selection cuts used in the $\mu\mu$ channel when determining VBF optimization. . . . 71
6.9 Resulting R-values from Higgs Combine Tool for 2017 Virtual W/Z scenario showing multiple signal mass points for VBF1 vs VBF2. $\mu\mu$ channel OS, LS, & combined results are all shown. 71

7.1 Central selection event criteria for Z+Jets background estimation. 74
7.2 Event yields for Z+Jets in Data and MC after central selection cuts have been applied. The full event yield can be found in appendix table A.7 75
7.3 Event yields after VBF I selections are applied in the Z+Jets CR. The full event yield can be found in appendix table A.8 78

7.4 Event yields after VBF II selections are applied in the Z+Jets CR. The full event yield can be found in appendix table A.9 . . . 78
7.5 Event yields after VBF3 selections are applied in the Z+Jets CR. The full event yield can be found in appendix table A.10 . . . 80
7.6 Central selection event criteria for W+Jets background estimation. . . . 84
7.7 Event yields after central selections are applied in the W+Jets CR. The full event yield can be found in appendix table A.11 . . . 85
7.8 Event yields after VBF1 selections are applied in the W+Jets CR. The full event yield can be found in appendix table A.12 . . . 87
7.9 Event yields after VBF2 selections are applied in the W+Jets CR. The full event yield can be found in appendix table A.13. . . . 87
7.10 Event yields after VBF3 selections are applied in the W+Jets CR. The full event yield can be found in appendix table A.14. . . . 92
7.11 Central selection event criteria for $t\bar{t}$ background estimation. . . . 93
7.12 Event yields for $t\bar{t}$ in the dimuon channel after central selection cuts and vetoes have been applied. The full event yield can be found in appendix table A.15 . . . 94
7.13 Event yields for $t\bar{t}$ in the dimuon channel after VBF1 selection cuts with modified $p_{\mathrm{T}}^{miss} >$ 100 GeV have been applied. The full event yield can be found in appendix table A.16 . . 96
7.14 Event yields for $t\bar{t}$ in the dimuon channel after VBF2 selection cuts have been applied. The full event yield can be found in appendix table A.18 . . . 97
7.15 Central selection event criteria for diboson background estimation. VBF criteria may be found in table 6.3 . . . 102
7.16 Event yields for diboson after central selection cuts have been applied. The full event yield can be found in appendix table A.19 . . . 103
7.17 Event yields for diboson after VB1 cuts have been applied. The full event yield can be found in appendix table A.20 . . . 105
7.18 Event yields for diboson after VBF2 cuts and vetoes have been applied. . . . 105

9.1 Predicted and observed rates in the signal region for 2016 VBF2 $\mu\mu$ (OS) channel. . . . 119
9.2 Predicted and observed rates in the signal region for 2016 VBF2 $\mu\mu$ (LS) channel. . . . 120
9.3 Predicted and observed rates in the signal region for 2017 VBF2 $\mu\mu$ (OS) channel. . . . 121
9.4 Predicted and observed rates in the signal region for 2017 VBF2 $\mu\mu$ (LS) channel. . . . 121
9.5 Predicted and observed rates in the signal region for 2018 VBF2 $\mu\mu$ (OS) channel. . . . 122
9.6 Predicted and observed rates in the signal region for 2018 VBF2 $\mu\mu$ (LS) channel. . . . 123
9.7 Predicted and observed rates in the signal region for 2016 VBF2 ee (OS) channel. . . . 124
9.8 Predicted and observed rates in the signal region for 2016 VBF2 ee (LS) channel. . . . 125
9.9 Predicted and observed rates in the signal region for 2017 VBF2 ee (OS) channel. . . . 126
9.10 Predicted and observed rates in the signal region for 2017 VBF2 ee (LS) channel. . . . 126
9.11 Predicted and observed rates in the signal region for 2018 VBF2 ee (OS) channel. . . . 127
9.12 Predicted and observed rates in the signal region for 2018 VBF2 ee (LS) channel. . . . 128
9.13 Predicted and observed rates in the signal region for 2016 VBF2 $e\mu$ (OS) channel. . . . 129
9.14 Predicted and observed rates in the signal region for 2016 VBF2 $e\mu$ (LS) channel. . . . 130
9.15 Predicted and observed rates in the signal region for 2017 VBF2 $e\mu$ (OS) channel. . . . 131
9.16 Predicted and observed rates in the signal region for 2017 VBF2 $e\mu$ (LS) channel. . . . 131
9.17 Predicted and observed rates in the signal region for 2018 VBF2 $e\mu$ (OS) channel. . . . 132
9.18 Predicted and observed rates in the signal region for 2018 VBF2 $e\mu$ (LS) channel. . . . 133

A.1 List of background simulation samples for 2016 in the NanoAODv6 data format. . . . 146
A.2 List of background simulation samples for 2016 in the NanoAODv6 data format (cont.). . 147
A.3 List of background simulation samples for 2017 in the NanoAODv6 data format. . . . 148
A.4 List of background simulation samples for 2017 in the NanoAODv6 data format (cont.). . 149
A.5 List of background simulation samples for 2018 in the NanoAODv6 data format. . . . 150
A.6 List of background simulation samples for 2018 in the NanoAODv6 data format (cont.). . 151

A.7 Event yields for Z+Jets (referred to as DY+jets in the table) after central selection cuts have been applied. 152
A.8 Event yields after VBF I selections are applied in the Z+Jets CR. 152
A.9 Event yields after VBF II selections are applied in the Z+Jets CR. 153
A.10 Event yields after VBF III selections are applied in the Z+Jets CR. 153
A.11 Event yields for W+Jets after central selection cuts and vetoes have been applied. 154
A.12 Event yields for VBF I selections applied, W+Jets. 154
A.13 Event yields for VBF II selections applied, W+Jets. 155
A.14 Event yields for VBF III selections applied, W+Jets. 155
A.15 Event yields for $t\bar{t}$ in the dimuon channel after central selection cuts and vetoes have been applied. 156
A.16 Event yields for $t\bar{t}$ in the dimuon channel after VBF1 selection cuts with modified $p_{\mathrm{T}}^{miss} >$ 100 GeV have been applied. 156
A.17 Event yields for $t\bar{t}$ in the dimuon channel after VBF1 selection cuts have been applied (including $p_{\mathrm{T}}^{miss} > 250$ GeV requirement). 157
A.18 Event yields for $t\bar{t}$ in the dimuon channel after VBF2 selection cuts have been applied. . . 157
A.19 Event yields for diboson after central selection cuts and vetoes have been applied. 158
A.20 Event yields for diboson after VBF1 cuts and vetoes have been applied. 158
A.21 Event yields for diboson after VBF2 cuts and vetoes have been applied. 159

LIST OF FIGURES

Figure Page

1.1 The Higgs potential before EWSB (left) and after EWSB (right) [4]. 7

2.1 Comoving number density of DM as a function of inverse temperature (time). From [5]. . 13
2.2 Exclusion limits for gluino and neutralino masses for simplified models assuming gluino pair production and subsequent gluino decay into 2 quarks + LSP [6]. 17
2.3 Exclusion limits for squark and neutralino masses for simplified models assuming squark pair production and subsequent squark decay into 1 quark of the same generation + LSP (top left, bottom left, bottom right) and more complicated decay scenarios (top right) [7]. 18
2.4 Exclusion limits for slepton and neutralino masses for simplified models assuming slepton pair production and subsequent decays into 1 slepton + LSP [7]. 19
2.5 Exclusion limits for chargino and neutralino masses for simplified models assuming direct production of charginos and neutralinos and subsequent decays into leptons + LSP [7]. . . 19
2.6 Exclusion limits for chargino and neutralino masses for simplified models which assume a compressed mass spectrum and primarily Wino/Bino-like light electroweakinos [8, 9]. . 20
2.7 Exclusion limits for chargino and neutralino masses for simplified models which assume a compressed mass spectrum primarily Higgsino-like light electroweakinos. 21

3.1 Aerial view of the LHC with relevant detectors shown [10]. 22
3.2 PDFs for different energy scales (Q^2). x is the longitudinal momentum fraction given by $x = p_{\text{parton}}/p_{\text{proton}}$ [11]. 23
3.3 Total integrated luminosity of pp collisions by the CMS detector broken out by year and center-of-mass energy (left). Average pileup (number of interactions per bunch crossing) recorded by the CMS detector, also broken out by year (right) [12]. 24
3.4 Cross sections for various SM processes (blue, red) in addition to theoretical cross sections for various new physics scenarios (green, SUSY; pink) [13]. 25
3.5 A digital rendering of CMS, showing its relevant size and various labeled sub-detectors [14]. 26
3.6 CMS coordinate system[15, 16]. 27
3.7 (3.7a) A view of the IT along the z-axis showing 1/4 of the apparatus. (3.7b) An overview of the location of the pixel detectors within the IT, showing the 2016 barrel region in green and 2016 endcap in pink (these regions were upgraded in 2017 to include four total barrel region layers and three total endcap region layers).[17]. 28
3.8 IT muon momentum resolution as a function of η [17]. 29
3.9 3D rendering of the CMS ECAL, showing the location of various sub-detectors (top). Coverage by ECAL in η (below) [18]. 30
3.10 A schematic view of the HCAL arrangement showing the location of the HB, HE, and HF as shown in yellow [19]. 31
3.11 Value of $|B|$ (left) and field lines (right) predicted on a longitudinal section of the CMS detector, for the underground model at a central magnetic flux density of 3.8 T. Each field line represents a magnetic flux increment of 6 Wb [19]. 32
3.12 Layout of the muon system, showing the barrel region (green) and endcap region (blue) as well as explicitly calling out the drift tubes (DT), resistive plate chambers (RPC), and cathode strip chambers (CSC) [20]. 33
3.13 Momentum resolution for muons detected solely within the barrel region (left) and solely within the endcap region (right). Blue indicates muons measured using solely the muon system, green indicates muons measured using solely the IT, while red represents muons measured using both [17]. 34

3.14 Overview of the CMS L1 trigger system. Data from ECAL and HCAL, are processed first regionally (RCT) and then globally (GCT). Similarly, energy deposits (hits) from the resistive- plate chambers (RPC), cathode strip chambers (CSC), and drift tubes (DT) are processed and sent onwards to a global muon trigger (GMT). The information from the GCT and GMT is combined in a global trigger (GT), which makes the final trigger decision. This decision is sent to the tracker (TRK), ECAL, HCAL or muon systems (MU) via the trigger, timing and control (TTC) system. The data acquisition system (DAQ) reads data from various subsystems for offline storage. [21]. 35

4.1 Diagrammatic overview of particle interactions with various CMS subdetector layers. Neutrinos notably do no interact with any detector layers, however their production can be inferred when “missing” transverse momentum ($p_{\mathrm{T}}^{\mathrm{miss}}$)is reconstructed in the detector [22]. 36
4.2 Reconstruction efficiency of electrons (top) over various p_T ranges versus η. Data to simulation (MC) ratio (bottom) [23]. 39
4.3 Number of misreconstructed electrons per event as a function of generated vertices for 2016, 2017, & 2018. Low p_T events (left) and high p_T events (right) are shown. The improvement seen in 2017 & 2018 versus 2016 is due to an upgraded pixel detector during those years [23]. 40
4.4 Muon identification efficiencies for LooseID (left) & TightID (right) for $p_{\mathrm{T}}(\mu) > 20$ GeV. Data to simulation (MC) agreement is shown below each respective plot. Results were derived using a $Z \to \mu\mu$ tag and probe method [24]. 41
4.5 A diagrammatic depiction of a pp collision producing a single quark which then fragments, producing further gluons and quarks. These particles hadronize and the resulting hadrons are shown to be detected in close proximity to each other. These close particles will be reconstructed as jets [25]. 43
4.6 Jet composition in terms of energy fraction as a function of jet p_{T}. It can be observed that jets are primarily composed of charged hadrons (usually charged pions) and neutral hadrons (π^0's) but that this composition changes as a function of p_{T} [26]. 44
4.7 A diagrammatic overview of techniques used to reduce PU in jet clustering. Solid (dashed) lines refer to charged (neutral) PF candidates. The weights applied by the PUPPI algorithm are represented by thin lines [27]. 45
4.8 The varying levels of Jet Energy Corrections (JEC) are shown here. All data and MC receive L1+1+L2+L3 corrections, with data receiving an additional L2L3 Residual correction. There are additional L5 and L7 (not shown in this diagram) corrections which can optionally be applied [28]. 45
4.9 (Left) The efficiency of τ_h identification, as measured via $Z \to \tau\tau \to \mu\tau_h$. (Center, Right) Misidentification rates of W+jets and multijet events, as a function of jet p_{T} [29]. 47
4.10 This diagram shows the input and resulting output of the PF algorithm, in which initial tracks and clusters of energy are grouped and linked, resulting in identified individual particles [30]. 48

5.1 Direct electroweakino production via DY processes (left) and W boson mediated processes (right). 49
5.2 Left, VBF production of charginos + VBF jets. The charginos then decay to sleptons which subsequently decay to leptons plus an LSP. These decay chains are ultimately model dependent however, and other models will dictate different decays. Right, the associated detector signature for an event such. The neutrinos and LSPs will be reconstructed as p_{T}^{miss}. 50
5.3 Feynman diagram of a VBF interaction in the virtual W/Z scenario. 53
5.4 Feynman diagram of a VBF interaction in the $\tilde{\tau}$-dominated scenario. 54
5.5 Feynman diagram of a VBF interaction in the democratic light slepton scenario. 55
5.6 Feynman diagram of a VBF interaction in the Higgsino scenario. 55
5.7 Overlaid plots showing before (blue) and after (red) the application of the HEM veto in ϕ (left) and η (right). All distributions have been normalized to unity in order to compare the overall shape. 61

6.1 Optimization results for the combination of μ ID + $p_{\mathrm{T}}^{min}(\mu)$, for the $\tilde{\tau}$-dominated scenario (left), and for the virtual W/Z scenario (right). 63
6.2 Optimization results for $p_{\mathrm{T}}^{max}(\mu)$ in the $\tilde{\tau}$-dominated scenario. 64
6.3 Optimization results for the combination of e ID + $p_{\mathrm{T}}(e)$, for the $\tilde{\tau}$-dominated scenario (left), and for the virtual W/Z scenario (right). 65
6.4 Optimization results for p_{T}^{miss} in the $\mu\tau_h$ channel using Loose τ_h ID working point (top left) and Tight τ_h ID working point (top right). Efficiency curve for the MET Trigger as a function of the offline p_{T}^{miss}, where one of the jets has $|\eta| < 3$ and the other $3 < |\eta| < 5$ [31]. 66
6.5 Background versus signal for $\Delta\eta(j_1, j_2$ (top left), $\eta(j)$ (top right), and largest m(jj) (bottom). All distributions are normalized to unity in order to compare the shape. 68
6.6 Largest $m(jj)$ after VBF1 cuts (left) and VBF2 cuts (right) applied in the ee channel, showing various signal mass points for the virtual W/Z scenario scenario (2016). The inclusion of the two lower $m(jj)$ bins along with the lower $p_{\mathrm{T}}(j)$ allows for a larger signal acceptance as well as better signal sensitivity. The background processes (shown in solid colors) are stacked in the distribution, whereas the signal points (shown dashed) are overlaid. All signal samples use a dummy cross-section of 100 fb. 70
6.7 Largest $m(jj)$ after VBF1 cuts (left) and VBF2 cuts (right) applied in the $\mu\mu$ channel, showing various signal mass points for the virtual W/Z scenario scenario (2016). The inclusion of the two lower $m(jj)$ bins along with the lower $p_{\mathrm{T}}(j)$ allows for a larger signal acceptance as well as better signal sensitivity. The background processes (shown in solid colors) are stacked in the distribution, whereas the signal points (shown dashed) are overlaid. All signal samples use a dummy cross-section of 100 fb. 72

7.1 Feynman diagrams for the three dominant backgrounds within the light lepton channels: Z+jets (top left), W+jets (top right), $t\bar{t}$ (bottom loft), diboson (bottom right). 74
7.2 $p_{\mathrm{T}}(\mu)$, $\eta(\mu)$, $m(\mu,\mu)$, and $\Delta p_{\mathrm{T}}(\mu,\mu)$ after central selection cuts, including veto selections, in Z+jets (2016). A scale factor of 0.95 has been applied to these plots. 76
7.3 $p_{\mathrm{T}}(\mu)$, $\eta(\mu)$, $m_T(\mu,\mu)$, and $\Delta p_{\mathrm{T}}(\mu,\mu)$ after central selection cuts, including veto selections, in Z+jets (2017). A scale factor of 0.93 has been applied to these plots. 76
7.4 $p_{\mathrm{T}}(\mu)$, $\eta(\mu)$, $m_T(\mu,\mu)$, and $\Delta p_{\mathrm{T}}\mu,\mu)$ after central selection cuts, including veto selections, in Z+jets (2018). A scale factor of 0.90 has been applied to these plots. 77
7.5 $p_{\mathrm{T}}(j)$, $\eta(j)$, $\Delta\eta_{jj}$, and m_{jj} after VBF I selections in Z+jets (2016). A scale factor of 1.02 has been applied to these plots. 78
7.6 $p_{\mathrm{T}}(j)$, $\eta(j)$, $\Delta\eta_{jj}$, and m_{jj} after VBF I selections in Z+jets (2017). A scale factor of 1.01 has been applied to these plots. 79
7.7 $p_{\mathrm{T}}(j)$, $\eta(j)$, $\Delta\eta_{jj}$, and m_{jj} after VBF I selections in Z+jets (2018). A scale factor of 0.91 has been applied to these plots. 79
7.8 $p_{\mathrm{T}}(j)$, $\eta(j)$, $\Delta\eta_{jj}$, and m_{jj} after VBF II selections in Z+jets (2016). A scale factor of 1.12 has been applied to these plots. 80
7.9 $p_{\mathrm{T}}(j)$, $\eta(j)$, $\Delta\eta_{jj}$, and m_{jj} after VBF II selections in Z+jets (2017). A scale factor of 0.95 has been applied to these plots. 81
7.10 $p_{\mathrm{T}}(j)$, $\eta(j)$, $\Delta\eta_{jj}$, and m_{jj} after VBF II selections in Z+jets (2018). A scale factor of 0.87 has been applied to these plots. 81
7.11 $p_{\mathrm{T}}(j)$, $\eta(j)$, $\Delta\eta_{jj}$, and m_{jj} after VBF3 selections in Z+jets (2016). A scale factor of 1.07 has been applied to these plots. 82
7.12 $p_{\mathrm{T}}(j)$, $\eta(j)$, $\Delta\eta_{jj}$, and m_{jj} after VBF3 selections in Z+jets (2017). A scale factor of 0.94 has been applied to these plots. 82
7.13 $p_{\mathrm{T}}(j)$, $\eta(j)$, $\Delta\eta_{jj}$, and m_{jj} after VBF3 selections in Z+jets (2018). A scale factor of 0.82 has been applied to these plots. 83
7.14 $p_{\mathrm{T}}(\mu)$, $\eta(\mu)$, $m_{\mathrm{T}}(\mu, p_{\mathrm{T}}^{miss})$, and p_{T}^{miss} after central selection cuts, including veto selections, in W+jets (2016). A central selection scale factor of 0.99 has been applied to these plots. . 85
7.15 $p_{\mathrm{T}}(\mu)$, $\eta(\mu)$, $m_{\mathrm{T}}(\mu, p_{\mathrm{T}}^{miss})$, and p_{T}^{miss} after central selection cuts, including veto selections, in W+jets (2017). A central selection scale factor of 0.92 has been applied to these plots. . 86

7.16 $p_{\mathrm{T}}(\mu)$, $\eta(\mu)$, $m_{\mathrm{T}}(\mu, p_{\mathrm{T}}^{miss})$, and p_{T}^{miss} after central selection cuts, including veto selections, in W+jets (2018). A central selection scale factor of 0.89 has been applied to these plots. . 86

7.17 $p_{\mathrm{T}}(j)$, $\eta(j)$, $\Delta\eta_{jj}$, and m_{jj} after VBF1 selections in W+jets (2016). A scale factor of 0.99 has been applied to these plots. 88

7.18 $p_{\mathrm{T}}(j)$, $\eta(j)$, $\Delta\eta_{jj}$, and m_{jj} after VBF1 selections in W+jets (2017). A scale factor of 0.95 has been applied to these plots. 88

7.19 $p_{\mathrm{T}}(j)$, $\eta(j)$, $\Delta\eta_{jj}$, and m_{jj} after VBF1 selections in W+jets (2018). A scale factor of 0.98 has been applied to these plots. 89

7.20 $p_{\mathrm{T}}(j)$, $\eta(j)$, $\Delta\eta_{jj}$, and m_{jj} after VBF2 selections in W+jets (2016). A scale factor of 1.06 has been applied to these plots. 89

7.21 $p_{\mathrm{T}}(j)$, $\eta(j)$, $\Delta\eta_{jj}$, and m_{jj} after VBF2 selections in W+jets (2017). A scale factor of 0.92 has been applied to these plots. 90

7.22 $p_{\mathrm{T}}(j)$, $\eta(j)$, $\Delta\eta_{jj}$, and m_{jj} after VBF2 selections in W+jets (2018). A scale factor of 0.87 has been applied to these plots. 90

7.23 $p_{\mathrm{T}}(j)$, $\eta(j)$, $\Delta\eta_{jj}$, and m_{jj} after VBF3 selections in W+jets (2016). A scale factor of 1.56 has been applied to these plots. 91

7.24 $p_{\mathrm{T}}(j)$, $\eta(j)$, $\Delta\eta_{jj}$, and m_{jj} after VBF3 selections in W+jets (2017). A scale factor of 0.83 has been applied to these plots. 91

7.25 $p_{\mathrm{T}}(j)$, $\eta(j)$, $\Delta\eta_{jj}$, and m_{jj} after VBF3 selections in W+jets (2018). A scale factor of 0.73 has been applied to these plots. 92

7.26 $p_{\mathrm{T}}(b)$, $\eta(b)$, $p_{\mathrm{T}}(\mu)$, $\eta(\mu)$ and p_{T}^{miss} after central selection cuts (2016). A SF of 0.66 has been applied to the plots shown. 95

7.27 $p_{\mathrm{T}}(b)$, $\eta(b)$, $p_{\mathrm{T}}(\mu)$, $\eta(\mu)$ and p_{T}^{miss} after central selection cuts (2017). A SF of 0.96 has been applied to the plots shown. 96

7.28 $p_{\mathrm{T}}(b)$, $\eta(b)$, $p_{\mathrm{T}}(\mu)$, $\eta(\mu)$ and p_{T}^{miss} after central selection cuts (2018). A SF of 0.97 has been applied to the plots shown. 97

7.29 $N(j)$ (left) and $p_{\mathrm{T}}(j)$ (right) before the p_{T}^{miss} requirement is applied (top) and after (bottom) (2018). A SF of 0.97 has been applied to the plots shown. It is observed that after requiring $p_{\mathrm{T}}^{miss} > 250$ GeV, events primarily have $N(j) > 1$ and $p_{\mathrm{T}}(j) > 50$ GeV. 98

7.30 $p_{\mathrm{T}}(j)$, $\eta(j)$, p_{T}^{miss}, and Largest $m(jj)$ after VBF1 cuts (2016). A SF of 0.81 has been applied to the plots shown. 98

7.31 $p_{\mathrm{T}}(j)$, $\eta(j)$, p_{T}^{miss}, and Largest $m(jj)$ after VBF1 cuts (2017). A SF of 0.75 has been applied to the plots shown. 99

7.32 $p_{\mathrm{T}}(j)$, $\eta(j)$, p_{T}^{miss}, and Largest $m(jj)$ after VBF1 cuts (2018). A SF of 0.80 has been applied to the plots shown. 99

7.33 $p_{\mathrm{T}}(j)$, $\eta(j)$, p_{T}^{miss}, and Largest $m(jj)$ after VBF2 cuts (2016). A SF of 0.72 has been applied to the plots shown. 100

7.34 $p_{\mathrm{T}}(j)$, $\eta(j)$, p_{T}^{miss}, and Largest $m(jj)$ after VBF2 cuts (2017). A SF of 0.68 has been applied to the plots shown. 100

7.35 $p_{\mathrm{T}}(j)$, $\eta(j)$, p_{T}^{miss}, and Largest $m(jj)$ after VBF2 cuts (2018). A SF of 0.71 has been applied to the plots shown. 101

7.36 $p_{\mathrm{T}}(\mu)$, $\eta(\mu)$, $m(\mu, \mu)$, and p_{T}^{miss} after central selection cuts, including veto selections, in diboson (2016). A central selection scale factor of 0.82 has been applied to these plots. . . 103

7.37 $p_{\mathrm{T}}(\mu)$, $\eta(\mu)$, $m(\mu, \mu)$, and p_{T}^{miss} after central selection cuts, including veto selections, in diboson (2017). A central selection scale factor of 0.97 has been applied to these plots. . . 104

7.38 $p_{\mathrm{T}}(\mu)$, $\eta(\mu)$, $m(\mu, \mu)$, and p_{T}^{miss} after central selection cuts, including veto selections, in diboson (2018). A central selection scale factor of 0.97 has been applied to these plots. . . 104

7.39 $p_{\mathrm{T}}(j)$, $\eta(j)$, $\Delta\eta(jj)$, and Largest $m(jj)$ after VBF1 cuts (2016). A SF of 1.16 has been applied to the plots shown. 106

7.40 $p_{\mathrm{T}}(j)$, $\eta(j)$, $\Delta\eta(jj)$, and Largest $m(jj)$ after VBF1 cuts (2017). A SF of 1.12 has been applied to the plots shown. 106

7.41 $p_{\mathrm{T}}(j)$, $\eta(j)$, $\Delta\eta(jj)$, and Largest $m(jj)$ after VBF1 cuts (2018). A SF of 1.22 has been applied to the plots shown.. 107

7.42 $p_T(j)$, $\eta(j)$, $\Delta\eta(jj)$, and Largest $m(jj)$ after VBF2 cuts (2016). A SF of 1.01 has been applied to the plots shown. 107
7.43 $p_T(j)$, $\eta(j)$, $\Delta\eta(jj)$, and Largest $m(jj)$ after VBF2 cuts (2017). A SF of 1.17 has been applied to the plots shown. 108
7.44 $p_T(j)$, $\eta(j)$, $\Delta\eta(jj)$, and Largest $m(jj)$ after VBF2 cuts (2018). A SF of 1.19 has been applied to the plots shown. 108

8.1 Largest dijet mass distribution after applying all selection cuts (including VBF2 selections) to $t\bar{t}$ MC samples produced for 2016 (left), 2017 (center), 2018 (right) in the 2ℓ channel. The nominal and $\pm 1\sigma$ variations to the min-bias cross section are shown in the top plot, where each distribution has been normalized to unity in order to compare the shapes. The bottom plot shows the ratio of the $\pm 1\sigma$ variations to the nominal value, with the magenta indicating the statistical uncertainty in each bin. 110
8.2 Largest dijet mass distribution after applying all selection cuts (including VBF2 selections) to virtual W/Z signal MC ($m(\tilde{\chi}_0^2)$ = 300 GeV, Δm = 50 GeV) produced for 2016 (left), 2017 (center), 2018 (right) in the 2ℓ channel. The nominal and $\pm 1\sigma$ variations to the min-bias cross section are shown in the top plot, where each distribution has been normalized to unity in order to compare the shapes. The bottom plot shows the ratio of the $\pm 1\sigma$ variations to the nominal value, with the magenta indicating the statistical uncertainty in each bin. 111
8.3 Largest dijet mass distribution after applying all selection cuts (including VBF2 selections) to Z+jets for 2016 (left), 2017 (center), 2018 (right) in the 0ℓ channel. The nominal and $\pm 1\sigma$ variations to the min-bias cross section are shown in the top plot, where each distribution has been normalized to unity in order to compare the shapes. The bottom plot shows the ratio of the $\pm 1\sigma$ variations to the nominal value, with the magenta indicating the statistical uncertainty in each bin. 111
8.4 Largest dijet mass distribution after applying all selection cuts (including VBF2 selections) in the 0ℓ channels to Z+jets MC samples produced for 2016 (top left) and 2017 (top right) and to virtual W/Z signal MC samples ($m(\tilde{\chi}_0^2)$ = 300 GeV, Δm = 5 GeV) produced for 2016 (bottom left) and 2017 (bottom right). The nominal and $\pm 1\sigma$ variations to JER are shown in the top plot, where each distribution has been normalized to unity in order to compare the shapes. The bottom plot shows the ratio of the $\pm 1\sigma$ variations to the nominal value, with the magenta indicating the statistical uncertainty in each bin. 112
8.5 Largest dijet mass distribution after applying all selection cuts (including VBF2 selections) in the 0ℓ channels to Z+jets MC samples produced for 2016 (top left) and 2017 (top right) and to virtual W/Z signal MC samples ($m(\tilde{\chi}_0^2)$ = 300 GeV, Δm = 5 GeV) produced for 2016 (bottom left) and 2017 (bottom right). The nominal and $\pm 1\sigma$ variations to JES are shown in the top plot, where each distribution has been normalized to unity in order to compare the shapes. The bottom plot shows the ratio of the $\pm 1\sigma$ variations to the nominal value, with the magenta indicating the statistical uncertainty in each bin. 113
8.6 Largest dijet mass distribution after applying all selection cuts (including VBF2 selections) in the 0ℓ channels to Z+jets MC samples produced for 2016 (top left) and 2017 (top right) and to virtual W/Z signal MC ($m(\tilde{\chi}_0^2)$ = 300 GeV, Δm = 5 GeV) produced for 2016 (bottom left) and 2017 (bottom right). The nominal and $\pm 1\sigma$ variations to L1-PreFiring weights are shown in the top plot, where each distribution has been normalized to unity in order to compare the shapes. The bottom plot shows the ratio of the $\pm 1\sigma$ variations to the nominal value, with the magenta indicating the statistical uncertainty in each bin. 114

9.1 Signal acceptance within the 0ℓ and 1ℓ channels (left) and the 2ℓ channels (right) after applying all signal region selection cuts on the virtual W/Z scenario signal MC samples. 117
9.2 Signal acceptance within the 0ℓ and 1ℓ channels (left) and the 2ℓ channels (right) after applying all signal region selection cuts on the $\tilde{\tau}$ dominated scenario signal MC samples. 118
9.3 2016 largest dijet mass for the $\mu\mu$ channel (left, OS; right, LS) with overlaid signal mass point of $m(\tilde{\chi}_2^0)$ = 300 GeV, ΔM = 50 GeV from the Wino-Bino Virtual WZ scenario. . . 120

9.4 2017 largest dijet mass for the $\mu\mu$ channel (left, OS; right, LS) with overlaid signal mass point of $m(\tilde{\chi}_2^0)$ = 300 GeV, ΔM = 50 GeV from the Wino-Bino Virtual WZ scenario. . . 122
9.5 2018 largest dijet mass for the $\mu\mu$ channel (left, OS; right, LS) with overlaid signal mass point of $m(\tilde{\chi}_2^0)$ = 300 GeV, ΔM = 50 GeV from the Wino-Bino Virtual WZ scenario. . . 123
9.6 2016 largest dijet mass for the ee channel (left, OS; right, LS) with overlaid signal mass point of $m(\tilde{\chi}_2^0)$ = 300 GeV, ΔM = 50 GeV from the Wino-Bino Virtual WZ scenario. . . 125
9.7 2017 largest dijet mass for the ee channel (left, OS; right, LS) with overlaid signal mass point of $m(\tilde{\chi}_2^0)$ = 300 GeV, ΔM = 50 GeV from the Wino-Bino Virtual WZ scenario. . . 127
9.8 2018 largest dijet mass for the ee channel (left, OS; right, LS) with overlaid signal mass point of $m(\tilde{\chi}_2^0)$ = 300 GeV, ΔM = 50 GeV from the Wino-Bino Virtual WZ scenario. . . 128
9.9 2016 largest dijet mass for the $e\mu$ channel (left, OS; right, LS) with overlaid signal mass point of $m(\tilde{\chi}_2^0)$ = 300 GeV, ΔM = 50 GeV from the Wino-Bino Virtual WZ scenario. . . 130
9.10 2017 largest dijet mass for the $e\mu$ channel (left, OS; right, LS) with overlaid signal mass point of $m(\tilde{\chi}_2^0)$ = 300 GeV, ΔM = 50 GeV from the Wino-Bino Virtual WZ scenario. . . 132
9.11 2018 largest dijet mass for the $e\mu$ channel (left, OS; right, LS) with overlaid signal mass point of $m(\tilde{\chi}_2^0)$ = 300 GeV, ΔM = 50 GeV from the Wino-Bino Virtual WZ scenario. . . 133
9.12 Predicted cross section upper limits for the $\tilde{\tau}$-dominated scenario with Δm = 50 GeV, showing the combined OS and LS ee channel (top left), combined OS and LS $e\mu$ channel (top right), combined OS and LS $\mu\mu$ channel (bottom left), and the three channels combined (bottom right). 136
9.13 Predicted cross section upper limits for the $\tilde{\tau}$-dominated scenario with Δm = 50 GeV, showing the 0ℓ channel (left), and combined $1\ell+2\ell$ channel (right). 136
9.14 Predicted cross section upper limits for the virtual W/Z scenario with Δm = 30 GeV, showing the 1ℓ channel (top left), combined 2ℓ channels top (right), and combined $1\ell+2\ell$ channels (bottom). 137
9.15 Predicted cross section upper limits for the virtual W/Z scenario with Δm = 5 GeV, showing the 0ℓ channel (left), and combined $1\ell+2\ell$ channels (right). 137
9.16 Predicted cross section upper limits for combined $0\ell+1\ell+2\ell$ channels in the virtual W/Z scenario with Δm = 5 GeV (top left), Δm = 30 GeV (top right). Similar results from the ATLAS Collaboration (bottom left) and CMS Collaboration (bottom right)[8, 9]. 138
9.17 Predicted cross section upper limits for combined $0\ell+1\ell+2\ell$ channels in the $\tilde{\tau}$-dominated scenario with Δm = 50 GeV. [32]. 139

CHAPTER 1

The Standard Model of Particle Physics

1.1 History

The standard model (SM) of particle physics represents one of the most robust theories ever formulated, able to account for physical phenomenon over an energy range of at least twelve orders of magnitude [33]. Historically, the SM was created by incorporating together a number of theoretical ideas, including but not limited to: electroweak unification by Weinberg, Salam, and Glashow in 1967; the demonstration of renormalizability of gauge theories with spontaneous symmetry breaking by ’t Hooft in 1971; and the formulation of the Quantum Chromodynamic Lagrangian by Fritzsch, Gell-Mann, and Leutwyler in 1973 [34]. The SM has since been able to correctly predict the existence of many particles, including the W and Z bosons (discovered in 1983 [35, 36]), the top quark (discovered in 1995 [37], the tau neutrino (discovered in 2000 [38]), and the higgs boson (discovered in 2012 [39]).

1.2 Mathematical Foundation

The SM is a quantum field theory which is invariant under transformations of the gauge group $SU(3)_C \times SU(2)_L \times U(1)_Y$, as well as transformations of the Poincaré group, which include translations, rotations, and boosts in spacetime. As a quantum field theory, the fields of the SM are operator valued distributions which act on a vacuum state to create excitations. These excitations are then the particles which we observe in nature, and which we detect in our detectors. The dynamics and interactions of these fields are determined by the Lagrangian of the theory, which allows one to make experimental predictions that can be tested. Per Noëther’s theorem, the invariance of a system under transformations of a group leads to a conserved quantity. Indeed, the three gauge groups of the SM lead to three conserved charges: color, weak isospin, and hypercharge. Similarly, the Poincaré group leads to conservation of energy, momentum, and angular momentum. These transformation groups have the additional benefit that they allow us to label and classify the particles of the SM according to which representation of the respective group they transform under, via the introduction of a Casimir element. From the Poincaré group, we are able to label particles according to their spin and mass, with particles transforming under integer spin representations being referred to as “bosons” and particles transforming under half-integer spin representations being referred to as “fermions” (for a detailed mathematical discussion, refer to appendix A.1). The gauge groups allow for further classification, as will be discussed in the following section.

1.3 Fermions

The SM contains two groups of fermions, the leptons and the quarks. Each group is subdivided into three generations, in which the quantum numbers of each generation (i.e. their representations under the SM gauge groups) are identical, and it is only the masses of the respective particles that differ. There are six quarks in total, with the first generation containing the up quark (u) and the down quark (d), the second generation containing the charm quark (c) and the strange quark (s), and the third generation containing the top quark (t) and the bottom quark (b). Similarly there are six total leptons, with the first generation containing the electron (e) and electron neutrino (ν_e), the second generation containing the muon (μ) and muon neutrino (ν_μ), and the third generation containing the tau (τ) and tau neutrino (ν_τ). The SM does not quantitatively explain why there are six total particles within each group, nor why each group repeats for three generations, and instead simply postulates it as part of the theory.

Although similar in number, quarks and leptons behave differently under the SM gauge groups. The quarks of the SM all exist within the **3** representation of $SU(3)_C$, which is the fundamental representation. As a result, quarks will carry one of three distinct color charge states, referred to as red, green, and blue (anti-red, anti-green, and anti-blue for anti-quarks) and will interact via the strong force. Due to a phenomenon known as color confinement, color charged particles can only exist in color neutral states. Quarks will therefore form composite, color neutral particles referred to as "mesons" for 2-quark particles, and "baryons" for 3-quark particles (larger composite quark states are possible as well, but will not be discussed here). The leptons exist in the trivial representation of $SU(3)_C$, meaning they do not carry color charge and do not participate in the strong force.

Leptons and quarks are both chiral spinors, meaning there exists left-chiral and right-chiral versions of each particle. Although one would naively expect these two chiral states to be identical, they are in fact not identical under the $SU(2)_L$ gauge group. The left chiral particles exist in the **2** representation, which is a doublet state, while the right chiral particles exist in the **1** representation, which is a singlet state. This causes a problem due to the fact that the SM Lagrangian contains terms such as $m\bar{\psi}_L\psi_R$ which would attempt to combine a right chiral singlet with a left chiral doublet together. It would seem that the SM could not then be invariant under $SU(2)_L$ as these two particles transform according to different representations. One solution is to require that these particles be massless, meaning that such terms are removed from the Lagrangian. Such a requirement is in obvious conflict with nature (e.g. electrons have mass). The Higgs mechanism is able to resolve this conflict in a relatively straightforward way, as explained in section 1.5.

Furthermore, the left handed and right handed quarks and leptons all exist in different representations of $U(1)_Y$, as can be seen in Table 1.1 which shows the fermion content of the SM with their masses and representations under the different gauge groups, where T^3 refers to the third component of isospin, Y refers to hypercharge, Q is the electric charge which is defined as $Q = T^3 + \frac{Y}{2}$, and Q_L & L_L are the left handed quark doublets and left handed lepton doublets respectively.

Field	$SU(3)_C$	$SU(2)_L$	T^3	$\frac{Y}{2}$	$Q = T^3 + \frac{Y}{2}$	Mass
$Q_L = \begin{pmatrix} u_L \\ d_L \end{pmatrix}$	**3**	**2**	$\begin{pmatrix} \frac{1}{2} \\ -\frac{1}{2} \end{pmatrix}$	$\frac{1}{6}$	$\begin{pmatrix} \frac{2}{3} \\ -\frac{1}{3} \end{pmatrix}$	$\begin{pmatrix} 2.16\text{ MeV} \\ 4.67\text{ MeV} \end{pmatrix}$
$Q_L = \begin{pmatrix} c_L \\ s_L \end{pmatrix}$	**3**	**2**	$\begin{pmatrix} \frac{1}{2} \\ -\frac{1}{2} \end{pmatrix}$	$\frac{1}{6}$	$\begin{pmatrix} \frac{2}{3} \\ -\frac{1}{3} \end{pmatrix}$	$\begin{pmatrix} 1.27\text{ GeV} \\ 93\text{ MeV} \end{pmatrix}$
$Q_L = \begin{pmatrix} t_L \\ b_L \end{pmatrix}$	**3**	**2**	$\begin{pmatrix} \frac{1}{2} \\ -\frac{1}{2} \end{pmatrix}$	$\frac{1}{6}$	$\begin{pmatrix} \frac{2}{3} \\ -\frac{1}{3} \end{pmatrix}$	$\begin{pmatrix} 172.76\text{ GeV} \\ 4.18\text{ GeV} \end{pmatrix}$
u_R	**3**	**1**	0	$\frac{2}{3}$	$\frac{2}{3}$	2.16 MeV
d_R	**3**	**1**	0	$-\frac{1}{3}$	$-\frac{1}{3}$	4.67 MeV
c_R	**3**	**1**	0	$\frac{2}{3}$	$\frac{2}{3}$	1.27 GeV
s_R	**3**	**1**	0	$-\frac{1}{3}$	$-\frac{1}{3}$	93 MeV
t_R	**3**	**1**	0	$\frac{2}{3}$	$\frac{2}{3}$	172.76 GeV
b_R	**3**	**1**	0	$-\frac{1}{3}$	$-\frac{1}{3}$	4.18 GeV
$L_L = \begin{pmatrix} \nu_{e,L} \\ e_L \end{pmatrix}$	**1**	**2**	$\begin{pmatrix} \frac{1}{2} \\ -\frac{1}{2} \end{pmatrix}$	$-\frac{1}{2}$	$\begin{pmatrix} 0 \\ -1 \end{pmatrix}$	$\begin{pmatrix} < 0.8\text{ eV} \\ 0.511\text{ MeV} \end{pmatrix}$
$L_L = \begin{pmatrix} \nu_{\mu,L} \\ \mu_L \end{pmatrix}$	**1**	**2**	$\begin{pmatrix} \frac{1}{2} \\ -\frac{1}{2} \end{pmatrix}$	$-\frac{1}{2}$	$\begin{pmatrix} 0 \\ -1 \end{pmatrix}$	$\begin{pmatrix} < 0.8\text{ eV} \\ 105.66\text{ MeV} \end{pmatrix}$
$L_L = \begin{pmatrix} \nu_{\tau,L} \\ \tau_L \end{pmatrix}$	**1**	**2**	$\begin{pmatrix} \frac{1}{2} \\ -\frac{1}{2} \end{pmatrix}$	$-\frac{1}{2}$	$\begin{pmatrix} 0 \\ -1 \end{pmatrix}$	$\begin{pmatrix} < 0.8\text{ eV} \\ 1.78\text{ GeV} \end{pmatrix}$
e_R	**1**	**1**	0	-1	-1	0.511 MeV
μ_R	**1**	**1**	0	-1	-1	105.66 MeV
τ_R	**1**	**1**	0	-1	-1	1.78 GeV

Table 1.1: Fermion content of the SM, showing representations under $SU(3)_C$, $SU(2)_L$, & $U(1)_y$ gauge groups and resulting electric charge Q. Q_L and L_L refer to the left handed quark doublet and left hand lepton doublet respectively. Table adapted from [1].

1.4 Bosons

Among the bosons, the SM contains two different varieties: scalar bosons, which are spin-0 particles, and vector bosons, which are spin-1 particles. Vector bosons and are often referred to as "gauge bosons" given that they enter into the SM by requiring local invariance under a gauge group (for a detailed mathematical discussion of this process, see Appendix A.3). The terms “vector boson” and “gauge boson” will be used interchangeably throughout this work. There are four distinct vector bosons: the photon (γ), the gluon (g), the Z boson (Z), and the $W^{\pm}$ boson ($W^{\pm}$). Each vector boson is responsible for mediating a fundamental force. The photon mediates electromagnetism, the gluon mediates the strong force, and the Z and $W^{\pm}$ bosons mediate the weak force. Notably absent is a particle to mediate gravity. Gravity is currently not incorporated into the SM, however it is suspected to be mediated by a spin-2 particle, the graviton. A summary of the four fundamental forces can be seen in table 1.2.

Force	mediator	Acts on	Relative Strength	Range
Strong	gluon	quarks	1	10^{-15} m
Electromagnetism	photon	electrical charges	10^{-2}	∞ ($1/r^2$)
Weak	$W^{\pm}, Z$	quarks and leptons	10^{-5}	10^{-18} m
Gravity	graviton (hypothetical)	mass and energy	10^{-39}	∞ ($1/r^2$)

Table 1.2: Summary of the four fundamental forces. Table adapted from [2].

In a similar fashion to the fermions, the bosons also exist within representations of the SM gauge groups. The gluons exist within the adjoint representation (**8**) of $SU(3)_C$. There are therefore 8 different gluons which each carry both color charge and anti-color charge. The 8 color states of the gluons can be written as: $r\bar{g}$, $g\bar{r}$, $r\bar{b}$, $b\bar{r}$, $g\bar{b}$, $b\bar{g}$, $\frac{1}{\sqrt{2}}(r\bar{r}-g\bar{g})$, and $\frac{1}{\sqrt{6}}(r\bar{r}+g\bar{g}-2b\bar{b})$. As a result of this, gluons also cannot be observed alone in nature and must remain confined to color neutral particles, similar to the quarks [1]. This additionally results in the strong force having a range of $\sim 10^{-15}$ m, despite the gluons being massless. All other bosons of the SM exist in the trivial representation of $SU(3)_C$, meaning they do not carry color charge.

In order to understand the vector boson's representations under $SU(2)_L$ and $U(1)_Y$, it is important to first note that the $W^{\pm}$ and Z bosons as well as the photon are a mixture of four different vector bosons which are initially distinct and massless before electroweak symmetry breaking (EWSB). These are the W^1, W^2, W^3 bosons of weak isospin which exist in the adjoint representation (**3**) of $SU(2)_L$ and the trivial representation (0) of $U(1)_Y$, and the B boson which exists in the trivial representation of both $SU(2)_L$ and $U(1)_Y$. It is after EWSB that the four underlying vector bosons mix to form the $W^{\pm}$, Z, and γ states observed in nature. It is also through this process that the $W^{\pm}$ & Z bosons become massive, gaining a mass of 80.433 ± 0.009 GeV and 91.1876 ± 0.0021 GeV respectively, while the photon remains massless [7]. It is because of these large masses of the $W^{\pm}$ & Z that the weak force has a limited range of $\sim 10^{-18}$ m, and it is due to the photon being massless that the electromagnetic force is infinite in range.

The only spin-0 boson of the SM is the higgs boson (h) which has a mass of 125.10 ± 0.14 GeV [7].

---

[1] Gluons should also be able to form color neutral particles on their own, referred to as glueballs. Searches for glueballs are ongoing [40]

The higgs boson arises from the higgs field which is a complex scalar field (consisting of four real degrees of freedom) existing in the **2** representation of $SU(2)_L$. This field and its complex conjugate can be written as:

$$\phi = \begin{pmatrix} \phi^+ \\ \phi^0 \end{pmatrix} \qquad \phi^\dagger = \begin{pmatrix} \phi^0 \\ \phi^- \end{pmatrix} \tag{1.1}$$

During EWSB, three of the four degrees of freedom are absorbed by the vector bosons in order to provide them with a longitudinal polarization, leaving a single unabsorbed field whose perturbations are the higgs boson observed in nature. The boson content of the SM is detailed in table 1.3

Field	$SU(3)_C$	$SU(2)_L$	T^3	$\frac{Y}{2}$	$Q = T^3 + \frac{Y}{2}$
g	**8**	**1**	0	0	$\frac{2}{3}$
$W^\pm, W^0$	**1**	**3**	(±1,0)	0	(±1,0)
b	**1**	**1**	0	0	0
$\phi = \begin{pmatrix} \phi^+ \\ \phi^0 \end{pmatrix}$	**1**	**2**	$\begin{pmatrix} \frac{1}{2} \\ -\frac{1}{2} \end{pmatrix}$	$\frac{1}{2}$	$\begin{pmatrix} 1 \\ 0 \end{pmatrix}$
$\phi = \begin{pmatrix} \phi^0 \\ \phi^- \end{pmatrix}$	**1**	**2**	$\begin{pmatrix} -\frac{1}{2} \\ \frac{1}{2} \end{pmatrix}$	-$\frac{1}{2}$	$\begin{pmatrix} 0 \\ -1 \end{pmatrix}$

Table 1.3: Boson content of the SM before electroweak symmetry breaking, showing representations under respective $SU(3)_C$, $SU(2)_L$, & $U(1)_y$ gauge groups and resulting electric charge Q. Table adapted from [1].

1.5 ElectroWeak Symmetry Breaking & The Higgs Mechanism

As extensively mentioned, the SM exhibits a $SU(3)_C \times SU(2)_L \times U(1)_Y$ symmetry. This is not the symmetry that is manifested at low energies however, which is discernible given that only the gluon and the photon are massless within the SM . The symmetry that we actually observe in our daily lives is $SU(3)_C \times U(1)_{em}$, where $U(1)_{em}$ refers to the $U(1)$ gauge symmetry of electromagnetism. The process through which $SU(3)_C \times SU(2)_L \times U(1)_Y$ "breaks down" into $SU(3)_C \times U(1)_{em}$ is referred to as "ElectroWeak Symmetry Breaking". Before EWSB, all the fermions and vector bosons of the SM are massless, as required to ensure proper gauge invariance. After EWSB, and through a process called the Higgs Mechanism, all fermions gain mass[2] as well as the $W^\pm$ and Z bosons. The actual mechanics of mass generation for the fermions differs slightly from the bosons. To understand how the Higgs Mechanism generates the boson masses, consider the following Lagrangian for a complex scalar field with a local U(1) gauge symmetry [2], where D_μ is the covariant

---

[2] The neutrinos are a possible exception to this. Experiments show they are massive, however the origin of their mass is still not well understood [41].

derivative $D_\mu = \partial_\mu - iqA_\mu$, A_μ is a massless vector field, and q is the charge associated with this field:

$$\mathscr{L} = (D_\mu \phi)^\dagger (D^\mu \phi) - V(\phi) \tag{1.2}$$

The potential $V(\phi)$ represents a mass term given by:

$$V(\phi) = m^2 \phi^\dagger \phi \tag{1.3}$$

This potential has a minimum around $|\phi|^2 = 0$. Consider if instead, the potential were to have the form:

$$V(\phi) = \lambda m^2 (\phi^\dagger \phi - \Phi^2)^2 \tag{1.4}$$

where λ and Φ are real constants. This potential still manifests the $U(1)$ gauge symmetry, however the minimum is no longer located at $|\phi|^2 = 0$ but instead at $|\phi| = \Phi$. If one expands around this new non-zero vacuum state, setting both the vacuum and ϕ to be real via the local $U(1)$ gauge, one gets:

$$\phi = \Phi + h \tag{1.5}$$

where h is a real scalar field, representing fluctuations around the vacuum. Writing out the entirety of the Lagrangian now:

$$\begin{aligned} \mathscr{L} &= (\partial_\mu + iqA_\mu)(\Phi + h)(\partial^\mu - iqA^\mu)(\Phi + h) - \lambda m^2 [(\Phi + h)(\Phi + h) - \Phi^2]^2 \\ &= \partial_\mu h \partial^\mu h - 4\lambda m^2 \Phi^2 h^2 - q^2 \Phi^2 A_\mu A^\mu + \mathscr{L}_{interactions} \end{aligned} \tag{1.6}$$

where $\mathscr{L}_{interactions}$ represents various further interaction terms that are not important for this discussion. The result of this process is that the previously massless vector field A_μ has now gained a mass of value $q\Phi$. Indeed, this is an example of the Higgs mechanism, whereby a good symmetry of a system may be “broken” spontaneously via the addition of a scalar field with a nonzero vacuum state, resulting in massive bosons. The field h is then referred to as a Higgs Boson. Although this was a toy model to demonstrate the process in action, the same mechanism takes place in the SM as shown in figure 1.1, in which the higgs field is a complex scalar doublet with an associated Lagrangian given by:

$$\mathscr{L} = \partial_\mu \phi^\dagger \partial^\mu \phi - V(\phi), \qquad V(\phi) = \mu^2 \phi^\dagger \phi + \lambda (\phi^\dagger \phi)^2 \tag{1.7}$$

Initially $\mu^2 \geq 0$ and the higgs potential has a zero valued vacuum expectation value (vev), corresponding with the left plot in figure 1.1. After EWSB, $\mu^2 < 0$ and the Higgs potential takes on a non-zero vev of $|\phi| = \sqrt{\frac{-\mu^2}{2\lambda}} = \frac{v}{\sqrt{2}}$, corresponding with the right plot in figure 1.1. Once this occurs, three of the four real scalar fields are absorbed to form the massive bosons, with the fourth remaining field being the SM Higgs Boson. After EWSB, the four vector boson fields mix to form the following linear combinations:

$$\begin{aligned} W_\mu^+ &= \frac{1}{\sqrt{2}}(W_\mu^1 - iW_\mu^2) \\ W_\mu^- &= \frac{1}{\sqrt{2}}(W_\mu^1 + iW_\mu^2) \\ Z_\mu &= c_W W_\mu^3 - s_W B_\mu \\ A_\mu &= s_W W_\mu^3 + c_W B_\mu \end{aligned} \tag{1.8}$$

Where $s_W = \sin(\theta_W)$, $c_W = \cos(\theta_W)$, and θ_W is the Weinberg angle, given by $\theta_W = \tan^{-1}(g_1/g_2)$, where g_1 and g_2 are the couplings of the underlying $U(1)_Y$ and $SU(2)_L$ fields respectively. Electric charge, which is the conserved quantity derived from $U(1)_{em}$, is then defined as $Q = T_3 + \frac{1}{2}Y_W$, where T_3 is the third component of weak isospin, and Y the generator of hypercharge.

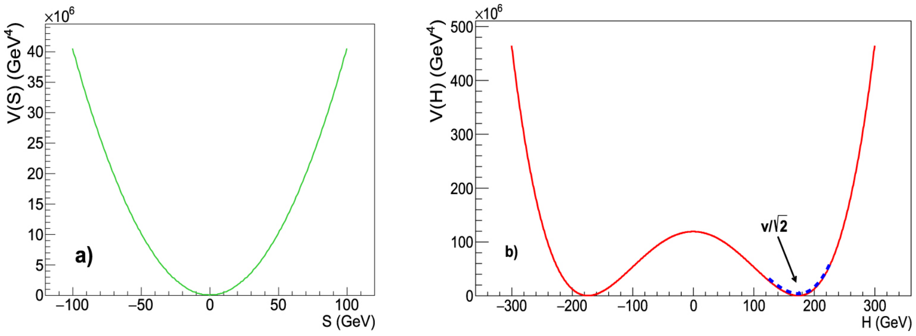

Figure 1.1: The Higgs potential before EWSB (left) and after EWSB (right) [4].

The fermion masses are also generated via the higgs, but through a different process. To better understand why fermion masses are not allowed, consider that the SM Lagrangian contains terms such as $m(\bar{\psi}_L\psi_R + \bar{\psi}_R\psi_L)$. Let $\bar{\psi}_L$ be the first generation lepton doublet containing $\bar{e}_L$ and $\bar{\nu}_L$, and ψ_R be e_R. This term within the SM Lagrangian would then be:

$$\mathscr{L} = m\bar{L}_L e_R + m\bar{e}_R L_L = m\begin{pmatrix} \bar{\nu}_L & \bar{e}_L \end{pmatrix} e_R + m\,\bar{e}_R \begin{pmatrix} \nu_L \\ e_L \end{pmatrix} \tag{1.9}$$

This is disallowed in part given that it is not a Lorentz scalar quantity, but also that it is clearly not $SU(2)$ invariant, as the lepton doublet transforms according to the **2** representation, and the lepton singlet according to the **1** representation. If instead however we allow an interaction between the SM higgs doublet of the following type:

$$\begin{aligned}\mathscr{L} &= g_e\bar{L}_L\phi e_R + g_e\bar{e}_R\phi^\dagger L_L \\ &= g_e\begin{pmatrix}\bar{\nu}_L & \bar{e}_L\end{pmatrix}\begin{pmatrix}0 \\ \frac{v+h}{\sqrt{2}}\end{pmatrix}e_R + g_e\,\bar{e}_R\begin{pmatrix}0 & \frac{v+h}{\sqrt{2}}\end{pmatrix}\begin{pmatrix}\nu_L \\ e_L\end{pmatrix} \\ &= \frac{g_e(v+h)}{\sqrt{2}}(\bar{e}_Le_R+\bar{e}_Re_L) \\ &= \frac{g_ev}{\sqrt{2}}(\bar{e}_Le_R+\bar{e}_Re_L)+\frac{g_eh}{\sqrt{2}}(\bar{e}_Le_R+\bar{e}_Re_L)\end{aligned} \tag{1.10}$$

then we can see that not only have we once again produced a Lorentz scalar quantity, but we have produced a $SU(2)_L$ invariant term as well. The first term in the last line of equation 1.10 represents the mass of the electron, given by $m_e = g_ev/\sqrt{2}$, where g_e is a coupling term and v is the higgs vev, while the second term represents an interaction vertex between electron pairs and the higgs boson. This process repeats itself for all fermions of the SM. The fermion masses can then be seen as a Yukawa coupling to the higgs field, which is qualitatively able to explain then why the fermions have different masses, given that their respective Yukawa couplings are different.

CHAPTER 2

Physics Beyond the Standard Model & Supersymmetry

Equations, tables, and discussion within this chapter have been adapted from [3, 33, 42].

2.1 Problems of the Standard Model

Despite the SM's successful history, there are numerous reasons to believe it is an incomplete description of our universe. These problems range from simple aesthetic considerations, to actual observational inconsistencies. These include (but are not limited to):

- The SM in its current form does not incorporate gravity, meaning it is not able to describe all the observed forces of the universe.
- There is overwhelming evidence for the existence of cold dark matter (DM), which the SM cannot account for [43].
- There is evidence that the expansion of the universe is accelerating due to what is referred to as "dark energy", which again the SM cannot account for [44].
- There are various hierarchy problems, including "why gravity is significantly weaker than the other known forces?", and "why the mass of the Higgs field is not significantly larger, given that it receives quantum corrections from other particles?".
- The gauge groups and particle representations of the SM are completely ad hoc, as well as the 19 input parameters which need to be experimentally measured.

There have been a recent number of experimental results which additionally hint at problems within the SM, including measurements of the anomalous magnetic dipole moment of the muon [45], lepton flavor universality violations [46], and inconsistencies between the predicted and measured mass of the $W^{\pm}$ boson [47].

2.2 Supersymmetry

Supersymmetry (SUSY) is a leading theory of physics beyond the SM which seeks to answer some of these fundamental questions. SUSY was originally discovered to be able to address the Higgs mass hierarchy problem, although it was later found to be able to address other problems as well, including the particle nature of DM. SUSY, as a theory, postulates an extension to the Poincaré group of the SM by adding an additional generator Q which carries a spinorial index (for the full Super-Poincaré algebra, see appendix A.2). The result is that all particles are proposed to exist in irreducible representations of the so called "Super-Poincaré" group which form supermultiplets. Particles within a supermultiplet differ from each other by 1/2 spin. In the case of the fermions, SUSY postulates new particles called "sfermions" or "scalar fermions", with the superpartners to the quarks being the "squarks" and the superpartners to the leptons being the "sleptons". The general notation is that SUSY particles carry a tilde (˜) whereas SM particles do not, so a left-handed electron is denoted e_L whereas a left-handed *selectron* is denoted $\tilde{e}_L$. It is important to note that within the SM, the left-handed and right-handed fermions are separate and distinct particles and as a result their SUSY particles are also distinct. Given that the "sfermions" are scalars, the "*L*" and "*R*" subscripts do not refer to the handedness of the SUSY particles, but instead to their SM counterparts. In order to not introduce any quantum anomalies, SUSY requires an additional complex scalar Higgs doublet, in which the (now two higgs doublets) are denoted $H_u = \begin{pmatrix} H_u^+ & H_u^0 \end{pmatrix}$ and $H_d = \begin{pmatrix} H_d^0 & H_d^- \end{pmatrix}$[1]. The physical higgs boson of the SM would be a linear combination of H_u^0 and H_d^0. Each of these SM higgs doublets will also have an associated fermion superpartner, one neutral and one charged, which are dubbed "higgsinos". This construction of placing all the particles of the SM into supermultiplets and adding an additional higgs doublet is often referred to as the Minimal SuperSymmetric Model (MSSM). It is possible to construct more complex SUSY models by adding additional Q generators to the Super-Poincaré group, however those scenarios will not be considered here and the MSSM will be the sole SUSY theory considered within this work. The chiral MSSM supermultiplets and their corresponding representations under the SM gauge groups are shown in table 2.1, where it is implied the sleptons and squarks also repeat for three generations in the same manner as the SM leptons and quarks.

Names	spin 0	spin 1/2	$SU(3)_C, SU(2)_L, U(1)_Y$
sleptons, leptons	$\begin{pmatrix} \tilde{\nu}_L & \tilde{e}_L \end{pmatrix}$	$\begin{pmatrix} \nu_L & e_L \end{pmatrix}$	$(\mathbf{1}, \mathbf{2}, -1)$
	$\tilde{e}_R$	e_R	$(\mathbf{1}, \mathbf{1}, -2)$
squarks, quarks	$\begin{pmatrix} \tilde{u}_L & \tilde{d}_L \end{pmatrix}$	$\begin{pmatrix} u_L & d_L \end{pmatrix}$	$(\mathbf{3}, \mathbf{2}, \frac{1}{3})$
	$\tilde{u}_R$	u_R	$(\mathbf{3}, \mathbf{1}, \frac{4}{3})$
	$\tilde{d}_R$	d_R	$(\mathbf{3}, \mathbf{1}, -\frac{2}{3})$
Higgs, Higgsinos	$\begin{pmatrix} H_u^+ & H_u^0 \end{pmatrix}$	$\begin{pmatrix} \tilde{H}_u^+ & \tilde{H}_u^0 \end{pmatrix}$	$(\mathbf{1}, \mathbf{2}, 1)$
	$\begin{pmatrix} H_d^0 & H_d^- \end{pmatrix}$	$\begin{pmatrix} \tilde{H}_d^0 & \tilde{H}_d^- \end{pmatrix}$	$(\mathbf{1}, \mathbf{2}, -1)$

Table 2.1: Chiral supermultiplets within the MSSM. Table adapted from [3].

The gauge bosons of the SM must also obtain SUSY superpartners, which are referred to as "'gauginos". The convention for the gauginos is that each individual gauge boson adds an "ino" to its name (the W boson becomes the "wino", the gluon becomes the "gluino"). Given that the gauge bosons are spin 1 particles, the

---

[1] We had previously used $\phi = \begin{pmatrix} \phi^+ & \phi^0 \end{pmatrix}$ to denote a higgs doublet.

gauginos will be spin 1/2 particles. The gauge bosons and gauginos can be found in table 2.2. It should be noted that the gauginos and higgsinos are allowed to mix with each other because of EWSB. The result is that the neutral higgsinos ($\tilde{H}_u^0$, $\tilde{H}_d^0$) and neutral gauginos ($\tilde{B}$, $\tilde{W}^0$) mix to form four mass eigenstates referred to as "neutralinos", denoted in descending mass order as $\tilde{\chi}_4^0$, $\tilde{\chi}_3^0$, $\tilde{\chi}_2^0$, & $\tilde{\chi}_1^0$. Likewise, the charged higgsinos ($\tilde{H}_u^+$, $\tilde{H}_d^-$) and charged gauginos ($\tilde{W}^+$, $\tilde{W}^-$) form two mass eigenstates (each with ± charge, for a total of four particles) referred to as "charginos", denoted in descending mass order as $\tilde{\chi}_2^\pm$ & $\tilde{\chi}_1^\pm$. If SUSY were to be an unbroken symmetry, one would expect the superpartner particles to be the exact same mass as their SM counterparts. We know this not to be the case, as there is no way for them to have evaded experimental detection thus far. As a result, SUSY must be a broken symmetry. The origin of SUSY breaking will not be discussed further, except to mention that phenomenologically if we want SUSY to account for the mass of the higgs then we expect the SUSY partners to have masses in the range of GeV to TeV — large enough to have evaded experimental detection, but small enough that radiative corrections to the higgs can still correctly cancel to render a natural higgs mass.

Names	spin 1/2	spin 1	$SU(3)_C, SU(2)_L, U(1)_Y$
gluinos, gluon	$\tilde{g}$	g	$(\mathbf{1}, \mathbf{2}, -1)$
winos, W bosons	$\tilde{W}^\pm\ \tilde{W}^0$	$W^\pm\ W^0$	$(\mathbf{3}, \mathbf{2}, \frac{1}{3})$
bino, B boson	$\tilde{B}^0$	B^0	$(\mathbf{1}, \mathbf{2}, 1)$

Table 2.2: Gauge supermultiplets within the MSSM. Table adapted from [3].

In order to better understand the motivation for SUSY and why it is a leading contender for physics beyond-the-Standard-Model (BSM), consider first the higgs mass hierarchy problem. The higgs field is responsible for generating the masses of all other particles within the SM (as previously discussed in section 1.5, with neutrinos being a possible exception). As a result, the higgs itself receives quantum corrections to its mass via loop diagrams of every particle it couples to. For fermions, these corrections take the form

$$\Delta m_H^2 = -\frac{|\lambda_f|^2}{8\pi^2}\Lambda_{\mathrm{UV}}^2 + ... \tag{2.1}$$

where λ_f is a coupling term and Λ_{UV}^2 represents an ultraviolet momentum cutoff, which could theoretically be as high as the Planck scale. This is a very serious problem, as it implies the higgs mass has no theoretical reason it shouldn't be many orders of magnitude larger than its experimentally measured value. Consider, however, if for every fermion there was an equivalent scalar partner as SUSY proposes. This would imply there would be an additional higgs mass correction term of the form

$$\Delta m_H^2 = \frac{|\lambda_{\tilde{f}}|^2}{8\pi^2}\Lambda_{\mathrm{UV}}^2 + ... \tag{2.2}$$

When adding up all the quantum corrections which the higgs mass receives, those from the new SUSY scalar particles would exactly cancel those the from their associated SM fermions, thus resolving the hierarchy problem.

Consider additionally that within the MSSM Lagrangian, it is possible to add gauge-invariant, renormalizable terms which violate baryon number (B) and lepton number (L). At first glance this is a problem, given that no L-violating or B-violating processes have been experimentally observed. Trying to treat B and L as fundamental symmetries of the SM is also difficult, however, given that they *should* be violated by non-perturbative electroweak effects, but whose contributions are negligible for experiments at ordinary energies. Both of these problems can be resolved if one imposes a new symmetry within the MSSM, referred to as "R-parity", which has the form

$$P_R = (-1)^{3(B-L)+2s} \tag{2.3}$$

where s refers to the spin of the particle. The result is that all particles of the SM including the higgs boson will have even R-parity ($P_R = +1$), while all squarks, sleptons, and neutralinos will have odd parity ($P_R = -1$). The advantage of this is that R-parity can be treated as an exact symmetry, whereas B and L cannot. Although this result might seem pedantic, the phenomenological implications are enormous. The lightest supersymmetric particle (LSP) will have odd parity, making it stable. If we take the LSP to be the lightest neutralino [2], then it will also be electrically neutral and weakly interacting with normal matter, making it a DM candidate particle. SUSY can therefore resolve not only the Higgs mass hierarchy problem, but also the particle nature of DM.

2.2.1 Cosmological Considerations & Compressed Mass Spectrum Supersymmetry

SUSY offers a large phase space for the masses, couplings, and flavor mixings of the neutralinos. Early universe cosmology can offer a hint at what these values should be if the LSP is indeed to account for DM. Such scenarios in this work will be referred to as being "cosmologically motivated" SUSY scenarios. According to Lambda Cold Dark Matter (ΛCDM) models, it is believed that DM was created in thermal equilibrium in the early universe when the temperature of the universe exceeded the mass of the DM particle [42]. Initially, DM particles and lighter particles underwent the following interaction $\chi\bar{\chi} \leftrightarrow f\bar{f}$ in which DM particles, denoted by χ, could annihilate to produce SM particles, denoted by f, and vice versa. This is sustained in equilibrium

---

[2] This is not the only SUSY particle that can be considered as a DM candidate. The sneutrino, gravitino (which is the SUSY partner to the graviton which is proposed to mediate gravity), and other SUSY extension particles can also be considered, however for this work we take the LSP to be the lightest neutralino.

until the universe cools to an energy below the mass of the DM particle, at which point the process can only proceed as $\chi\bar{\chi} \rightarrow f\bar{f}$ and we see a reduction in the total abundance of DM. Eventually, the annihilation rate falls below the expansion rate of the universe, a point which is often referred to as "freeze out", leaving behind the currently observed relic abundance of DM particles. This relic abundance is referred to as the "DM relic density". This model can be described using the Boltzmann equation:

$$\frac{\mathrm{d}n_\chi}{\mathrm{d}t} + 3Hn_\chi = -\langle\sigma_\mathrm{A} v\rangle[(n_\chi)^2 - (n_\chi^\mathrm{eq})^2] \tag{2.4}$$

where $\mathrm{d}n_\chi$ is the number density of the DM particle, $H = \dot{a}/a$ is the Hubble expansion rate of the universe, $\langle\sigma_A v\rangle$ is the thermally averaged total cross section for the annihilation of $\chi\bar{\chi}$ into lighter particles (σ_A) times the relative velocity (v), and n_χ^eq is the number density of the DM particle when in thermal equilibrium. Figure 2.1 shows the resulting comoving number density of DM in the universe as a function of the inverse temperature of the universe (and therefore time). An important point that can be gleaned from this plot is that

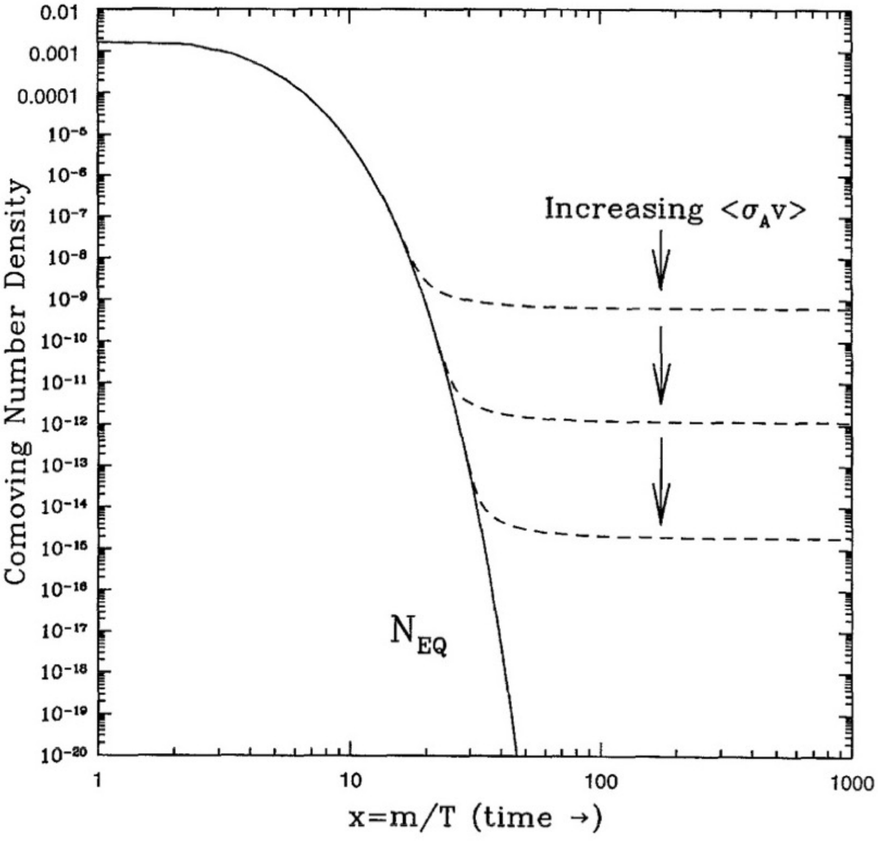

Figure 2.1: Comoving number density of DM as a function of inverse temperature (time). From [5].

increasing the thermally averaged cross section for DM annihilation in the early universe results in a lower total DM relic density. Indeed, it can be shown that the present mass density in units of the critical density is given by [42]:

$$\Omega_\chi h^2 \simeq \frac{3\times 10^{-27}\mathrm{cm}^2\mathrm{s}^{-1}}{\langle \sigma_\mathrm{A} v\rangle}. \tag{2.5}$$

The Planck Collaboration has measured this value using the anisotropies of the cosmic microwave background and determined it to be [48]:

$$\Omega_\mathrm{CDM}h^2 = 0.120 \pm 0.001. \tag{2.6}$$

This value now provides us with an upper limit on the density of any individual DM candidate (DM could theoretically be comprised of more than one particle type) and a handle as to which areas of the SUSY parameter phase space offer valid DM candidate particles. Various SUSY models predict a DM relic density which is larger than the Planck value (for example mSUGRA) [49]. One way to resolve problems of overabundance is to consider a coannihilation (CA) partner which may also reduce the total number of DM in the early universe [50]. The discussion surrounding equation 2.4 assumed that the mass difference between the LSP and the next-lightest-supersymmetrical-particle (NLSP) was large, meaning reduction of the LSP by the process $\chi\bar{\chi} \to f\bar{f}$ was not significantly affected by the NLSP. If we instead consider scenarios in which this mass gap is small, one finds that the effective cross section for the reduction of χ becomes:

$$\sigma_\mathrm{eff} = \sum_{ij}^{N} \sigma_{ij}\frac{g_i g_j}{g_{eff}^2}(1+\Delta_i)^{3/2}(1+\Delta_j)^{3/2} \times \exp[-x(\Delta_i+\Delta_j)] \tag{2.7}$$

where σ_eff is the effective cross section, i and j are labels over the particles involved where it is assumed that $m_i < m_j$ when $i < j$, g_i and g_j are the degrees of freedom (spin, color, etc.) of the particle, and g_{eff} is defined as:

$$g_{eff} = \sum_{i=1}^{N} g_i(1+\Delta_i)^{3/2}\exp(-x\Delta_i) \tag{2.8}$$

where $\Delta_i = (m_i - m_1)/m_1$ and x is the scaled inverse temperature $x = m/T$. This result implies that the cross section for scenarios with small mass differences between the LSP and NLSP will have an exponential dependence on their mass gap. Such scenarios are referred to as being “compressed mass spectrum” and will be the main focus of this study. As will be demonstrated in the future sections, these scenarios have additional experimental motivation to help explain the current search bounds for SUSY, in that the reconstructed decay products in these scenarios are more difficult to detect, meaning new techniques must be employed to probe them. The methodology for extracting the relevant parameters in order to quantify DM, if produced at particle colliders, as consisting of the LSP has been demonstrated in reference [51].

2.3 Status of Current SUSY Searches

Traditional searches for R-parity conserving SUSY at hadron colliders such as the Large Hadron Collider (LHC) have targeted decay chains from squarks and gluinos which produce high momentum jets as well as large missing transverse momentum due to the presence of LSPs at the end of the decay chain which cannot be directly detected. These searches are motivated by the large cross sections for QCD-mediated processes present at hadron colliders which might produce colored sparticles such as squarks and gluinos [7]. The exclusion reach of any SUSY search however will depend largely on the free parameters of the theory, including the SUSY breaking mechanism. For the MSSM, this would include 105 free parameters. Performing a phenomenological search without constraining some of these parameters is simply not possible. In order to mitigate this problem, simplified SUSY models are often constructed in which the masses, couplings, mixings, and branching ratios might be set which greatly reduces the complexity of the model. These models have the drawback however that it can become difficult to compare exclusion results from one model to another, and care must be taken when applying these limits to other SUSY models.

For the simplified model in which gluinos are pair produced and cascade decay into first and second generation quarks ($pp \to \tilde{g}\tilde{g},\ \tilde{g} \to q\bar{q}\tilde{\chi}_1^0$), gluino masses have been excluded out to approximately 2.1 TeV for neutralino masses of 600 GeV, as seen in figure 2.2a. For decays into heavier bottom (b) and top (t) quarks, these limits are even more stringent, with gluino masses being excluded out to approximately 2.3 TeV for neutralino masses as high as 1.5 TeV, as seen in figure 2.2b and 2.2c.

Similarly, for simplified models in which squarks are pair produced and cascade decay into quarks ($pp \to \tilde{q}\tilde{q},\ \tilde{q} \to q\tilde{\chi}_0^1$), first and second generation squarks have been excluded out to approximately 1.75 TeV for neutralino masses of around 400 GeV, as seen in figure 2.3a. For more complicated decay chains, these squark mass limits can be extended as far out as 1.8 TeV for neutralino masses as heavy as ≈1.8 TeV, as seen in figure 2.3b. In scenarios where third generations squarks are pair produced, bottom squark masses have been excluded out to 1.28 TeV for neutralino masses of 800 GeV, and top squark masses out to 1.3 TeV for neutralino masses of 700 GeV, as seen in figures 2.3c and 2.3d respectively.

In addition to searches for colored particles, searches for direct slepton and electroweakino production have also been performed. These searches often target Drell-Yan (DY) production in which sleptons and electroweakinos are pair produced ($pp \to Z \to \tilde{\ell}^+\tilde{\ell}^-$, $pp \to Z \to \tilde{\chi}_1^\pm\tilde{\chi}_1^\mp$), or produced via W bosons ($pp \to W^\pm \to \tilde{\chi}_2^0\tilde{\chi}_1^\pm$). These searches suffer from lower theoretical cross sections and therefore reduced signal event yields as compared to squarks and gluinos. Despite these drawbacks, strong exclusion limits have also been set on these particles. If we look at the slepton sector, we find that searches have excluded slepton masses for the first and second generation particles out to masses around 700 GeV for neutralino masses of around

300 GeV, assuming the sleptons are pair produced and decay to leptons ($pp \rightarrow \tilde{\ell}^+\tilde{\ell}^-$, $\tilde{\ell} \rightarrow \ell\tilde{\chi}_1^0$), as seen in figure 2.4. For third generation sleptons (staus), these bounds are much less stringent with masses excluded out to only 380 GeV for massless neutralinos. For electroweakinos, similar bounds have been drawn. It is important to note however that these scenarios are heavily dependent on the flavor mixing of the simplified model being studied. As seen in figure 2.5, masses for the lightest charginos and next to lightest neutralinos can be excluded in certain scenarios out to masses of 1050 GeV, assuming a massless LSP. For compressed mass spectrum scenarios, which are cosmologically motivated in order to produce the observed DM relic density, these excluded mass ranges are significantly reduced. Figures 2.6a and 2.6b show such exclusion bounds, assuming the lightest electroweakinos are primarily Wino/Bino-like. Similarly, figures 2.7a and 2.7b show the same exclusion limits when the lightest electroweakinos are primarily Higgsino-like. For these specific scenarios, the excluded masses can be as low as below 100 GeV for charginos and heavier neutralinos ($\tilde{\chi}_0^2$), when assuming the mass gap between the chargino and lightest neutralino is as low as a few GeV. These regions are historically difficult to probe when targeting traditional search methods, such as direct production of charginos and neutralinos. This is due to the fact that any SM decay products will be “soft” (low momentum) and therefore suffer from reduced reconstruction efficiency in the detector. This analysis will probe exactly these regions by targeting unique production mechanisms, as will be discussed in detail in chapter 5.

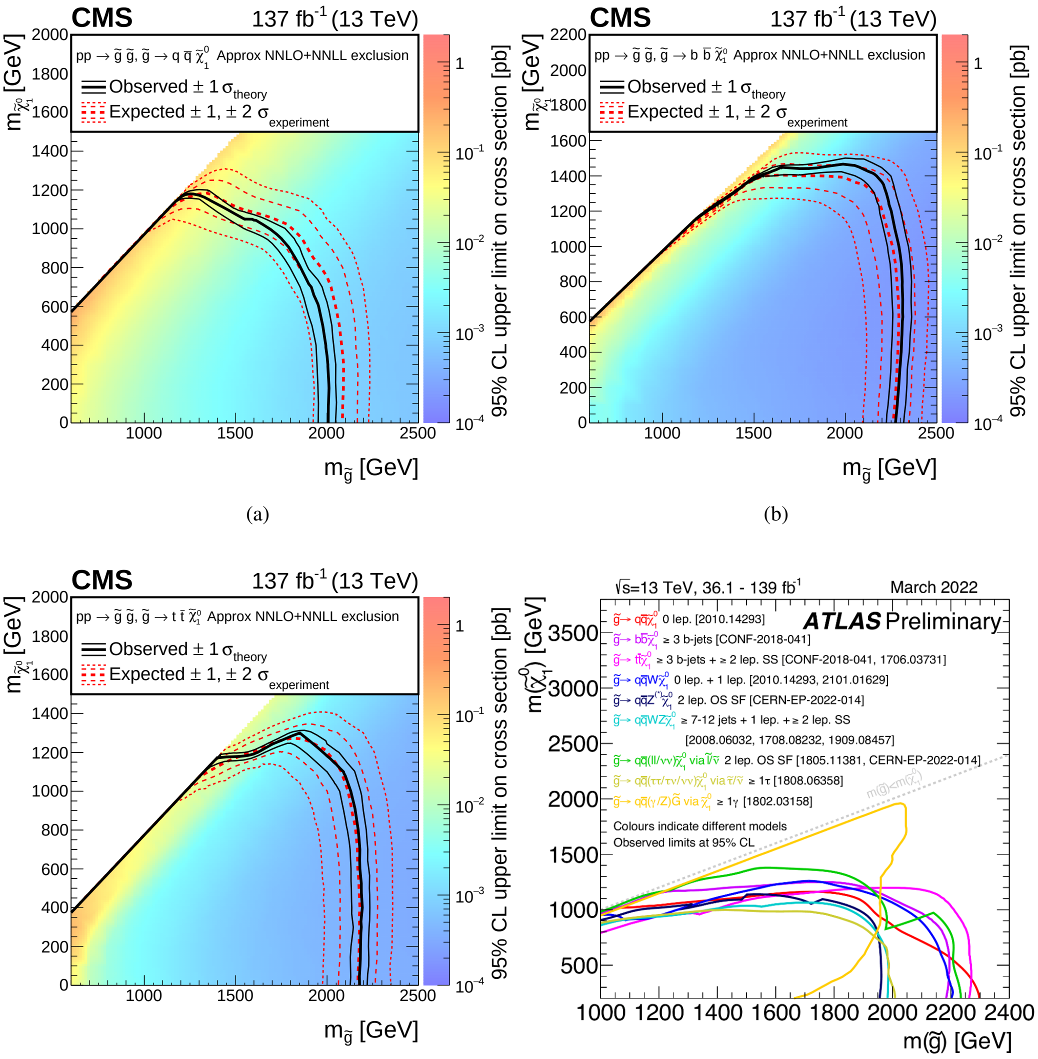

(a) (b) (c) (d)

Figure 2.2: Exclusion limits for gluino and neutralino masses for simplified models assuming gluino pair production and subsequent gluino decay into 2 quarks + LSP [6].

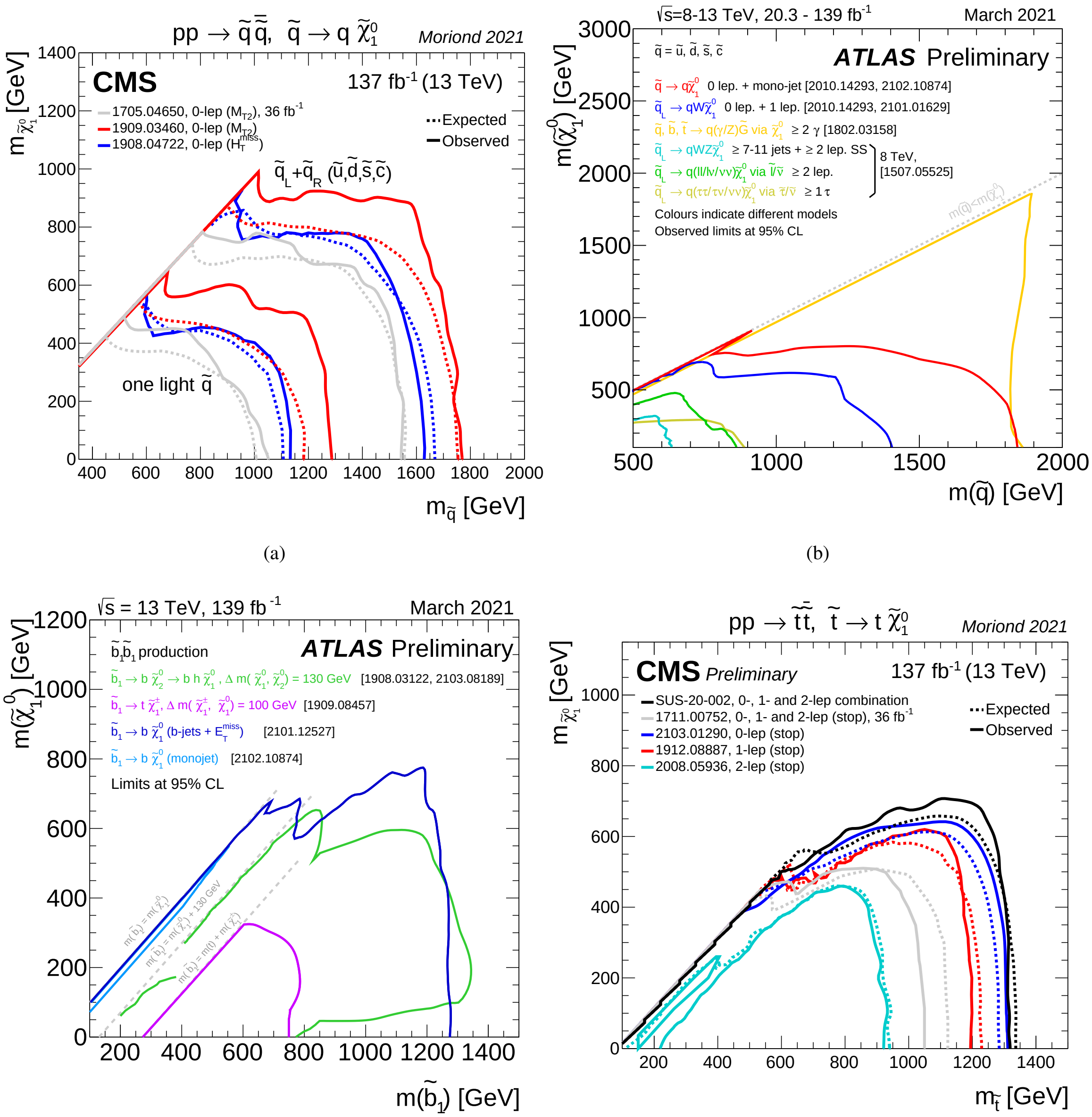

(a)

(b)

(c)

(d)

Figure 2.3: Exclusion limits for squark and neutralino masses for simplified models assuming squark pair production and subsequent squark decay into 1 quark of the same generation + LSP (top left, bottom left, bottom right) and more complicated decay scenarios (top right) [7].

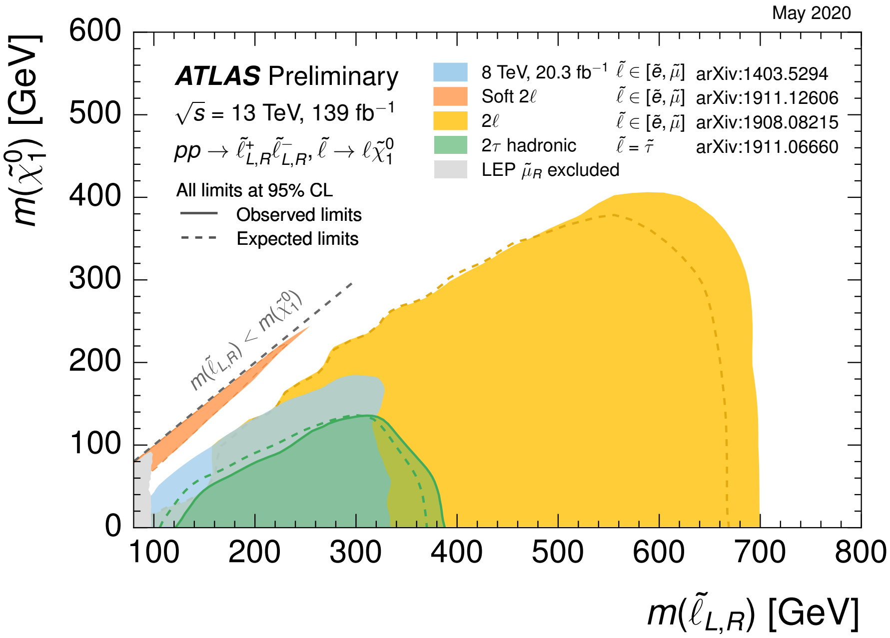

Figure 2.4: Exclusion limits for slepton and neutralino masses for simplified models assuming slepton pair production and subsequent decays into 1 slepton + LSP [7].

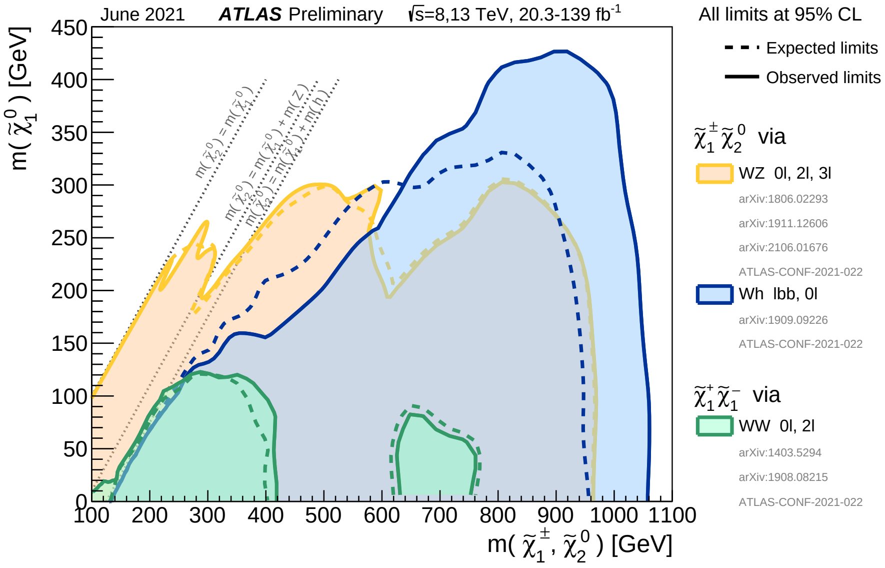

Figure 2.5: Exclusion limits for chargino and neutralino masses for simplified models assuming direct production of charginos and neutralinos and subsequent decays into leptons + LSP [7].

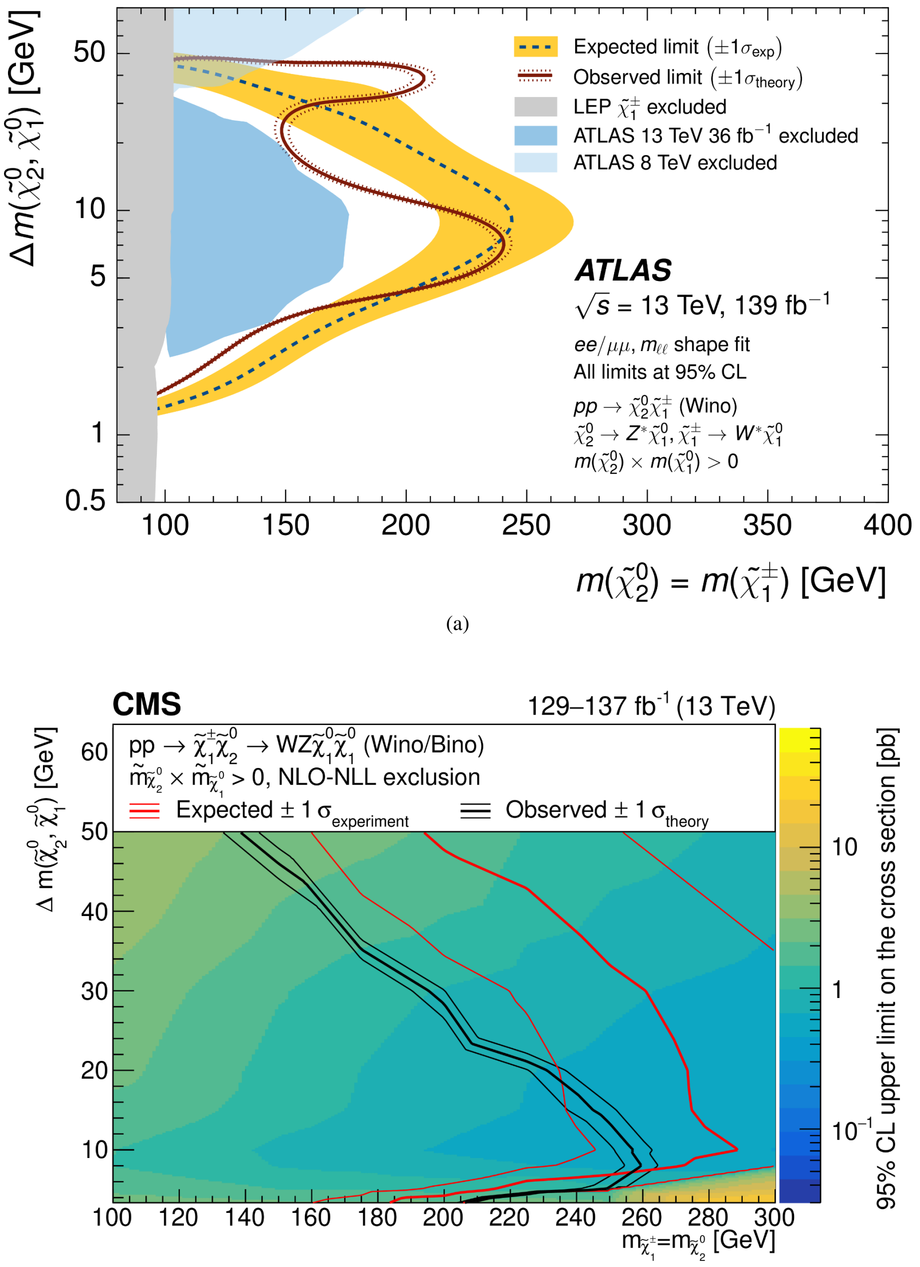

(a)

(b)

Figure 2.6: Exclusion limits for chargino and neutralino masses for simplified models which assume a compressed mass spectrum and primarily Wino/Bino-like light electroweakinos [8, 9].

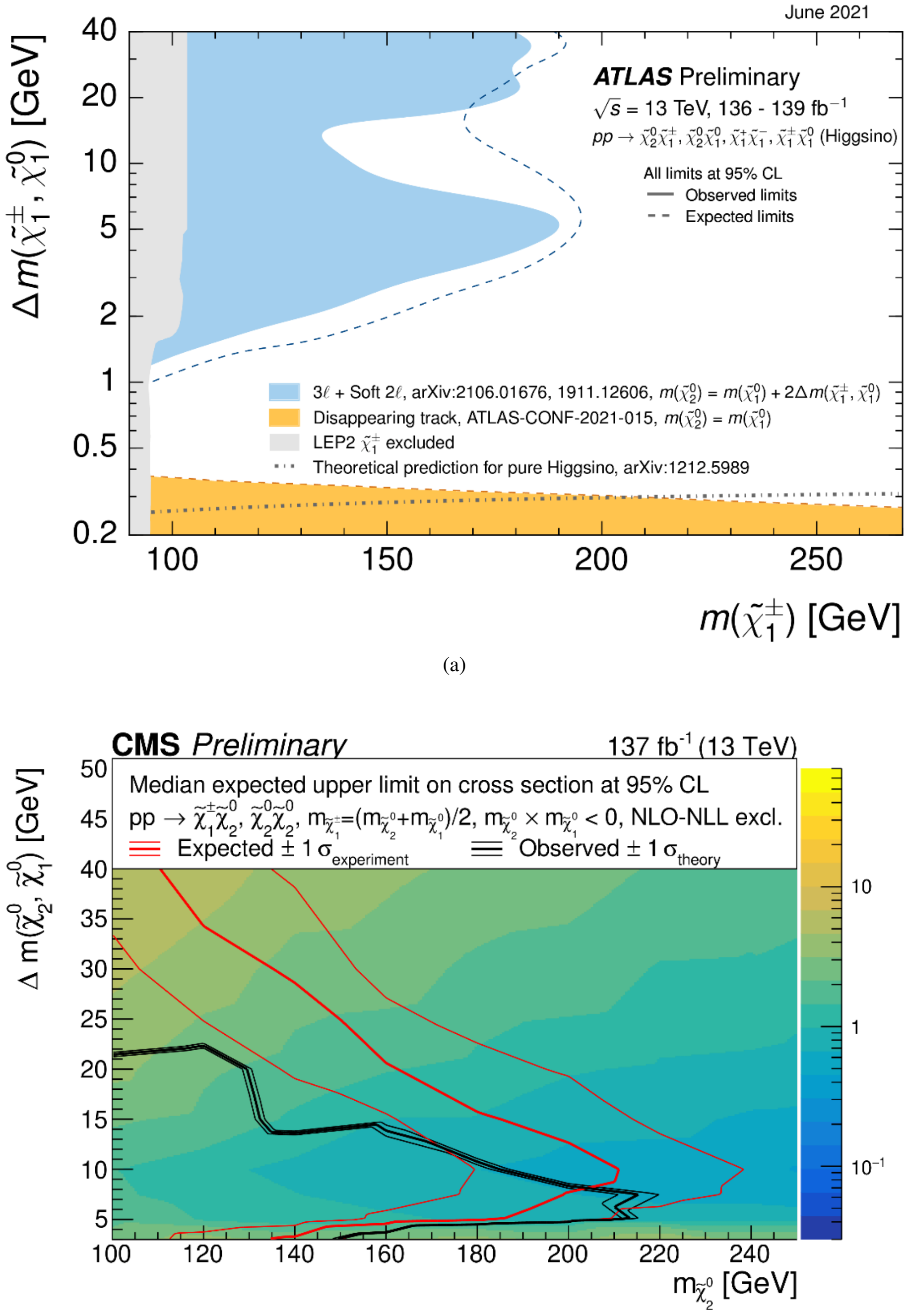

(a)

(b)

Figure 2.7: Exclusion limits for chargino and neutralino masses for simplified models which assume a compressed mass spectrum primarily Higgsino-like light electroweakinos.

CHAPTER 3

The Large Hadron Collider & the Compact Muon Solenoid Detector

3.1 The Large Hadron Collider

The Large Hadron Collider (LHC), as seen in figure 3.1, is a two-ring-superconducting-hadron accelerator and collider located at the international border of Switzerland and France, near Geneva, Switzerland [52]. As a hadron collider, the LHC primarily collides protons at a center-of-mass energy of 13 TeV[1] and a luminosity of 10^{34} cm^{-2}s^{-1}, with additional heavy nuclei collisions also being conducted throughout the year (primarily in the last month of running). The LHC was completed in 2008 and is currently operated by the European Organization for Nuclear Research (CERN). The LHC consists of two all-purpose, high luminosity detectors (ATLAS & CMS) and seven smaller specialized detectors (LHCb, ALICE, TOTEM, LHCf, MoEDAL, FASER, SND). The primary motivation for the LHC was to elucidate the nature of electroweak symmetry breaking for which the Higgs mechanism is presumed to be responsible. The experimental study of the Higgs mechanism can also shed light on the mathematical consistency of the Standard Model at energy scales above about 1 TeV [53]. Perhaps the most famous discovery made by the LHC thus far was the detection of the higgs boson in 2012, first detected by the CMS detector, and then validated by the ATLAS detector shortly thereafter [54].

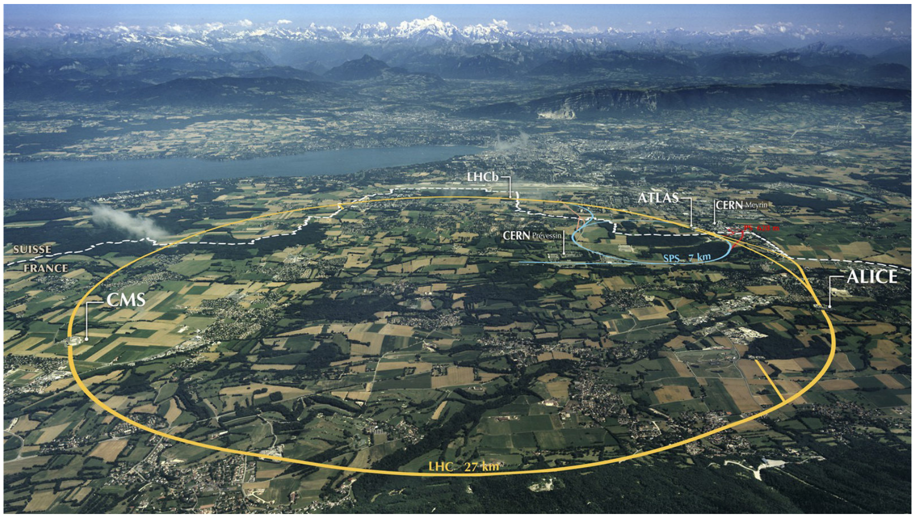

Figure 3.1: Aerial view of the LHC with relevant detectors shown [10].

---

[1] At the time of writing, the center-of-mass energy has recently been increased to 13.6 TeV. All data used within this analysis however was recorded at a center-of-mass energy of 13 TeV

3.2 Proton-Proton Collisions

Protons are not fundamental particles but are instead composite particles with charge $+1e$ which are formed out of two up quarks and a down quark (which are referred to as valence quarks) in addition to gluons which carry the strong interaction force that keeps the quarks bound together. Due to quantum fluctuations, there will also be present quark–anti-quark pairs within the proton which are referred to as virtual quarks [55]. When one collides protons, it is actually these constituent particles, referred to as partons, which are interacting. We cannot know a priori which partons will collide within any given event, nor what amount of the proton's overall momentum such a parton will carry, and therefore these quantities must be modeled using a parton distribution function (PDF), as shown in figure 3.2. The PDFs which govern the proton-proton interactions are dependent on the energy scale at which the protons are collided (Q^2). PDFs have been studied and measured experimentally at previous colliders, such as the ZEUS and H1 experiments conducted at the HERA accelerator [56].

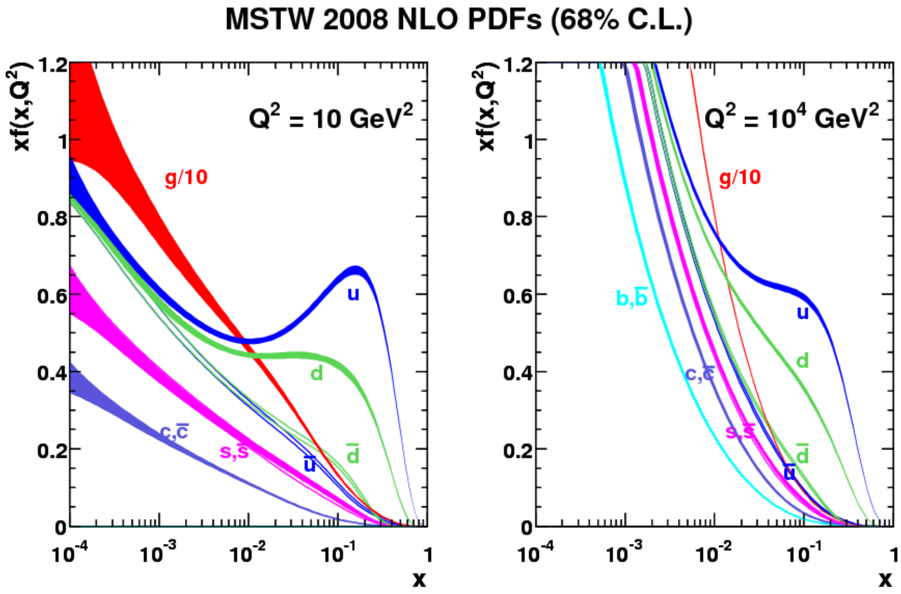

Figure 3.2: PDFs for different energy scales (Q^2). x is the longitudinal momentum fraction given by $x = p_{\text{parton}}/p_{\text{proton}}$ [11].

When colliding particles, one can predict the number of events which produce a specific set of final state particles using the following equation:

$$N_{\text{process}} = \sigma_{\text{process}} \int L dt \tag{3.1}$$

where N_{process} is the number of expected events for any specific process, σ_{process} is the associated cross section for the process of interest which can be calculated theoretically using QFT and the SM via the the matrix element, and L is the luminosity, which can be seen in figure 3.3 (left). The cross sections for various SM processes can be seen in figure 3.4. When studying new physics at a particle collider, one is typically interested in studying events from “hard” collisions in which there is large momentum transfer present and new particles are created. Interactions which produce a new physics phenomenon are expected to be exceedingly rare (depending on the theory of new physics being considered) which is why large luminosities are often required in order to probe these scenarios.

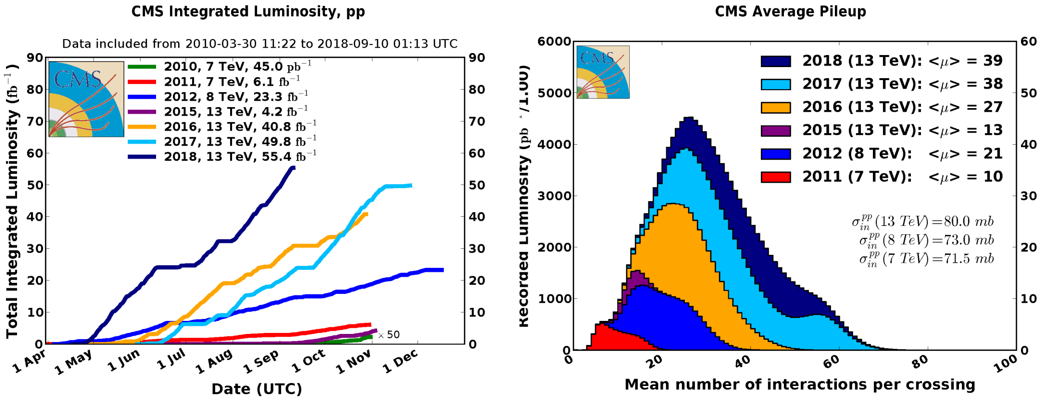

Figure 3.3: Total integrated luminosity of pp collisions by the CMS detector broken out by year and center-of-mass energy (left). Average pileup (number of interactions per bunch crossing) recorded by the CMS detector, also broken out by year (right) [12].

The LHC collides protons at a rate of a bunch crossing every 25 ns, with each bunch containing $\sim 10^{11}$ protons and a total inelastic cross section of $\sim 80\ m$b [57, 12]. The result of this is multiple inelastic interactions per bunch crossing, producing what is referred to as pile-up interactions (PU). The mean number of PU interactions per crossing for various years can be seen in figure 3.3 (right). PU interactions are a large nuisance when analyzing data, as the extraneous particles can cause a number of detector problems, including incorrect reconstruction of particle energy, momentum, and identification. In order to alleviate these problems from PU, the detectors at the LHC must be designed with high granularity, excellent time resolution, and accurate synchronization in order to correctly identify and account for which interactions are PU interactions and which are not. The treatment of PU jets at CMS will be discussed further in section 4.4.1.

An additional consideration is the large amount of data produced at the LHC. It is simply not feasible to record and keep all interactions produced at the LHC, nor is it desirable to do so given the large QCD cross section which produces interactions that are not of interest when probing new physics scenarios. LHC detectors must therefore implement a “triggering” system to reduce the overall recorded and analyzed data. The details of these systems will be discussed in section 3.4.

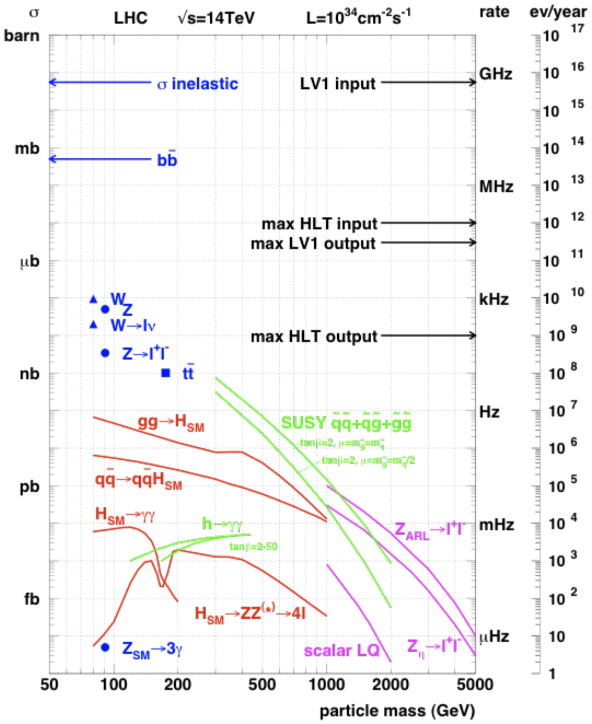

Figure 3.4: Cross sections for various SM processes (blue, red) in addition to theoretical cross sections for various new physics scenarios (green, SUSY; pink) [13].

3.3 The Compact Muon Solenoid Detector

The Compact Muon Solenoid (CMS) detector is one of two all-purpose detectors located at the LHC and is installed approximately 100 meters beneath the French village of Cessy. The detector, as seen in figure 3.5, was designed to meet the following performance requirements [53]:

- Good muon identification and momentum resolution over a wide range of momenta and angles, good dimuon mass resolution ($\approx$1% at 100 GeV), and the ability to determine unambiguously the charge of muons with momentum less than 1 TeV.

- Good charged-particle momentum resolution and reconstruction efficiency in the inner tracker. Efficient triggering and offline tagging of τ's and b-jets, requiring pixel detectors close to the interaction region.

- Good electromagnetic energy resolution, good diphoton and dielectron mass resolution ($\approx$ 1% at 100 GeV), wide geometric coverage, π^0 rejection, and efficient photon and lepton isolation at high luminosities.

- Good missing-transverse-energy (E_T^{miss}) and dijet-mass resolution, requiring hadron calorimeters with a large hermetic geometric coverage and with fine lateral segmentation.

CMS consists of five main sub-detectors: the inner tracker (IT); the electromagnetic calorimeter (ECAL); the hadronic calorimeter (HCAL); the superconducting solenoid magnet; and the muon system. The purpose of the solenoid magnet, which has a strength of 3.8T, is to bend charged particles as they move through the detector, allowing for the measurement of their momenta.

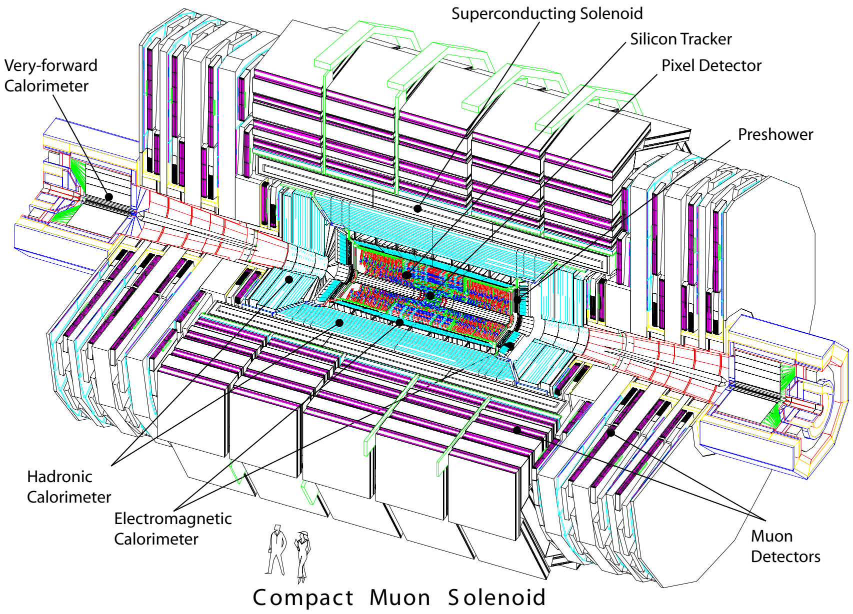

Figure 3.5: A digital rendering of CMS, showing its relevant size and various labeled sub-detectors [14].

The coordinate system that CMS uses, which can be seen in figure 3.6a, has its center at the nominal collision point within the detector. The *xyz* axes are oriented such that the *x*-direction points towards the ring center, the *y*-axis points directly upward, and the *z*-axis points towards the Jura mountains. A much more commonly used convention however is to express the coordinates using a cylindrical coordinate system, where the azimuthal angle ϕ is measured from the *x*-axis towards the *y*-axis in the *x*-*y* plane, and the polar angle θ is measured from the *z*-axis. Even more common than using the polar angle however, is to use the pseudorapidity (η), given by:

$$\eta = -\ln\tan(\frac{\theta}{2}) \tag{3.2}$$

The motivation of using the pseudorapidity instead of the polar angle is that the pseudorapidity is an approximately lorentz invariant quantity, meaning it is an equivalent value in both the reference frame of the detector and the highly boosted reference frame of the relativistic decay products coming from particle collisions. Various values of θ and their corresponding η values are shown for reference in figure 3.6b. It is additionally common to consider the component of an object solely within the $x-y$ plane, which is referred to as the "transverse plane". For instance, when studying the momentum of a charged particle, it is common to consider only the transverse component, which we refer to as the transverse momentum (p_{T}).

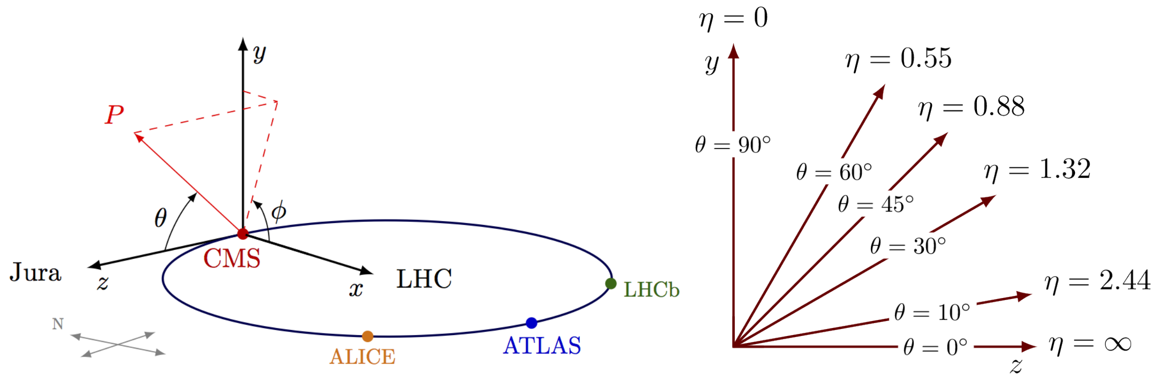

(a) (b)

Figure 3.6: CMS coordinate system[15, 16].

3.3.1 Inner Tracking System

The inner tracker (IT) is the sub-detector which is closest to the interaction point (IP) where proton collisions occur. As a result, the IT will experience the highest particle flux and radiation. The purpose of the IT is to reconstruct the paths of charged particles as they move through the detector and bend in the 3.8T magnetic field generated by the superconducting solenoid magnet. Reconstructing the paths of charged particles helps in their identification and is crucial to measuring their momenta. The IT extends radially to nearly 110 cm with a total length of 540 cm, and is able to provide coverage to $\eta < 2.4$. A cross section view of a quarter of the IT can be seen in figure 3.7a where the slice has been taken along the beam line.

The IT is comprised of two different detector technologies which are intended to achieve different outcomes. Located closest to the IP ($r < 20$ cm) is the pixel tracker, as seen in figure 3.7b, consisting of three barrel layers (shown in green) and two endcap layers (shown in pink). In 2017, the pixel tracker was upgraded to include an additional barrel layer (four in total) and additional endcap layer (three in total). The pixel detectors are approximately $100 \times 150\ \mu\mathrm{m}^2$ in size and allow for high granularity. Their small size allows for an occupancy of $\sim 10^{-4}$ per pixel per bunch crossing. In total there are 66 million pixels within CMS (123.5 million pixels after the 2017 upgrade). Located just beyond the pixel tracker are silicon strip trackers. At this distance ($20 < r < 55$ cm) the particle flux is low enough such that silicon microstrip detectors with a minimum cell size of $10\ \mathrm{cm} \times 80\ \mu\mathrm{m}$ can be used. These detectors have an occupancy of $\approx 2-3\%$ per LHC bunch crossing. The silicon strip trackers are divided into barrel tracker regions and endcap tracker regions. The barrel tracker regions are further subdivided into a tracker inner barrel, consisting of 4 layers, and a tracker outer barrel, consisting of 6 layers. Similarly, the endcap tracker regions are subdivided into 3 tracker

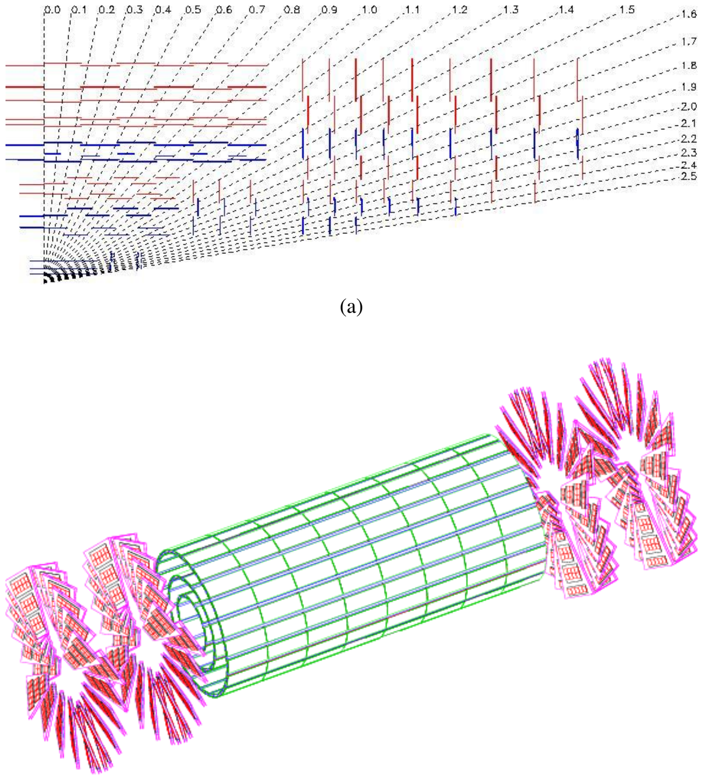

(a)

(b)

Figure 3.7: (3.7a) A view of the IT along the z-axis showing 1/4 of the apparatus. (3.7b) An overview of the location of the pixel detectors within the IT, showing the 2016 barrel region in green and 2016 endcap in pink (these regions were upgraded in 2017 to include four total barrel region layers and three total endcap region layers).[17].

inner disks and 9 tracker endcap disks. In total there are 9.6 million silicon strips within CMS. As previously mentioned, being able to accurately reconstruct the track of charged particles within the IT allows for precise measurement of their momenta. Figure 3.8 shows the resolution the IT can achieve for muons with transverse momentum (p_T) of 1 GeV, 10 GeV, and 100 GeV, as a function of the muons pseudorapidity. It is interesting to note that muons of low p_T (1 GeV) and muons of high p_T (100 GeV) have worse momentum resolution than those of moderate p_T (10 GeV). This is due to different phenomenon. For very low p_T muons, these particles will “corkscrew” within the detector meaning they bend too greatly and do not interact with as many different IT layers, making path reconstruction more difficult. Very high p_T muons on the other hand follow a very straight path in the detector. As a result the curvature of their path (which is what is needed to measure their momentum) is difficult to measure, leading to worse resolution. Moderate p_T muons however bend adequately and interact with enough IT layers to allow for the best possible momentum resolution values.

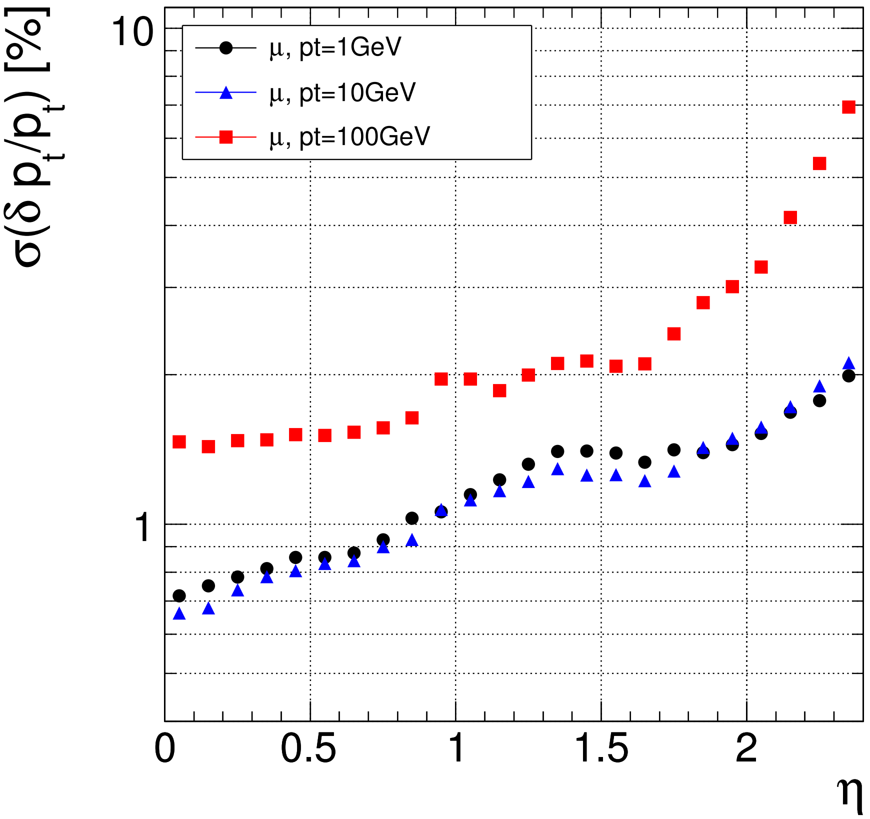

Figure 3.8: IT muon momentum resolution as a function of η [17].

3.3.2 Electromagnetic Calorimeter

Just beyond the IT is the electromagnetic calorimeter (ECAL). The ECAL is a hermetic, homogeneous calorimeter comprising 61,200 lead tungstate ($PbWO_4$) crystals mounted in the central barrel part, closed by 7324 crystals in each of the 2 endcaps [17]. The purpose of the ECAL is to measure the energy of electrons and photons and aid in their identification. When a photon or electron moves through the ECAL, the lead tungstate crystals begin to scintillate. This scintillation is detected by a photo-detector located at the rear of the device. The ECAL was designed to meet the following requirements [18]:

- Excellent energy and position/angle resolution up to $|\eta| < 2.5$, to match the tracker coverage.

- Hermeticity, compactness and high granularity.

- Fast response ($\sim$ 25 ns) and particle id, energy and isolation measurement at trigger level.

- Large dynamic range (5 GeV to 5 TeV) and excellent linearity (at the per-mill level).

- Radiation tolerance (ECAL was designed for 14 TeV and L = 10^{34} cm^{-2}s^{-1}, and for a total luminosity of 500 fb^{-1}).

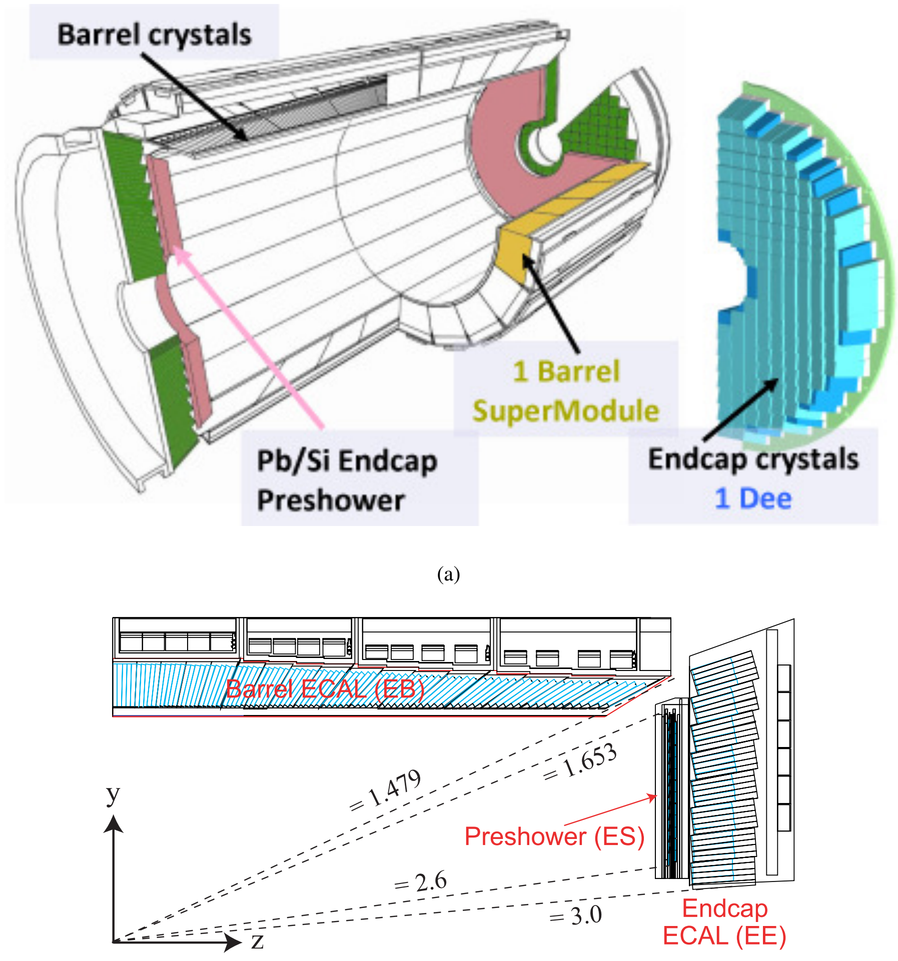

Figure 3.9: 3D rendering of the CMS ECAL, showing the location of various sub-detectors (top). Coverage by ECAL in η (below) [18].

Figure 3.9 shows a 3D rendering of the ECAL detector with various sub-detectors (top) as well as coverage in η (below).

3.3.3 Hadronic Calorimeter

Located beyond the ECAL from the IP is the hadronic calorimeter (HCAL). The purpose of the HCAL is to measure the energy and aid in the identification of hadrons. The HCAL is divided into three sub-detectors: the barrel (HB), which provides coverage out to $|\eta| = 1.4$; the endcap (HE), which provides coverage between $1.3 < |\eta| < 3.0$; and the forward calorimeter (HF), which provides coverage from $2.9 < |\eta| < 5.0$. The HCAL consists of 17 layers of plastic scintillator tiles sandwiched between layers of stainless steel and brass. The stainless steel and brass act as absorber materials. The barrel layers and their associated thickness are as follows [53]:

- (Layer 0) 9 mm Scintillator/61 mm Stainless Steel
- (Layers 1-8) 3.7 mm Scintillator/50.5 mm Brass
- (Layers 9-14) 3.7 mm Scintillator/56.5 mm Brass
- (Layers 15+16) 3.7 mm Scintillator/75 mm Stainless Steel/9 mm Scintillator

A schematic view of the HCAL arrangement can be seen in figure 3.10, where the HCAL barrel, HCAL endcap, and forward calorimeter regions are highlighted in yellow.

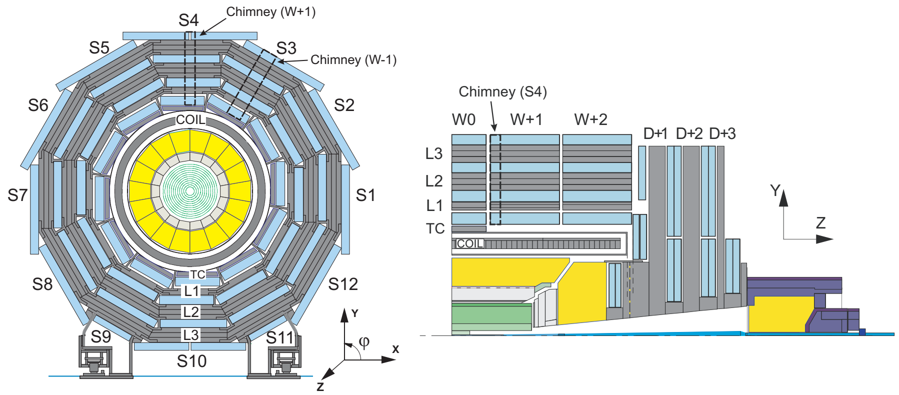

Figure 3.10: A schematic view of the HCAL arrangement showing the location of the HB, HE, and HF as shown in yellow [19].

3.3.4 Superconducting Solenoid Magnet

Surrounding and enveloping the IT, ECAL, and HCAL is the 3.8T superconducting solenoid magnet. As previously mentioned, the large magnetic field is required in order to sufficiently bend charged particles as they move through the detector, due to the Lorentz force they experience. A detailed rendering of the magnetic field within the CMS detector is shown in figure 3.11. The magnetic field is generated by a nominal current of 19.5kA which is carried by a conductor comprised of 3 components: a Rutherford type superconducting cable, a high purity aluminum stabilizer, and an aluminum alloy reinforcement [58].

3.3.5 The Muon System

Located furthest from the IP is the muon system. The muon system plays the extremely crucial role of accurately identifying and measuring the momentum of muons (this importance will be expanded upon in section 3.4 when discussing triggering). The muon system is divided into two main regions, the barrel region which covers $|\eta| < 1.2$, and the endcap region which covers $(0.9 < |\eta| < 2.4)$, as can be seen in

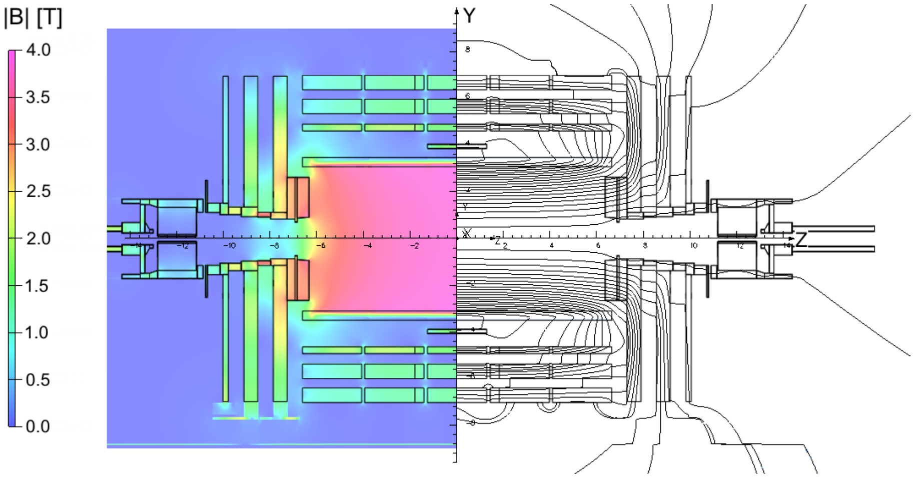

Figure 3.11: Value of $|B|$ (left) and field lines (right) predicted on a longitudinal section of the CMS detector, for the underground model at a central magnetic flux density of 3.8 T. Each field line represents a magnetic flux increment of 6 Wb [19].

figure 3.12. The muon system employs three different gas ionization technologies: drift tubes (DT), cathode strip chambers (CSC), and resistive plate chambers (RPC). The muon system was designed to meet the following operational goals [20]:

- Excellent trigger performances on single and multi-muons events and an unambiguous identification of the bunch crossing to be obtained by combining fast dedicated trigger detectors, (RPCs) with detectors having precise spatial resolution (DTs, CSCs).
- Redundancy in both trigger and reconstruction which is obtained by using three technologies, combined in order to have two independent muon systems in the whole angular region.
- Operate within a magnetic field of 4 Tesla and have the possibility to measure muons twice, once in the tracker and again in the muon spectrometer in order to perform very good results in the muon momentum and charge measurements in the whole η region and from few GeV up to a TeV.
- Achieve a very high efficiency muon identification rate ($> 95\%$) up to $\eta = 2.4$.
- The detectors must be capable to work with a strong magnetic field and high radiation and interaction background.

The muon system operates via the ionization of gas within the chambers of the various subsystems. When a charged particle moves through the system, the ionized gas causes electrical signals to be produced which are then recorded as “hits”. These hits then allow for the reconstruction of the particles path through the muon system. The muon system can then work in tandem with the IT in order to correctly measure and identify

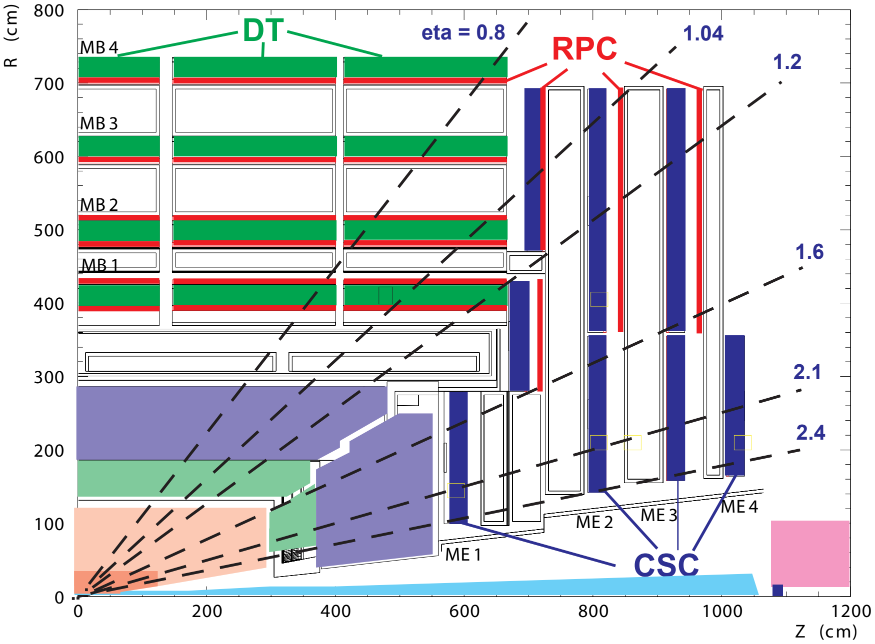

Figure 3.12: Layout of the muon system, showing the barrel region (green) and endcap region (blue) as well as explicitly calling out the drift tubes (DT), resistive plate chambers (RPC), and cathode strip chambers (CSC) [20].

muons. This is performed algorithmically by tracing "tracks" (deposits of energy left within the IT) as part of the particle identification process. The result is the measurement and identification of a "global muon" (i.e. a muon identified using both the muon system and the IT). The muon system is also able to operate alone, resulting in "local muons". The performance of such measurements is comparatively worse however. This can be seen in figure 3.13 which compares the resolution of momentum measurements between local muons (blue), muons reconstructed solely by the IT (green), and global muons reconstructed using both detectors (red).

3.4 Triggering & Data Acquisition

The LHC collides particles at a rate which is impractical for recording, processing, and storing all of their associated data. In addition, the large cross sections of SM physics processes compared to the extremely small cross sections of theoretical new physics processes means the majority of collisions which take place do not result in interactions of particular interest for physics analyses. In order to combat this problem, a "triggering" system is employed which has the designated purpose to reduce the number of recorded and analyzed events into a more manageable amount, as well as indicate that an interesting physics event has occurred. The CMS trigger system is comprised of two levels. The first level (L1) is made up of hardware triggers which must fire within $4\mu s$ of an event occurring. The L1 system combines information from ECAL,

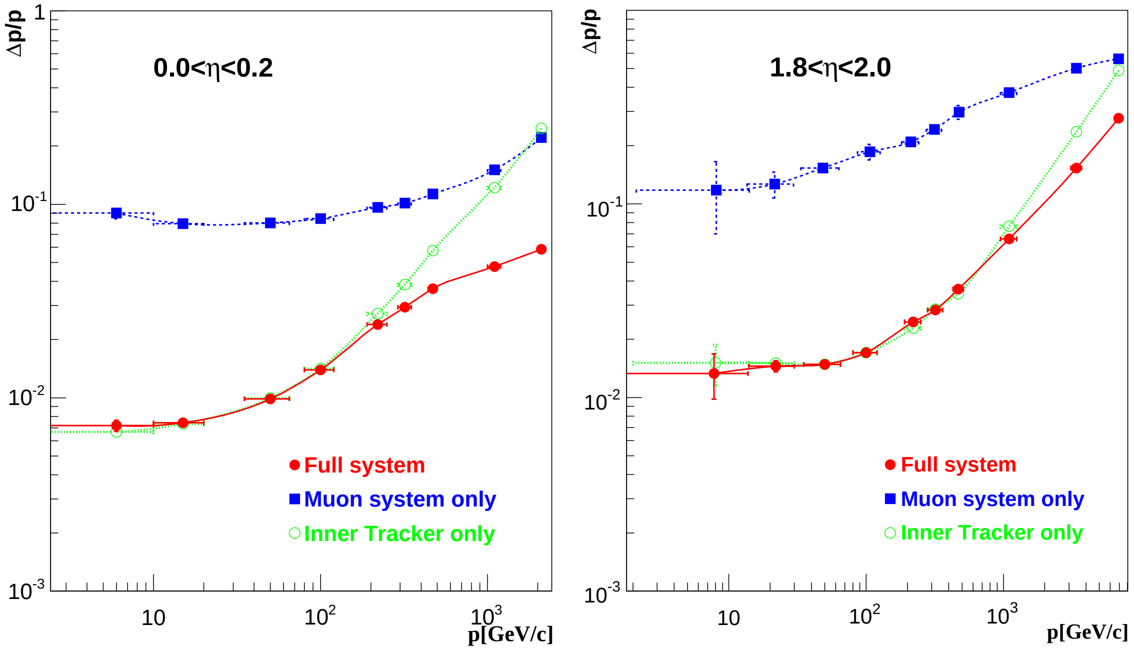

(a) (b)

Figure 3.13: Momentum resolution for muons detected solely within the barrel region (left) and solely within the endcap region (right). Blue indicates muons measured using solely the muon system, green indicates muons measured using solely the IT, while red represents muons measured using both [17].

HCAL, and the muon system before combining the information which is evaluated by a global trigger (GT) that ultimately decides whether or not to reject the event. A flow chart of the L1 trigger process can be seen in figure 3.14. The result of L1 triggering is a reduction in total data taking to an output around 100kHz.

Once an event is registered by the L1 trigger, it is transferred to the second level of the triggering system, referred to as the “high-level trigger” (HLT). The HLT is purely software based in nature. Event selection at this level is performed similarly to that used in offline processing. Objects such as electrons, muons, and jets are reconstructed and identified on an event by event basis and certain criteria are applied in order to select events of possible interest for later analysis. The result of HLT triggering is a further reduction of events recorded, to a level of $\sim 1kHz$. The data is then moved to tier-0 CMS computing centers for archival offline storage of events.

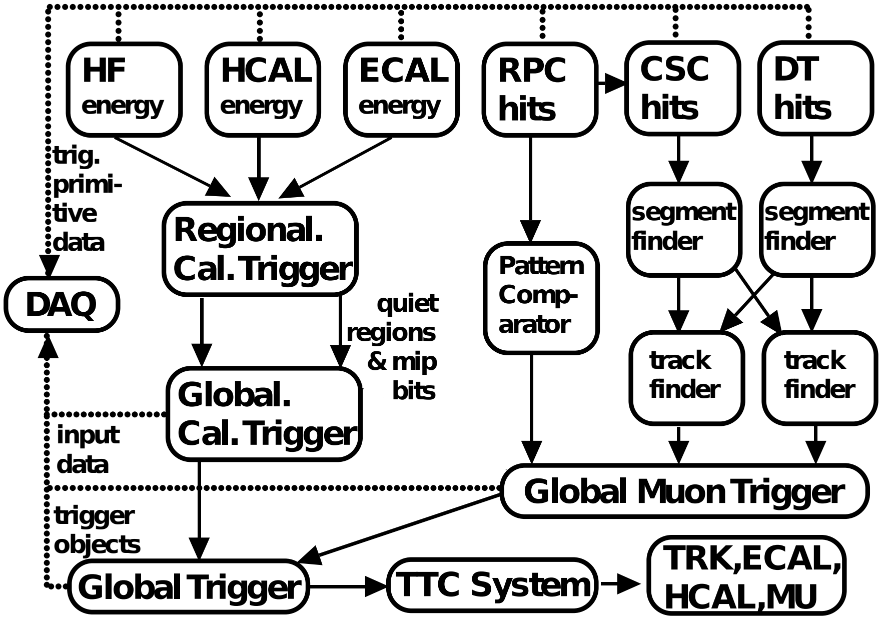

Figure 3.14: Overview of the CMS L1 trigger system. Data from ECAL and HCAL, are processed first regionally (RCT) and then globally (GCT). Similarly, energy deposits (hits) from the resistive- plate chambers (RPC), cathode strip chambers (CSC), and drift tubes (DT) are processed and sent onwards to a global muon trigger (GMT). The information from the GCT and GMT is combined in a global trigger (GT), which makes the final trigger decision. This decision is sent to the tracker (TRK), ECAL, HCAL or muon systems (MU) via the trigger, timing and control (TTC) system. The data acquisition system (DAQ) reads data from various subsystems for offline storage. [21].

CHAPTER 4

Particle Identification & Event Reconstruction

This chapter will detail how physics objects of interest are identified, measured, and reconstructed at CMS. Many sections will reference the particle flow algorithm (PF) which is discussed in detail in section 4.7. Figure 4.1 shows a brief overview of how various particles interact with the different detector layers, which will be expanded upon in greater detail in the following sections.

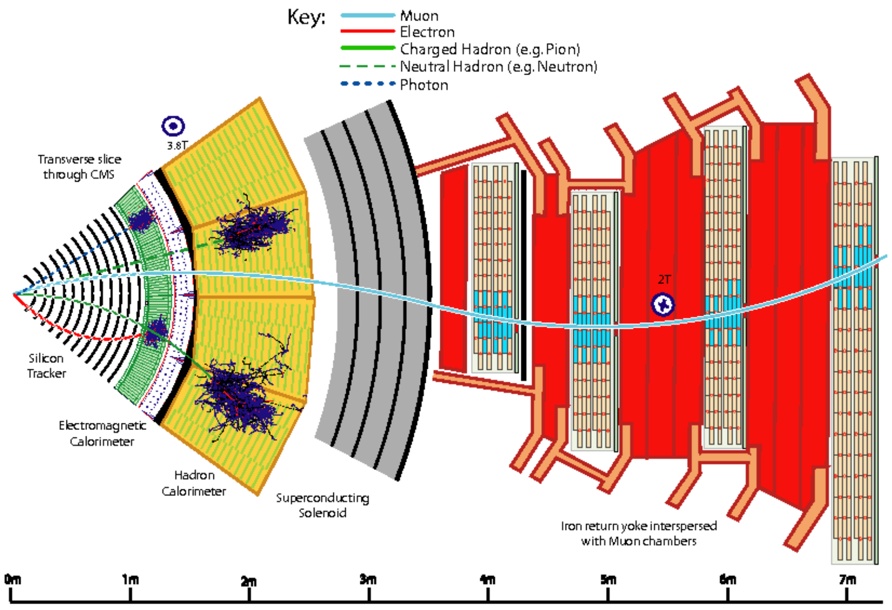

Figure 4.1: Diagrammatic overview of particle interactions with various CMS subdetector layers. Neutrinos notably do no interact with any detector layers, however their production can be inferred when “missing” transverse momentum ($p_{\mathrm{T}}^{\mathrm{miss}}$)is reconstructed in the detector [22].

4.1 Tracking & Vertex Finding

Tracking and vertex finding, which refers to finding the path of charged particles as they move through the detector including their origin point, are both of crucial importance for performing physics analyses. This knowledge is required to accurately identify and resolutely measure the momentum of particles produced within the CMS detector. As mentioned in section 3.3.1, deposits of energy referred to as “tracks” are left within the inner tracker by charged particles as they move through the detector. These tracks are then fitted using tracking algorithms (of which there are many) to determine the position parameters and momentum of the charged particles. These algorithms can be costly in terms of CPU cycles and there is therefore often a trade off between efficiency and accuracy [21]. The collection of reconstructed tracks at CMS is produced by multiple passes (iterations) of the tracking reconstruction algorithm, in a process called iterative tracking. The basic idea of iterative tracking is that the initial iterations search for tracks that are easiest to find (e.g., of relatively large transverse momentum (p_T), and produced near the interaction region). After each iteration, hits associated with tracks are removed, thereby reducing the combinatorial complexity, and simplifying subsequent iterations in a search for more difficult classes of tracks (e.g., low momentum, or greatly displaced tracks). The iterations proceed as follows [59]:

- Iteration 0, the source of most reconstructed tracks, is designed for prompt tracks (originating near the pp interaction point) with $p_\mathrm{T} > 0.8$ GeV that have three pixel hits.
- Iteration 1 is used to recover prompt tracks that have only two pixel hits. Iteration 2 is configured to find low-p_T prompt tracks.
- Iterations 3–5 are intended to find tracks that originate outside the beam spot (luminous region of the pp collisions) and to recover tracks not found in the previous iterations. At the beginning of each iteration, hits associated with high-purity tracks (defined in section 4.4) found in previous iterations are excluded from consideration (masked).

The primary vertex from a pp collision refers to the interaction vertex with the largest total p_T originating from it, which is assumed to originate from a hard scattering event. This definition is reasonable due to the fact that we expect inelastic hard scattering interactions to produce large p_T decay products. The primary vertex can then be reconstructed using tracking (although there is some interplay, as an initial approximate beam spot is required to start the tracking algorithm). Knowledge of the primary vertex is useful, for instance to remove physics objects such as muons which may come from the "non-prompt" decay of a heavy quark rather than being created by a pp interaction, or to correctly identify PU jets.

4.2 Electrons & Photons

Electrons and photons are reconstructed in similar fashion to each other in the sense that both objects are expected to leave large energy deposits in ECAL. Due to electrons being charged objects, they will additionally leave tracks in the IT which can be reconstructed and should point to an ECAL energy deposit. As an electron or photon propagates through the detector, it may interact with the surround material where the electron will emit bremsstrahlung photons, and the photon can convert into an electron-positron pair. The result then is that what may have initially been a single electron or photon will be reconstructed as a shower consisting of multiple electrons and photons [23]. An algorithm is then used to combine the clusters of individual particles into a single object in order to reconstruct the energy of the initial electron or photon. Electrons additionally lose momentum when emitting bremsstrahlung photons and therefore the curvature of such particles will change. A dedicated algorithm is used then to estimate the track-parameters of electrons. A general outline of how the full reconstruction is performed is as follows [23]:

- The energy reconstruction algorithm starts with the formation of clusters by grouping together crystals with energies exceeding a predefined threshold (typically ~ 80 MeV in ECAL barrel region and ~ 300 MeV in ECAL endcap region), which is generally 2 or 3 times bigger than the electronic noise expected for these crystals. A seed cluster is then defined as the one containing most of the energy deposited in any specific region, with a minimum transverse energy ($E_{\mathrm{T}}^{\mathrm{seed}}$) above 1 GeV. E_{T} is defined as $E_{\mathrm{T}} = \sqrt{m^2 + p_{\mathrm{T}}^2}$ for an object of mass m and transverse momentum p_{T}.

- ECAL clusters within a certain geometric area ("window") around the seed cluster are combined into superclusters (SC) to include photon conversions and bremsstrahlung losses. This procedure is referred to as "superclustering".

- Trajectory seeds in the pixel detector that are compatible with the SC position and the trajectory of an electron are used to seed the GSF tracking step.

- In parallel to the above steps, all tracks reconstructed in the event are tested for compatibility with an electron trajectory hypothesis; if successful they are also used to seed the GSF tracking step. The "generic tracks" are a collection of tracks (not specific to electrons) selected with $p_{\mathrm{T}} > 2$ GeV, reconstructed from hits in the tracker through an iterative algorithm known as the Kalman filter (KF).

- A dedicated algorithm is used to find the generic tracks that are likely to originate from photons converting into e^+e^- pairs.

- ECAL clusters, SCs, GSF tracks and generic tracks associated with electrons, as well as conversion tracks and associated clusters, are all imported into the PF algorithm that links the elements together into blocks of particles.

- These blocks are resolved into electron and photon objects, starting from either a GSF track or a SC, respectively. At this point, there is no differentiation between electron and photon candidates. The final list of linked ECAL clusters for each candidate is promoted to a refined supercluster.

- Electron or photon objects are built from the refined SCs based on loose selection requirements. All objects passing the selection with an associated GSF track are labeled as electrons; without a GSF track they are labeled as photons. This collection is known as the unbiased e/γ collection and is used as a starting point by the vast majority of analyses involving electrons and photons.

- To separate electrons and photons from hadrons in the PF framework, a tighter selection is applied to these e/γ objects to decide if they are accepted as an electron or an isolated photon. If the e/γ object passes both the electron and the photon selection criteria, its object type is determined by whether it has a GSF track with a hit in the first layer of the pixel detector. If it fails the electron and photon selection criteria, its basic elements (ECAL clusters and generic tracks) are further considered to form neutral hadrons, charged hadrons or nonisolated photons in the PF framework.

The result of this process is an electron reconstruction efficiency that is higher than 95% for $E_{\mathrm{T}}(e) >$20 GeV, as shown in figure 4.2. this rate was determined using a tag-and-probe method using $Z \to ee$ events. An additional consideration which is important for this analysis is the rate at which other objects (namely hadronic jets) can be incorrectly reconstructed and identified as electrons (henceforth referred to as a "*fake* electron"). These fake rates are shown in figure 4.3. Despite the excellent identification rate of CMS, these fake electrons become impactful when studying extremely rare processes (i.e. those with very small cross sections), in which the rate at which electrons are incorrectly identified is greater than the rate at which such rare events are produced.

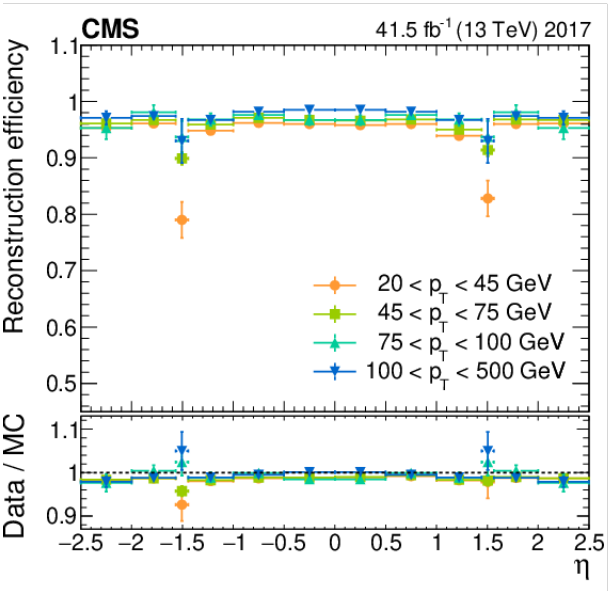

Figure 4.2: Reconstruction efficiency of electrons (top) over various p_T ranges versus η. Data to simulation (MC) ratio (bottom) [23].

4.3 Muons

Muons are reconstructed and identified using information primarily from the IT and the muon system. This is due to the fact that muons do not leave large deposits of energy in either ECAL or HCAL and therefore trying to use information from those sub detectors would be minimally beneficial. The track reconstruction of

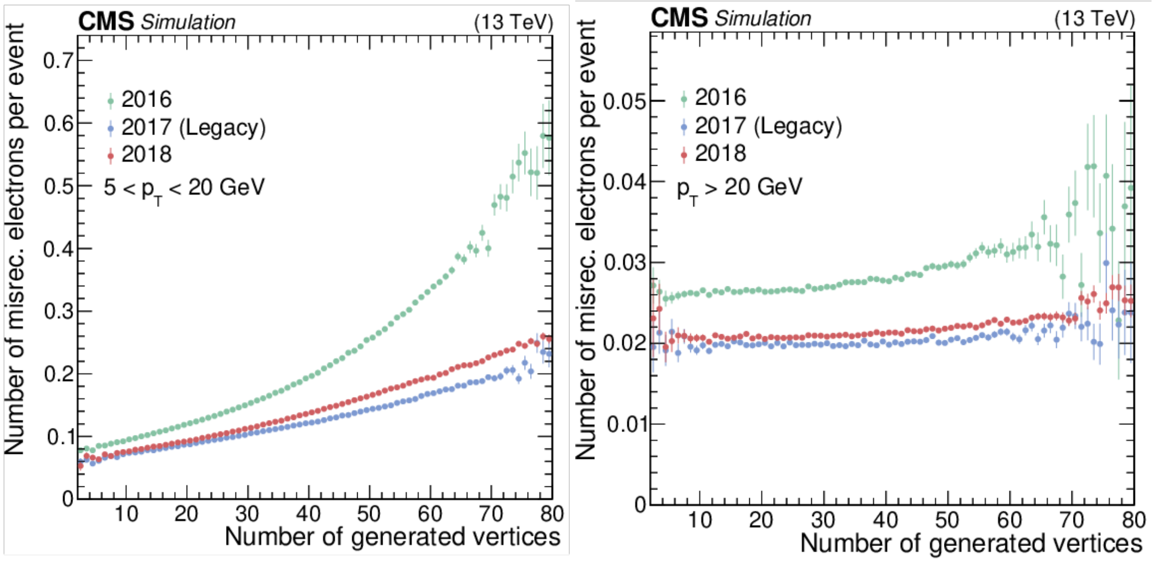

(a) (b)

Figure 4.3: Number of misreconstructed electrons per event as a function of generated vertices for 2016, 2017, & 2018. Low p_T events (left) and high p_T events (right) are shown. The improvement seen in 2017 & 2018 versus 2016 is due to an upgraded pixel detector during those years [23].

muons is initially performed separately, with tracks in the IT being reconstructed (as detailed in section 4.1) independently of tracks in the muon system. The reconstructed tracks within the muon system are pieced together using a Kalman-filter technique which takes as its input the hits from the CSCs, DTs, and RPCs to reproduce the particle's trajectory. This results in a *standalone-muon tracks* which does not contain additional info from the IT. *Tracker muons* on the other hand primarily use information from the IT. If there is at least one muon segment in the muon system which can be extrapolated back to an IT track, then the track qualifies as a tracker muon track. A third such option, *Global muon tracks*, are built by matching standalone-muon tracks to tracker tracks. The result is that $\sim 99\%$ of muons produced within the geometrical acceptance of the muon system will be reconstructed as either a global muon track or a tracker muon track, with a large number being reconstructed as both [24]. A number of identification (ID) types for muons are defined for use in CMS analyses. These include [24]:

- *Loose muon ID:* this ID aims to identify prompt muons originating at the primary vertex, and muons from light and heavy flavor decays, as well as maintain a low rate of the misidentification of charged hadrons as muons. A loose muon is a muon selected by the PF algorithm that is also either a tracker or a global muon.

- *Medium muon ID:* this ID is optimized for prompt muons and for muons from heavy flavor decay. A medium muon is a loose muon with a tracker track that uses hits from more than 80% of the inner tracker layers it traverses. The constraints on the segment compatibility were tuned after the application of the other constraints to target an overall efficiency of 99.5% for muons from simulated W and Z events.

- *Tight muon ID:* this ID aims to suppress muons from decay in flight and from hadronic punch-through. A tight muon is a loose muon with a tracker track that uses hits from at least six layers of the inner tracker including at least one pixel hit. The muon must be reconstructed as both a tracker muon and a global muon. The tracker muon must have segment matching in at least two of the muon stations. The global muon fit must have χ^2/dof < 10 and include at least one hit from the muon system. A tight muon must be compatible with the primary vertex, having a transverse impact parameter $|dXY| < 0.2$ cm and a longitudinal impact parameter $|dz| < 0.5$ cm.

The resulting efficiencies of these IDs can be seen in figure 4.4 (LooseID, left; TightID, right) for $p_{\mathrm{T}}(\mu) > 20$ GeV, as derived using a $Z \to \mu\mu$ tag and probe method.

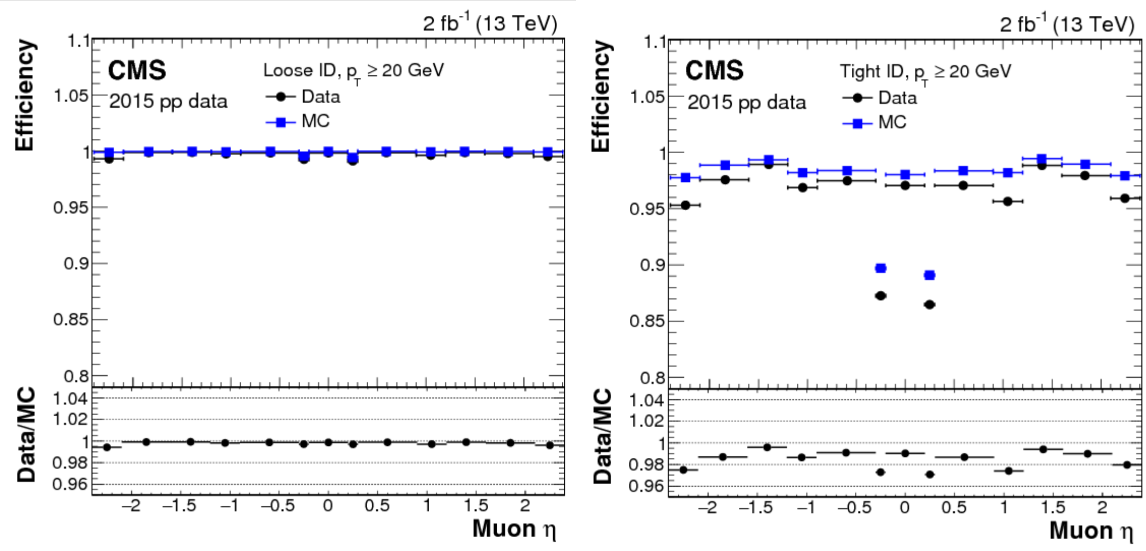

(a)

(b)

Figure 4.4: Muon identification efficiencies for LooseID (left) & TightID (right) for $p_{\mathrm{T}}(\mu) > 20$ GeV. Data to simulation (MC) agreement is shown below each respective plot. Results were derived using a $Z \to \mu\mu$ tag and probe method [24].

4.4 Jets

Jets are physics objects which are formed from the decays of either quarks or gluons. As mentioned in section 1.3, colored particles cannot exist in isolated states (due to QCD confinement) and must form color-neutral particles, such as pions, kaons, protons, and neutrons. When a quark or gluon is produced during *pp* collisions, it will quickly produce new particles from the vacuum in a process referred to as *hadronization*. This process will produce large numbers of particles, often collimated into a single region of the detector. This large set of particles is referred to as a *jet* and is often treated as a single object. A depiction of this process can be seen in figure 4.5, where a *pp* collision produces a single quark which then radiates further gluons and quarks, resulting in multiple hadrons which are then detected within the detector. It should be noted that jets need not only contain hadronic material but can also consist of non-isolated photons coming from π^0 decays, and even muons or electrons coming from *b* decays. Figure 4.6 shows such jet composition as a function of jet p_{T}. There are many different types of jets depending on the origin of the jet (Pile-Up jet versus a hard scatter jet), the flavor of the underlying quark which produced the jet (*b*-jet), whether the jet came from initial state radiation (ISR) or final state radiation (FSR), and even the algorithm with which the jet was grouped and identified (AK4 jets, AK8 jets). In order to identify jets, the particle flow (PF) algorithm is applied using information combined from each sub-detector to identify particles produced in each event [27]. These particles are then clustered together using a jet clustering algorithm. There are a large number of jet clustering algorithms which are often employed for different desired results. Perhaps the most common however is the *anti-*k_T algorithm, which clusters high momentum particles first, resulting in jets which are very circular looking when viewed in the $\phi - \eta$ plane.

4.4.1 Pile-Up Jets

Due to the high instantaneous luminosities reached by the LHC, it is exceedingly likely that multiple *pp* collisions will occur during each bunch crossing, resulting in additional particles being produced from secondary vertices. These interactions, referred to as pile-up (PU) need to be accounted for and subtracted when clustering and measuring jets. A number of different techniques are employed at CMS, including charged hadron subtraction (CHS) and pileup per particle identification (PUPPI). In CHS, the tracks of charged particles originating from pileup vertices are identified and removed from consideration in jet clustering. This is limited in η however only to jets within the tracker. Additional jet energy corrections are need to be applied to account for charged PU which occurs outside the tracker, or for neutral PU in all regions of the detector. This technique does not generally affect the shape or structure of jets, but only the measured four-momentum. In contrast, PUPPI calculates on an event by event basis the likelihood that a particle originated from the leading vertex and scales the energy accordingly. The result is that physics objects are less susceptible to PU [27].

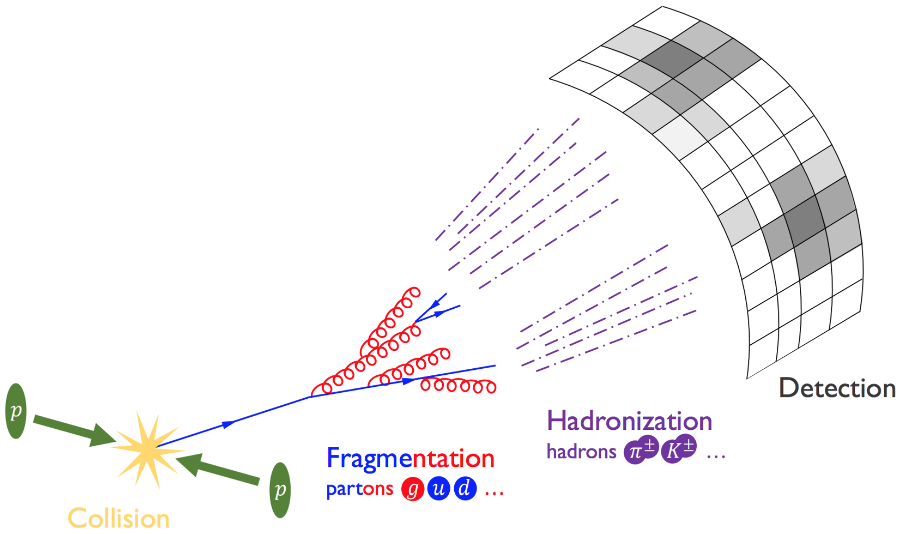

Figure 4.5: A diagrammatic depiction of a pp collision producing a single quark which then fragments, producing further gluons and quarks. These particles hadronize and the resulting hadrons are shown to be detected in close proximity to each other. These close particles will be reconstructed as jets [25].

A diagrammatic overview of these techniques is shown in 4.7. PU can occur from in-time objects, meaning these objects are a result of interactions that occurred in the same bunch crossing as a hard scattering which fires a trigger, or out-of-time objects, meaning objects which resulted from a previous or later bunch crossing.

4.4.2 Jet Energy Corrections

The CMS detector is unable to perfectly reconstruct jets. This is due to a myriad of reasons including (but not limited to): in-time and out-of-time PU can add additional energy to jets, the response of the calorimeters is not constant in p_{T} or η, the detector can respond differently to heavy jets and different parton flavors, electrical noise within the detector which disturbs the measurements, etc. Therefore jet energy corrections (JEC) are implemented in order to account for these effects and to more accurately and consistently measure jet energy relative to the true particle energy. JECs are a factorized solution which apply varying levels of corrections, in which each level is essentially a scale factor which corrects the jet four-momentum, and where the scale factor will depend on various event and jet quantities such as ρ (median energy density), p_{T}, η, flavor, etc. Each level of corrections is applied sequentially, with the output of the previous level acting as the input of the next level. These corrections can be seen in figure 4.8. Interestingly, this is one of the few instances in which corrections are made to the actual data itself (as well as MC), as data is usually unmanipulated in order to introduce as few biases as possible. The first set of corrections are *L1 corrections*, which seek to correct for additional energy introduced to the jet measurement by PU interactions. This may include the application of techniques such as charged hadron subtraction or PUPPI, both of which are

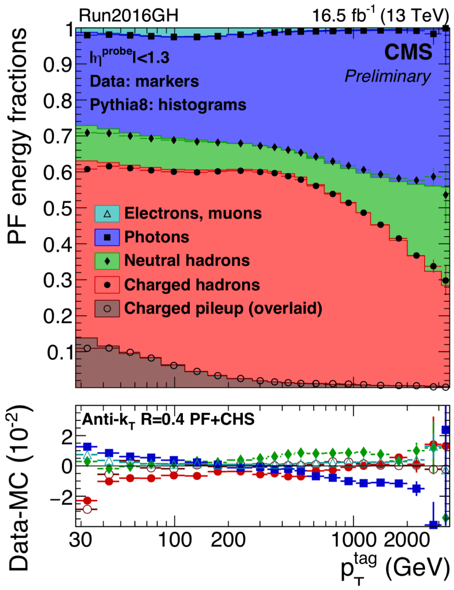

Figure 4.6: Jet composition in terms of energy fraction as a function of jet p_{T}. It can be observed that jets are primarily composed of charged hadrons (usually charged pions) and neutral hadrons (π^0's) but that this composition changes as a function of p_{T} [26].

discussed in the previous section. These corrections are done on an event-by-event basis and a jet-by-jet basis. This is followed by the *L2 corrections* and *L3 corrections* which seek to flatten the jet response in both p_{T} and η. These results are derived using QCD samples, but are intended to be applicable to all physics processes. The application of the L1+L2+L3 corrections should scale the energy of the average QCD jet in order to agree with corresponding generator level particle jets (gen jets). This however can lead to an over-correction or under-correction as compared to jets with a flavor composition different from QCD jets. This is compensated for by the application of optional *L5 corrections*, which correct for jet flavor dependence, and even further *L7 corrections*, that intend to correct jet p_{T} such that it is equal on average to the originating parton p_{T}. The minimum L1+L2+L3 corrections are applied to all MC and data on any CMS analysis, with data receiving an additional *L2L3Residual* correction that corrects for remaining percent-level differences. The result of this entire process then are properly calibrated jets.

Jet Energy Resolution (JER) & Jet Energy Scale (JES)

If it were possible to reconstruct the same jet many times over, the resulting distribution would be Gaussian in nature, with an associated mean and width. The mean of this “jet energy” distribution is referred to as the *jet energy scale* (JES), while the width is referred to as the *jet energy resolution* (JER). It is known from studies that the JES and JER in data is worse than in simulation, and as a result the jets in MC need to be “smeared” in order to accurately describe the data [60]. There are two different general methods used in practice with

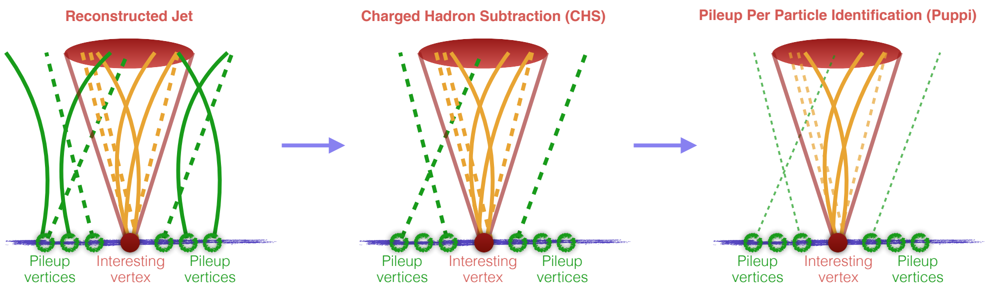

Figure 4.7: A diagrammatic overview of techniques used to reduce PU in jet clustering. Solid (dashed) lines refer to charged (neutral) PF candidates. The weights applied by the PUPPI algorithm are represented by thin lines [27].

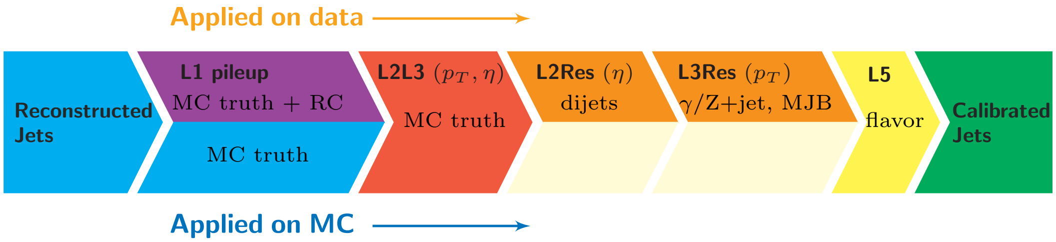

Figure 4.8: The varying levels of Jet Energy Corrections (JEC) are shown here. All data and MC receive L1+1+L2+L3 corrections, with data receiving an additional L2L3 Residual correction. There are additional L5 and L7 (not shown in this diagram) corrections which can optionally be applied [28].

which to smear reconstructed jets in simulation. These are:

1. **Scaling method**: The 4-momentum of a reconstructed jet is rescaled with a factor:

$$c_{\mathrm{JER}} = 1 + (s_{\mathrm{JER}} - 1)\frac{p_{\mathrm{T}} - p_{\mathrm{T}}^{\mathrm{ptcl}}}{p_{\mathrm{T}}} \tag{4.1}$$

   where p_{T} is the transverse momentum of the jet, $p_{\mathrm{T}}^{\mathrm{ptcl}}$ is the transverse momentum of the corresponding jet clustered from generator-level particles and s_{JER} is the data-to-simulation core resolution scale factor. The factor c_{JER} is truncated at zero (i.e., if it is negative, it is set to zero). This method only works if a well-matched particle-level jet is present and can result in a large shift of the response otherwise. The requirements imposed for the matching are

$$\Delta R < R_{\mathrm{cone}}/2. \; |p_{\mathrm{T}} - p_{\mathrm{T}}^{\mathrm{ptcl}}| < 3\sigma_{\mathrm{JER}} p_{\mathrm{T}} \tag{4.2}$$

   where R_{cone} is the jet cone size parameter and σ_{JER} is the relative p_{T} resolution as measured in simulation.

2. **Stochastic smearing**: This approach does not require the presence of a matching particle level jet. The

4-momentum of the reconstructed jet is re-scaled with a factor

$$c_{\mathrm{JER}} = 1 + \mathcal{N}(0, \sigma_{\mathrm{JER}})\sqrt{\max(s_{\mathrm{JER}}^2 - 1, 0)} \tag{4.3}$$

where σ_{JER} and s_{JER} are the relative p_{T} resolution in simulation and data-to-simulation scale factors, and $\mathcal{N}(0, \sigma_{\mathrm{JER}})$ denotes a random number sampled from a normal distribution with a zero mean and variance σ_{JER}^2 , with a similar truncation at zero as in the scaling method. This method only allows to degrade the resolution.

For this analysis, a custom method was derived, referred to as *Modified Forward JER Smearing* and defined in the following way:

- The energy of central jets ($|\eta| \leq 2.5$) are smeared according to their gen-level matching status, i.e. the corrections for genuine jets is derived using the scaling method, and for pileup jets using the stochastic method.
- The energy resolution of forward jets ($2.5 < |\eta| < 4.7$) with $p_{\mathrm{T}} > 50$ GeV is smeared in a similar fashion to central jets as described above.
- Forward jets with $p_{\mathrm{T}} < 50$ GeV do not receive any corrections for energy resolution.

The Modified Forward JER Smearing was applied to all jets in simulation for this analysis.

4.5 Hadronic Taus

The tau lepton is the most massive of the SM leptons, with a lifetime of 2.9×10^{-13} s. As a result, taus produced within CMS will only travel a distance of ~ 1 mm before decaying into other particles. This decay will always produce a tau-neutrino, in addition to hadrons (65% of the time) or a charged lepton (35% of the time). The decays which produce hadrons are referred to as *hadronic taus* (τ_h). These hadronic tau decays will produce one charged hadron (11.5% of the time), one charged hadron plus neutral hadrons (35.5% of the time), or three charged hadrons plus neutral hadrons (15% of the time) [61]. The reconstruction algorithm which identifies τ_h's is referred to as the *hadrons-plus-strips* (HPS) algorithm. This algorithm uses as its input anti-k_T jets with $p_{\mathrm{T}} > 14$ GeV and $|\eta| < 2.5$. The HPS algorithm is performed in the following two steps [29]:

- *Reconstruction:* combinations of charged and neutral particles reconstructed by the PF algorithm that are compatible with specific τ_h decays are constructed, and the four-momentum expressed in terms of (p_{T}, η, ϕ, and mass) of τ_h candidates is computed.

- *Identification:* discriminators that separate τ_h decays from quark and gluon jets, and from electrons and muons, are computed. This provides a reduction in the jet$\to \tau_h$, $e \to \tau_h$, and $\mu \to \tau_h$ misidentification rates.

The efficiency of τ_h identification, as measured in simulation via $Z \to \tau\tau \to \mu\tau_h$, can be seen in figure 4.9a, in which a Loose, Medium, and Tight ID criteria have been defined. The resulting efficiency is approximately flat at 60%, as a function of τ_h p_{T}. An important consideration is the misidentification rate for hadronic taus, in which either a hadronic W decay not coming from a true tau, or a multijet QCD event is incorrectly reconstructed as a τ_h. These results can be seen in figures 4.9b and 4.9b, in which the misidentificaiton rate for W+jets events is $\sim 1\%$ when using TightID, and $< 1\%$ for multijet events.

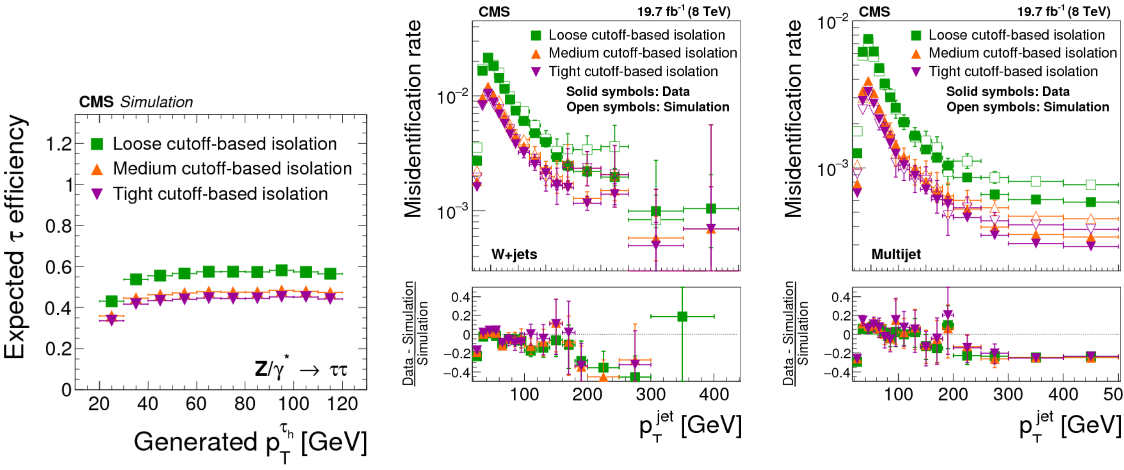

(a) (b) (c)

Figure 4.9: (Left) The efficiency of τ_h identification, as measured via $Z \to \tau\tau \to \mu\tau_h$. (Center, Right) Misidentification rates of W+jets and multijet events, as a function of jet p_{T} [29].

4.6 Missing Transverse Momentum

Any weakly interacting neutral particle cannot be directly detected by CMS. This includes all three neutrinos of the SM, as well as many theoretical BSM particles, such as the lightest neutralino predicted by SUSY. These particles can however be inferred based off of the momentum imbalance of reconstructed objects within any given event. This imbalance, referred to as *missing transverse momentum* ($\vec{p}_{\mathrm{T}}^{\,miss}$) is defined in the following way:

$$\vec{p}_{\mathrm{T}}^{\,miss} = -\sum \vec{p}_{\mathrm{T}}^{\,vis} \tag{4.4}$$

where $\sum \vec{p}_{\mathrm{T}}^{vis}$ is the sum of the transverse momentum over all visible objects. p_{T}^{miss} is additionally used to denote the magnitude of $\vec{p}_{\mathrm{T}}^{miss}$. p_{T}^{miss} provides an excellent indication that an interesting physics event has taken place and therefore is an important object in triggering. It is also essential for many tests of new physics, in addition to precise measurements of objects involving neutrinos. The ability to reconstruct p_{T}^{miss} coming from actual weakly interacting objects (referred to as *genuine* p_{T}^{miss}) is sensitive to many detector effects including experimental resolutions, pile-up, mismeasurement of reconstructed particles, and detector artifacts [62].

4.7 Particle Flow Algorithm

The *particle-flow reconstruction algorithm* (PF) is a particle reconstruction algorithm which attempts to use information from multiple detector layers in order to accurately identify physics objects. The initial step of the PF algorithm is the reconstruction of the tracks of charged particles within the IT. These tracks, along with energy deposit clusters from the ECAL and HCAL, are linked using a nearest neighbors algorithm, with the distance between two linked elements determining the quality of the link. The result of this is a PF block of elements associated via either a direct link or indirect link through another element. Within each PF block, the muons are reconstructed first and those corresponding elements are then removed from the PF block. Electrons are then reconstructed second, along with isolated photons, with those elements also being removed from the PF block. Finally, the remaining elements are cross identified as consisting of charged hadrons, neutral hadrons, and photons [63]. The difference between detector level objects and physics objects after the PF algorithm has been applied can be seen in figure 4.10, in which there are initially a set of uncombined detector measurements, and afterwards there are individual identified and reconstructed particles.

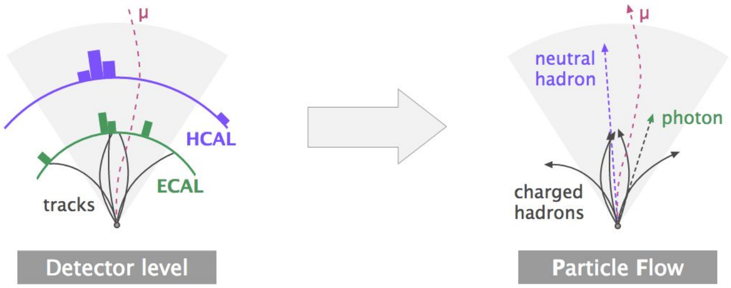

Figure 4.10: This diagram shows the input and resulting output of the PF algorithm, in which initial tracks and clusters of energy are grouped and linked, resulting in identified individual particles [30].

CHAPTER 5

Analysis Strategy & Sample Production

5.1 Vector Boson Fusion Processes

As detailed in section 2.3, traditional SUSY searches for electroweakinos have typically targeted direct production via Drell-Yan (DY) processes ($pp \to Z/\gamma^* \to \tilde{\chi}_1^\pm \tilde{\chi}_1^\mp$, figure 5.1a), or production via W bosons ($pp \to W^\pm \to \tilde{\chi}_2^0 \tilde{\chi}_1^\pm$, figure 5.1b). These searches perform poorly when probing compressed mass spectrum scenarios, as the decay products are often too soft to be efficiently reconstructed. In contrast, this analysis will target electroweakino production via *Vector Boson Fusion* (VBF) interactions. VBF interactions are characterized by the radiation of a vector boson (either a Z or $W^\pm$) from an incoming parton. These radiated bosons then interact, while the outgoing partons hadronize and form jets in the detector. A typical Feynman diagram for such an interaction as well as the resulting detector signature can be seen in figure 5.2a and 5.2b.

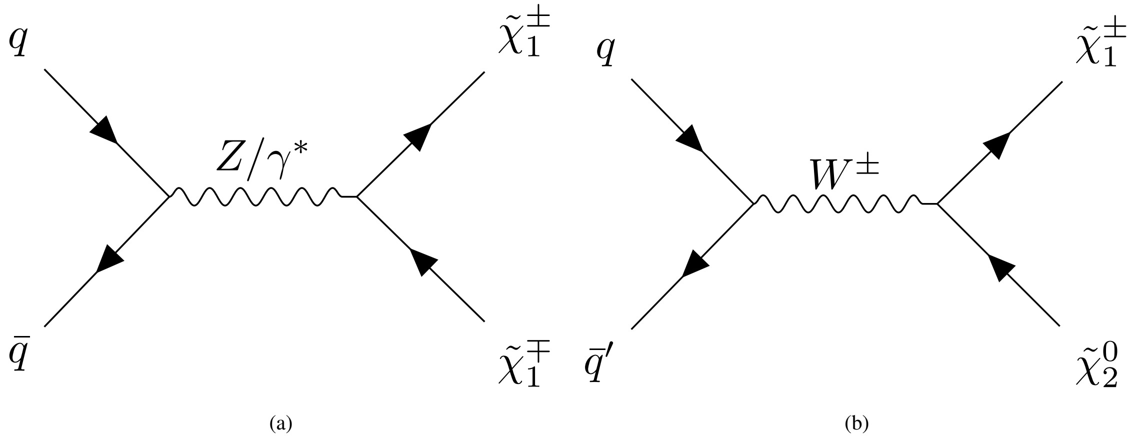

Figure 5.1: Direct electroweakino production via DY processes (left) and W boson mediated processes (right).

Using VBF interactions as a probe for compressed mass spectrum SUSY scenarios has many advantages over traditional search methods, as well as a few disadvantages. VBF has the notable disadvantage of a smaller typical cross section as compared to other production methods. This however is not true for the entirety of the phase space, and indeed DY production cross sections can fall faster than VBF cross sections for increasing sparticle mass within certain models (see reference [64]). VBF has a particularly unique detector signature which makes it ideal for differentiating new physics from SM backgrounds which will be produced at significantly higher rates. VBF processes result in at least two jets, each typically with high η and large p_{T} values which comes from the outgoing parton recoiling off the heavy vector boson. The two jets

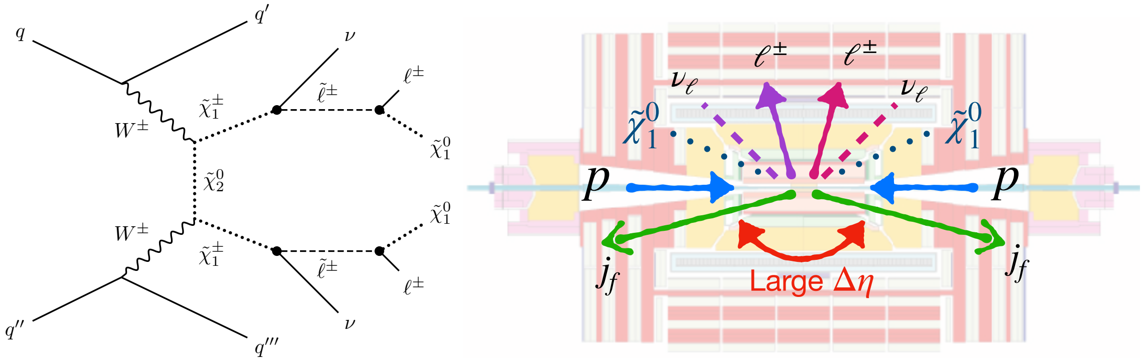

(a) (b)

Figure 5.2: Left, VBF production of charginos + VBF jets. The charginos then decay to sleptons which subsequently decay to leptons plus an LSP. These decay chains are ultimately model dependent however, and other models will dictate different decays. Right, the associated detector signature for an event such. The neutrinos and LSPs will be reconstructed as p_{T}^{miss}.

will have a large η gap between them ($\Delta\eta_{jj}$) which is defined as:

$$\Delta\eta_{jj} = |\eta(j_1) - \eta(j_2)| \tag{5.1}$$

as well as a large invariant dijet mass (m_{jj}), which is calculated by taking the invariant mass between the two leading jets within an event and can be expressed mathematically as a function of the individual jet p_{T} and $\Delta\eta_{jj}$ as:

$$m_{jj}^2 \propto 2p_{\mathrm{T}}(j_1)p_{\mathrm{T}}(j_2)\cosh(\Delta\eta_{jj}) \tag{5.2}$$

In addition to the two VBF jets, such interactions may result in additional leptons (or jets) being produced. These particles can gain a boost from the decay of the massive vector bosons or any momentum imbalance carried by the vector bosons themselves, which aids in their reconstruction and allows VBF sensitivity to compressed mass spectrum SUSY scenarios where one expects the decay products of sparticles to be soft. Given that this analysis is interested in R-parity conserving SUSY scenarios, the production of any sparticle will result in an LSP, which we take to be the lightest neutralino. The LSP will leave the detector undetected, producing large p_{T}^{miss}.

The general analysis strategy will then be to select events with at least 2 VBF jets, characterized by high jet η and large jet p_{T} in opposite hemispheres ($\eta(j_1) \times \eta(j_2) < 0$), with a requirement of large $\Delta\eta_{jj}$, and large m_{jj}. In addition, events will be required to pass a large p_{T}^{miss} requirement. This analysis will search for events producing 0 leptons (0ℓ), 1 lepton (1ℓ), and 2 lepton (2ℓ) final states, with an emphasis for this thesis on the light lepton final states of the 2ℓ channel which will produce electron-electron, electron-muon, and muon-

muon pairs (for charge of both opposite sign (OS) and like sign (LS) between the pair). Kinematic selections (cuts) will be applied to physics objects sequentially, with cuts affecting objects reconstructed within the central part of the detector ($|\eta| < 2.1$), referred hereto as *central selection* (CS) cuts), being applied first followed by VBF cut selections which will select for the VBF jets. For this analysis, p_{T}^{miss} will be considered part of the central selection cuts. In order to quantify the significance of any observed excess, a fit of the largest dijet mass (as determined by taking the invariant dijet mass between all combinations of jets within an event and selecting the largest value) will be performed and compared between data and simulation. The estimation of background within the signal region (SR) will be performed by defining background enriched control regions (CR) which are orthogonal to the SR and contain negligible signal contamination. Scale factors (SF) will then be derived for these processes of interest, which are used to correct the overall yield for any given process that might be mismodeled, assuming the shape of the distributions being studied are correctly modeled. The process of deriving a SF is performed using the following equation:

$$SF_{\mathrm{CR}} = \frac{N_{\mathrm{CR}}^{\mathrm{Data}} - N_{\mathrm{Non-process,\,CR}}^{\mathrm{Simulation}}}{N_{\mathrm{process,\,CR}}^{\mathrm{Simulation}}} \tag{5.3}$$

In which SF_{CR} is the SF derived for a specific CR, $N_{\mathrm{CR}}^{\mathrm{Data}}$ is the total number of events present in recorded data after applying the selection cuts for that CR, $N_{\mathrm{Non-process,\,CR}}^{\mathrm{Simulation}}$ is the total contribution of simulated events from processes other than the process of interest after applying selection cuts, and $N_{\mathrm{process,\,CR}}^{\mathrm{Simulation}}$ is the contribution of simulated events from the process of interest. It can be seen that for high purity CRs (which are desirable) where $N_{\mathrm{Non-process,\,CR}}^{\mathrm{Simulation}} \to 0$, the SF represents the overall yield difference between data and simulation for that process of interest. It is important to note that potential mismodeling of simulated events can occur from both mismodeled central selection objects (namely p_{T}^{miss}) as well as VBF objects. Within any given CR then, the methodology will be to therefore first derive a SF after applying only central selection cuts ($SF_{\mathrm{CS\,cuts}}$), and then derive a second SF after applying central selection + VBF selection cuts ($SF_{\mathrm{VBF\,cuts}}$). The first SF will then be factored out of the second SF in following way:

$$SF_{\mathrm{VBF\,cuts}} = \frac{SF_{\mathrm{VBF\,cut\,level}}}{SF_{\mathrm{CS\,cuts}}} \tag{5.4}$$

where $SF_{\mathrm{VBF\,cut\,level}}$ is the SF as derived after both CS cuts and VBF cuts have been applied. The intention of doing this is that we are left with two separate SFs which independently represent the mismodeling of either CS objects alone, or VBF objects alone. This includes object isolation, misidentification rates, efficiency of topological cuts, etc.. One may then perform further studies or apply further corrections to the simulated events and rederive these SFs in order to understand how those corrections affect the different physics objects.

When predicting the total event yield of simulated events within the SR, the mismodeling of each process will be corrected in the following way:

$$N_{\mathrm{BG}}^{\mathrm{Data}} = N_{\mathrm{BG}}^{\mathrm{Simulated}}(\mathrm{SR\ cuts}) \cdot SF_{\mathrm{CS\ cuts}} \cdot SF_{\mathrm{VBF\ cuts}} \tag{5.5}$$

Simulated samples will be used to check the closure of this methodology by ensuring that object kinematics, event composition (e.g. what fraction of events are due to fakes), and the VBF shapes are similar between the CR and SR.

5.2 Monte Carlo Sample Production

Simulated events within this analysis (for both signal and background) are prepared using the *Monte Carlo* (MC) method. The MC method refers to a mathematical technique in which randomly generated numbers are used to obtain numerical results. For MC event generators simulating pp collisions, incoming partons are generated with a randomly sampled value of momentum as determined by a parton distribution function. Particles are allowed to interact via the interactions dictated by the Lagrangian of the theory being modeled and momentum and energy conservation are required at each vertex. If interactions are only allowed to take place at tree level (the first level of the perturbative QFT expansion) then the samples are referred to as being *leading order* (LO). Higher order effects can also be calculated, which are said to be at *next-to-leading-order* (NLO) or *next-to-next-to-leading-order* (NNLO).

5.3 Signal Samples

Signal samples for this analysis were prepared using the LO event generators MadGraph (MG) and Pythia, using the R-parity conserving simplified MSSM model. Samples for multiple SUSY scenarios have been generated, in which the electroweakino flavor mixings are varied in order to produce different phenomenological outcomes (as will be detailed shortly, see sections 5.3.1- 5.3.4). For all samples produced, the colored sector has been effectively decoupled by setting the masses of such particles to a large value (10^5 GeV) and by excluding such diagrams from the MG generate command in order to reduce the computing time for sample production. For all samples, the production of the following processes were included: $pp > \tilde{\chi}_1^0\tilde{\chi}_1^0 jj$, $pp > \tilde{\chi}_1^0\tilde{\chi}_1^{\pm} jj$, $pp > \tilde{\chi}_1^0\tilde{\chi}_2^0 jj$, $pp > \tilde{\chi}_1^{\pm}\tilde{\chi}_1^{\pm} jj$, $pp > \tilde{\chi}_1^{\pm}\tilde{\chi}_2^0 jj$, $pp > \tilde{\chi}_2^0\tilde{\chi}_2^0 jj$. This was achieved using the following MG generate command:

```
define ewkinos = x1+ x2+ n1 n2

define colored = go dl dr ul ur sl sr cl cr b1 b2 t1 t2 dl~

dr~ ul~ ur~ sl~ sr~ cl~ cr~ b1~ b2~ t1~ t2~

generate p p > ewkinos ewkinos j j / colored QCD=0 @1
```

Additionally, each SUSY scenario was generated for a variety of different mass gaps (Δm) ranging from 75 GeV down to 0.5 GeV, in which the mass gap is defined as the difference between the LSP, always taken to be the lightest neutralino ($\tilde{\chi}_1^0$), and the second generation neutralino ($\tilde{\chi}_2^0$):

$$\Delta m = m(\tilde{\chi}_2^0) - m(\tilde{\chi}_1^0) \tag{5.6}$$

The motivation for this range of mass gaps is in order to fully probe the compressed mass spectrum range. An addition generator level cut requirement of $|\Delta\eta_{jj}| > 3.5$ between the two jets was imposed in order to further suppress contribution from non-VBF diagrams. The SUSY scenarios for which samples have been produced are as follows:

5.3.1 Wino-Bino "Virtual W/Z" Scenario

In this scenario, the $\tilde{\chi}_1^0$ is purely bino while the $\tilde{\chi}_2^0$ and $\tilde{\chi}_1^{\pm}$ are purely wino. The masses are set such that $m(\tilde{\chi}_2^0) = m(\tilde{\chi}_1^{\pm}) > m(\tilde{\chi}_1^0)$. Additionally, the branching fractions are set so that $\text{Br}(\tilde{\chi}_1^{\pm} \to \tilde{\chi}_1^0 W^{\pm *}) = 1$ and $\text{Br}(\tilde{\chi}_2^0 \to \tilde{\chi}_1^0 Z^*) = 1$, where $W^{\pm *}$ and Z^* indicate virtual bosons (off-mass shell). A representative Feynman diagram for a VBF interaction in the virtual W/Z model is shown in figure 5.3.

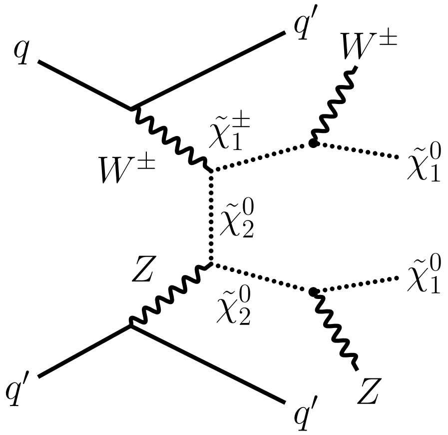

Figure 5.3: Feynman diagram of a VBF interaction in the virtual W/Z scenario.

5.3.2 Wino-Bino "Stau-Dominated" Scenario

In this scenario, the $\tilde{\tau}$ is the next-to-lightest supersymmetric particle (NLSP) while the other sleptons have been effectively decoupled by setting $m(\tilde{e}), m(\tilde{\mu}) \gg m(\tilde{\chi}_2^0)$. The branching fractions are set such that $\text{Br}(\tilde{\chi}_1^{\pm} \rightarrow \tilde{\tau}^{\pm}\nu_{\tau}) = 1$, $\text{Br}(\tilde{\tau} \rightarrow \tilde{\chi}_1^0 \tau) = 1$, $\text{Br}(\tilde{\chi}_2^0 \rightarrow \tilde{\tau}^{\pm}\tau^{\mp}) = 1$. Sparticle masses are defined such that:

$$m(\tilde{\chi}_2^0) = m(\tilde{\chi}_1^{\pm}), \quad m(\tilde{\tau}) = \frac{m(\tilde{\chi}_2^0) + m(\tilde{\chi}_1^0)}{2} \tag{5.7}$$

A representative Feynman diagram for a VBF interaction in the $\tilde{\tau}$-dominated model is shown in figure 5.4.

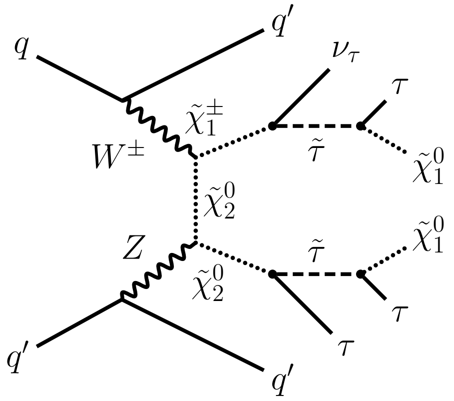

Figure 5.4: Feynman diagram of a VBF interaction in the $\tilde{\tau}$-dominated scenario.

5.3.3 Democratic Light Slepton Scenario

In this scenario, the $\tilde{\chi}_1^0$ is purely bino while the $\tilde{\chi}_2^0$ and $\tilde{\chi}_1^{\pm}$ are purely wino. The three sleptons ($\tilde{e}$,$\tilde{\mu}$,$\tilde{\tau}$) are mass degenerate, left-handed, and are the NLSPs. The branching fractions are set such that $\text{Br}(\tilde{\chi}_1^{\pm} \rightarrow \tilde{\ell}\nu_{\ell}) = \frac{1}{3}$, $\text{Br}(\tilde{\ell} \rightarrow \tilde{\chi}_1^0 \ell) = 1$, and $\text{Br}(\tilde{\chi}_2^0 \rightarrow \tilde{\ell}^{\pm}\ell^{\mp}) = \frac{1}{3}$, where ℓ is any of the three SM leptons (e,μ,τ). The sparticle masses are defined as:

$$m(\tilde{\chi}_2^0) = m(\tilde{\chi}_1^{\pm}), \quad m(\tilde{\ell}) = \frac{m(\tilde{\chi}_2^0) + m(\tilde{\chi}_1^0)}{2} \tag{5.8}$$

A representative Feynman diagram for a VBF interaction in the democratic light slepton model is shown in figure 5.5.

5.3.4 Higgsino Scenario

In this scenario, the neutralino and chargino mixing matrices are fixed such that $\tilde{\chi}_1^0$, $\tilde{\chi}_2^0$, and $\tilde{\chi}_1^{\pm}$ are all pure higgsino states, regardless of the Δm value. $\tilde{\chi}_1^0$ is the LSP and $\tilde{\chi}_1^{\pm}$ is the NLSP. As a result, the cross sections to be used for this interpretation will be different from those obtained in the simplified SUSY signal samples,

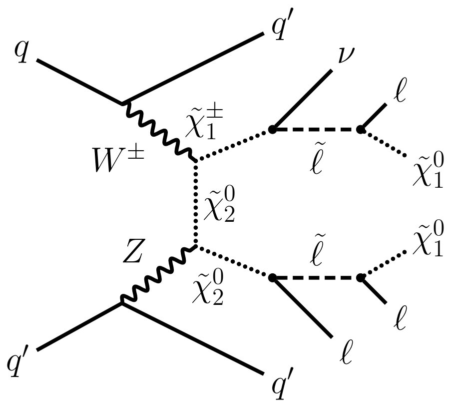

Figure 5.5: Feynman diagram of a VBF interaction in the democratic light slepton scenario.

in order to be consistent with theoretical constraints. The $\tilde{\chi}_1^\pm$ mass is calculated according to:

$$m(\tilde{\chi}_1^\pm) = \frac{m(\tilde{\chi}_2^0) + m(\tilde{\chi}_1^0)}{2} \tag{5.9}$$

Similar to the wino-bino virtual *W*/*Z* decays, sleptons are heavier than the $\tilde{\chi}_2^0$ and $\tilde{\chi}_1^\pm$ and will therefore decay through virtual *W* and *Z* bosons. The branching ratios in this case are $\text{Br}(\tilde{\chi}_1^\pm \to \tilde{\chi}_1^0 W^{\pm *}) = 1$, where $W^{\pm *}$ again refers to a virtual *W* boson. The dominant production mechanism in this case is via s-channel, in contrast to the wino-bino model which is through t-channel production. A representative Feynman diagram for a VBF interaction in the Higgsino model is shown in figure 5.6.

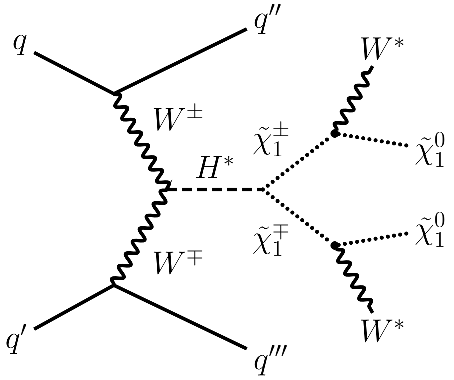

Figure 5.6: Feynman diagram of a VBF interaction in the Higgsino scenario.

5.4 Background Samples

All background samples for this analysis are official CMS MC samples, produced using the LO even generators MadGraph, POWHEG, and Pythia 8. The list of these samples can be found in appendix A.4. Cross sections were calculated using NLO or NNLO diagrams when possible. H_T binned samples for DY+jets and

W+jets are produced only for $H_{\mathrm{T}} > 100$ GeV, therefore a filter which selects for $0 < H_{\mathrm{T}} < 100$ GeV was employed and run over inclusive DY+jets and W+jets samples. In some instances, the Higgs, WW/ZZ double parton scattering (DPS), triboson, and $V\gamma$+jets samples will be grouped together into a single sample referred to as “Rares”.

5.5 Data Samples

This analysis uses proton-proton collision data with a center-of-mass energy of 13 TeV collected by the CMS detector during 2016, 2017, and 2018 data-taking runs which are prepared using the NanoAOD format (see reference [65] for details). The three years of data taking accounted for integrated luminosities of 35.92 fb^{-1}, 41.53 fb^{-1}, and 59.74 fb^{-1} respectively, for a total integrated luminosity of 137.19 fb^{-1}. Multiple primary datasets (PD) will be used for different purposes. The signal search region uses the MET PD which was recorded when an event registers (triggers) large p_{T}^{miss}. The use of this PD is motivated by the expected large p_{T}^{miss} present in signal events. These samples can be seen in table 5.1. Additional muon (table 5.2), electron (table 5.3), and tau (table 5.4) PDs are used for the purpose of background estimation.

Run II collision data samples: MET primary datasets (NanoAODv6)

Era	Physics sample	Official CMS datasets
2016	Run 2016Bv1	/MET/Run2016B_ver1-Nano25Oct2019_ver1-v1/NANOAOD
	Run 2016Bv2	/MET/Run2016B_ver2-Nano25Oct2019_ver2-v1/NANOAOD
	Run 2016C	/MET/Run2016C-Nano25Oct2019-v1/NANOAOD
	Run 2016D	/MET/Run2016D-Nano25Oct2019-v1/NANOAOD
	Run 2016E	/MET/Run2016E-Nano25Oct2019-v1/NANOAOD
	Run 2016F	/MET/Run2016F-Nano25Oct2019-v1/NANOAOD
	Run 2016G	/MET/Run2016G-Nano25Oct2019-v1/NANOAOD
	Run 2016H	/MET/Run2016H-Nano25Oct2019-v1/NANOAOD
2017	Run 2017B	/MET/Run2017B-Nano25Oct2019-v1/NANOAOD
	Run 2017C	/MET/Run2017C-Nano25Oct2019-v1/NANOAOD
	Run 2017D	/MET/Run2017D-Nano25Oct2019-v1/NANOAOD
	Run 2017E	/MET/Run2017E-Nano25Oct2019-v1/NANOAOD
	Run 2017F	/MET/Run2017F-Nano25Oct2019-v1/NANOAOD
2018	Run 2018A	/MET/Run2018A-Nano25Oct2019-v1/NANOAOD
	Run 2018B	/MET/Run2018B-Nano25Oct2019-v1/NANOAOD
	Run 2018C	/MET/Run2018C-Nano25Oct2019-v1/NANOAOD
	Run 2018Dv2	/MET/Run2018D-Nano25Oct2019_ver2-v1/NANOAOD

Table 5.1: Run II MET Primary Datasets

Run II collision data samples: muon primary datasets (NanoAODv6).

Era	Physics sample	Official CMS datasets
2016	Run 2016Bv1	/SingleMuon/Run2016B_ver1-Nano25Oct2019_ver1-v1/NANOAOD
	Run 2016Bv2	/SingleMuon/Run2016B_ver2-Nano25Oct2019_ver2-v1/NANOAOD
	Run 2016C	/SingleMuon/Run2016C-Nano25Oct2019-v1/NANOAOD
	Run 2016D	/SingleMuon/Run2016D-Nano25Oct2019-v1/NANOAOD
	Run 2016E	/SingleMuon/Run2016E-Nano25Oct2019-v1/NANOAOD
	Run 2016F	/SingleMuon/Run2016F-Nano25Oct2019-v1/NANOAOD
	Run 2016G	/SingleMuon/Run2016G-Nano25Oct2019-v1/NANOAOD
	Run 2016H	/SingleMuon/Run2016H-Nano25Oct2019-v1/NANOAOD
2017	Run 2017B	/SingleMuon/Run2017B-Nano25Oct2019-v1/NANOAOD
	Run 2017C	/SingleMuon/Run2017C-Nano25Oct2019-v1/NANOAOD
	Run 2017D	/SingleMuon/Run2017D-Nano25Oct2019-v1/NANOAOD
	Run 2017E	/SingleMuon/Run2017E-Nano25Oct2019-v1/NANOAOD
	Run 2017F	/SingleMuon/Run2017F-Nano25Oct2019-v1/NANOAOD
2018	Run 2018A	/SingleMuon/Run2018A-Nano25Oct2019-v1/NANOAOD
	Run 2018B	/SingleMuon/Run2018B-Nano25Oct2019-v1/NANOAOD
	Run 2018C	/SingleMuon/Run2018C-Nano25Oct2019-v1/NANOAOD
	Run 2018D	/SingleMuon/Run2018D-Nano25Oct2019-v1/NANOAOD

Table 5.2: Run II Muon Primary Datasets

Run II collision data samples: electron primary datasets (NanoAODv6)

Era	Physics sample	Official CMS datasets
2016	Run 2016Bv1	/SingleElectron/Run2016B_ver1-Nano25Oct2019_ver1-v1/NANOAOD
	Run 2016Bv2	/SingleElectron/Run2016B_ver2-Nano25Oct2019_ver2-v1/NANOAOD
	Run 2016C	/SingleElectron/Run2016C-Nano25Oct2019-v1/NANOAOD
	Run 2016D	/SingleElectron/Run2016D-Nano25Oct2019-v1/NANOAOD
	Run 2016E	/SingleElectron/Run2016E-Nano25Oct2019-v1/NANOAOD
	Run 2016F	/SingleElectron/Run2016F-Nano25Oct2019-v1/NANOAOD
	Run 2016G	/SingleElectron/Run2016G-Nano25Oct2019-v1/NANOAOD
	Run 2016H	/SingleElectron/Run2016H-Nano25Oct2019-v1/NANOAOD
2017	Run 2017B	/SingleElectron/Run2017B-Nano25Oct2019-v1/NANOAOD
	Run 2017C	/SingleElectron/Run2017C-Nano25Oct2019-v1/NANOAOD
	Run 2017D	/SingleElectron/Run2017D-Nano25Oct2019-v1/NANOAOD
	Run 2017E	/SingleElectron/Run2017E-Nano25Oct2019-v1/NANOAOD
	Run 2017F	/SingleElectron/Run2017F-Nano25Oct2019-v1/NANOAOD
2018	Run 2018A	/EGamma/Run2018A-Nano25Oct2019-v1/NANOAOD
	Run 2018B	/EGamma/Run2018B-Nano25Oct2019-v1/NANOAOD
	Run 2018C	/EGamma/Run2018C-Nano25Oct2019-v1/NANOAOD
	Run 2018D	/EGamma/Run2018D-Nano25Oct2019-v1/NANOAOD

Table 5.3: Run II Electron Primary Datasets

Run II collision data samples: tau primary datasets (NanoAODv6)

Era	Physics sample	Official CMS datasets
2016	Run 2016Bv1	/Tau/Run2016B_ver1-Nano25Oct2019_ver1-v1/NANOAOD
	Run 2016Bv2	/Tau/Run2016B_ver2-Nano25Oct2019_ver2-v1/NANOAOD
	Run 2016C	/Tau/Run2016C-Nano25Oct2019-v1/NANOAOD
	Run 2016D	/Tau/Run2016D-Nano25Oct2019-v1/NANOAOD
	Run 2016E	/Tau/Run2016E-Nano25Oct2019-v1/NANOAOD
	Run 2016F	/Tau/Run2016F-Nano25Oct2019-v1/NANOAOD
	Run 2016G	/Tau/Run2016G-Nano25Oct2019-v1/NANOAOD
	Run 2016H	/Tau/Run2016H-Nano25Oct2019-v1/NANOAOD
2017	Run 2017B	/Tau/Run2017B-Nano25Oct2019-v1/NANOAOD
	Run 2017C	/Tau/Run2017C-Nano25Oct2019-v1/NANOAOD
	Run 2017D	/Tau/Run2017D-Nano25Oct2019-v1/NANOAOD
	Run 2017E	/Tau/Run2017E-Nano25Oct2019-v1/NANOAOD
	Run 2017F	/Tau/Run2017F-Nano25Oct2019-v1/NANOAOD
2018	Run 2018A	/Tau/Run2018A-Nano25Oct2019-v1/NANOAOD
	Run 2018B	/Tau/Run2018B-Nano25Oct2019-v1/NANOAOD
	Run 2018C	/Tau/Run2018C-Nano25Oct2019-v1/NANOAOD
	Run 2018Dv2	/Tau/Run2018D-Nano25Oct2019_ver2-v1/NANOAOD

Table 5.4: Run II Tau Primary Datasets

5.6 Data Corrections

Despite more than a decade of excellent operation of the CMS detector, there are a number of known operational issues which affect the ability to record and measure certain physics objects. These issues are not accounted or corrected for in MC samples, as those samples were generally produced before the issues were discovered. Specific corrections are therefore needed to be applied in order to ensure good agreement between data and MC, and to remove the possibility of creating biased outcomes as a result of these issues. These include L1-PreFiring which effects 2016 and 2017 samples, the EE noise veto which affects 2017 samples, and the 2018 HEM veto which affects 2018 samples.

5.6.1 L1 Pre-firing (2016 & 2017)

The lead tungstate crystals which comprise the ECAL sub-detector naturally darken over time as a result of the large radiation dosage they are exposed to. As a result of this darkening, the light which propagates through them becomes increasingly delayed. It is possible then for the trigger electronics to assign a trigger tower to the incorrect bunch crossing (referred to as *pre-firing*), and the possiblity for such a mis-association was found to increase with the opacity of the ECAL crystal. This pre-firing was not accounted for when 2016 and 2017 MC samples were produced, and its effect can be significant. As a result, it is unlikely that such events can pass certain HLT requirements and the event can effectively become vetoed. In addition, CMS L1 triggers cannot fire on two successive bunch crossings, so even if there are other objects present in the event which can fire the trigger at L1 in the correct bunch crossing, the event is self-vetoed if a significant amount of ECAL energy is found in the region of $2.0 < |\eta| < 3.0$. This L1 pre-firing effect can therefore be regarded as a event level trigger inefficiency which has not been accounted for in certain measurements. The *EGamma* Physics Object Group (POG) at CMS has therefore formulated the following recipe for the probability of an event to prefire as a function of the jets and photons present in an event, which can then be applied to MC in the form of an event weight [66]:

$$\omega_{\text{L1 PreFiring}} = 1 - P(\text{PreFiring}) = \prod_{i=\text{photons, jets}} (1 - \varepsilon_i^{pref}(\eta, p_{\text{T}})) \tag{5.10}$$

where $\varepsilon_i^{pref}(\eta, p_{\text{T}})$ is the pre-firing probability of a photon/jet measured as a function of p_{T} and η, and ω is the resulting weight derived. In addition, overlap removal between jets and photons is applied.

Studies were performed on Z+jets and W+jets control regions in order to better understand how these weights affected processes of interest in this analysis. The results for the Z+jets study for 2016 and 2017 can be seen in tables 5.5 and 5.6, respectively. The results for both years indicate that there is little change after the application of central selections, which is expected as these selections do not explicitly require jets to be present in the event. After VBF selections are applied, there is a $\sim 2\%$ change, which is not particularly impactful on the resulting SFs, although they do increase slightly closer to unity. No noticeable changes were observed in regards to the shape of various kinematic plots produced in this control region, indicating the corrections do not significantly bias the shape in any way.

Selection type	Data	Total MC yield without L1 pre-firing weights	Total MC yield with L1 pre-firing weights	Total MC yield % difference	SF without L1 pre-firing weights	SF with L1 pre-firing weights	SF % difference
Central	14410792	4905818.4 ± 4465.7	14877093.3 ± 4462.5	-0.2%	0.967 ± 0.000	0.968 ± 0.000	0.1%
VBF II	67700	96015.7 ± 311.4	94260.2 ± 309.6	-1.8%	0.715 ± 0.004	0.728 ± 0.004	1.8%

Table 5.5: The effects of L1 Pre-firing weights on the event yields in data, MC, and SFs, after the application of central selections and VBF2 selections in Z+jets, 2016.

Selection type	Data	Total MC yield without L1 pre-firing weights	Total MC yield with L1 pre-firing weights	Total MC yield % difference	SF without L1 pre-firing weights	SF with L1 pre-firing weights	SF % difference
Central	17739983	18496595.1 ± 6509.5	18483314.1 ± 6506.1	-0.1%	0.959 ± 0.000	0.960 ± 0.000	0.1%
VBF II	98967	151425.5 ± 508.4	147991.1 ± 505.9	-2.3%	0.674 ± 0.003	0.687 ± 0.003	1.9%

Table 5.6: The effects of L1 Pre-firing weights on the event yields in data, MC, and SFs, after the application of central selections and VBF2 selections in Z+jets, 2017.

Similar results for the W+jets CR for 2016 and 2017 can be seen in tables 5.7 and 5.8, respectively. This CR requires a $p_{\mathrm{T}}^{miss} > 200$ GeV selection as part of the central selections. As a result, it is expected for there to be more high-p_{T} jets to be present in events after both central selections and VBF selections, which are required in order to create the large boost which enables the presence of large p_{T}^{miss}. This is indeed observed, as there is a greater reduction in total MC yield in this CR as opposed to Z+jets for both 2016 and 2017 when applying the L1 pre-firing weights. There is likewise an improvement in the resulting SFs for both years. No noticeable changes were observed in regards to the shape of various kinematic plots produced in this control region either, again indicating the corrections do not significantly bias the shape in any way. The resulting weights derived in this study have been applied to all MC samples for 2016 and 2017.

Selection type	Data	Total MC yield without L1 pre-firing weights	Total MC yield with L1 pre-firing weights	Total MC yield % difference	SF without L1 pre-firing weights	SF with L1 pre-firing weights	SF % difference
Central	59583	66078.6 ± 285.2	63548.1 ± 279.0	-3.8%	0.878 ± 0.007	0.923 ± 0.007	5.1%
VBF II	6322	7642.9 ± 117.7	6974.9 ± 115.1	-8.7%	0.867 ± 0.025	0.945 ± 0.027	9.0%

Table 5.7: The effects of L1 Pre-firing weights on the event yields in data, MC, and SFs, after the application of central selections and VBF2 selections in W+jets, 2016.

Selection type	Data	Total MC yield without L1 pre-firing weights	Total MC yield with L1 pre-firing weights	Total MC yield % difference	SF without L1 pre-firing weights	SF with L1 pre-firing weights	SF % difference
Central	49859	49690.5 ± 139.7	48462.5 ± 138.3	-2.5%	1.00 ± 0.01	1.03 ± 0.01	2.9%
VBF II	5050	5546.2 ± 50.9	5237.4 ± 50.1	-5.6%	0.866 ± 0.022	0.917 ± 0.023	5.9%

Table 5.8: The effects of L1 Pre-firing weights on the event yields in data, MC, and SFs, after the application of central selections and VBF2 selections in W+jets, 2017.

5.6.2 EE Noise Veto (2017)

Additional issues concerning ECAL were discovered in the tails of $p_{T_{miss}}$ distributions in 2017 when comparing data and MC. This effect was a result of the combination of several factors including ECAL aging in the high η region of the detector (endcap region), out-of-time pile-up, and selective readout at PF and LHC bunch structure [67]. In order to mitigate this effect, we followed the official recipe applied to data and simulation, which consists of fully dropping jets and unclustered PF candidates with $2.65 < |\eta| < 3.14$ and $p_{T^{raw}<}$ 50 GeV in the PF p_T^{miss} calculation. Only jets satisfying these requirements, besides being above the jet unclustered energy threshold of 15 GeV are considered for JER smearing. In addition, these jets are removed from the jet collection and not considered for analysis. It was discovered in subsequent validation studies that when applying the modified JER corrections, a disagreement was observed at high-p_T^{miss}. This was ultimately mitigated by extending the veto to reject events in data with ≥ 1 jet with $p_T < 80$ GeV and $2.65 < |\eta| < 3.15$, when running over the 2017E and 2017F eras. These corrections are therefore applied when running over relevant data in 2017.

5.6.3 HEM Veto (2018)

In 2018, a large section of the hadronic endcap calorimeter (HEM) covering $-3 \leq \eta \leq -1.65$ and $-1.57 \leq \phi \leq -0.87$ became unpowered. As a result, any jets which fall within this area of the detector in MC will need to be vetoed, as they would not have correspondingly been detected in data. Such a veto was implemented, the results of which can be seen in figure 5.7.

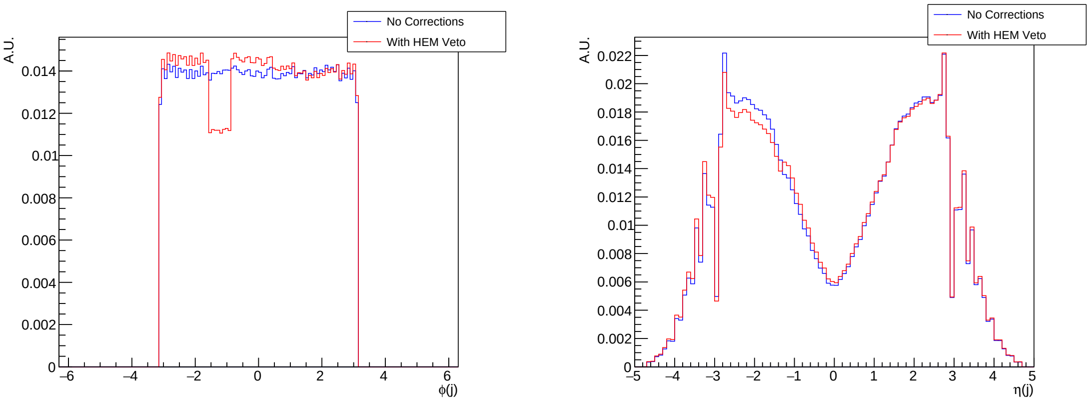

(a)

(b)

Figure 5.7: Overlaid plots showing before (blue) and after (red) the application of the HEM veto in ϕ (left) and η (right). All distributions have been normalized to unity in order to compare the overall shape.

CHAPTER 6

Signal Optimization

Signal optimization for this analysis will be divided into optimization of central objects (i.e. objects within the geometrical central region of the detector) and optimization of VBF jets. The optimal cut value for each selection is determined using the Higgs Combine Tool, in which the minimum theoretical cross section upper limit (UL) is calculated using signal and background yields after all cuts are applied, and the cut value which produces the smallest minimum theoretical cross section is chosen as the optimal value (see section 9.2 for a more detailed description of this process).

6.1 Central Selection Optimization

The baseline selections for the signal region (SR) in this analysis are based off of those in reference [31], which were derived for 0ℓ and 1ℓ channels. These selections can be seen in table 6.1, where entries in bold will be re-optimized for this analysis. This analysis additionally includes 2ℓ channels. Optimized selections for any individual object (e.g. electron p_{T} window) will be used consistently for that object in all channels.

			$\mu^{\pm}$ Channel	$e^{\pm}$ Channel	$\tau_h^{\pm}$ Channel
Central	Trigger		HLT_PFMETNoMu120_PFMHTNoMu120_IDTight		
	Lepton ID		**Tight PF**	**Medium CB**	**Deep Tau Tight WP**
	Lepton Iso.		0.15	0.15	
	Lepton p_{T} [GeV]	$\mu^{\pm}$	[**8**, **40**], veto 2$^{\text{nd}}$ $\mu > 8$	veto > 8	veto > 8
		$e^{\pm}$	veto > 10	[**10**, **40**], veto 2$^{\text{nd}}$ $e > 10$	veto > 10
		$\tau_h^{\pm}$	veto > 20	veto > 20	[**20**, **40**], veto 2$^{\text{nd}}$ $\tau_h > 20$
	$m_{\mathrm{T}}(l, p_{\mathrm{T}}^{miss})$ [GeV]	$\mu^{\pm}$	> 110	No Cut	No Cut
		$e^{\pm}$	No Cut	> 110	No Cut
		$\tau_h^{\pm}$	No Cut	No Cut	> 110
	Lepton η		< 2.1		
	p_{T}^{miss}		**>250 GeV**		
	b-jet		$N(b) = 0$, $p_{\mathrm{T}}(b) > 30$ GeV, $\lvert\eta\rvert < 2.4$, medium DeepCSV WP		
	QCD rejection		$\lvert\Delta\phi(j, p_{\mathrm{T}}^{miss})\rvert_{min} > 0.5$		

Table 6.1: Initial Event selections for signal region. Values shown in **bold** will be re-optimized

The use of a p_{T}^{miss} trigger in conjunction with a large p_{T}^{miss} value is motivated by the presence of the LSP which is produced in all signal events and leaves the detector undetected. This requirement also allows for trigger efficiency $>95\%$. This cut has the additional benefit that it suppresses both $Z \to \ell\ell$, which produces no real p_{T}^{miss}, as well as QCD multijet events. The lepton ID and lepton isolation are both required in order to efficiently reconstruct real leptons while rejecting fakes. The lepton p_{T} window is motivated by the compressed mass spectra SUSY scenarios this analysis looks to probe. One expects the leptons produced by these interactions to be soft. Larger lepton p_{T} values will therefore include more background events without actually including more signal events, and hence why an upper limit threshold is needed. The lower limit is motivated by the efficiency that CMS can reconstruct and identify leptons, without the intrusion of fakes. These values differ for the different leptons, as the different leptons are each reconstructed using different parts of the detector. The $m_{\mathrm{T}}(l, p_{\mathrm{T}}^{miss})$ requirement is only applied to the 1ℓ channel and is intended to remove events from W decays which produce a $m_{\mathrm{T}}(l, p_{\mathrm{T}}^{miss})$ peak around m_W. The lepton η requirement ensures leptons are reconstructed fully within the tracker. The rejection of b-jets reduces the contribution from $t\bar{t}$ events which can easily mimic our signal selections. Finally, the QCD rejection cut further suppresses contribution from QCD events by requiring a large $\Delta\phi$ cut between any jets and p_{T}^{miss}. This is due to the fact that QCD generally does not create real p_{T}^{miss} and instead produces fake p_{T}^{miss} due to incorrect detector reconstruction of jets.

Lepton ID & Lepton p_{T} Optimization

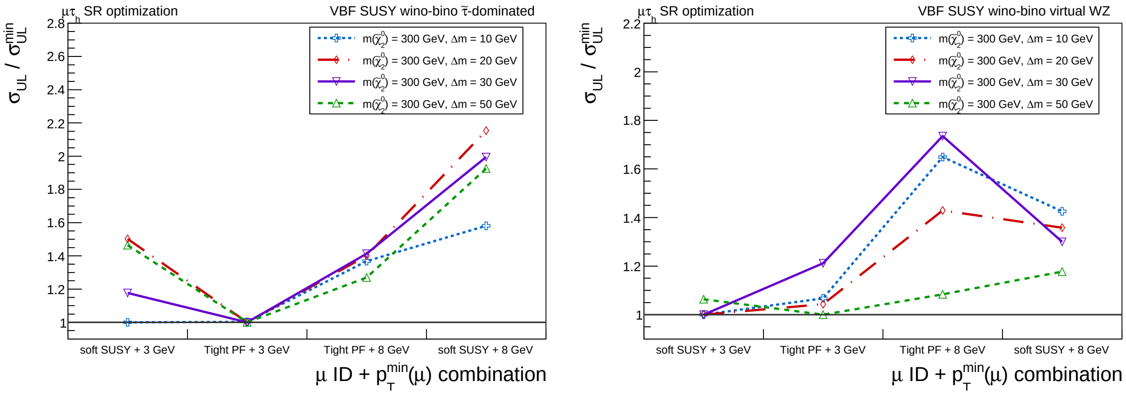

(a) (b)

Figure 6.1: Optimization results for the combination of μ ID + $p_{\mathrm{T}}^{min}(\mu)$, for the $\tilde{\tau}$-dominated scenario (left), and for the virtual W/Z scenario (right).

Lepton IDs and Lepton p_{T} were optimized for the $\tilde{\tau}$-dominated scenario and Virtual W/Z scenarios for various Δm values. A difficulty presented by the different SUSY scenarios we look to investigate is that phenomenologically they may produce a different spectrum of particles with different kinematics, meaning that optimization of a variable to one scenario or Δm might produce a different value than optimizing to other scenarios. There is therefore often a trade-off, and the value selected may not be the optimal value in all cases. Figure 6.1 shows the performance of the different combinations of μ ID and $p_{\mathrm{T}}^{min}(\mu)$ window for the $\tilde{\tau}$-dominated scenario (left) and virtual W/Z scenario (right). The μ IDs tested were TightID and soft SUSY ID, with the latter being formulated in order to probe SUSY events producing soft decay products such as ours more efficiently. The $p_{\mathrm{T}}^{min}(\mu)$ being tested was 8 GeV and 3 GeV. For both scenarios, the $p_{\mathrm{T}}^{min}(\mu)$ of 3 GeV performed better. Surprisingly however, the TightID performed only marginally better (typically $<10\%$)

in the virtual W/Z scenario, and significantly worse in the $\tilde{\tau}$-dominated scenario. This was discovered to be caused by a requirement within the soft SUSY ID of an impact parameter (IP_{3D}) requirement for leptons of < 0.01cm, which was formulated to suppress non-prompt leptons coming from b-jet decays, but had the unintended effect of rejecting τ decays as well. It was therefore decided to continue to use TightID for the μ ID and reduce $p_{\mathrm{T}}^{min}(\mu)$ to 3 GeV.

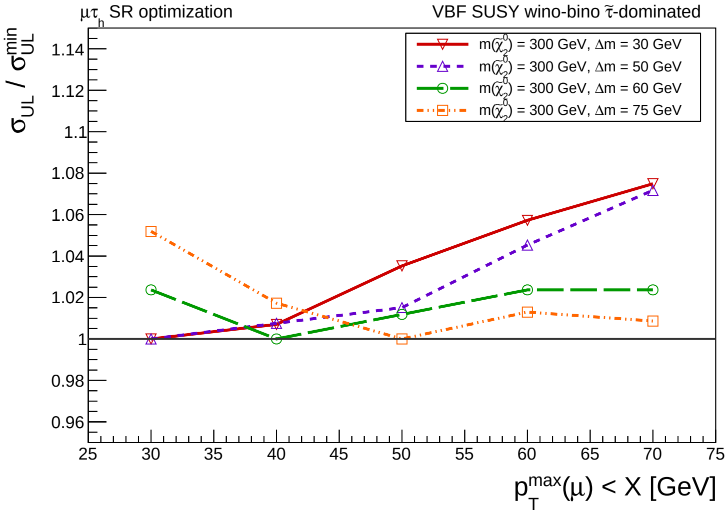

Figure 6.2: Optimization results for $p_{\mathrm{T}}^{max}(\mu)$ in the $\tilde{\tau}$-dominated scenario.

The optimization of $p_{\mathrm{T}}^{max}(\mu)$ within the $\tilde{\tau}$ dominated scenario is shown in figure 6.2 for various Δm values. This optimization showcases the difficulty in optimizing to multiple Δm values, as the $p_{\mathrm{T}}(\mu)$ produced in these events is highly dependent on the Δm of the scenario. Smaller Δm values produce low p_{T} muons and therefore increasing $p_{\mathrm{T}}^{max}(\mu)$ increases the total amount of background events present without also necessarily increasing signal events. The opposite is true for larger Δm values for which increasing $p_{\mathrm{T}}^{max}(\mu)$ allows for the inclusion of more signal events. Given that the improvements on the UL are typically small (<5%), the $p_{\mathrm{T}}^{max}(\mu)$ value was not changed, and 40 GeV was chosen to still be the selection value.

Figure 6.3 shows the performance of the different combinations of e ID and $p_{\mathrm{T}}^{min}(e)$ window for the $\tilde{\tau}$-dominated scenario (left) and virtual W/Z scenario (right), in which the e ID was tested between Medium Cut Based (CB) ID and soft SUSY ID, and $p_{\mathrm{T}}^{min}(e)$ was tested between 10 GeV and 5 GeV. A similar trend is observed to that of muons, by which the $\tilde{\tau}$-dominated scenario typically suffers when using the soft SUSY ID. It is found that lower $p_{\mathrm{T}}^{min}(e)$ value of 5 GeV performs better however for both IDs. Within the virtual W/Z scenario, the results are typically dependent on the Δm value, with smaller Δm performing better for 5 GeV. As a result, the Medium CB ID and $p_{\mathrm{T}}^{min}(e)$ value of 5 GeV was selected.

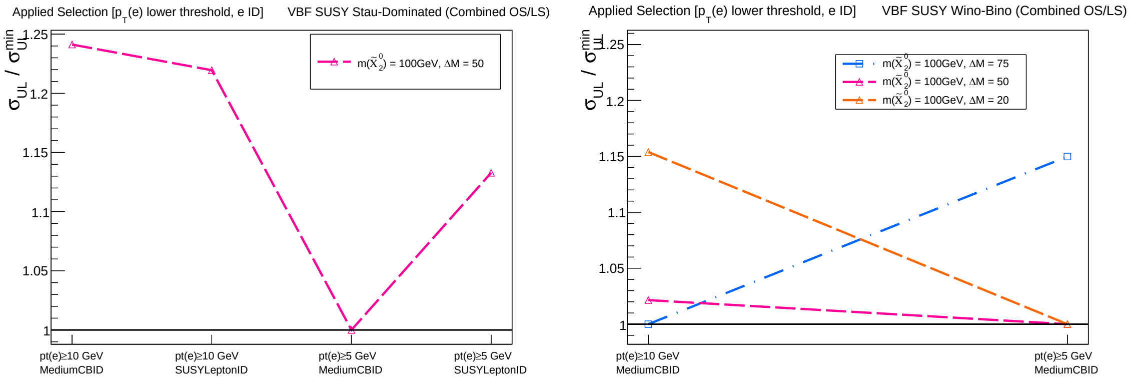

(a) (b)

Figure 6.3: Optimization results for the combination of e ID + $p_{\mathrm{T}}(e)$, for the $\tilde{\tau}$-dominated scenario (left), and for the virtual W/Z scenario (right).

p_{T}^{miss} Optimization

The optimization of p_{T}^{miss} was performed in the $\mu\tau_h$ channel. The results using a loose τ_hID working point (WP) can be seen in figure 6.4a and using a tight τ_hID WP can be seen in figure 6.4b. In order to interpret these results, it is important consider the efficiency curve of the p_{T}^{miss} trigger being used, which can be seen in figure 6.4c. This curve indicates that the trigger reaches maximum efficiency above 250 GeV. Choosing values below this would increase the systematic uncertainty on your study and therefore negatively impact the final signal sensitivity reach, which is not reflected in these plots. Additionally, decreasing the p_{T}^{miss} cut value could increase contribution from backgrounds with fake τ_h's such as QCD multijet or W+jets. Furthermore, the systematic uncertainty for similar searches (for example, see reference [31]) has been on the order of 25%, indicating that the reduction in the UL for smaller p_{T}^{miss} values will produce only small improvements ultimately. For these reasons, it was decided not to change the p_{T}^{miss} cut, and leave its values as >250 GeV.

Finalized Central Selection Values

The finalized central selection cut values can be seen in table 6.2, where values indicated in **red** indicate they have been updated relative to their previous value.

6.2 VBF Selection Optimization

The baseline VBF selections in this analysis are also based off of those in reference [31]. There was previously only one VBF category defined (which we denote VBF1), however two additional VBF categories have been defined as well (VBF2, VBF3). These categories can be seen in table 6.3. All three VBF criteria share a jet multiplicity requirement of at least 2 jets ($N(j) \geq 2$) which are required to be in opposite hemispheres

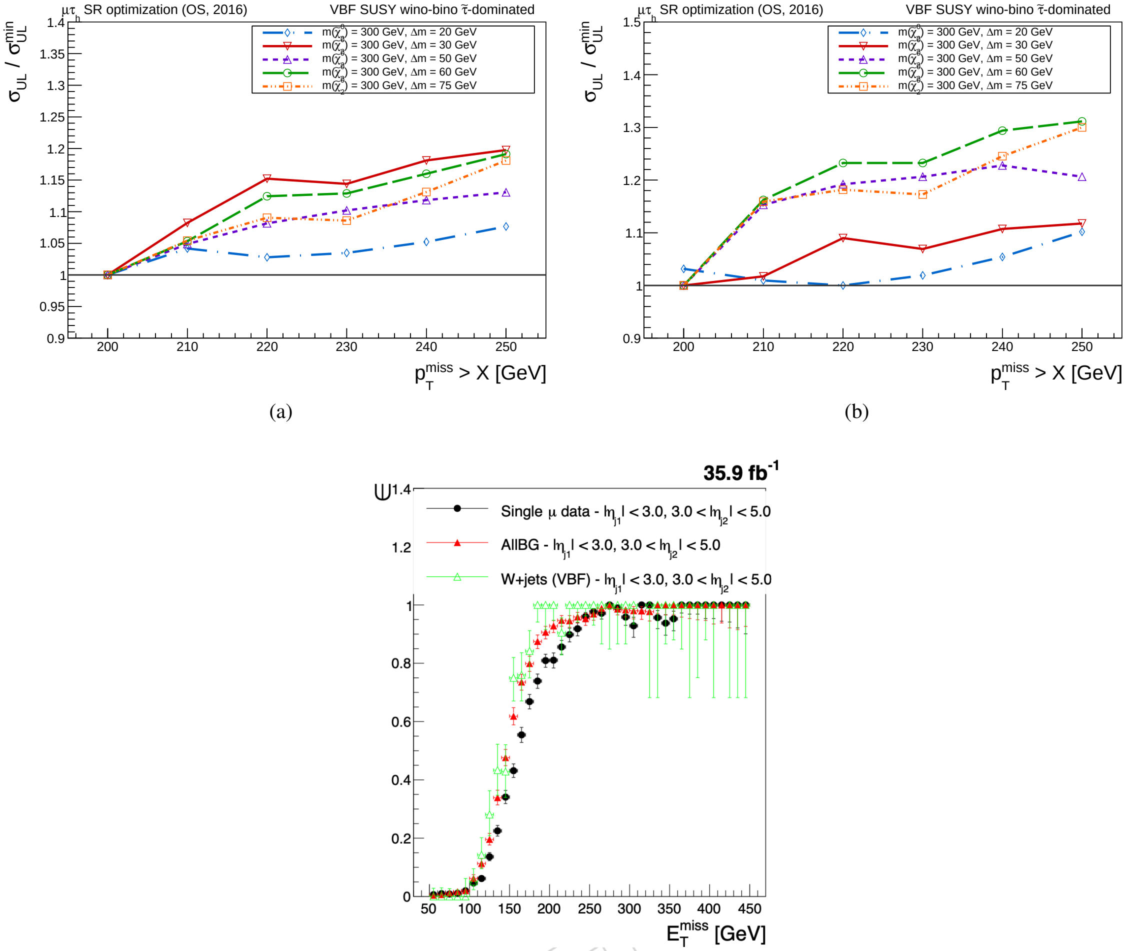

(a)

(b)

(c)

Figure 6.4: Optimization results for p_{T}^{miss} in the $\mu\tau_h$ channel using Loose τ_h ID working point (top left) and Tight τ_h ID working point (top right). Efficiency curve for the MET Trigger as a function of the offline p_{T}^{miss}, where one of the jets has $|\eta| < 3$ and the other $3 < |\eta| < 5$ [31].

($\eta(j_1) \times \eta(j_2) < 0$) and have a absolute pseudorapidity value to ensure the entire jet is reconstructed within the detector ($|\eta(j)| < 4.7$). There is also a requirement that the jets not overlap with any other physics objects ($\Delta R(e/\mu/\tau, j) > 0.4$). These jets must pass Loose ID in 2016, and Tight ID for 2017 and 2018, which are the official recommendations by CMS. These selections are motivated by the two real jets produced in VBF interactions and have the effect of reducing background yields in the signal region. There is additionally a dijet requirement of at least 1 dijet candidate, in which dijet candidates criteria differ between the three categories. VBF1 has the most stringent of these cuts, requiring $p_{\mathrm{T}}(j) > 60$ GeV for all jets, and $\Delta\eta(j_1, j_2) > 3.8$ and m$(jj) > 1000$ GeV for all dijet candidates. This has the effect of reducing the complications arising due to PU jets (e.g. particle mismeasurement, fakes, etc.), but also removes signal events in the process. VBF2 however lowers the jet p_{T} requirement to $p_{\mathrm{T}}(j) > 30$ GeV and has a dijet $m(jj)$ candidate requirement of

			$\mu^{\pm}$ Channel	$e^{\pm}$ Channel	$\tau_h^{\pm}$ Channel
Central	Trigger		HLT_PFMETNoMu120_PFMHTNoMu120_IDTight		
	Lepton ID		Tight PF	Medium CB	Deep Tau Tight WP
	Lepton Iso.		0.15	0.15	
	Lepton p_{T} [GeV]	$\mu^{\pm}$	**[3, 40]**	veto > 3	veto > 3
		$e^{\pm}$	veto > 5	**[5, 40]**	veto > 5
		$\tau_h^{\pm}$	veto > 20	veto > 20	**[20, 70]**
	$m_T(l, p_{\mathrm{T}}^{miss})$ [GeV]	$\mu^{\pm}$	> 110	No Cut	No Cut
		$e^{\pm}$	No Cut	> 110	No Cut
		$\tau_h^{\pm}$	No Cut	No Cut	> 110
	Lepton η		< 2.1		
	p_{T}^{miss}		**>250 GeV**		
	b-jet		$N(b) = 0$, $p_{\mathrm{T}}(b) > 30$ GeV, $\lvert\eta\rvert < 2.4$, medium DeepCSV WP		
	QCD rejection		$\lvert\Delta\phi(j, p_{\mathrm{T}}^{miss})\rvert_{min} > 0.5$		

Table 6.2: Final Event selection cuts for the signal region. Values shown in **bold** have been re-optimized, while values shown in **bold red** are the new value (not all values changed after re-optimization).

m$(jj) > 500$ GeV. There is also a requirement for jets of $p_{\mathrm{T}} \in [30, 50]$ GeV to pass PileupJetID. The effect is an increase in signal yield, but a possible larger inclusion of PU jets and the problems that arise therein. VBF3 is similar to VBF2 except for that it requires $\Delta\eta(j_1, j_2) > 6.0$. This category will mainly be used for reinterpretations such as anapole moment DM (ADM) which focuses on photon fusion events that produce very far forward jets, and which have thus far not been discussed in this thesis. Figure 6.5 shows $\Delta\eta(j_1, j_2$, $\eta(j)$, and largest m(jj), when comparing background processes in MC to the Virtual W/Z scenario with a mass gap of $\Delta m = 30$ GeV, where all distributions have been normalized to unity. These plots are intended to provide an indication of the difference in signal shape versus background and therefore motivate the ultimate optimization selections.

	Object	Selection cuts
VBF1	Jet selection	$N(j) \geq 2$, $p_{\mathrm{T}}(j) >$ **60 GeV**, $\lvert\eta(j)\rvert < 4.7$, $\Delta R(e/\mu/\tau, j) > 0.4$ loose (2016)/ tight (2017 & 2018) ID
	Dijet selections	$\Delta\eta(j_1, j_2) >$ **3.8**, $\eta(j_1) \times \eta(j_2) < 0$, $m(jj) >$ **1000 GeV**
VBF2	Jet selection	$N(j) \geq 2$, $p_{\mathrm{T}}(j) >$ **30 GeV**, $\lvert\eta(j)\rvert < 4.7$, $\Delta R(e/\mu/\tau, j) > 0.4$ loose (2016)/ tight (2017 & 2018) ID & PU jet ID
	Dijet selections	$\Delta\eta(j_1, j_2) >$ **3.8**, $\eta(j_1) \times \eta(j_2) < 0$, $m(jj) >$ **500 GeV**
VBF3	Jet selection	$N(j) \geq 2$, $p_{\mathrm{T}}(j) >$ **30 GeV**, $\lvert\eta(j)\rvert < 4.7$, $\Delta R(e/\mu/\tau, j) > 0.4$ loose (2016)/ tight (2017 & 2018) ID & PU jet ID
	Dijet selections	$\Delta\eta(j_1, j_2) >$ **6.0**, $\eta(j_1) \times \eta(j_2) < 0$, $m(jj) >$ **500 GeV**

Table 6.3: Event selection criteria for VBF1, VBF2, & VBF3.

Results Using *ee* Channel Central Selections

VBF selection optimization was performed in a similar manner to the central selection optimization, in which the optimal cut value for each selection was determined using the Higgs Combine Tool after all cuts had been applied and the cut value which resulted in the smallest theoretical upper limit on the cross section was chosen

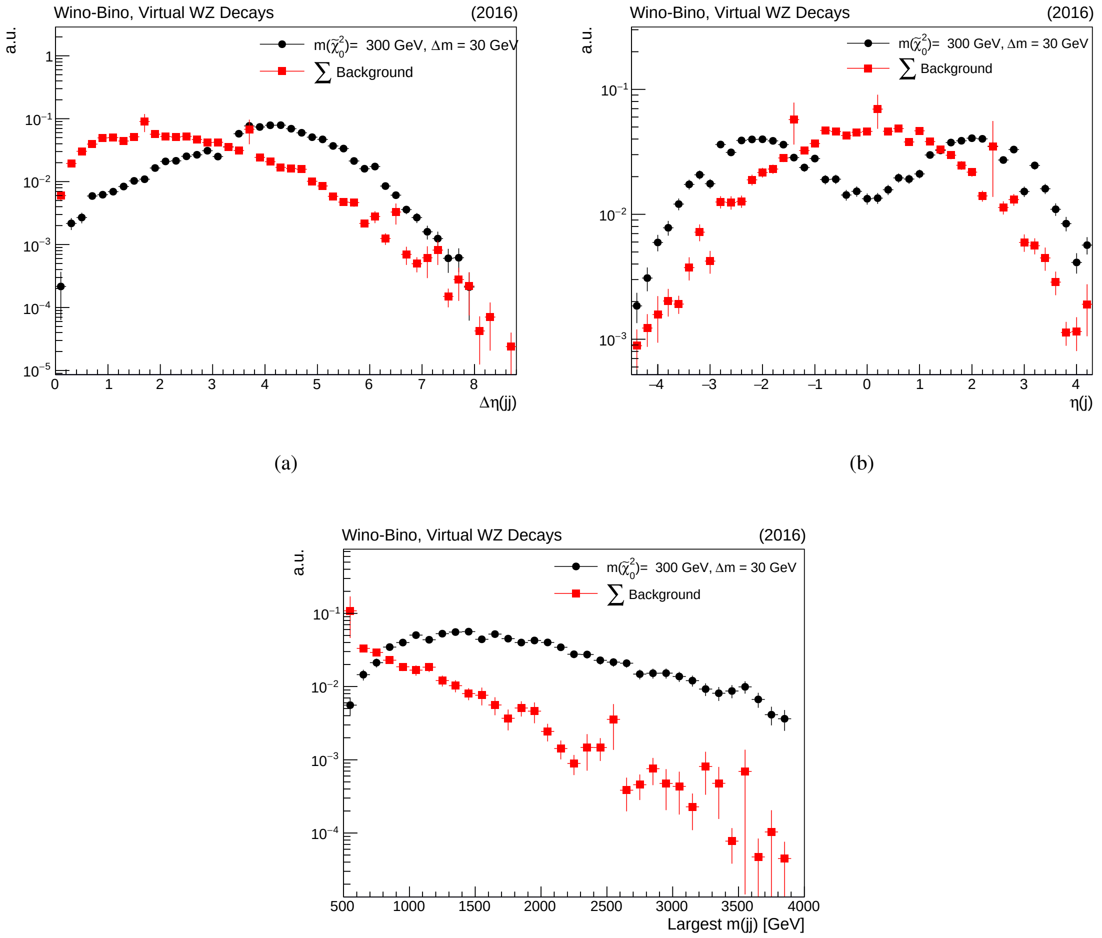

(a)

(b)

(c)

Figure 6.5: Background versus signal for $\Delta\eta(j_1, j_2$ (top left), $\eta(j)$ (top right), and largest m(jj) (bottom). All distributions are normalized to unity in order to compare the shape.

as the optimal value. These studies were first performed in the *ee* channel, using the central selections shown in table 6.4. A distinction was made between opposite sign electron pairs (OS) and like-sign pairs (LS) in separate studies, and these results were then combined. These studies were performed using the virtual W/Z scenario using $\tilde{\chi}^0_2$ masses of 150 GeV and 300 GeV, and mass gaps of Δm = 5, 30, and 50 GeV. The results for studies performed over 2016 MC, 2017 MC, and 2018 MC can be seen in tables 6.5, 6.6, and 6.7. These results indicate that VBF2 performs better across nearly all signal mass points tested, with the exception of 2018, albeit by only a small percentage. If we examine the largest dijet mass distributions, as seen in figure 6.6 which shows the results of VBF1 on the left and VBF2 on the right, we can see that the inclusion of the two extra low mass bins within VBF2 will help when fitting the distribution using a binned likelihood fit. Given the close performance between the two VBF categories and the added benefit of higher signal yield for

VBF2, it was determined that VBF2 selections would be used as the optimized signal selections. Background estimations will still be performed for all three different categories however.

Channel	Object	Selection cuts
ee	Trigger	HLT_PFMETNoMu120_PFMHTNoMu120_IDTight
	e	$N(e) = 2$ (OS/LS discr.), $5 < p_{\mathrm{T}}(e) < 40$ GeV, $\lvert\eta(e)\rvert < 2.1$, $I_{rel} < 0.15$, Medium CBID
	ee pair	OS/LS discr., $\Delta R(e,e) > 0.4$
	μ veto	$N(\mu) = 0$, $p_{\mathrm{T}}(\mu) > 3$ GeV, $\lvert\eta(\mu)\rvert < 2.1$, $I_{rel} < 0.15$, Tight PF ID
	b-jet veto	$N(\mathrm{b}) = 0$, $p_{\mathrm{T}}(\mathrm{b}) > 30$ GeV, $\lvert\eta(\mathrm{b})\rvert < 2.4$, medium DeepCSV WP
	τ veto	$N(\tau) = 0$, $p_{\mathrm{T}}(\tau) > 20$ GeV, $\lvert\eta(\tau)\rvert < 2.5$, tight anti-$e/\mu$ discr. prong: 1or3hps
	p_{T}^{miss}	$p_{\mathrm{T}}^{miss} > 250$ GeV

Table 6.4: Central Selection cuts used in the *ee* channel when determining VBF optimization.

Region	VBF1 OS	VBF1 LS	VBF1 Combined	VBF2 OS	VBF2 LS	VBF2 Combined
$\mathrm{m}(\tilde{\chi}_2^0) = 300$ GeV, Δm = 50 GeV	10.41	21.50	8.56	9.56	18.31	7.84
$\mathrm{m}(\tilde{\chi}_2^0) = 300$ GeV, Δm = 30 GeV	7.38	14.00	5.92	6.81	10.66	5.25
$\mathrm{m}(\tilde{\chi}_2^0) = 300$ GeV, Δm = 5 GeV	62.88	42.75	31.81	57.88	27.88	23.44
$\mathrm{m}(\tilde{\chi}_2^0) = 150$ GeV, Δm = 50 GeV	24.94	45.75	19.97	23.63	54.75	20.25
$\mathrm{m}(\tilde{\chi}_2^0) = 150$ GeV, Δm = 30 GeV	13.69	45.38	12.41	12.56	28.13	10.69
$\mathrm{m}(\tilde{\chi}_2^0) = 150$ GeV, Δm = 5 GeV	45.75	34.38	24.63	39.25	28.75	21.13

Table 6.5: Resulting R-values from Higgs Combine Tool for 2016 Virtual W/Z scenario showing multiple signal mass points for VBF1 vs VBF2. *ee* channel OS, LS, & combined results are all shown.

Region	VBF1 OS	VBF1 LS	VBF1 Combined	VBF2 OS	VBF2 LS	VBF2 Combined
$\mathrm{m}(\tilde{\chi}_2^0) = 300$ GeV, Δm = 50 GeV	9.50	24.50	8.34	8.69	20.13	7.53
$\mathrm{m}(\tilde{\chi}_2^0) = 300$ GeV, Δm = 30 GeV	6.34	15.25	5.47	5.73	19.38	5.30
$\mathrm{m}(\tilde{\chi}_2^0) = 300$ GeV, Δm = 5 GeV	42.25	42.25	27.38	38.25	26.13	19.69
$\mathrm{m}(\tilde{\chi}_2^0) = 150$ GeV, Δm = 50 GeV	22.25	46.13	18.50	21.63	29.88	16.06
$\mathrm{m}(\tilde{\chi}_2^0) = 150$ GeV, Δm = 30 GeV	14.19	43.94	12.81	11.84	29.13	10.34
$\mathrm{m}(\tilde{\chi}_2^0) = 150$ GeV, Δm = 5 GeV	35.13	21.25	16.38	31.88	28.38	19.06

Table 6.6: Resulting R-values from Higgs Combine Tool for 2017 Virtual W/Z scenario showing multiple signal mass points for VBF1 vs VBF2. *ee* channel OS, LS, & combined results are all shown.

Region	VBF1 OS	VBF1 LS	VBF1 Combined	VBF2 OS	VBF2 LS	VBF2 Combined
m($\tilde{\chi}_2^0$) = 300 GeV, Δm = 50 GeV	6.91	11.81	5.38	6.72	14.56	5.70
m($\tilde{\chi}_2^0$) = 300 GeV, Δm = 30 GeV	4.77	11.25	4.05	4.83	9.94	4.05
m($\tilde{\chi}_2^0$) = 300 GeV, Δm = 5 GeV	23.25	21.94	14.13	24.75	27.1 3	16.56
m($\tilde{\chi}_2^0$) = 150 GeV, Δm = 50 GeV	13.94	21.00	10.47	15.19	26.38	12.13
m($\tilde{\chi}_2^0$) = 150 GeV, Δm = 30 GeV	8.94	22.31	7.72	8.97	19.81	7.69
m($\tilde{\chi}_2^0$) = 150 GeV, Δm = 5 GeV	30.88	19.25	14.81	31.25	16.56	13.69

Table 6.7: Resulting R-values from Higgs Combine Tool for 2018 Virtual W/Z scenario showing multiple signal mass points for VBF1 vs VBF2. *ee* channel OS, LS, & combined results are all shown.

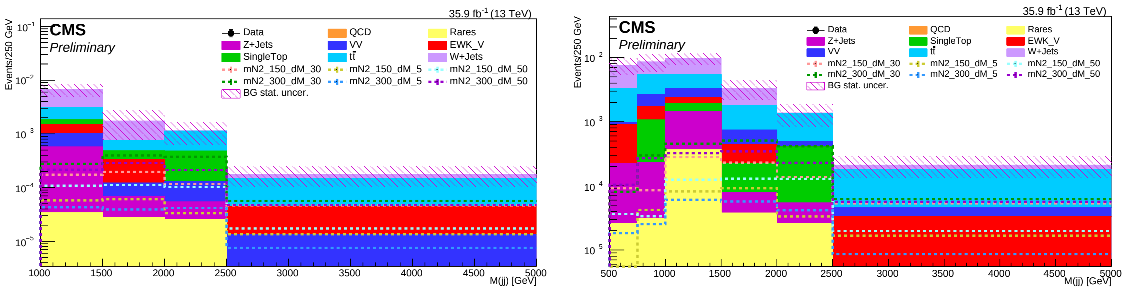

(a)

(b)

Figure 6.6: Largest $m(jj)$ after VBF1 cuts (left) and VBF2 cuts (right) applied in the *ee* channel, showing various signal mass points for the virtual W/Z scenario scenario (2016). The inclusion of the two lower $m(jj)$ bins along with the lower $p_T(j)$ allows for a larger signal acceptance as well as better signal sensitivity. The background processes (shown in solid colors) are stacked in the distribution, whereas the signal points (shown dashed) are overlaid. All signal samples use a dummy cross-section of 100 fb.

Validation Using $\mu\mu$ Channel Central Selections

An additional validation study was performed using the $\mu\mu$ channel after applying the selection cuts listen in table 6.8. The results can be seen in table 6.9, which mirror the same results observed in the *ee* channel. Again, the addition of the two extra low mass bins within VBF2 as seen in figure 6.7 will aid in performing a best fit on the data.

Channel	Object	Selection cuts
$\mu\mu$	Trigger	HLT_PFMETNoMu120_PFMHTNoMu120_IDTight
	μ	$N(\mu) = 2$ (OS/LS discr.), 3< $p_{\mathrm{T}}(\mu)$ <40 GeV, $\lvert\eta(\mu)\rvert < 2.1$, I_{rel} <0.15, Tight PFID
	$\mu\mu$ pair	OS/LS discr., $\Delta R(\mu,\mu) > 0.4$
	e veto	$N(e) = 0$, $p_{\mathrm{T}}(e)$ >5 GeV, $\lvert\eta(e)\rvert < 2.1$, I_{rel} <0.15, Medium CB ID
	b-jet veto	$N(\mathrm{b})$ =0, $p_{\mathrm{T}}(\mathrm{b})$ >30 GeV, $\lvert\eta(\mathrm{b})\rvert < 2.4$, medium DeepCSV WP
	τ veto	$N(\tau) = 0$, $p_{\mathrm{T}}(\tau)$ >20 GeV, $\lvert\eta(\tau)\rvert < 2.5$, tight anti-$e/\mu$ discr. prong: 1or3hps
	p_{T}^{miss}	p_{T}^{miss} >250 GeV

Table 6.8: Central Selection cuts used in the $\mu\mu$ channel when determining VBF optimization.

Region	VBF1 OS	VBF1 LS	VBF1 Combined	VBF2 OS	VBF2 LS	VBF2 Combined
m($\tilde{\chi}_2^0$) = 300 GeV, Δm = 50 GeV	2.33	6.81	2.13	2.27	7.19	2.10
m($\tilde{\chi}_2^0$) = 300 GeV, Δm = 30 GeV	1.67	4.84	1.51	1.67	4.67	1.52
m($\tilde{\chi}_2^0$) = 300 GeV, Δm = 5 GeV	11.03	8.72	6.34	10.84	8.09	6.09
m($\tilde{\chi}_2^0$) = 150 GeV, Δm = 50 GeV	5.73	22.50	5.42	5.84	16.56	5.34
m($\tilde{\chi}_2^0$) = 150 GeV, Δm = 30 GeV	3.53	11.03	3.25	3.50	9.94	3.20
m($\tilde{\chi}_2^0$) = 150 GeV, Δm = 5 GeV	9.38	6.56	5.05	9.34	5.66	4.61

Table 6.9: Resulting R-values from Higgs Combine Tool for 2017 Virtual W/Z scenario showing multiple signal mass points for VBF1 vs VBF2. $\mu\mu$ channel OS, LS, & combined results are all shown.

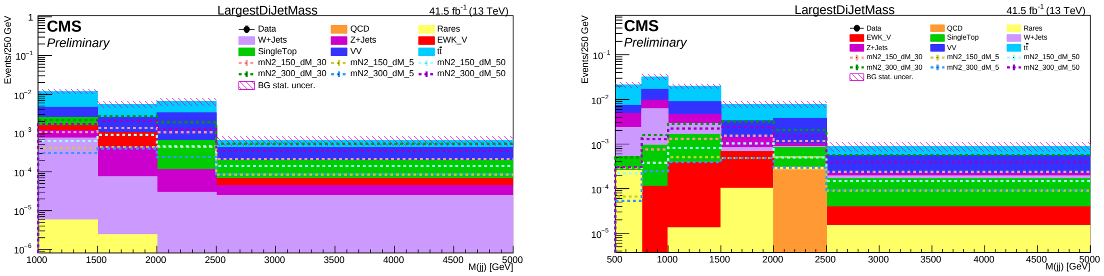

(a)

(b)

Figure 6.7: Largest $m(jj)$ after VBF1 cuts (left) and VBF2 cuts (right) applied in the $\mu\mu$ channel, showing various signal mass points for the virtual W/Z scenario scenario (2016). The inclusion of the two lower $m(jj)$ bins along with the lower $p_{\mathrm{T}}(j)$ allows for a larger signal acceptance as well as better signal sensitivity. The background processes (shown in solid colors) are stacked in the distribution, whereas the signal points (shown dashed) are overlaid. All signal samples use a dummy cross-section of 100 fb.

CHAPTER 7

Background Estimation

A *background* is any SM process which can also produce the same final state particles of your search channel and mimic their kinematics. Ideally, one would want to choose the search region in such a way that only signal events are selected and all other events are rejected. This however is not feasible in practice. It is therefore imperative that the background processes which will be recorded in data are well modeled in simulation so that in the event an excess is observed, one can be confident it is a true sign of new physics and not instead poor modeling of known physics. Studies which try to understand the modeling of such backgrounds are referred to as *background estimation* studies. As detailed in section 5.1, any mismodeling will be corrected for through the use of scale factors (SF), or when necessary, using shape-based corrections. These studies will first be performed by applying central selection cuts, in order to understand the modeling of physics objects reconstructed in the central region of the detector, followed by VBF selections to understand the modeling of jets reconstructed in the forward region of the detector. Figure 7.1 shows four dominant backgrounds within the light lepton channels: Z+jets, W+jets, $t\bar{t}$, and diboson. Independent background estimations will be performed for each of these channels. As a reminder, the VBF selections being studied here can be found in table 6.3.

7.1 Z+Jets

Z bosons will naturally produce dilepton pairs of opposite sign when the Z decays via $Z \rightarrow \ell\ell$. If the Z is produced in conjunction with "initial state radiation" (ISR) jets as seen in figure 7.1a, then it is possible for these events to satisfy all lepton and jet selection criteria in the OS dilepton SRs. The SR selection of $p_{\mathrm{T}}^{miss} > 250$ GeV will suppress this background process as there is no "real" p_{T}^{miss} produced, however if the ISR jets are incorrectly reconstructed then it is possible for large "fake" p_{T}^{miss} to pass this selection cut. It is estimated that $\sim 10^8$ Z bosons will be generated at CMS over the 2016, 2017 and 2018 data taking runs [68]. If even a small fraction of these events pass the strict SR cuts, then these events will represent a sizable background present within the SR. A $Z \rightarrow \mu\mu$+jets background estimation is therefore performed using the central selection cuts shown in Table 7.1. The dimuon channel is chosen specifically due to the high reconstruction efficiency of muons and the high $p_{\mathrm{T}}(\mu)$ resolution measurement capabilities of the CMS detector. The SFs derived in this study will also be applied to all other channels except in certain scenarios in which channel specific Z+jets background estimation studies have been performed. (i.e. 0L channels, channels involving τ_h decays). The selection events in this CR were chosen in order to produce a Z enriched

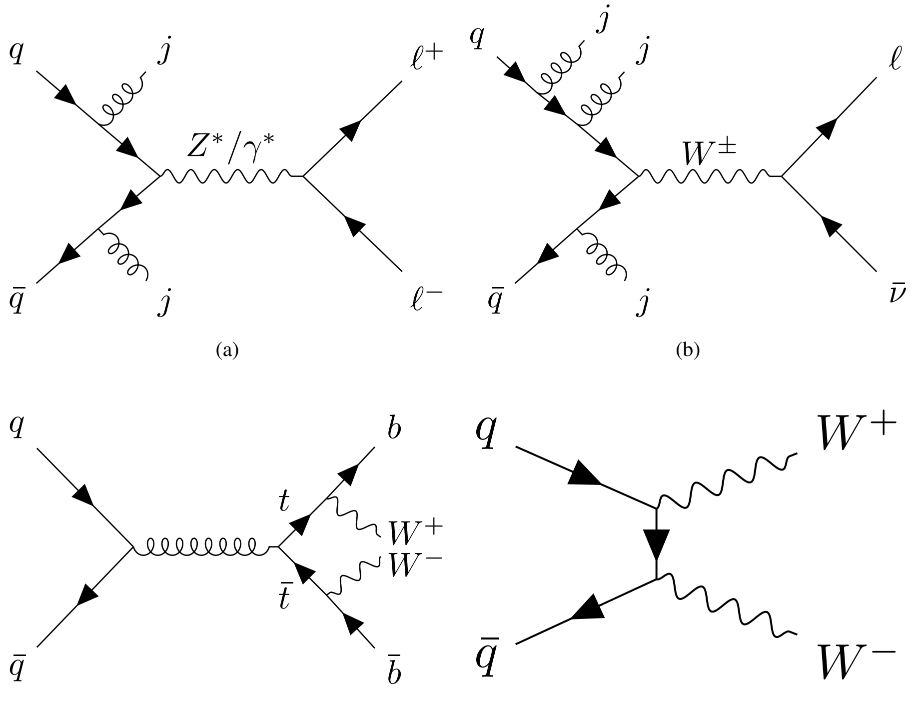

(a) (b)

(c) (d)

Figure 7.1: Feynman diagrams for the three dominant backgrounds within the light lepton channels: Z+jets (top left), W+jets (top right), $t\bar{t}$ (bottom loft), diboson (bottom right).

CR with high purity. This study was performed by running over the muon PD using the IsoMu24 and IsoMu27 triggers in a "logical OR" configuration. Exactly two muons are selected for, each with $p_{\mathrm{T}}(\mu) > 30$ GeV in order to ensure the trigger has high efficiency and with $|\eta| < 2.1$ to ensure the muon is fully reconstructed inside the tracker. An isolation of < 0.15 is applied to reduce muons produced from heavy flavor decays or fakes. It is additionally required that the muons have opposite charge, and an invariant mass around the m_Z peak. The p_{T}^{miss} selection is inverted in order to ensure orthogonality to the SR. All events containing electrons, taus, or b-jets are additionally vetoed.

	Object	Selection cuts
Z+Jets	Trigger	HLT_IsoMu24 or HLT_IsoMu27
	Muon selection	$N(\mu) = 2$, $p_{\mathrm{T}}(\mu) > 30$ GeV, $\|\eta(\mu)\| < 2.1$, tight ID, Isolation: I < 0.15, $q(\mu_1) \times q(\mu_2) < 0$, $m(\mu,\mu) \in [80,100]$ GeV
	p_T^{miss} selection	< 250 GeV
	Electron veto	$N(e) = 0$, $p_{\mathrm{T}}(e) > 5$ GeV, $\|\eta\| < 2.1$, Medium ID (cut-based)
	Tau veto	$N(\tau) = 0$, $p_{\mathrm{T}}(\tau) > 20$ GeV, $\|\eta\| < 2.1$, tight anti-$e\mu$ discr., prong: 1or3hps
	b-jet veto	$N(b) = 0$, $p_{\mathrm{T}}(b) > 30$ GeV, $\|\eta\| < 2.4$, Medium DeepCSV WP

Table 7.1: Central selection event criteria for Z+Jets background estimation.

Z+Jets Modeling After Central Selections:

Table 7.2 shows purities, SFs, and event yields in data and MC for 2016, 2017, and 2018, after applying CS cuts. The full event yield including contributions from each individual MC process can be found in appendix table A.7. It is observed that the CS cuts provide excellent purity with >99% of events coming from Z+jets MC samples for all three years. It is additionally observed that the CS SFs derived for all three years are within 10% of unity, indicating the CR is well modeled. Figures 7.2, 7.3, and 7.4 show $p_{\mathrm{T}}(\mu)$, $\eta(\mu)$, $m(\mu,\mu)$ and $\Delta p_{\mathrm{T}}(\mu,\mu)$ after CS cuts have been applied in 2016, 2017, and 2018, respectively. Kinematically, one would expect the following behavior in Z+jets events; Given that the vast majority of muons in these events are created from real Z bosons, the $p_{\mathrm{T}}(\mu)$ distribution should peak around $m_Z/2$ and then exponentially decay. The η distribution for muons is not expected to have any η dependence (i.e. muons are expected to be produced centrally and not in the forward region of the detector like VBF jets) but instead remain flat with only a slight decrease in production for increasing η values due to the fact that pseudorapidity is not linear in azimuthal angle (θ). When taking the invariant mass between the two muons produced, there should be a peak around m_Z as the invariant mass of the two daughter particles corresponds to the invariant mass of the mother particle that produced them. $\Delta p_{\mathrm{T}}(\mu,\mu)$ corresponds to momentum carried by the Z boson itself. This value can be non-zero due to the interacting partons carrying different momentum as determined by the parton distribution function, or if there is ISR jet activity present in the event. It is observed that for all three years these distributions have very good agreement between MC and data. It is therefore concluded that no shape based correction is needed for central selections in Z+jets, and that only a CS SF will need to be applied in order to correct for discrepancies in total event yield for each year.

Sample	2016	2017	2018
Z+Jets MC	14833626.6 ± 4465.6	18455293.7 ± 6511.4	25675036.2 ± 9107.0
Total MC	14913009 ± 4467.5	18520640.7 ± 6512.4	25766877.6 ± 9346.7
Data	14174710	17146880	23298593
Purity [%]	99.5%	99.6%	99.6%
Central Selection Scale Factor	0.95 ± 0.001	0.93 ± 0.001	0.90 ± 0.001

Table 7.2: Event yields for Z+Jets in Data and MC after central selection cuts have been applied. The full event yield can be found in appendix table A.7

Z+Jets Modeling After VBF Selections:

Tables 7.3, 7.4, and 7.5 show purities, SFs, and event yields in data and MC for 2016, 2017, and 2018, after VBF1, VBF2, and VBF3 selections are applied, respectively. The full event yields can be found in appendix tables A.8, A.9, and A.10. VBF2 and VBF3 selections provide the highest purities of >90%, while VBF1 provides a purity ∼ 80%. This conclusion implies that jets produced in Z+jets events are primarily

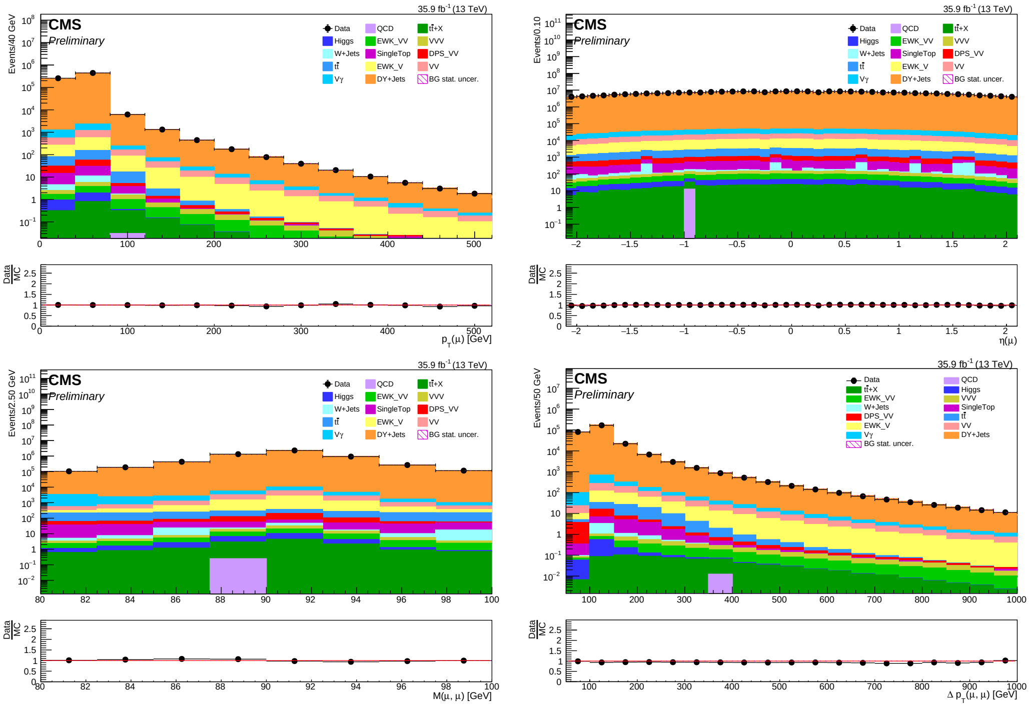

Figure 7.2: $p_{\mathrm{T}}(\mu)$, $\eta(\mu)$, $m(\mu,\mu)$, and $\Delta p_{\mathrm{T}}(\mu,\mu)$ after central selection cuts, including veto selections, in Z+jets (2016). A scale factor of 0.95 has been applied to these plots.

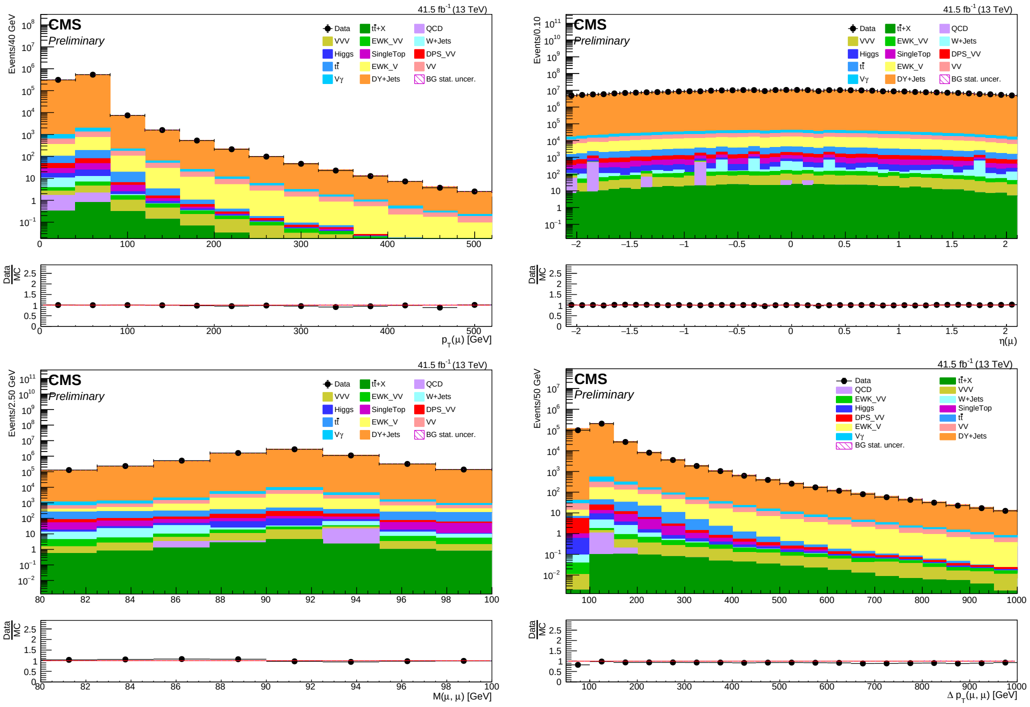

Figure 7.3: $p_{\mathrm{T}}(\mu)$, $\eta(\mu)$, $m_T(\mu,\mu)$, and $\Delta p_{\mathrm{T}}(\mu,\mu)$ after central selection cuts, including veto selections, in Z+jets (2017). A scale factor of 0.93 has been applied to these plots.

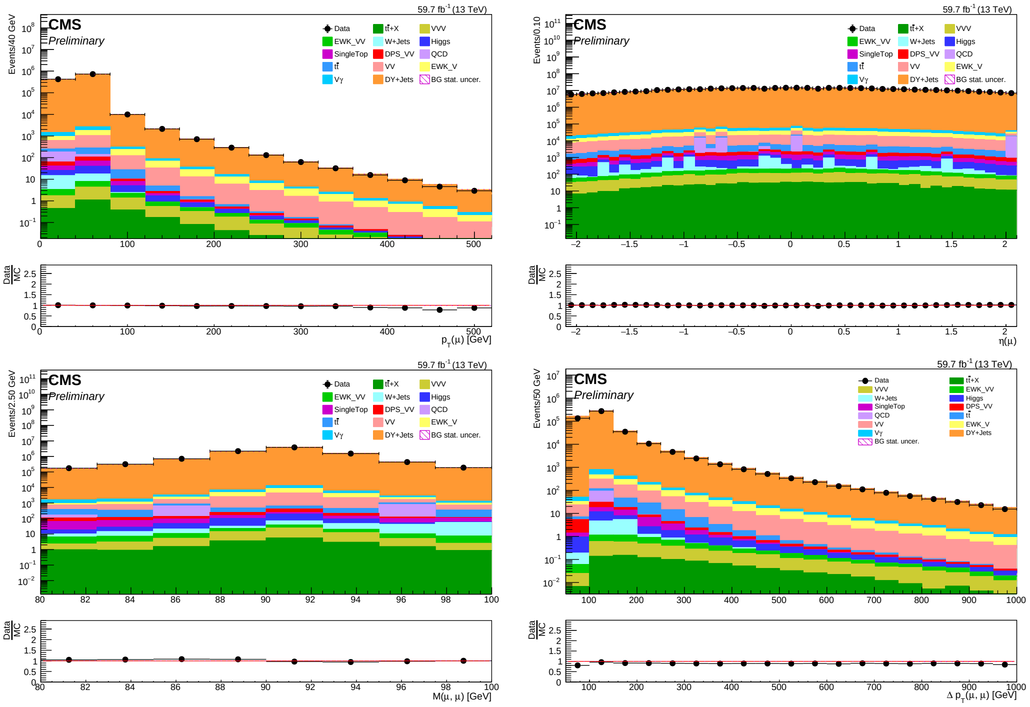

Figure 7.4: $p_\mathrm{T}(\mu)$, $\eta(\mu)$, $m_T(\mu,\mu)$, and $\Delta p_\mathrm{T}\mu,\mu)$ after central selection cuts, including veto selections, in Z+jets (2018). A scale factor of 0.90 has been applied to these plots.

low-p_T jets, given that increasing the jet p_T requirement when going from VBF2→VBF1 causes a more impactful reduction in Z+jets MC than in other processes. This result is consistent with the expectation that the jets produced in these events are primarily ISR jets. Kinematic distributions produces after applying VBF1 selections for 2016, 2017, and 2018 can be found in figures 7.5, 7.6, and 7.7. The same distributions after VBF2 and VBF3 selections have been applied for all three years can be found in figures 7.8, 7.9, 7.10, and in figures 7.11, 7.12, and 7.13 respectively. Kinematically, one would expect the $p_\mathrm{T}(j)$ distribution for ISR jets to be a decaying exponential. The subset of jets being selected for must pass the $\Delta\eta(jj)$ and m_{jj} cut, however, which will require the jets to be more far forward and have higher average p_T. It is therefore expected for there to be a "hump" in the distribution for $p_\mathrm{T}(j)$, which is indeed observed in all distributions. $\eta(j)$ should also have a "double hump" structure, with the humps being even further separated in VBF3. Both of these behaviors are indeed observed in all VBF categories as expected. $\Delta\eta(jj)$ and m_{jj} also match their expected behavior, with VBF3 showing a hump structure in m_{jj} which is caused by the increased $\Delta\eta(jj) > 6.0$ requirement that pushes the peak of m_{jj} to be larger. It is important to note that although small disagreements (statistical fluctuations) exist within individual plots, these disagreements do not affect the m_{jj} distribution which is the distribution we are ultimately interested in. The conclusion of this study then is that Z+jets appears to be well modeled across all years, and across all three VBF categories. It

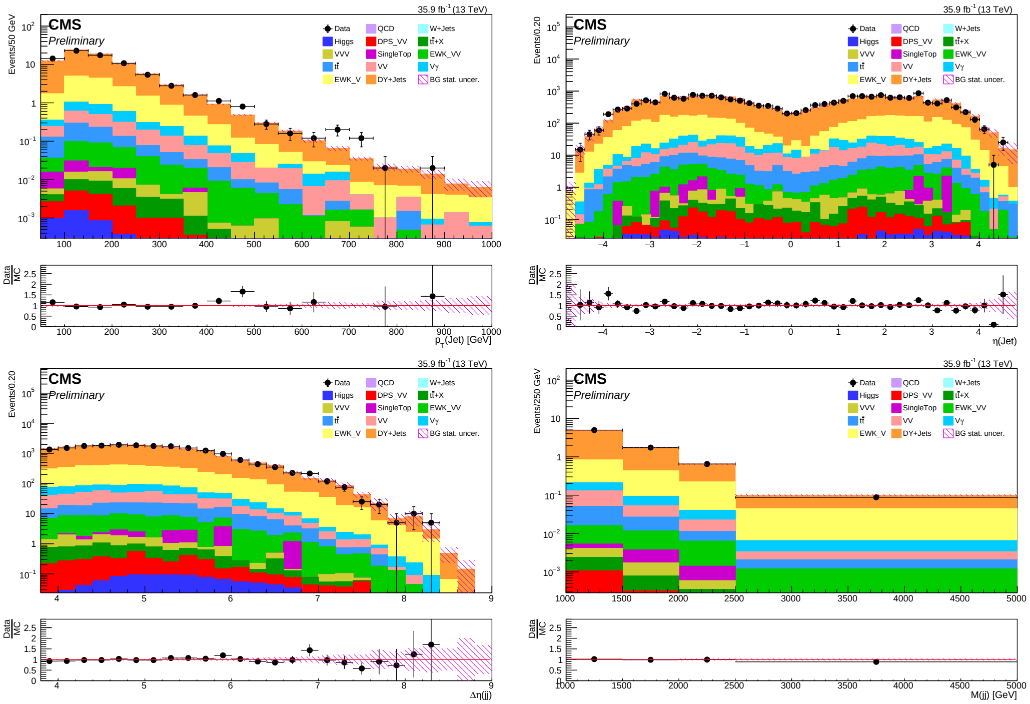

Figure 7.5: $p_{\mathrm{T}}(j)$, $\eta(j)$, $\Delta\eta_{jj}$, and m_{jj} after VBF I selections in Z+jets (2016). A scale factor of 1.02 has been applied to these plots.

is therefore concluded that no shape based corrections will be needed, and that only a SF will be needed to correct for event yields.

Sample	2016	2017	2018
DY+Jets	2984.7 ± 31.4	4216.0 ± 43.9	5838.6 ± 59.8
Total MC	3841.1 ± 33.1	5116.4 ± 45.5	7204.3 ± 62.5
Data	3900.0	5145.0	6663.0
Purity [%]	77.7 %	82.4 %	81.0 %
VBF1 Scale Factor	1.07 ± 0.02	1.09 ± 0.02	1.00 ± 0.02
Combined VBF1 & CS Sale Factor	1.02 ± 0.02	1.01 ± 0.02	0.91 ± 0.02

Table 7.3: Event yields after VBF I selections are applied in the Z+Jets CR. The full event yield can be found in appendix table A.8

Sample	2016	2017	2018
DY+Jets	34092.9 ± 159.9	37564.6 ± 189.2	61969.5 ± 299.0
Total MC	37089.1 ± 161.2	40139.7 ± 190.2	66057.2 ± 300.5
Data	41287.0	38165.0	58172.0
Purity [%]	91.9 %	93.4 %	93.8 %
VBF2 Scale Factor	1.18 ± 0.01	1.03 ± 0.01	0.97 ± 0.01
Combined VBF2 & CS Sale Factor	1.12 ± 0.01	0.95 ± 0.01	0.87 ± 0.01

Table 7.4: Event yields after VBF II selections are applied in the Z+Jets CR. The full event yield can be found in appendix table A.9

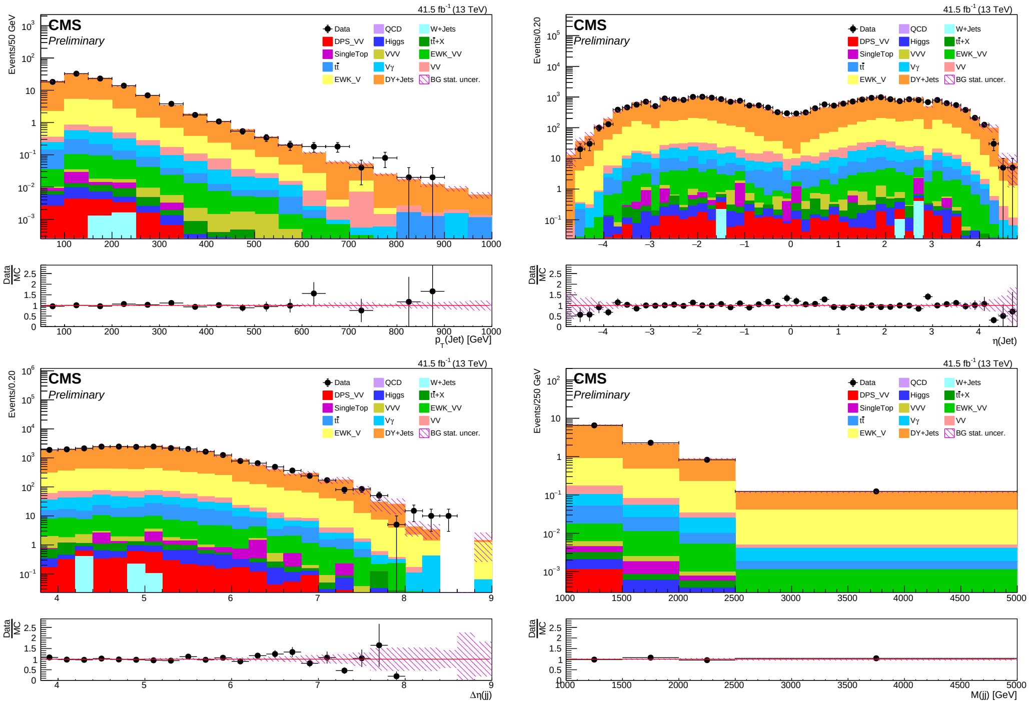

Figure 7.6: $p_{\mathrm{T}}(j)$, $\eta(j)$, $\Delta\eta_{jj}$, and m_{jj} after VBF I selections in Z+jets (2017). A scale factor of 1.01 has been applied to these plots.

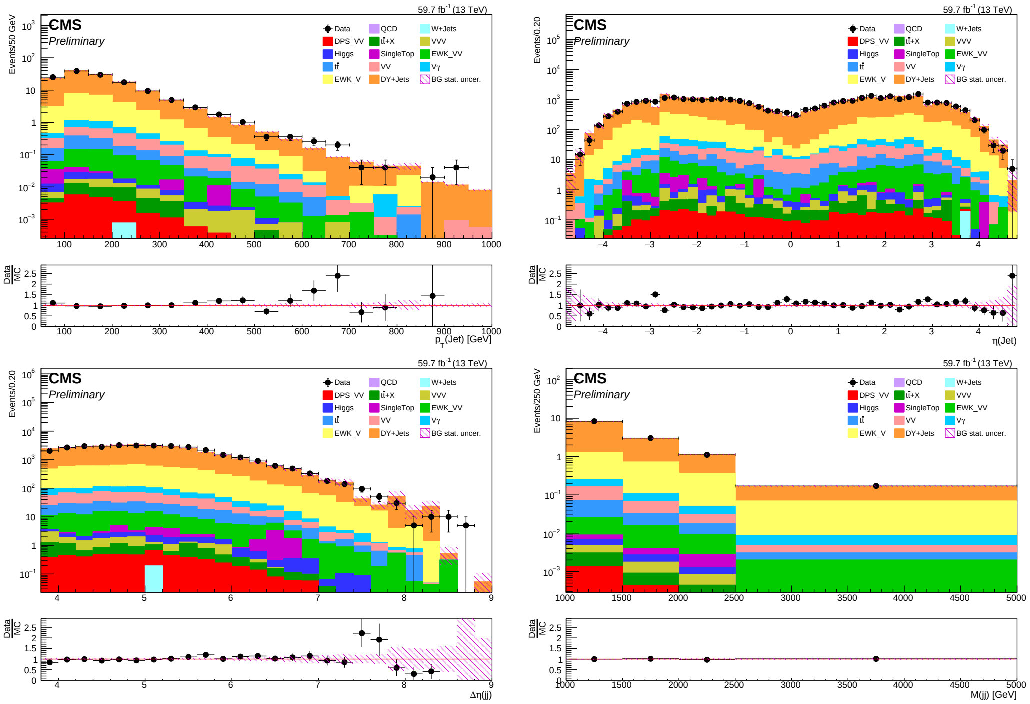

Figure 7.7: $p_{\mathrm{T}}(j)$, $\eta(j)$, $\Delta\eta_{jj}$, and m_{jj} after VBF I selections in Z+jets (2018). A scale factor of 0.91 has been applied to these plots.

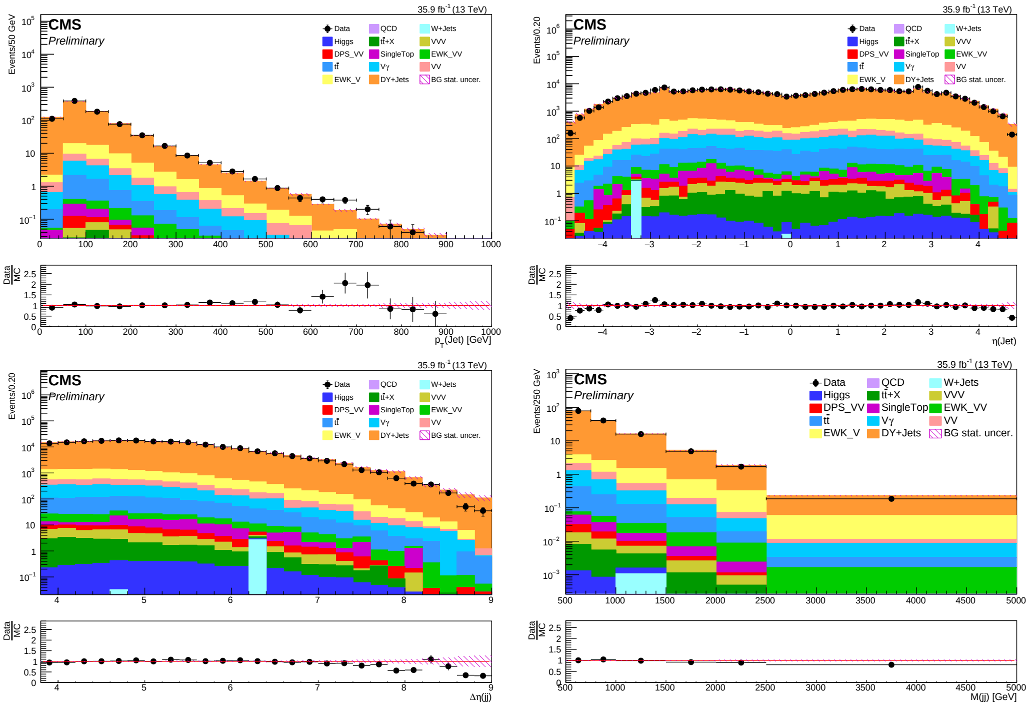

Figure 7.8: $p_T(j)$, $\eta(j)$, $\Delta\eta_{jj}$, and m_{jj} after VBF II selections in Z+jets (2016). A scale factor of 1.12 has been applied to these plots.

Sample	2016	2017	2018
DY+Jets	6917.2 ± 87.1	5102.5 ± 88.3	10760.5 ± 156.5
Total MC	7414.8 ± 87.5	5453.3 ± 88.6	11349.3 ± 156.9
Data	7872.0	5142.0	9416.0
Purity [%]	93.3 %	93.6 %	94.8 %
VBF3 Scale Factor	1.12 ± 0.02	1.02 ± 0.02	0.91 ± 0.01
Combined VBF3 & CS Sale Factor	1.07 ± 0.02	0.94 ± 0.02	0.82 ± 0.01

Table 7.5: Event yields after VBF3 selections are applied in the Z+Jets CR. The full event yield can be found in appendix table A.10

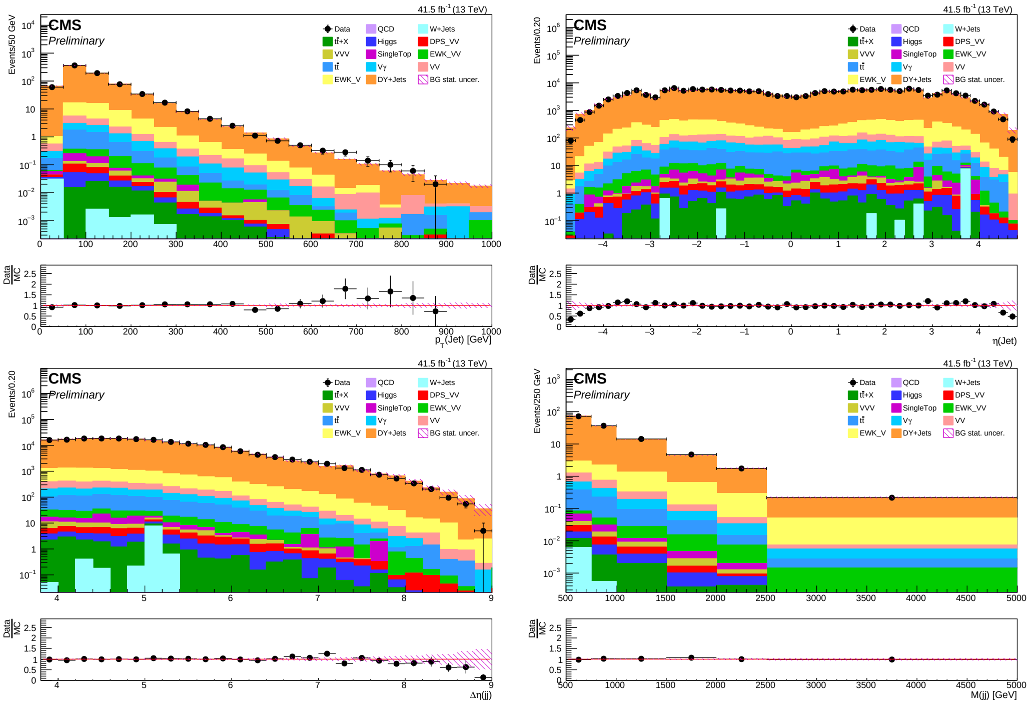

Figure 7.9: $p_{\mathrm{T}}(j)$, $\eta(j)$, $\Delta\eta_{jj}$, and m_{jj} after VBF II selections in Z+jets (2017). A scale factor of 0.95 has been applied to these plots.

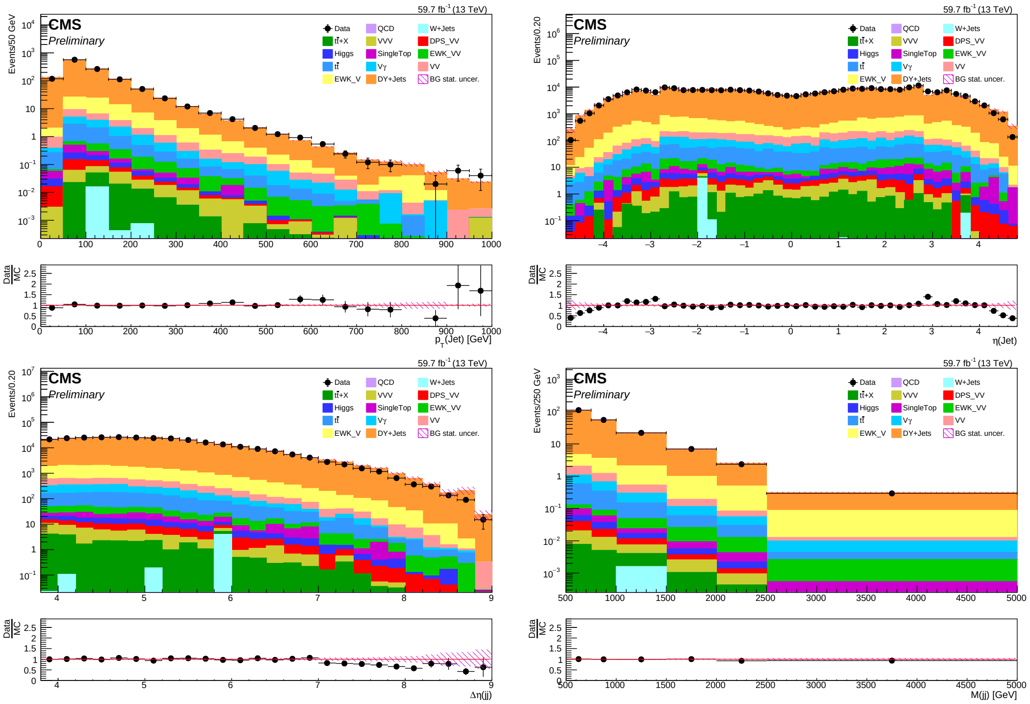

Figure 7.10: $p_{\mathrm{T}}(j)$, $\eta(j)$, $\Delta\eta_{jj}$, and m_{jj} after VBF II selections in Z+jets (2018). A scale factor of 0.87 has been applied to these plots.

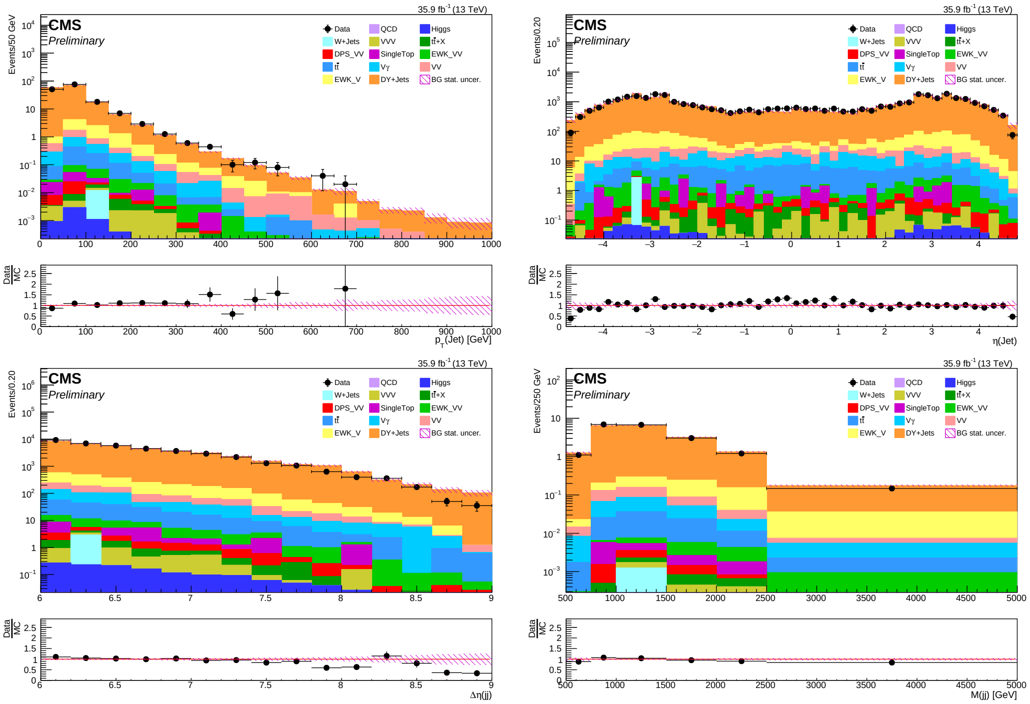

Figure 7.11: $p_{\mathrm{T}}(j)$, $\eta(j)$, $\Delta\eta_{jj}$, and m_{jj} after VBF3 selections in Z+jets (2016). A scale factor of 1.07 has been applied to these plots.

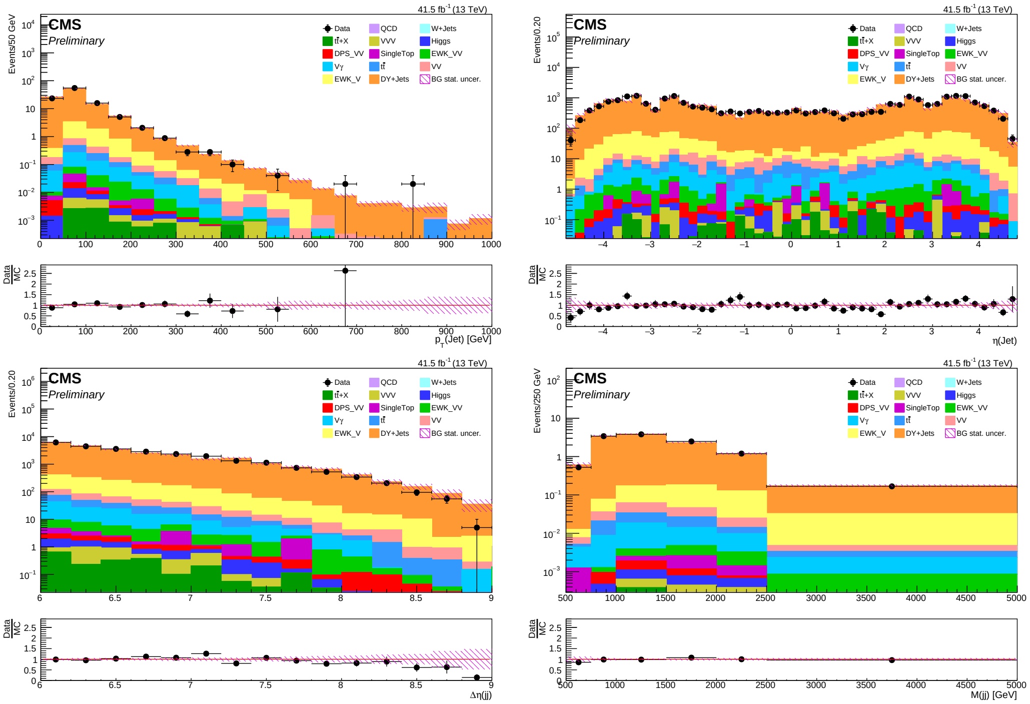

Figure 7.12: $p_{\mathrm{T}}(j)$, $\eta(j)$, $\Delta\eta_{jj}$, and m_{jj} after VBF3 selections in Z+jets (2017). A scale factor of 0.94 has been applied to these plots.

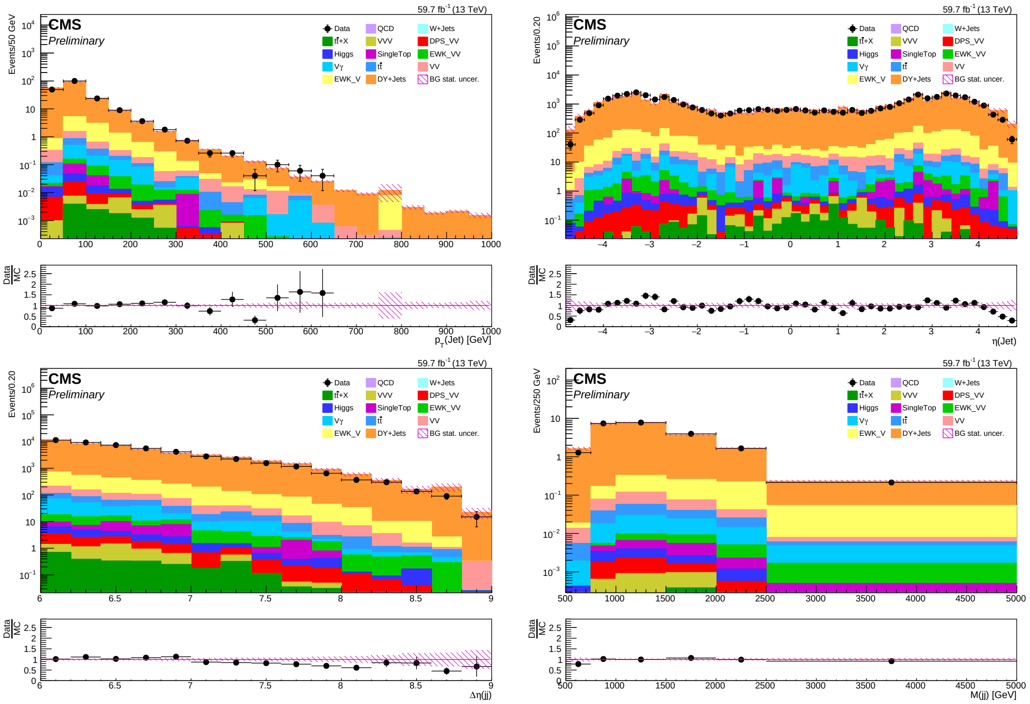

Figure 7.13: $p_{\mathrm{T}}(j)$, $\eta(j)$, $\Delta\eta_{jj}$, and m_{jj} after VBF3 selections in Z+jets (2018). A scale factor of 0.82 has been applied to these plots.

7.2 W+Jets

W bosons are also expected to be created in large quantities at the LHC. These particles can undergo the decay $W \to \ell\nu$, in which ℓ can be any of the three lepton flavors and ν its associated neutrino. Neutrinos cannot be experimentally detected at CMS and will therefore by reconstructed as p_{T}^{miss}. If there is an additional jet produced in the event, this jet may be incorrectly be reconstructed as a lepton. These fake leptons are "charge blind" meaning they are just as likely to be reconstructed with charge either $+e$ or $-e$ and as a result will affect the LS and OS channels equally. If such an event has sufficient p_{T}^{miss} due to the W being produced with momentum that it passes along to the neutrino, then this process can easily pass the SR criteria. It is therefore important to perform a background estimation study for W+jets. Such a study is performed here using the selection cuts shown in table 7.6. The muon channel is again chosen due to the high reconstruction efficiency of muons and the high $p_{\mathrm{T}}(\mu)$ resolution measurement capabilities of the CMS detector. This study will use the muon PD and a "logical or" combination of the IsoMu24 trigger and IsoMu27 trigger. 1 muon is selected with $p_{\mathrm{T}}(\mu) > 30$ GeV in order for the trigger to have high efficiency, and with $|\eta(\mu)| < 2.1$ in order for the muon to be reconstructed entirely within the tracker coverage. A relative isolation of < 0.15 is applied in order to ensure the muon is isolated and not produced as a heavy flavor decay such as a b-jet. There is additionally a selection window on the transverse mass between the muon and p_{T}^{miss} centered around m_W in order to further select for real $W \to \mu\nu$ events. We additionally select for events with $p_{\mathrm{T}}^{miss} > 250$ GeV so that this requirement lines up squarely with the SR. Any low p_{T} muons are rejected which further suppresses contributions from other processes such as $Z \to \mu\mu$. Taus, electrons, and b-jets are also vetoed.

	Object	Selection cuts
W+Jets	Trigger	HLT_IsoMu24 or HLT_IsoMu27
	Muon selection	$N(\mu) = 1$, $p_{\mathrm{T}}(\mu) > 30$ GeV, $\lvert\eta(\mu)\rvert < 2.1$, tight ID, Isolation: I < 0.15, $m(\mu, p_{\mathrm{T}}^{miss}) \in [60,100]$ GeV
	p_{T}^{miss} selection	> 250 GeV
	Muon veto	$N(\mu) = 0$, 10 GeV $< p_{\mathrm{T}}(\mu) <$ 30 GeV, $\lvert\eta(\mu)\rvert < 2.1$, tight ID, Isolation: I < 0.15
	Electron veto	$N(e) = 0$, $p_{\mathrm{T}}(e) > 10$ GeV, $\lvert\eta\rvert < 2.1$, Medium ID (cut-based)
	Tau veto	$N(\tau) = 0$, $p_{\mathrm{T}}(\tau) > 20$ GeV, $\lvert\eta\rvert < 2.1$, tight anti-$e\mu$ discr., prong: 1or3hps
	b-jet veto	$N(b) =0$, $p_{\mathrm{T}}(b) > 30$ GeV, $\lvert\eta\rvert < 2.4$, Medium DeepCSV WP

Table 7.6: Central selection event criteria for W+Jets background estimation.

W+Jets Modeling After Central Selections:

Table 7.7 shows purities, SFs, and event yields in data and MC for 2016, 2017, and 2018, after applying CS cuts. The full event yield including contributions from each individual MC process can be found in appendix table A.11. The purity of this region is $\sim 80\%$ for each year, which is due primarily to the inclusion of large p_{T}^{miss} which can be difficult to model correctly. The CS SFs derived are within $\sim$10% of unity for each year,

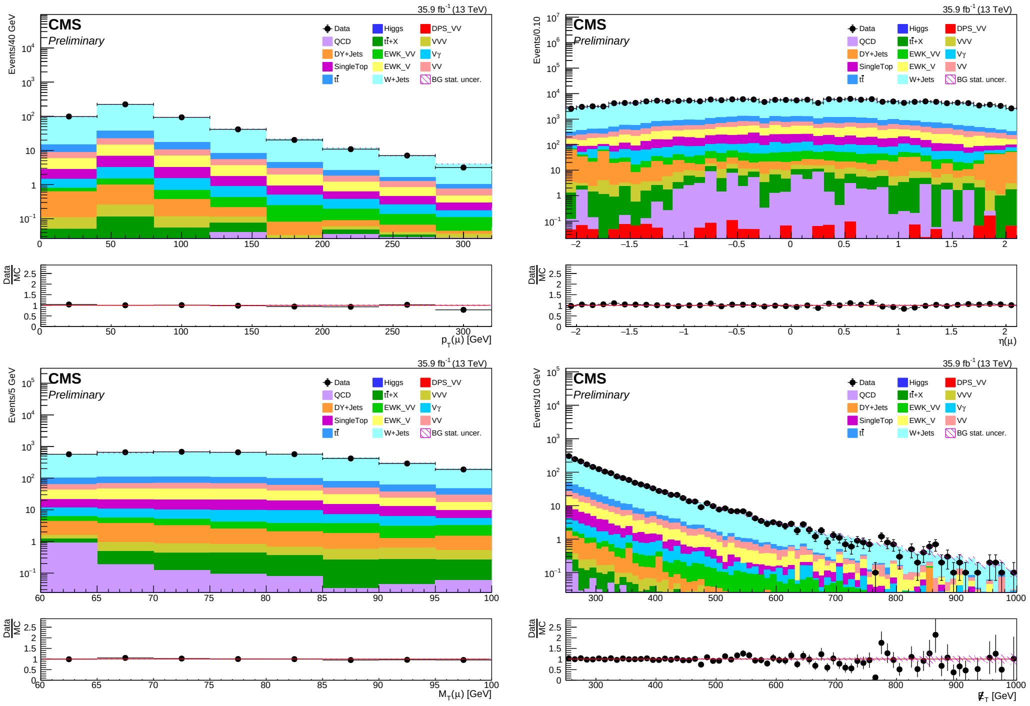

Figure 7.14: $p_{\mathrm{T}}(\mu)$, $\eta(\mu)$, $m_{\mathrm{T}}(\mu, p_{\mathrm{T}}^{miss})$, and p_{T}^{miss} after central selection cuts, including veto selections, in W+jets (2016). A central selection scale factor of 0.99 has been applied to these plots.

indicating the yields are well modeled. Figures 7.14, 7.15, and 7.16 show $p_{\mathrm{T}}(\mu)$, $\eta(\mu)$, $m(\mu, p_{\mathrm{T}}^{miss})$, and p_{T}^{miss} for 2016, 2017, and 2018 respectively. The expected kinematics for W+jets is similar to Z+jets, and indeed we see similar results: the $p_{\mathrm{T}}(\mu)$ should peak around $m_W/2$ and decay exponentially, $\eta(j)$ values should be approximately flat across the entire spectrum sampled, and $m(\mu, p_{\mathrm{T}}^{miss})$ should peak around m_W. For this study, we additionally inspect p_{T}^{miss} as a distribution of interest. It should appear as an exponentially falling function, given that we are selecting for values > 250 GeV (a distribution with a smaller p_{T}^{miss} requirement might contain structures due to the W, e.g. a hump near $m_W/2$ and similar shape to $p_{\mathrm{T}}(\mu)$). We see good agreement across all years for the distributions studied. The conclusion is therefore that the central selections are well modeled.

Sample	2016	2017	2018
W+Jets	16767.1 ± 74.4	20525.2 ± 120.6	28328.7 ± 148.8
Total MC	20308.0 ± 77.67	24673.0 ± 124.06	33874.5 ± 152.84
Data	20171	23003	30620
Purity [%]	82.6 %	83.2 %	83.6 %
Central Selection Scale Factor	0.99 ± 0.01	0.92 ± 0.01	0.89 ± 0.01

Table 7.7: Event yields after central selections are applied in the W+Jets CR. The full event yield can be found in appendix table A.11

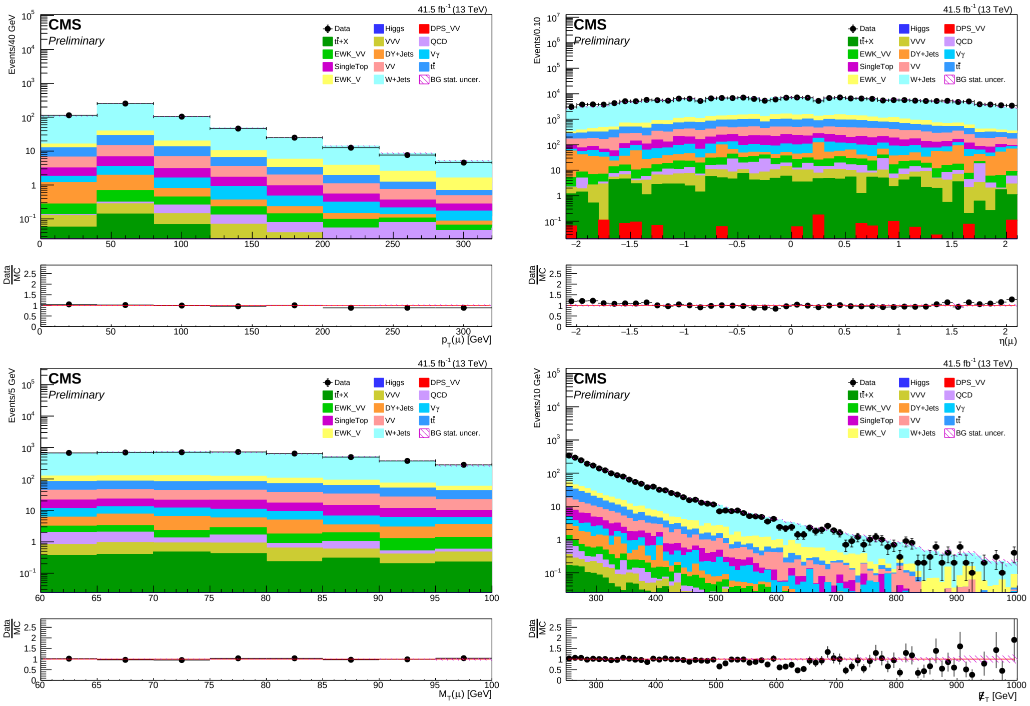

Figure 7.15: $p_\mathrm{T}(\mu)$, $\eta(\mu)$, $m_\mathrm{T}(\mu, p_\mathrm{T}^{miss})$, and p_T^{miss} after central selection cuts, including veto selections, in W+jets (2017). A central selection scale factor of 0.92 has been applied to these plots.

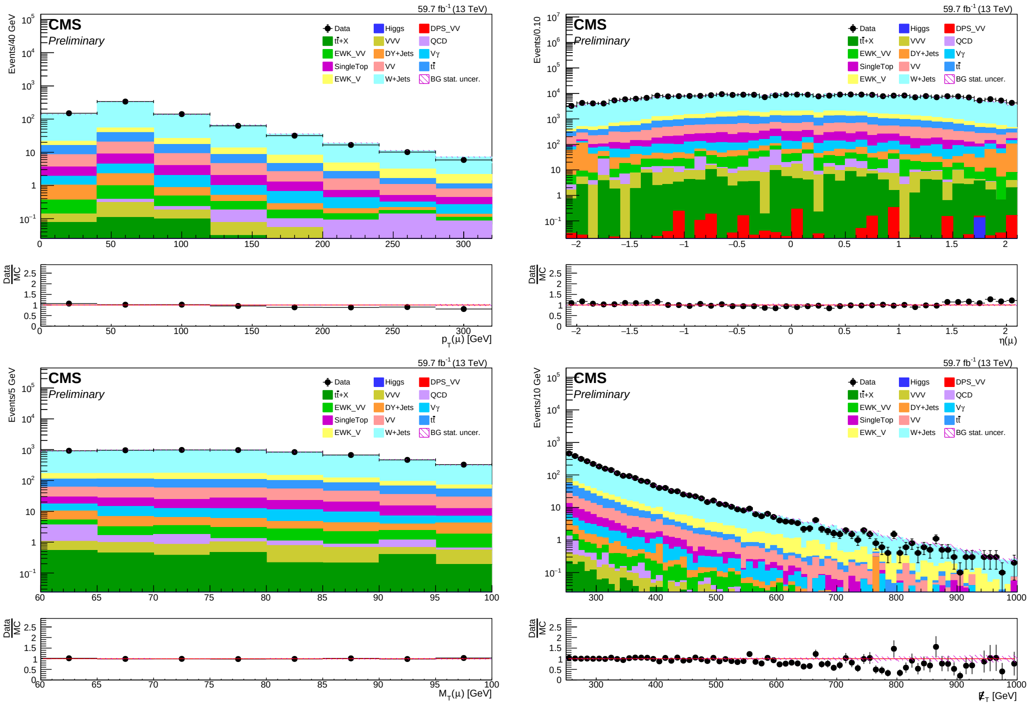

Figure 7.16: $p_\mathrm{T}(\mu)$, $\eta(\mu)$, $m_\mathrm{T}(\mu, p_\mathrm{T}^{miss})$, and p_T^{miss} after central selection cuts, including veto selections, in W+jets (2018). A central selection scale factor of 0.89 has been applied to these plots.

W+Jets Modeling After VBF Selections:

Tables 7.8, 7.9, and 7.10 show purities, SFs, and event yields in data and MC for 2016, 2017, and 2018, after VBF1, VBF2, and VBF3 selections are applied, respectively. The full event yields can be found in appendix tables A.12, A.13, and A.14. For W+jets it is once again observed that VBF2 consistently provides a higher purity than VBF1, which is expected for jets coming from ISR rather than other processes which naturally produce high-p_{T} jets such as hadronic W decays in the case of $t\bar{t}$. Both VBF1 and VBF2 provide SFs consistent within $\sim 10\%$ of unity which indicate the total event yields are accurate (although the lower purity can affect this conclusion). Kinematically the results after applying VBF selections are similar to the Z+jets CR results, with a few exceptions. First, the jet p_{T} peaks at a higher value. This is expected and is due to the large p_{T}^{miss} selection requirement. In order for the neutrino to carry such large momentum, there must be other high-p_{T} objects involved in the interaction, and those objects must be jets (the only other object involved is the muon, but this is also a decay product and therefore cannot transfer momentum to the neutrino). Secondly, this CR will produce significantly smaller event yields, also due to the large p_{T}^{miss} selection. This has the effect of causing larger statistical uncertainties, which are also observed in the associated plots. The most important conclusion of this study is that the m_{jj} distribution shapes look well modeled between all three years, and therefore no shape-based correction will be applied. It is therefore concluded that the distributions and event yields in the W+jets CR are well modeled.

Sample	2016	2017	2018
W+Jets	337.5 ± 8.9	439.4 ± 45.0	539.1 ± 16.8
Total MC	589.9 ± 10.8	706.7 ± 45.7	933.2 ± 19.7
Data	587.0	685.0	923.0
Purity [%]	57.2%	62.2%	57.8%
VBF1 Scale Factor	1.00 ± 0.08	1.03 ± 0.12	1.11 ± 0.07
Combined VBF1 & CS Sale Factor	0.99 ± 0.08	0.95 ± 0.12	0.98 ± 0.07

Table 7.8: Event yields after VBF1 selections are applied in the W+Jets CR. The full event yield can be found in appendix table A.12

Sample	2016	2017	2018
W+Jets	1098.8 ± 17.3	1177.9 ± 48.3	1784.9 ± 33.4
Total MC	1686.0 ± 19.6	1737.0 ± 49.6	2630.4 ± 36.4
Data	1748.0	1639.0	2397.0
Purity [%]	65.2 %	67.8 %	67.8 %
VBF2 Scale Factor	1.07 ± 0.04	1.00 ± 0.05	0.98 ± 0.03
Combined VBF2 & CS Sale Factor	1.06 ± 0.04	0.92 ± 0.05	0.87 ± 0.03

Table 7.9: Event yields after VBF2 selections are applied in the W+Jets CR. The full event yield can be found in appendix table A.13.

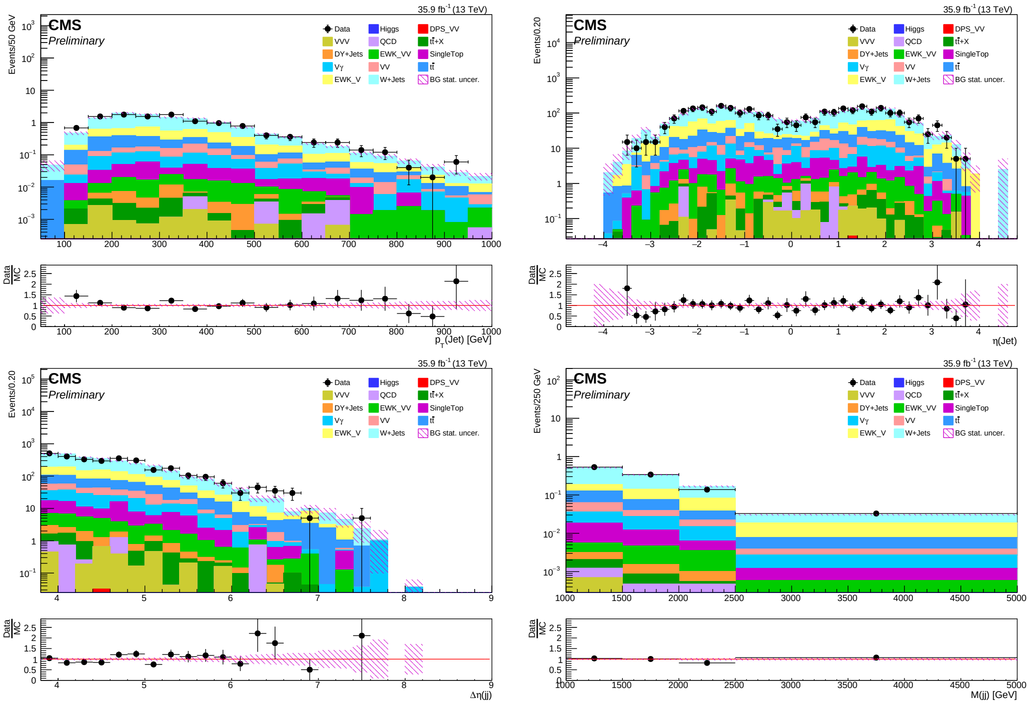

Figure 7.17: $p_{\mathrm{T}}(j)$, $\eta(j)$, $\Delta\eta_{jj}$, and m_{jj} after VBF1 selections in W+jets (2016). A scale factor of 0.99 has been applied to these plots.

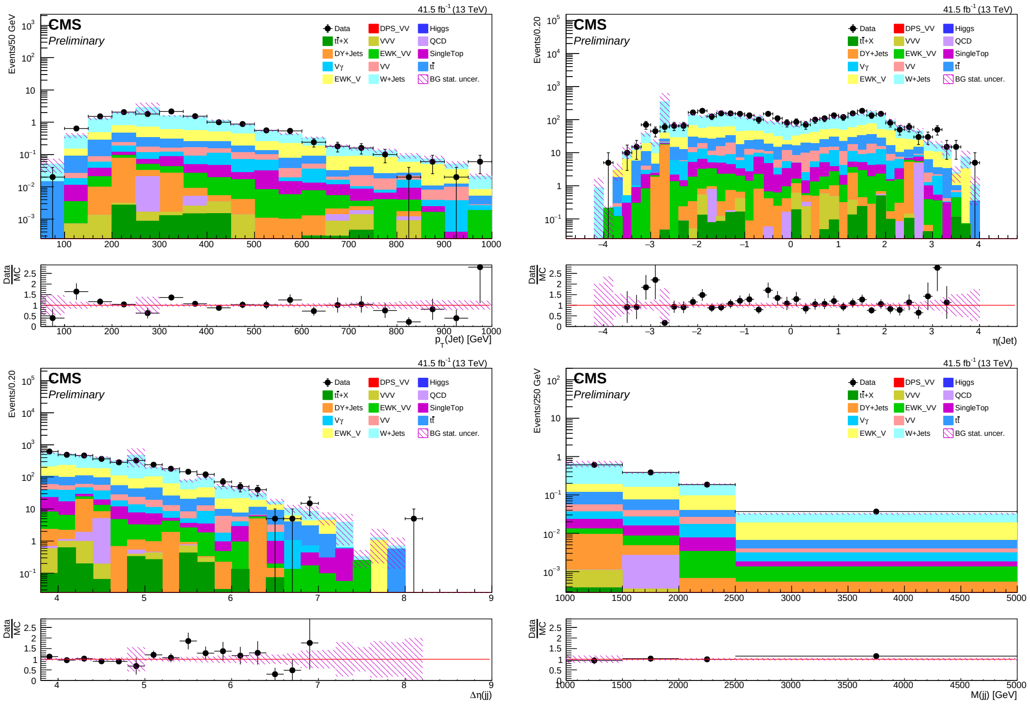

Figure 7.18: $p_{\mathrm{T}}(j)$, $\eta(j)$, $\Delta\eta_{jj}$, and m_{jj} after VBF1 selections in W+jets (2017). A scale factor of 0.95 has been applied to these plots.

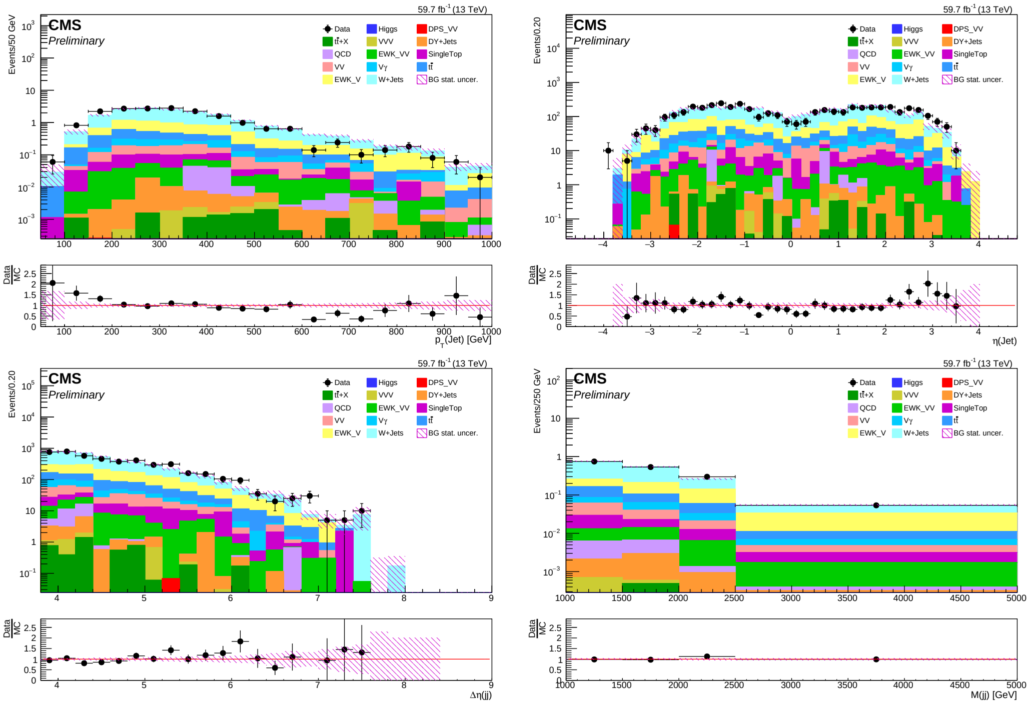

Figure 7.19: $p_{\mathrm{T}}(j)$, $\eta(j)$, $\Delta\eta_{jj}$, and m_{jj} after VBF1 selections in W+jets (2018). A scale factor of 0.98 has been applied to these plots.

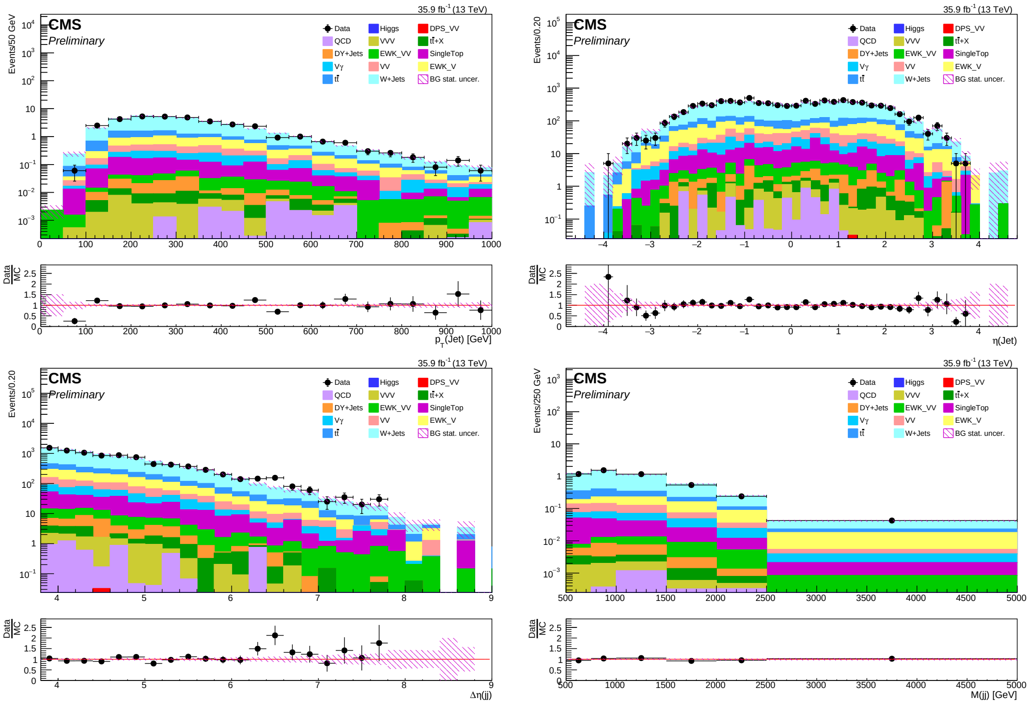

Figure 7.20: $p_{\mathrm{T}}(j)$, $\eta(j)$, $\Delta\eta_{jj}$, and m_{jj} after VBF2 selections in W+jets (2016). A scale factor of 1.06 has been applied to these plots.

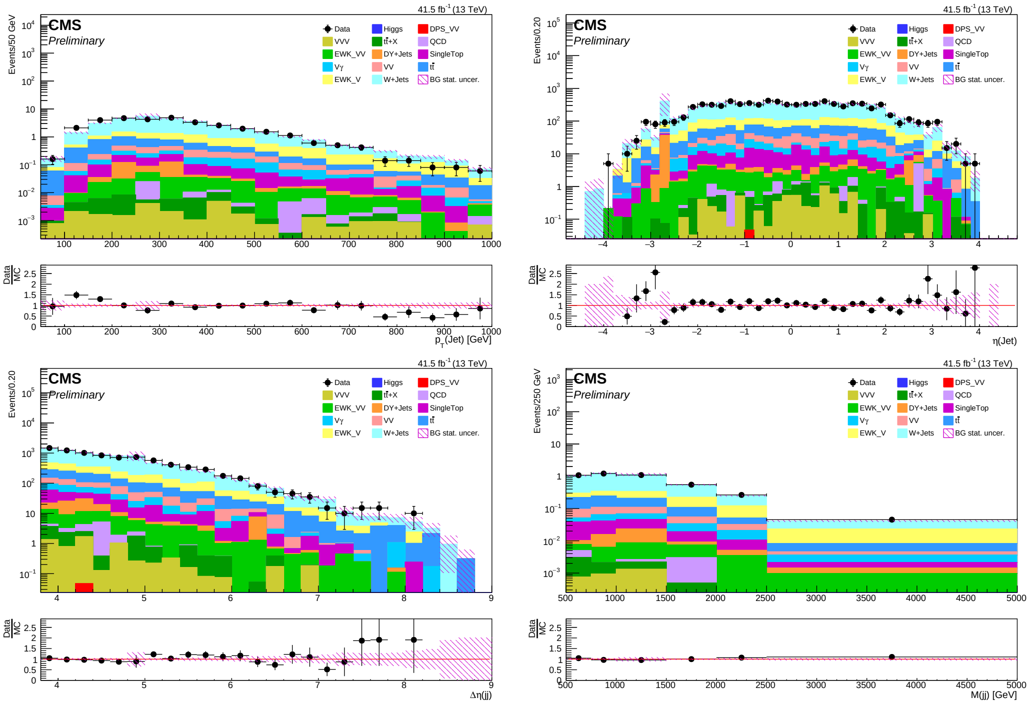

Figure 7.21: $p_{\mathrm{T}}(j)$, $\eta(j)$, $\Delta\eta_{jj}$, and m_{jj} after VBF2 selections in W+jets (2017). A scale factor of 0.92 has been applied to these plots.

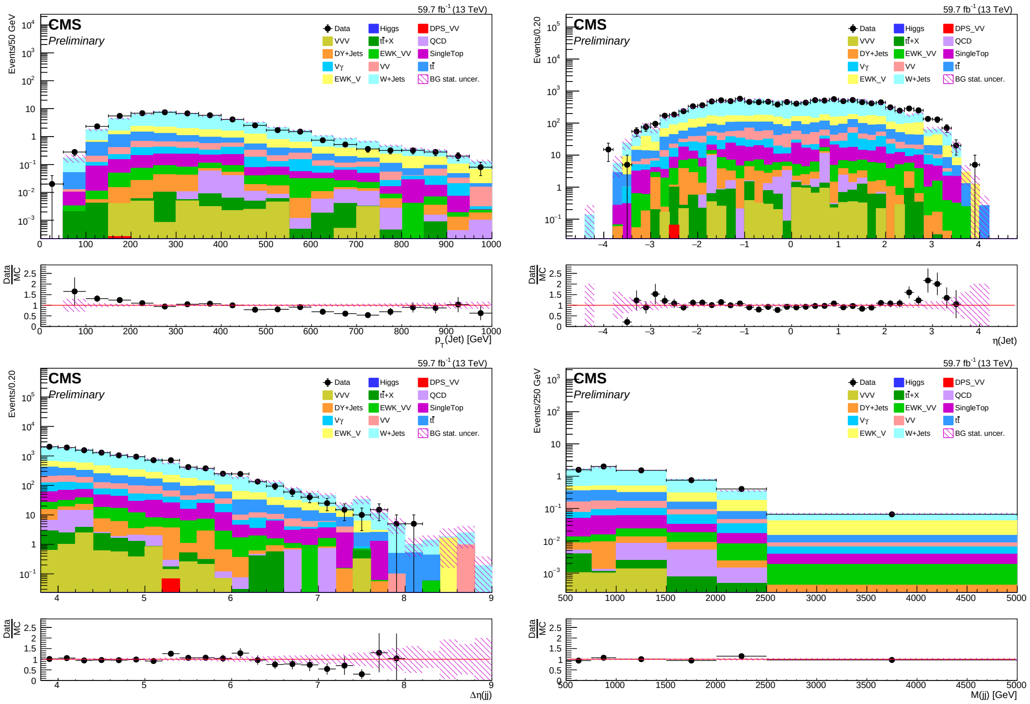

Figure 7.22: $p_{\mathrm{T}}(j)$, $\eta(j)$, $\Delta\eta_{jj}$, and m_{jj} after VBF2 selections in W+jets (2018). A scale factor of 0.87 has been applied to these plots.

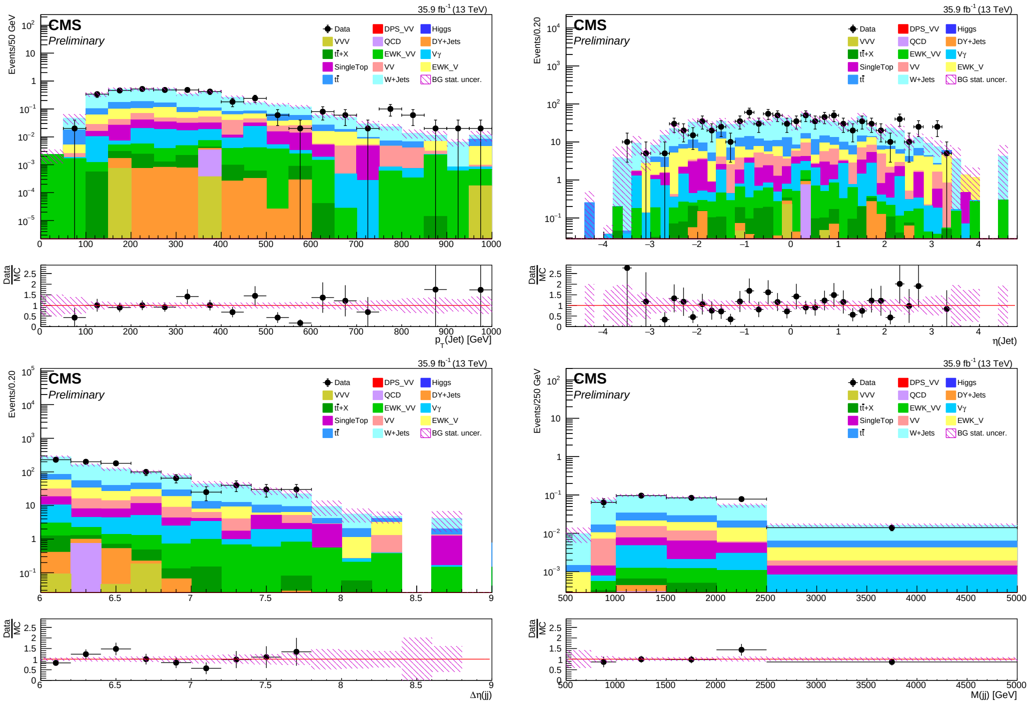

Figure 7.23: $p_{\mathrm{T}}(j)$, $\eta(j)$, $\Delta\eta_{jj}$, and m_{jj} after VBF3 selections in W+jets (2016). A scale factor of 1.56 has been applied to these plots.

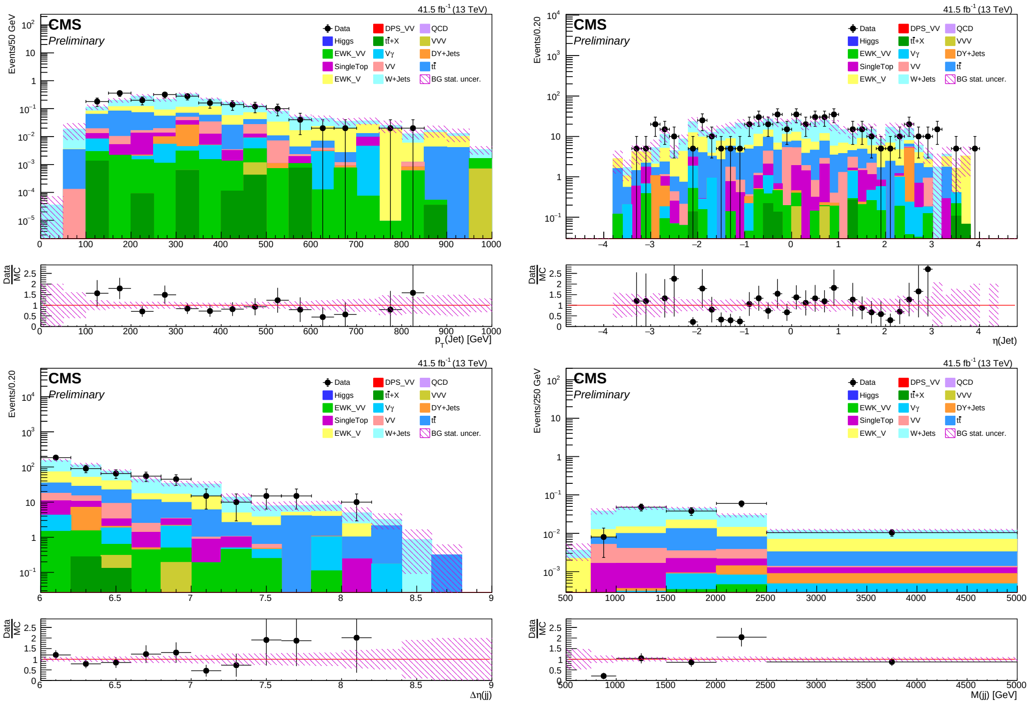

Figure 7.24: $p_{\mathrm{T}}(j)$, $\eta(j)$, $\Delta\eta_{jj}$, and m_{jj} after VBF3 selections in W+jets (2017). A scale factor of 0.83 has been applied to these plots.

Sample	2016	2017	2018
W+Jets	75.7 ± 4.6	64.5 ± 4.6	135.0 ± 9.4
Total MC	137.8 ± 5.5	111.9 ± 5.6	205.1 ± 10.2
Data	180.0	101.0	169.0
Purity [%]	54.9 %	57.6 %	65.8 %
VBF3 Scale Factor	1.57 ± 0.20	0.91 ± 0.17	0.83 ± 0.11
Combined VBF3 & CS Sale Factor	1.56 ± 0.20	0.83 ± 0.17	0.73 ± 0.11

Table 7.10: Event yields after VBF3 selections are applied in the W+Jets CR. The full event yield can be found in appendix table A.14.

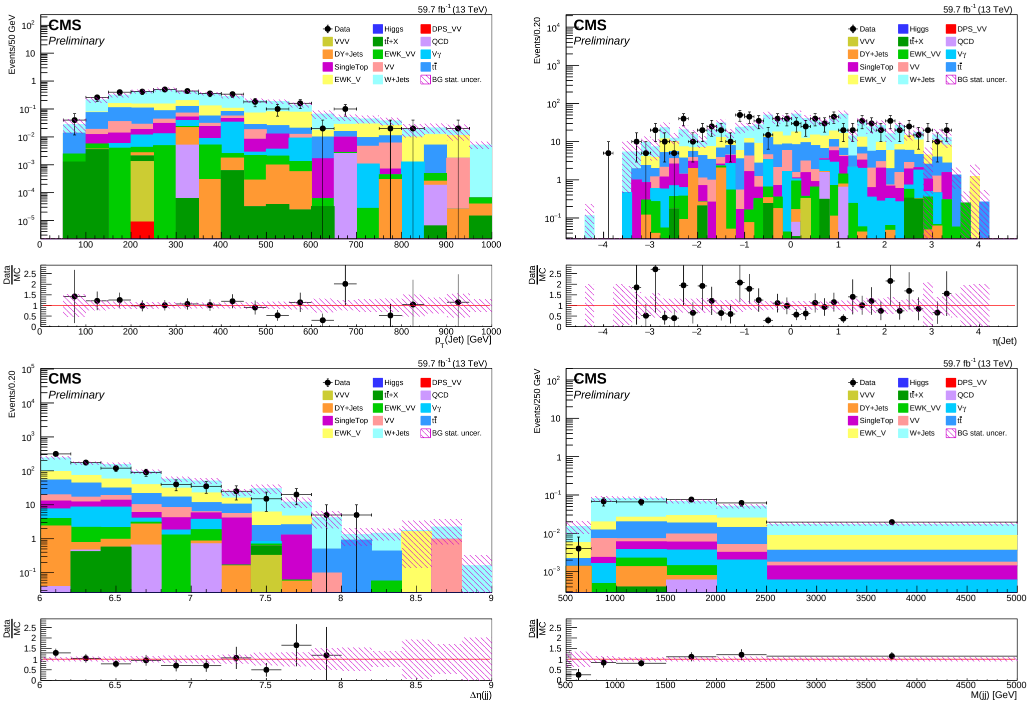

Figure 7.25: $p_T(j)$, $\eta(j)$, $\Delta\eta_{jj}$, and m_{jj} after VBF3 selections in W+jets (2018). A scale factor of 0.73 has been applied to these plots.

7.3 $t\bar{t}$

$t\bar{t}$ represents an important background in the dilepton channels. This background can directly produce two real opposite-signed leptons of either the same flavor or different flavors. This occurs when each t decays via $t \to bW$, and each W subsequently decays via $W \to \ell\nu$. Each ν will then be reconstructed as p_{T}^{miss}. If the b-jets are not correctly tagged and instead reconstructed as regular jets, then each event will also contain two jets. Such events can therefore pass all lepton requirements, p_{T}^{miss} requirements, jet requirements, and be present in the SR. A $t\bar{t}$ background estimation has therefore been performed in order to understand the potential mismodeling of this process. The selection cuts applied to this CR are those seen in table 7.11. The muon channel is again chosen due to the high reconstruction efficiency of muons and the high $p_{\mathrm{T}}(\mu)$ resolution measurement capabilities of the CMS detector. This study will use the muon PD and a "logical or" combination of the IsoMu24 trigger and IsoMu27 trigger. Two muons are selected for with OS charge and a separation of $\Delta R(\mu,\mu) > 0.4$. Each muon must have $p_{\mathrm{T}}(\mu) > 30$ GeV and $|\eta(\mu)| < 2.1$ in order to ensure high trigger efficiency and that the muons are reconstructed entirely within the tracker coverage. A relative isolation of < 0.15 is applied in order to ensure each muon is isolated. In addition, two b-jets are also selected for, each having $p_{\mathrm{T}}(b) > 30$ GeV and $|\eta(b)| < 2.4$. The b-jet tagging algorithm employed was DeepCSV (see reference [69]) using the medium WP. A $p_{\mathrm{T}}^{miss} > 250$ GeV selection was employed in order to align with the SR. Additional vetoes on electrons and taus were applied to further reduce other processes, and only select for dimuon events.

	Object	Selection cuts
$t\bar{t}$+Jets	Trigger	HLT_IsoMu24 or HLT_IsoMu27
	Muon selection	$N(\mu) = 2$, $p_{\mathrm{T}}(\mu) > 30$ GeV, $\lvert\eta(\mu)\rvert < 2.1$, tight ID, Isolation: I < 0.15, OS charge, $\Delta R(\mu,\mu) > 0.4$
	b-jet selection	$N(b) = 2$, $p_{\mathrm{T}}(b) > 30$ GeV, $\lvert\eta\rvert < 2.4$, Medium DeepCSV WP
	p_{T}^{miss} selection	> 250 GeV
	Electron veto	$N(e) = 0$, $p_{\mathrm{T}}(e) > 5$ GeV, $\lvert\eta\rvert < 2.1$, Medium ID (cut-based)
	Tau veto	$N(\tau) = 0$, $p_{\mathrm{T}}(\tau) > 20$ GeV, $\lvert\eta\rvert < 2.1$, tight anti-$e\mu$ discr., prong: 1or3hps

Table 7.11: Central selection event criteria for $t\bar{t}$ background estimation.

$t\bar{t}$ Modeling After Central Selections:

Table 7.12 shows purities, SFs, and event yields in data and MC for 2016, 2017, and 2018 after applying CS cuts. The full event yield including contributions from each individual MC process can be found in appendix table A.15. The purity of each year is $> 85\%$ which indicates the CS cuts are successful in selecting only $t\bar{t}$ events. The SFs in 2017 and 2018 are within $< 5\%$ of unity, indicating good modeling of event yield. The SF in 2016 however was lower, reaching 0.66. It was ultimately discovered that this was due to a larger contribution from single-top events in 2016, due to a different parton distribution function being used in the creation of MC samples in 2016 versus 2017 and 2018. When inspecting the various kinematic distributions after central selection cuts are applied, as seen in figure 7.26 which shows $p_{\mathrm{T}}(b)$, $\eta(b)$, $p_{\mathrm{T}}(\mu)$, $\eta(\mu)$, and p_{T}^{miss}, it is seen that this does not cause considerable disagreement in the shape of any distribution. Therefore the application of the CS SF is sufficient to correct for the yield discrepancy. Additionally, figures 7.27 and 7.28 show the same kinematic distributions for 2017 and 2018, respectively. Kinematically in this region one would expect the b-jet to carry some momentum from the decay of the t, roughly on the order of $(m_T - m_W)/2$ as it is created in conjunction with a massive real W (this is in contrast to a region like $Z \to \mu\mu$ in which $m_Z >> m_\mu$ and therefore the momentum taken by each muon is $\sim m_Z/2$). This shape is correctly observed in all three years. Furthermore, the p_{T}^{miss} requirement is satisfied when events are created with two high-p_{T} neutrinos pointing in the same direction of the detector, so that experimentally their momentum (reconstructed as p_{T}^{miss}) does not cancel each other out. Therefore we are selecting for events in which the momentum from the t is primarily transferred to the W. This is seen in the $p_{\mathrm{T}}(\mu)$ plots which shows the distribution peaking at a value higher than $m_W/2$. One would also expect these events to be created primarily with high-p_{T} jets which provide the additional momentum as a "recoil" against the $t\bar{t}$ system and aids in creating large p_{T}^{miss}. This is seen in figure 7.29 which shows the $N(j)$ and $p_{\mathrm{T}}(j)$ distributions in 2018 both before and after the p_{T}^{miss} requirement applied. Indeed, we see that the majority of events after requiring p_{T}^{miss} have at least 1 high-p_{T} jet. Given the correct kinematics shape and agreement between data and MC, it is therefore concluded the central selections are well modeled.

Sample	2016	2017	2018
$t\bar{t}$	190.7 ± 3.0	204.0 ± 3.3	300.9 ± 4.9
Total MC	224.1 ± 4.0	230.8 ± 4.1	337.8 ± 5.8
Data	160.0	223.0	330.0
Central Selection Purity [%]	85.1 %	88.4 %	89.1%
Central Selection Scale Factor	0.66 ± 0.07	0.96 ± 0.08	0.97 ± 0.06

Table 7.12: Event yields for $t\bar{t}$ in the dimuon channel after central selection cuts and vetoes have been applied. The full event yield can be found in appendix table A.15

$t\bar{t}$ Modeling After VBF Selections:

Tables 7.13 and 7.14 show purities, SFs, and event yields in data and MC for 2016, 2017, and 2018, after VBF1 and VBF2 selections are applied, respectively (A dedicated study for VBF3 was not performed). The full event yields can be found in appendix tables A.17 and A.18. For VBF1, it was initially observed that the $p_{\mathrm{T}^{miss}} > 250$ GeV requirement caused very low event yields, such that it was difficult to make conclusions regarding the quality of the modeling of the MC samples. This is expected given that $t\bar{t}$ events which decay fully leptonically have a very small cross section (roughly of order 90 pb) which is then reduced by a factor

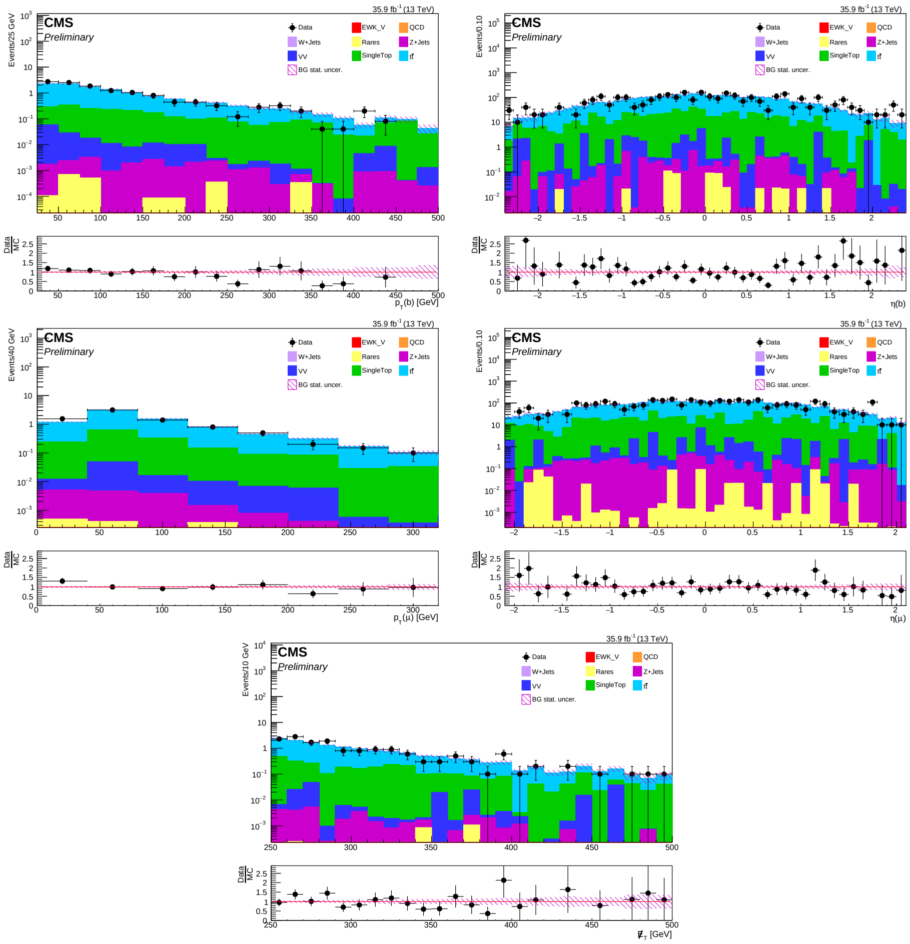

Figure 7.26: $p_{\mathrm{T}}(b)$, $\eta(b)$, $p_{\mathrm{T}}(\mu)$, $\eta(\mu)$ and p_{T}^{miss} after central selection cuts (2016). A SF of 0.66 has been applied to the plots shown.

of $1/9^{\text{th}}$ due to the dimuon branching fraction [70]. Therefore, the $p_{\mathrm{T}miss}$ requirement in VBF1 was reduced to $p_{\mathrm{T}miss} > 100$ GeV in order to increase statistics. Those initial results are included for completeness and can be found exclusively in table A.17. Both VBF1 and VBF2 provide a purity of $\sim> 90\%$. It is observed that the VBF1 and VBF2 SFs for 2017 and 2018 are consistent but significantly lower than 2016, for which is closer to unity (and in contrast to the CS SFs which observed the opposite effect). It is again concluded that this is a result of a different PDF being used in 2017 and 2018 MC production. The ultimate result however is that when considering the final SF, which combines the CS SF and the VBF SF, these two effects cancel to produce a consistent SF across all three years, in both VBF1 and VBF2. The kinematic results for 2016, 2017, and 2018 in VBF1 can be seen figures 7.30, 7.31 and 7.32, while the same results for VBF2 can be seen in figures 7.33, 7.34, and 7.35. For both regions, the results are once again what is to be expected and are consistent with well modeled MC regions. In VBF1, even though the $p_{\mathrm{T}miss}$ requirement has been loosened the $p_{\mathrm{T}}(j)$ distribution still peaks at an expected value given that we are selecting for $p_{\mathrm{T}}(j) > 60$ GeV. The jets

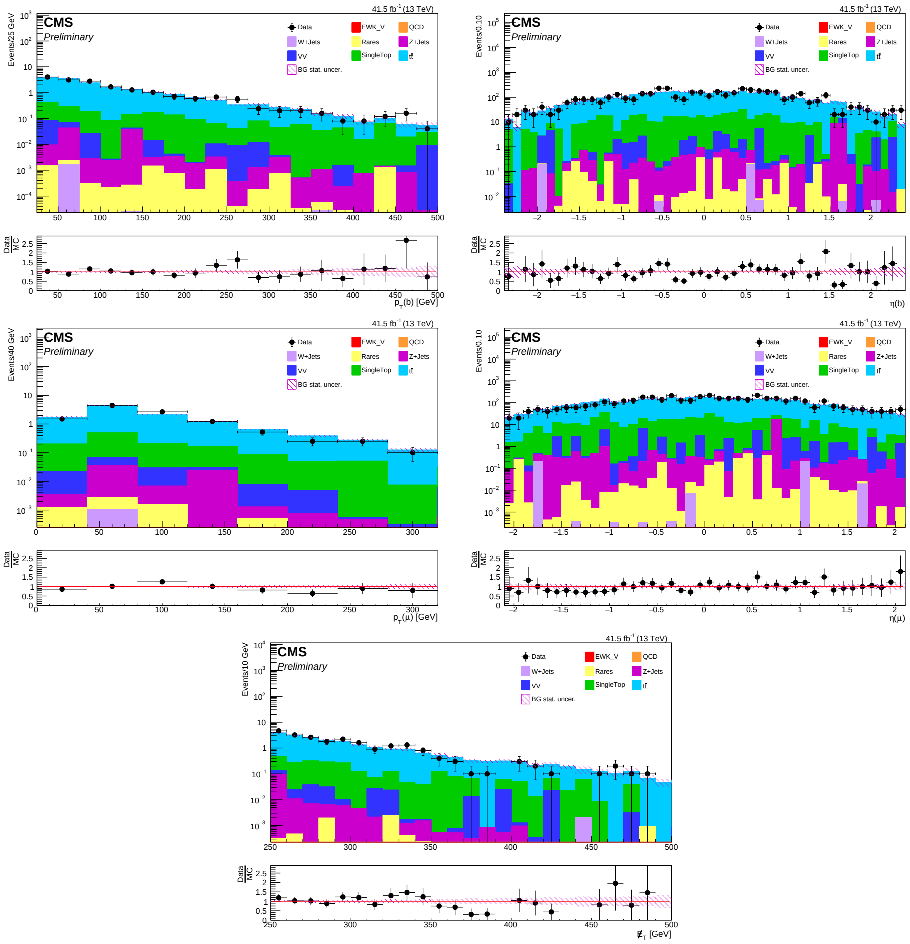

Figure 7.27: $p_{\mathrm{T}}(b)$, $\eta(b)$, $p_{\mathrm{T}}(\mu)$, $\eta(\mu)$ and p_{T}^{miss} after central selection cuts (2017). A SF of 0.96 has been applied to the plots shown.

also must be more far forward than in VBF2 and have a larger $\Delta\eta(jj)$ gap in order to meet the $m_{jj} > 1000$ GeV requirement. This is correctly observed. In contrast, for VBF2 we again see a $p_{\mathrm{T}}(j)$ distribution which peaks at $\sim > 50$ GeV, which is required in order for large $p_{\mathrm{T}miss}$ to be present in the event. The conclusion for this study then is that there appears to be good modeling in the CR, and that the CS SFs and VBF SFs derived herein will be applied to the SR in order to correct for the proper event yields.

Sample	2016	2017	2018
$t\bar{t}$	89.2 ± 2.1	88.2 ± 2.2	127.8 ± 3.2
Total MC	92.7 ± 2.2	90.3 ± 2.3	132.1 ± 3.3
Data	76.0	68.0	106.0
Purity [%]	96.2 %	97.7 %	96.7 %
VBF1 Scale Factor	0.94 ± 0.10	0.76 ± 0.10	0.82 ± 0.08
Combined VBF1 & CS Sale Factor	0.81 ± 0.10	0.75 ± 0.10	0.80 ± 0.08

Table 7.13: Event yields for $t\bar{t}$ in the dimuon channel after VBF1 selection cuts with modified $p_{\mathrm{T}}^{miss} > 100$ GeV have been applied. The full event yield can be found in appendix table A.16

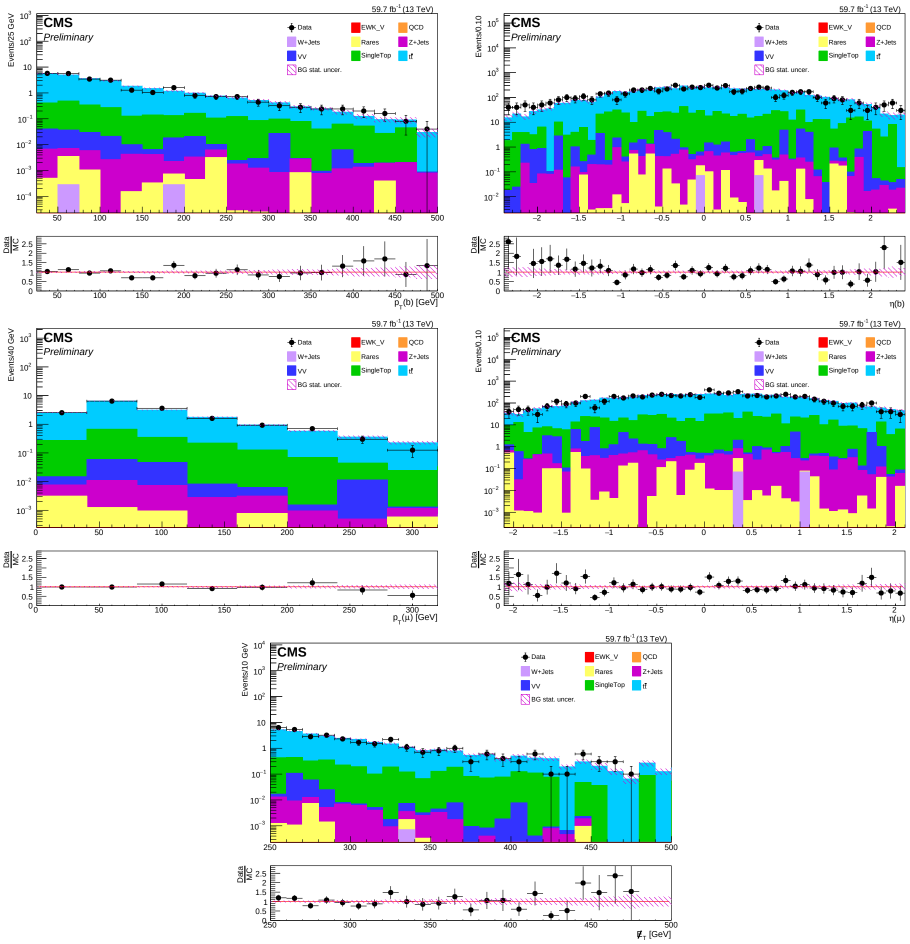

Figure 7.28: $p_{\mathrm{T}}(b)$, $\eta(b)$, $p_{\mathrm{T}}(\mu)$, $\eta(\mu)$ and p_{T}^{miss} after central selection cuts (2018). A SF of 0.97 has been applied to the plots shown.

Sample	2016	2017	2018
$t\bar{t}$	18.8 ± 0.9	19.2 ± 1.0	31.1 ± 1.6
Total MC	21.2 ± 1.1	20.1 ± 1.1	33.9 ± 1.8
Data	16.0	14.0	25.0
Purity [%]	88.7 %	95.5 %	91.7 %
VBF2 Sale Factor	1.09 ± 0.22	0.71 ± 0.20	0.73 ± 0.17
Combined VBF2 & CS Sale Factor	0.72 ± 0.22	0.68 ± 0.20	0.71 ± 0.17

Table 7.14: Event yields for $t\bar{t}$ in the dimuon channel after VBF2 selection cuts have been applied. The full event yield can be found in appendix table A.18

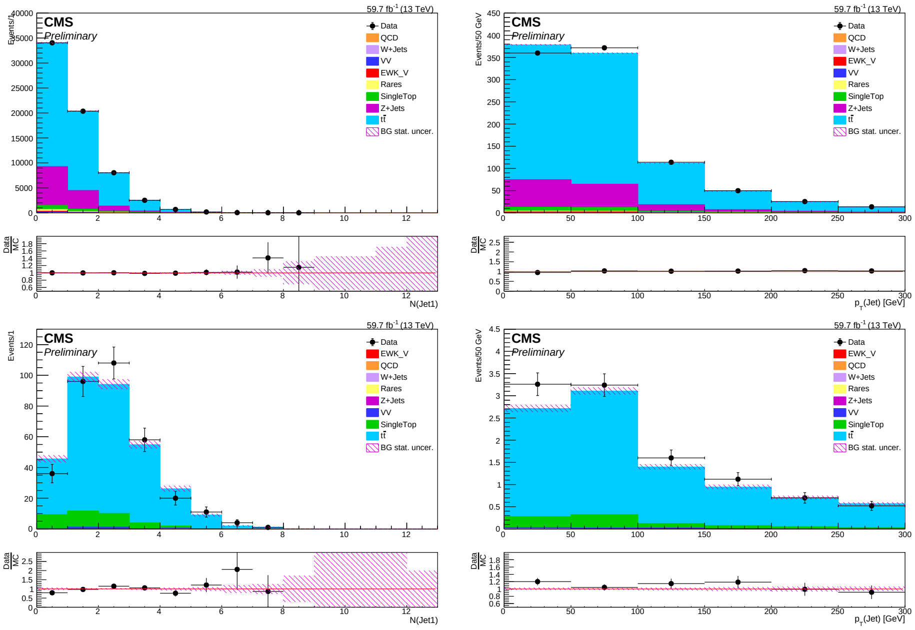

Figure 7.29: $N(j)$ (left) and $p_T(j)$ (right) before the p_T^{miss} requirement is applied (top) and after (bottom) (2018). A SF of 0.97 has been applied to the plots shown. It is observed that after requiring $p_T^{miss} > 250$ GeV, events primarily have $N(j) > 1$ and $p_T(j) > 50$ GeV.

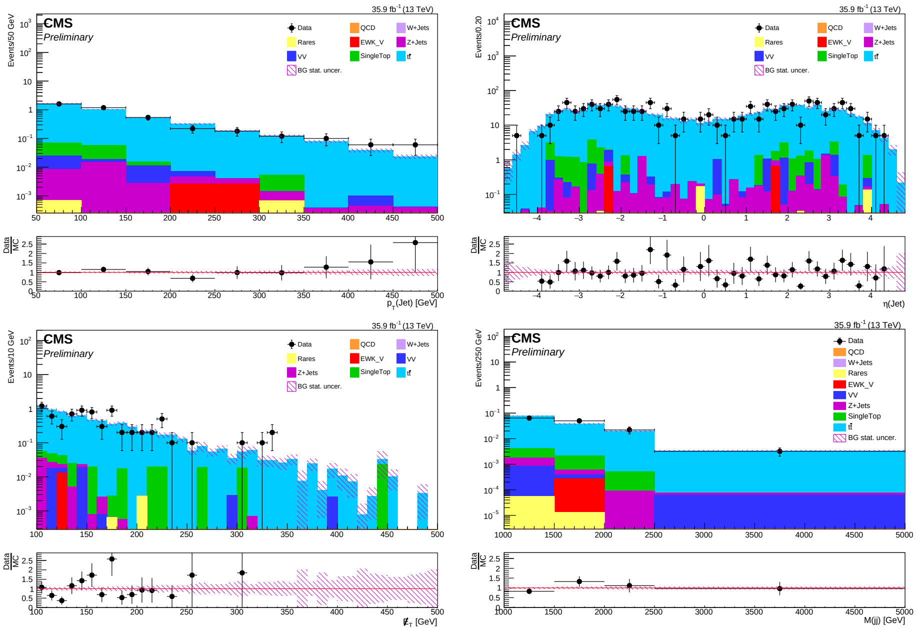

Figure 7.30: $p_T(j)$, $\eta(j)$, p_T^{miss}, and Largest $m(jj)$ after VBF1 cuts (2016). A SF of 0.81 has been applied to the plots shown.

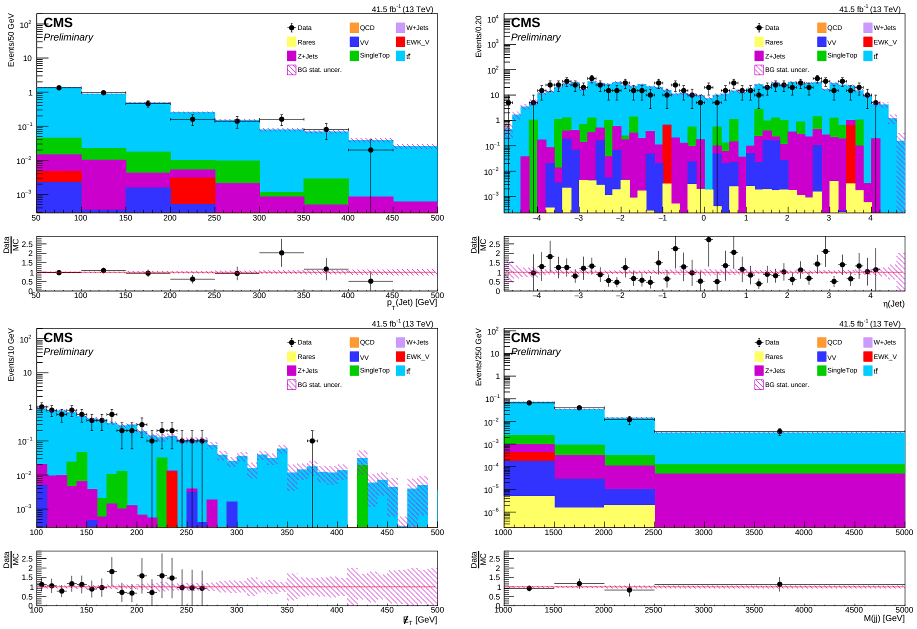

Figure 7.31: $p_{\mathrm{T}}(j)$, $\eta(j)$, p_{T}^{miss}, and Largest $m(jj)$ after VBF1 cuts (2017). A SF of 0.75 has been applied to the plots shown.

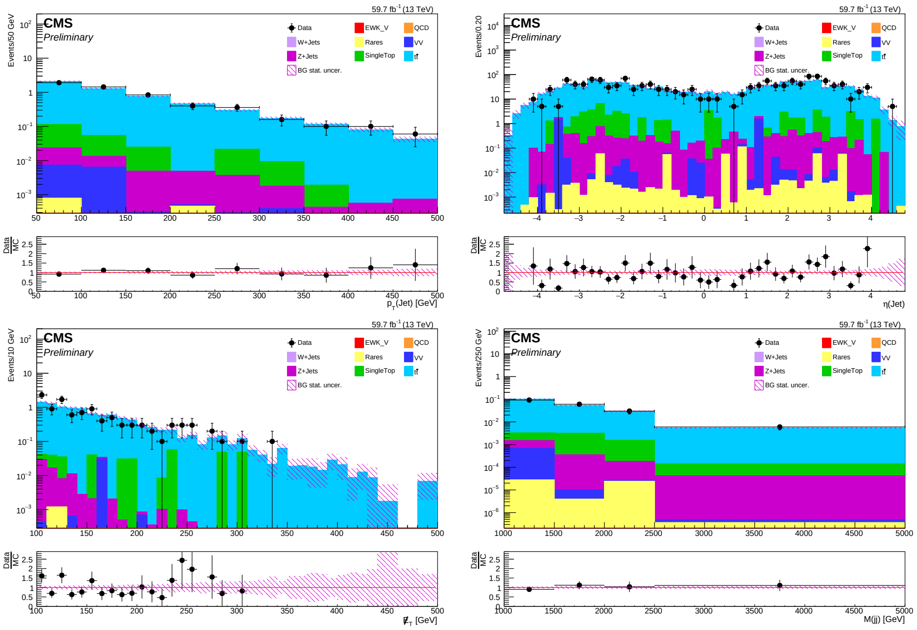

Figure 7.32: $p_{\mathrm{T}}(j)$, $\eta(j)$, p_{T}^{miss}, and Largest $m(jj)$ after VBF1 cuts (2018). A SF of 0.80 has been applied to the plots shown.

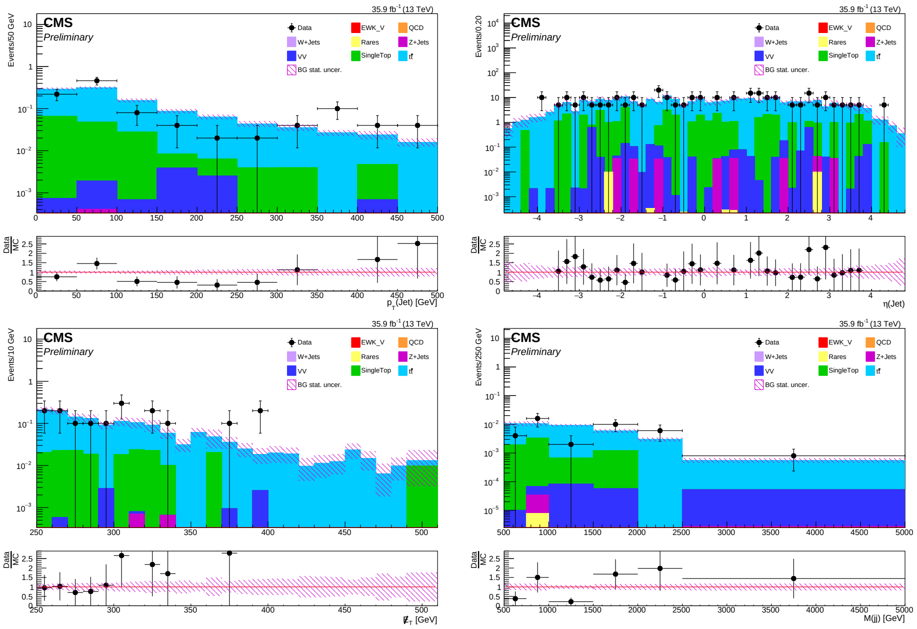

Figure 7.33: $p_{\mathrm{T}}(j)$, $\eta(j)$, p_{T}^{miss}, and Largest $m(jj)$ after VBF2 cuts (2016). A SF of 0.72 has been applied to the plots shown.

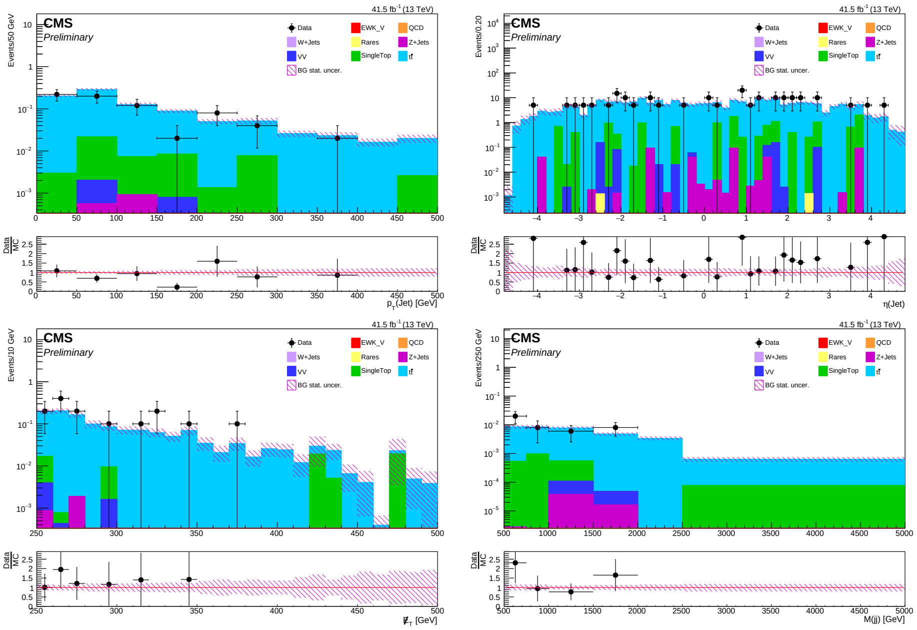

Figure 7.34: $p_{\mathrm{T}}(j)$, $\eta(j)$, p_{T}^{miss}, and Largest $m(jj)$ after VBF2 cuts (2017). A SF of 0.68 has been applied to the plots shown.

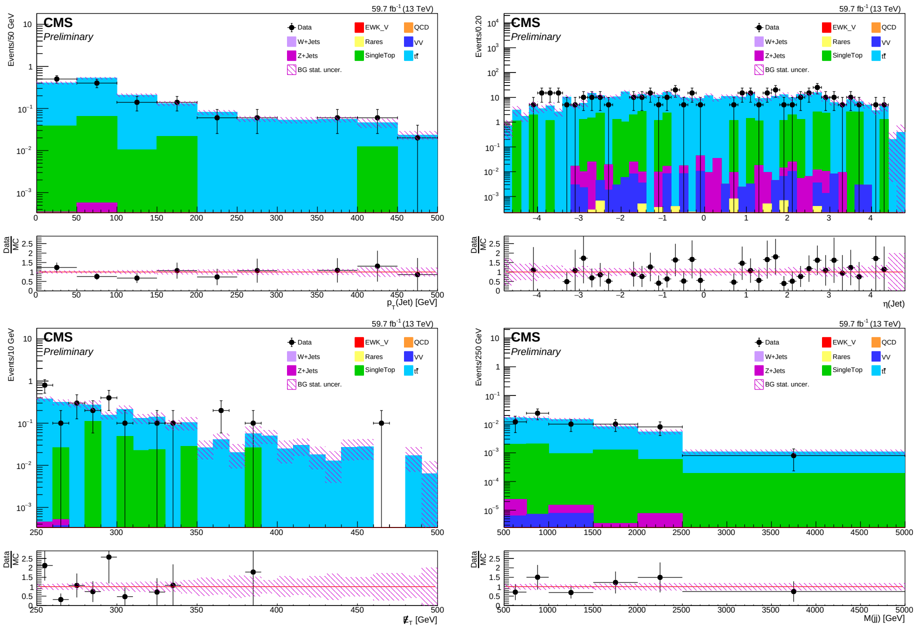

Figure 7.35: $p_{\mathrm{T}}(j)$, $\eta(j)$, p_{T}^{miss}, and Largest $m(jj)$ after VBF2 cuts (2018). A SF of 0.71 has been applied to the plots shown.

7.4 Diboson

Diboson is another important background that can easily mimic the kinematics and object selections of a signal event. This is especially true for (but not limited to) the "virtual W/Z" scenario, in which charginos and neutralinos always decay to vector bosons and are produced along with multiple jets and large p_{T}^{miss}. Diboson events occur when two vector bosons (WW, WZ, or ZZ) are produced in a single event. If the vector bosons decay to two total leptons, or if more leptons are produced but are not correctly identified, and the event contains additional neutrinos and jets, then this process can enter into the SR. Therefore a diboson background estimation study has been performed using the selection criteria shown in table 7.15. The selection criteria is similar to that used for Z+jets (along with the reasoning discussed in section 7.1), with the exception that a third muon is required in order to ensure orthogonality to the SR, there is no selection on p_{T}^{miss} applied, and the dimuon pair is not required to have a reconstructed mass near m_Z.

	Object	Selection cuts
Diboson	Trigger	2016 and 2018: HLT_IsoMu24; 2017: HLT_IsoMu27
	μ	$N(\mu) \geq 3$, $p_{\mathrm{T}}(\mu) > 20$ GeV, $\lvert\eta(\mu)\rvert < 2.1$ and tight ID, $I_{rel} < 0.15$; $N(\mu) \geq 2$ with $p_{\mathrm{T}}(\mu) > 30$ GeV
	$\mu\mu$ combinations	$N(\mu\mu) \geq 1$, $q_1(\mu) \times q_2(\mu) < 0$, $\Delta R(\mu,\mu) > 0.4$
	p_{T}^{miss}	$p_{\mathrm{T}}^{miss} > 30$ GeV
	e veto	$N(e) = 0$ with $p_{\mathrm{T}} > 5$ GeV, $\lvert\eta\rvert < 2.1$, medium ID (cut-based)
	τ_h	$N(\tau_h) = 0$, $p_{\mathrm{T}}(\tau_h) > 20$ GeV, $\lvert\eta(\tau_h)\rvert < 2.1$, tight ID (Deep Tau), medium (tight) anti-$e(\mu)$ discr., 1- or 3-prongs
	b-jet veto	$N(\mathrm{b}) = 0$, $p_{\mathrm{T}}(b) > 30$ GeV, $\lvert\eta\rvert < 2.4$, medium DeepCSV WP
	QCD rejection	$\lvert\Delta\phi(j, p_{\mathrm{T}}^{miss})\rvert_{min} > 0.5$, jet defined as in VBF2 selections.

Table 7.15: Central selection event criteria for diboson background estimation. VBF criteria may be found in table 6.3

Diboson Modeling After Central Selections:

Table 7.16 shows purities, SFs, and event yields in data and MC for 2016, 2017, and 2018 after applying CS cuts. The full event yield including contributions from each individual MC process can be found in appendix table A.19. It is observed that this region contains good statistics and although the purity is lower than would be desired ($\sim 60\%$), it is still sufficient with which to make conclusions about the CR. The kinematics of this region, which can be seen in figures 7.36, 7.37, and 7.38, for 2016, 2017, and 2018 respectively, are expected to largely mirror that of the the Z+jets CR. Specifically, the muons within this CR will again be produced by real Z and W decays and therefore the $p_{\mathrm{T}}(\mu)$ distribution should peak near $m_Z/2$ (which is approximately equivalent to $m_W/2$) and the $m(\mu,\mu)$ distribution should peak near m_Z (or again, near m_W). $\eta(\mu)$ shows the expected shape of objects reconstructed within the tracker coverage. It is further expected that any real p_{T}^{miss} produced in these events will come from neutrinos produced in W decays and should therefore peak at $m_W/2$ before decaying exponentially, which is correctly observed. Given that the kinematics correctly produce these expectations and that the CF SFs appropriately correct for event yield such that the MC and data are in good agreement after their application, it can be concluded that the central selections are well modeled.

Sample	2016	2017	2018
Diboson MC	459.2 ± 1.9	516.5 ± 9.1	675.9 ± 8.8
Total MC	664.0 ± 9.1	863.3 ± 15.4	1092.9 ± 19.6
Data	582	848	1074
Purity [%]	69.2	59.8	61.8
Central Selection Scale Factor	0.82 ± 0.056	0.97 ± 0.064	0.97 ± 0.056

Table 7.16: Event yields for diboson after central selection cuts have been applied. The full event yield can be found in appendix table A.19

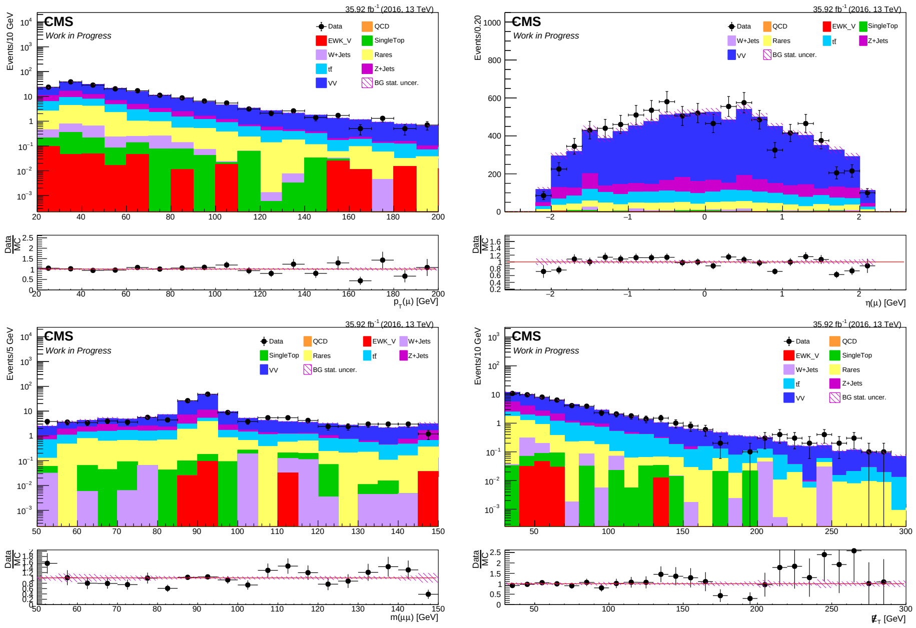

Figure 7.36: $p_T(\mu)$, $\eta(\mu)$, $m(\mu,\mu)$, and p_T^{miss} after central selection cuts, including veto selections, in diboson (2016). A central selection scale factor of 0.82 has been applied to these plots.

Diboson Modeling After VBF Selections:

Diboson events, similar to $t\bar{t}$, are expected to naturally be rare due to their low cross section. This is again further exacerbated by adding the additional stringent requirements of the VBF selections. Therefore it is expected that a region such as this would suffer from low statistics, and indeed this is observed after applying both VBF1 and VBF2 selections. Tables 7.17 and 7.18 show purities, SFs, and event yields in data and MC for 2016, 2017, and 2018, after VBF1 and VBF2 selections are applied, respectively. The full event yields can be found in appendix tables A.20 and A.21. Low purity is again observed within both the VBF1 and

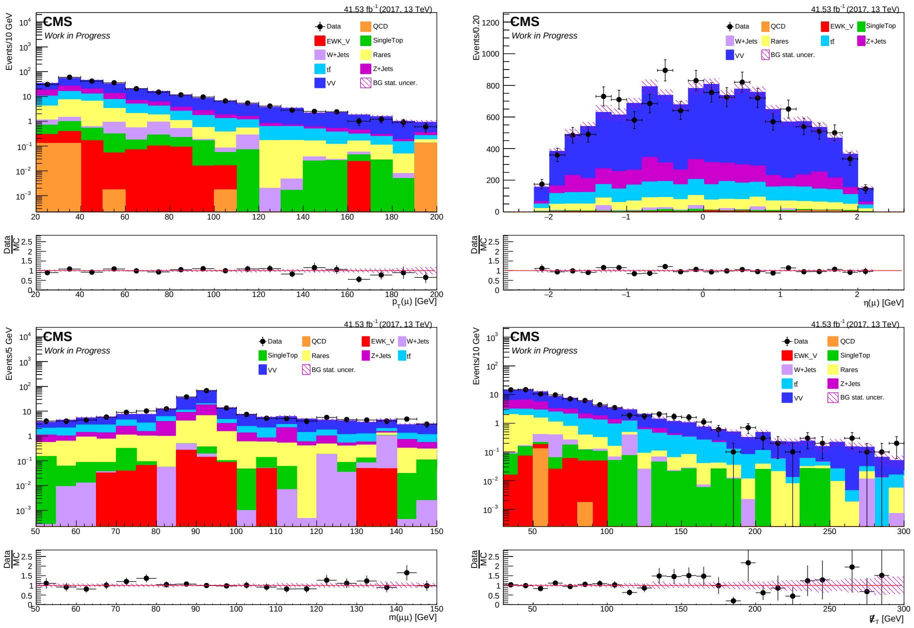

Figure 7.37: $p_{\mathrm{T}}(\mu)$, $\eta(\mu)$, $m(\mu,\mu)$, and p_{T}^{miss} after central selection cuts, including veto selections, in diboson (2017). A central selection scale factor of 0.97 has been applied to these plots.

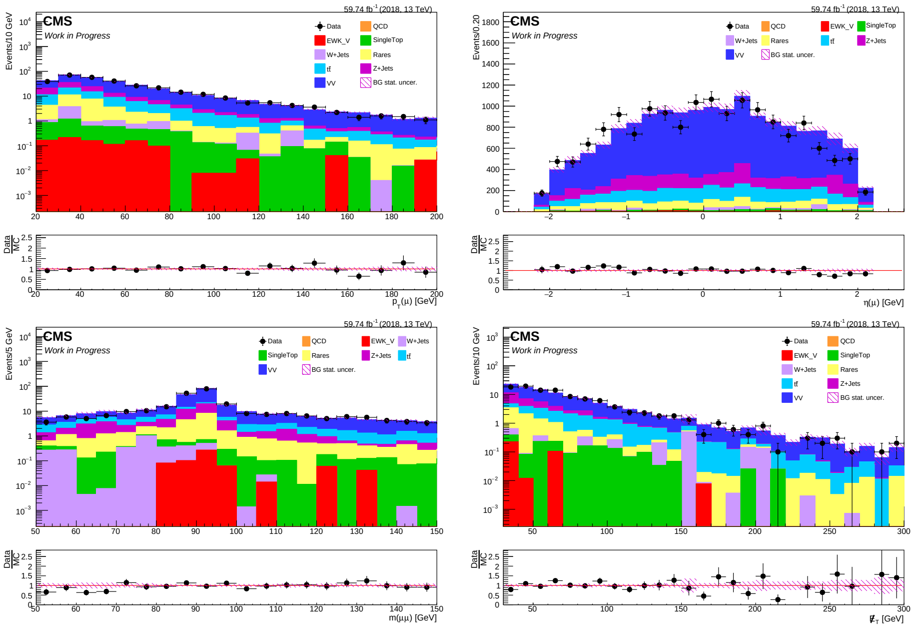

Figure 7.38: $p_{\mathrm{T}}(\mu)$, $\eta(\mu)$, $m(\mu,\mu)$, and p_{T}^{miss} after central selection cuts, including veto selections, in diboson (2018). A central selection scale factor of 0.97 has been applied to these plots.

VBF2 regions, with the main contamination coming from Z+jets and $t\bar{t}$ in which an ISR jet has likely been misidentified as a low momentum muon, or a b-jet was incorrectly reconstructed as a separate muon and jet. The VBF SFs derived from these regions appear reasonable and largely agree with unity within their respective statistical uncertainties. Kinematically, the shapes and distributions for $p_{\mathrm{T}}(j)$, $\eta(j)$, $\Delta\eta(jj)$, and largest $m(jj)$ agree with expectations. These results for VBF1 for 2016, 2017, and 2018 can be seen in figures 7.39, 7.40, and 7.41, while the same results for VBF2 can be seen in figures 7.42, 7.43, and 7.44. The $p_{\mathrm{T}}(j)$ and m_{jj} distributions both follow the shape of a falling exponential as expected, with conclusions in m_{jj} being difficult to gain due to the low statistics. The $\eta(j)$ distribution does not follow the normal "double hump" structure of VBF events, however there is good agreement between data and MC in all regions. Likewise, the $\Delta\eta(jj)$ distribution shows the correct shape, but suffers from low statistics. Given that it can be difficult to increase statistics without further reducing the purity, and that this CR is expected to produce low event yields, it is concluded that current modeling is sufficient and that the SFs derived herein will be used to correct for the diboson event yields in the SR.

Sample	2016	2017	2018
Diboson MC	69.5 ± 0.7	77.2 ± 3.5	86.9 ± 3.1
Total MC	96.5 ± 1.8	121.1 ± 4.1	135.6 ± 4.3
Data	108	130	100
Purity [%]	72.1	63.7	64.1
VBF1 Scale Factor	1.42 ± 0.24	1.15 ± 0.20	1.26 ± 0.19
Combined VBF1 & CS Scale Factor	1.16 ± 0.24	1.12 ± 0.20	1.22 ± 0.19

Table 7.17: Event yields for diboson after VB1 cuts have been applied. The full event yield can be found in appendix table A.20

Sample	2016	2017	2018
Diboson	164.8 ± 1.1	168.9 ± 5.2	204.0 ± 4.8
Total MC	241.0 ± 4.4	281.6 ± 7.1	342.9 ± 7.6
Data	213	305	375
Purity [%]	68.4	60.0	59.5
VBF2 Scale Factor	1.01 ± 0.16	1.17 ± 0.17	1.19 ± 0.15
Combined VBF1 & CS Scale Factor	0.83 ± 0.16	1.13 ± 0.17	1.15 ± 0.15

Table 7.18: Event yields for diboson after VBF2 cuts and vetoes have been applied.

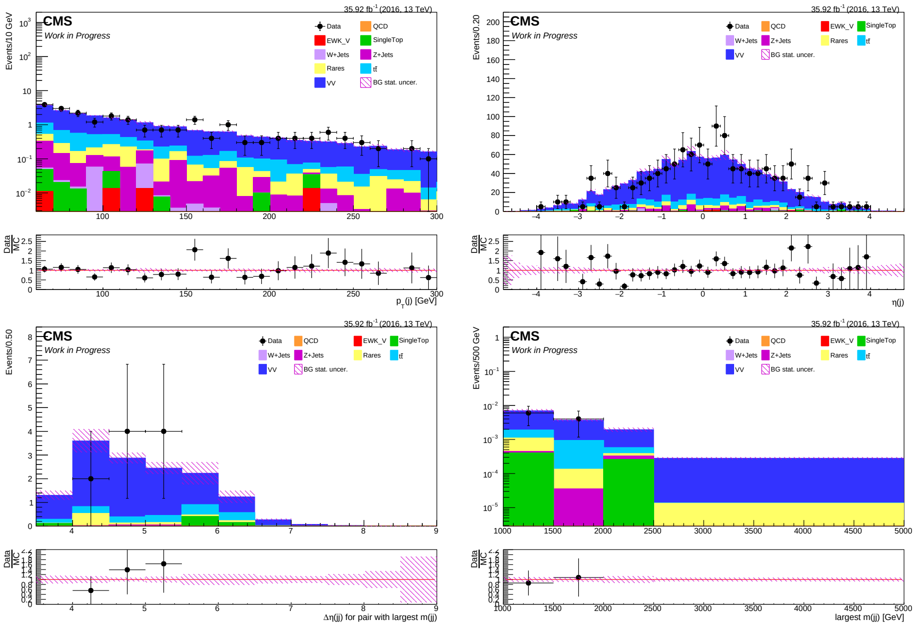

Figure 7.39: $p_\mathrm{T}(j)$, $\eta(j)$, $\Delta\eta(jj)$, and Largest $m(jj)$ after VBF1 cuts (2016). A SF of 1.16 has been applied to the plots shown.

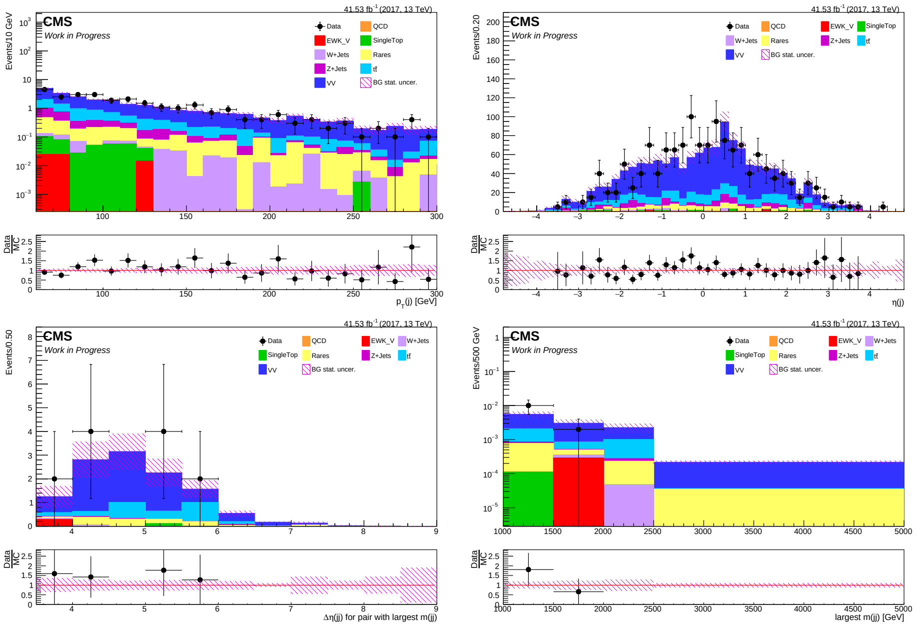

Figure 7.40: $p_\mathrm{T}(j)$, $\eta(j)$, $\Delta\eta(jj)$, and Largest $m(jj)$ after VBF1 cuts (2017). A SF of 1.12 has been applied to the plots shown.

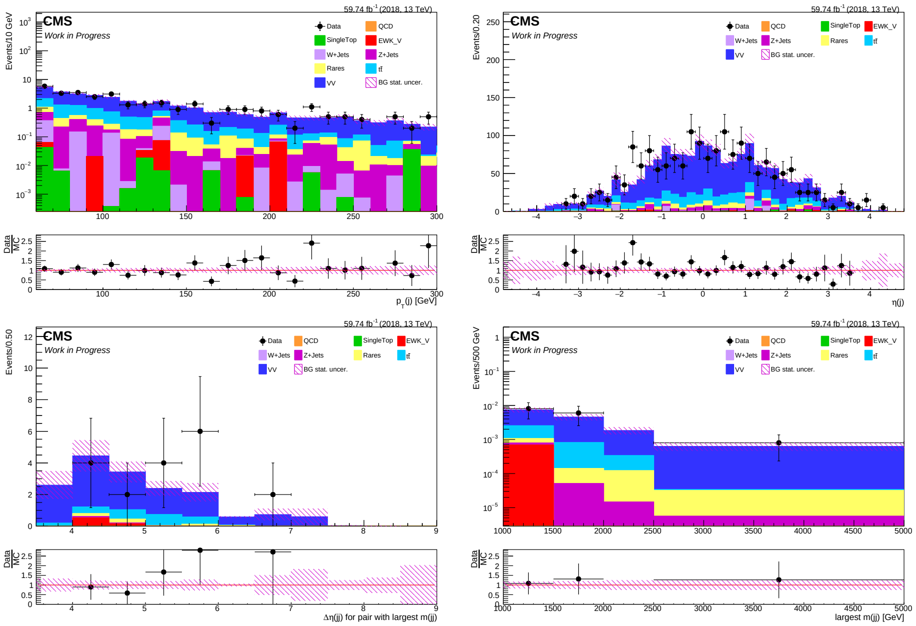

Figure 7.41: $p_{\rm T}(j)$, $\eta(j)$, $\Delta\eta(jj)$, and Largest $m(jj)$ after VBF1 cuts (2018). A SF of 1.22 has been applied to the plots shown..

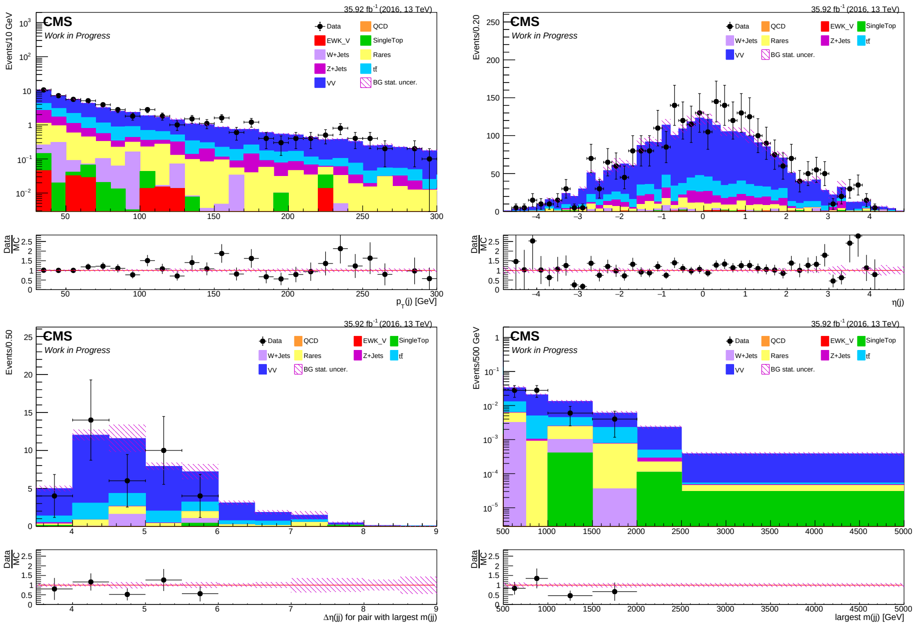

Figure 7.42: $p_{\rm T}(j)$, $\eta(j)$, $\Delta\eta(jj)$, and Largest $m(jj)$ after VBF2 cuts (2016). A SF of 1.01 has been applied to the plots shown.

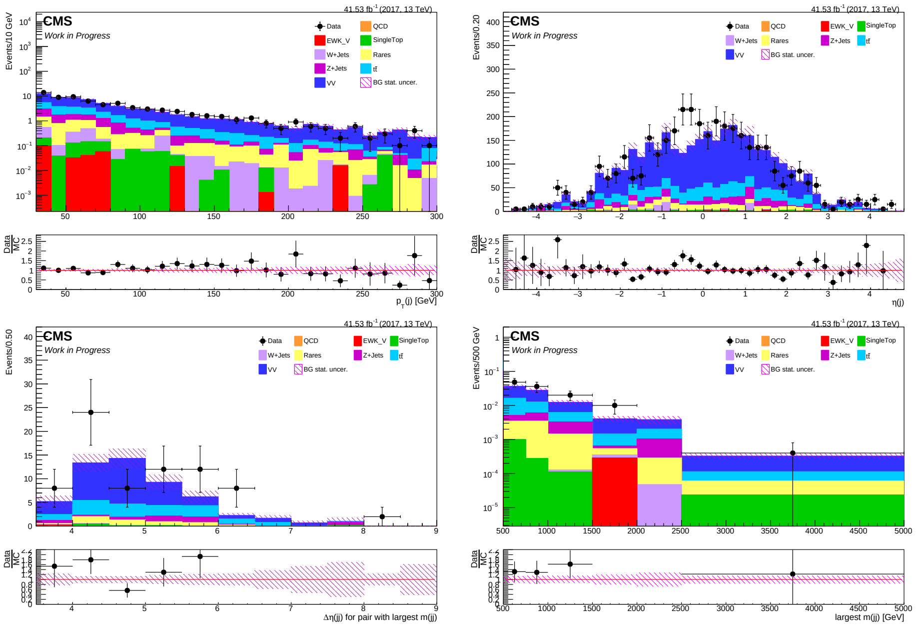

Figure 7.43: $p_\mathrm{T}(j)$, $\eta(j)$, $\Delta\eta(jj)$, and Largest $m(jj)$ after VBF2 cuts (2017). A SF of 1.17 has been applied to the plots shown.

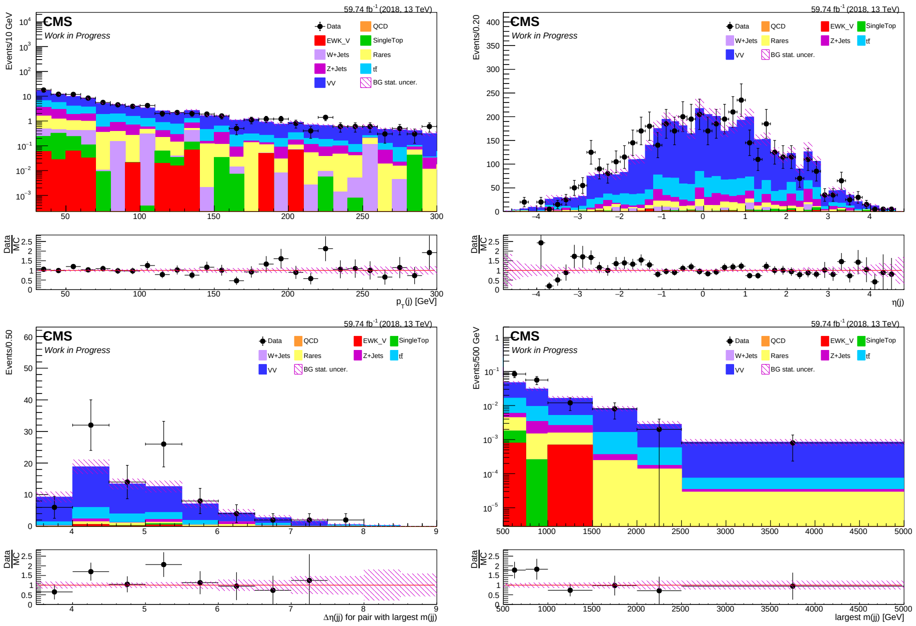

Figure 7.44: $p_\mathrm{T}(j)$, $\eta(j)$, $\Delta\eta(jj)$, and Largest $m(jj)$ after VBF2 cuts (2018). A SF of 1.19 has been applied to the plots shown.

CHAPTER 8

Systematic Uncertainties

Uncertainty, in the context of a data analysis, is defined as the variation in a measurement around a given value due to either natural fluctuations or errors coming from the measuring apparatus. A statistical uncertainty is an uncertainty of the first variety, arising due to natural fluctuations in the data, be it in actual recorded data or simulated MC data. If one expects a process to follow a Poisson distribution with N events, then the standard deviation of such a distribution will be $\sigma = \sqrt{N}$ and the associated relative error is $1/\sqrt{N}$. For an experiment with a predicted yield of 9 events, this means a standard deviation of ± 3 events and a 33.3% relative statistical uncertainty. If the experiment were to be repeated but with an increase in data such that an event yield of 100 events was predicted, then the standard deviation would be ± 10 events with a relative statistical uncertainty of 10%. Thus it can be seen that statistical uncertainties can be reduced with an increase in the overall statistics by recording more data. This in contrast to systematic uncertainties, which are uncertainties of the second variety which can arise due to mismeasurements and errors within the detector itself. If there is a relative uncertainty of 33.3% when predicting 9 events, there will likewise be an uncertainty of 33.3% when predicting 100 events. To make matters worse, systematic uncertainties cannot necessarily be expected to follow nice distributions like statistical yields, and must instead be inferred using other methods. Such systematic uncertainties arise due to imprecise knowledge about the detector and how exactly it might preform under varying conditions and separate runs. Therefore, in order to determine the systematic errors associated with these various experimental quantities, dedicated studies have been performed which are presented here. These include systematic studies which are most applicable to the high-p_{T} and far-forward jets present in VBF interactions, including pile-up (PU), jet energy resolution (JER), jet energy scale (JES), and L1-PreFiring. These quantities are expected to be the most impactful to this study, and might not have been studied in detail previously by the wider collaboration. Additional results for various other quantities will be presented at the end of this chapter.

8.1 Pile-Up (PU)

As discussed in section 3.2, the number of PU interactions per bunch crossing can be predicted as a function of the cross section, which in this context is often referred to as the *minimum-bias* cross section as it is intended to be measured using the least amount of biasing as possible. The total number of PU interactions per bunch crossing can be calculated using the following formula:

$$\mu = L^{i}_{\text{inst}}\sigma_{\text{inel}}/f_{\text{rev}} \tag{8.1}$$

where μ in this case is the total number of PU interactions, L^{i}_{inst} is the instantaneous luminosity of a single bunch, σ_{inel} is the total pp inelastic cross section, and f_{rev} is the LHC orbit frequency of 11246 Hz which is necessary to convert from a per-time quantity (instantaneous luminosity) to a per-collision quantity. The quantity μ obtained from the instantaneous luminosity will therefore be an averaged quantity during a single lumi section, and the distribution for individual events will be a Poisson distribution around this average. Per the CMS lumi group, the recommended minimum-bias cross section for Run 2 is 69.2 mb, with an associated uncertainty of 4.6% [71]. This study was therefore performed by calculating PU weights using the nominal minimum-bias cross section, the $+1\sigma$ variation, and the -1σ variation, and calculating the resultant yields after applying the newly derived PU weight.

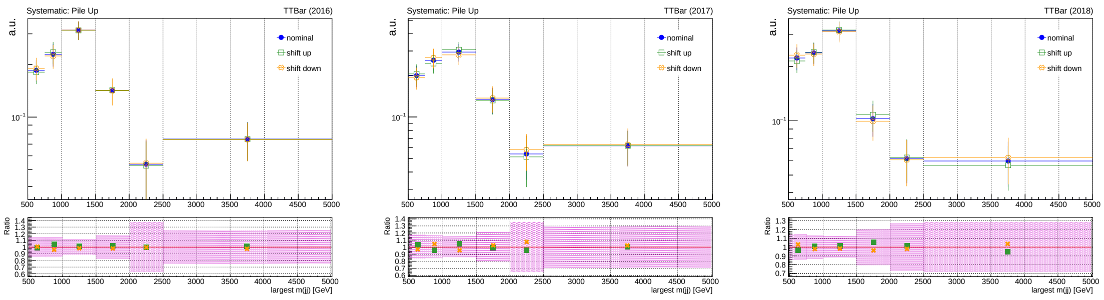

(a) (b) (c)

Figure 8.1: Largest dijet mass distribution after applying all selection cuts (including VBF2 selections) to $t\bar{t}$ MC samples produced for 2016 (left), 2017 (center), 2018 (right) in the 2ℓ channel. The nominal and $\pm1\sigma$ variations to the min-bias cross section are shown in the top plot, where each distribution has been normalized to unity in order to compare the shapes. The bottom plot shows the ratio of the $\pm1\sigma$ variations to the nominal value, with the magenta indicating the statistical uncertainty in each bin.

Figure 8.1 shows the resulting largest dijet mass distribution in the dimuon channel after applying all selection cuts (including VBF2 selections) to $t\bar{t}$ MC samples for all three years. The nominal and $\pm1\sigma$ variations are shown overlaying each other with each distribution being normalized to unity in order to compare the overall shape. An identical study can be seen in figure 8.2, but applied to the virtual W/Z signal MC samples with $m(\tilde{\chi}^{2}_{0})$ = 300 GeV and Δm = 50 GeV instead. The lower plot on each histogram shows the ratio of the $\pm1\sigma$ variations to the nominal value, with the magenta shading indicating the statistical uncertainty. As can be seen from each plot, the statistical uncertainty is larger than the systematic uncertainty in each bin. We cannot therefore with confidence determine the true value of the systematic uncertainty. Instead, the same

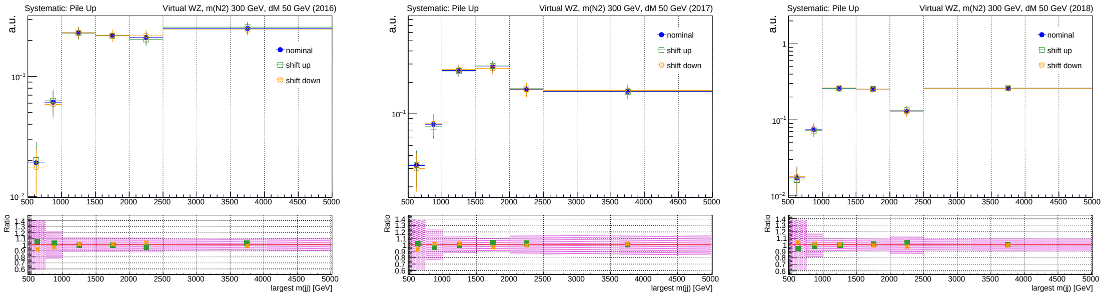

(a) (b) (c)

Figure 8.2: Largest dijet mass distribution after applying all selection cuts (including VBF2 selections) to virtual W/Z signal MC ($m(\tilde{\chi}_0^2)$ = 300 GeV, Δm = 50 GeV) produced for 2016 (left), 2017 (center), 2018 (right) in the 2ℓ channel. The nominal and $\pm1\sigma$ variations to the min-bias cross section are shown in the top plot, where each distribution has been normalized to unity in order to compare the shapes. The bottom plot shows the ratio of the $\pm1\sigma$ variations to the nominal value, with the magenta indicating the statistical uncertainty in each bin.

study was performed in the 0ℓ channel, the results of which can be seen in figure 8.3. Due to the significantly larger statistical yields in the 0ℓ channel, it is possible to see the effects of the $\pm1\sigma$ variation and the resultant systematic uncertainty. It is additionally observed that such results are small, typically order $1-2\%$. The resulting PU systematic uncertainties, which are independent of the lepton channel they are derived from, will be taken from the 0ℓ channel and applied to the 2ℓ channel, in which the uncertainties will be treated as 100% correlated between all samples.

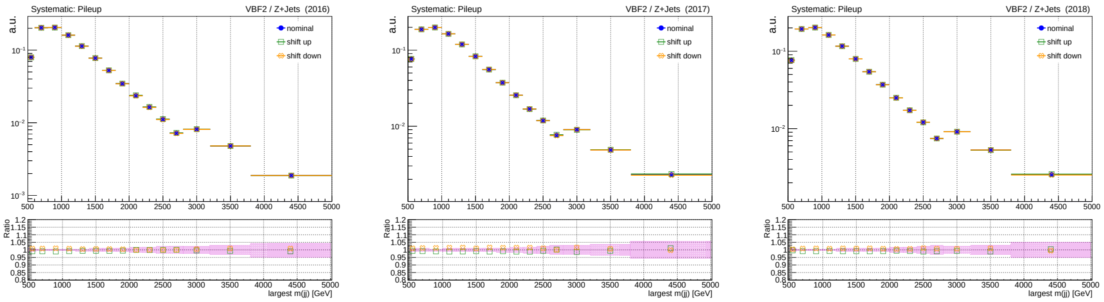

(a) (b) (c)

Figure 8.3: Largest dijet mass distribution after applying all selection cuts (including VBF2 selections) to Z+jets for 2016 (left), 2017 (center), 2018 (right) in the 0ℓ channel. The nominal and $\pm1\sigma$ variations to the min-bias cross section are shown in the top plot, where each distribution has been normalized to unity in order to compare the shapes. The bottom plot shows the ratio of the $\pm1\sigma$ variations to the nominal value, with the magenta indicating the statistical uncertainty in each bin.

8.2 Jet Energy Resolution (JER)

In order to understand the systematic uncertainties related to JER (which is discussed in length in section 4.4.2), the JER scale factors were scaled via $\pm 1\sigma$ variations. These variations are provided by, and at the behest of, the JetMET group (see reference [60]). These results can be seen in figure 8.4, in which the 0ℓ channel will again be used in order to decrease the associated statistical uncertainty. The results indicate the systematic uncertainty from JER is generally $< 5\%$. These results will be treated as uncorrelated across all years.

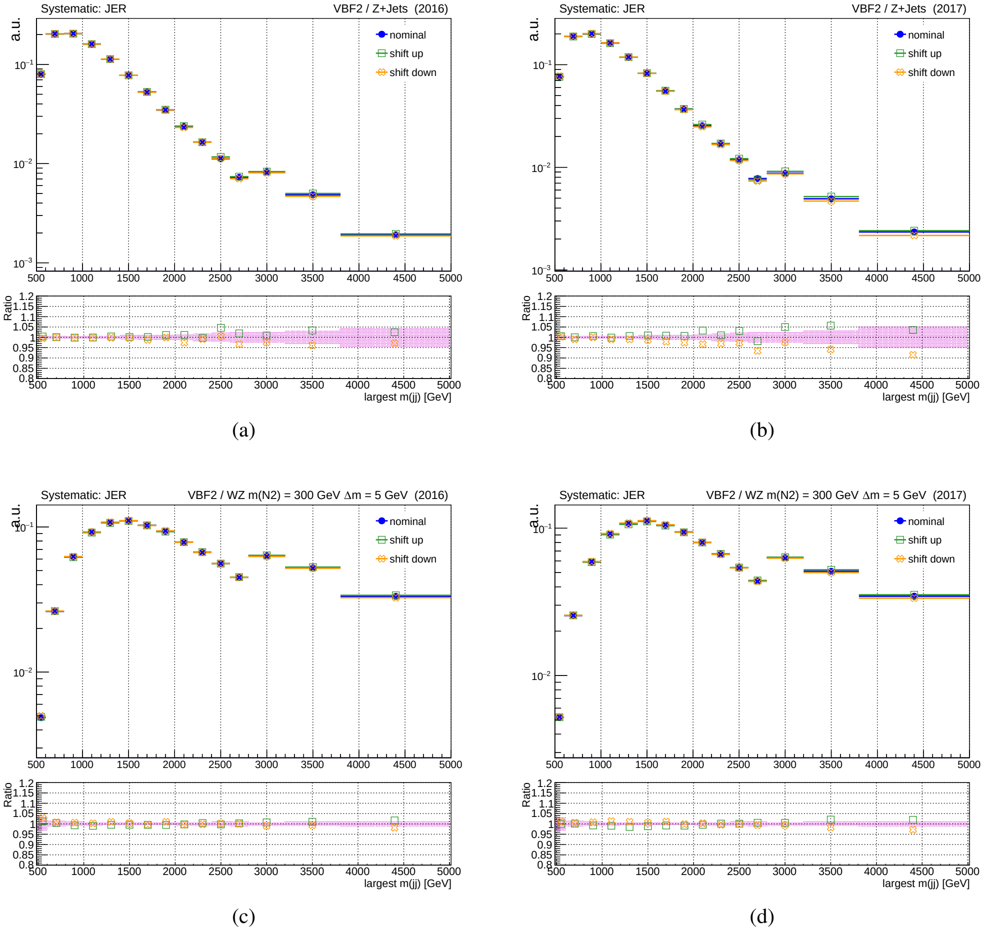

(a) (b) (c) (d)

Figure 8.4: Largest dijet mass distribution after applying all selection cuts (including VBF2 selections) in the 0ℓ channels to Z+jets MC samples produced for 2016 (top left) and 2017 (top right) and to virtual W/Z signal MC samples ($m(\tilde{\chi}_0^2)$ = 300 GeV, Δm = 5 GeV) produced for 2016 (bottom left) and 2017 (bottom right). The nominal and $\pm 1\sigma$ variations to JER are shown in the top plot, where each distribution has been normalized to unity in order to compare the shapes. The bottom plot shows the ratio of the $\pm 1\sigma$ variations to the nominal value, with the magenta indicating the statistical uncertainty in each bin.

8.3 Jet Energy Scale (JES)

Similar studies to JER were performed for JES in which $\pm 1\sigma$ variations were applied (according to prescriptions provided by the JetMET POG). These results can be seen in figure 8.5, showing the largest dijet mass distribution after applying all selection cuts (including VBF2 selections) in the 0ℓ channels to Z+jets MC samples produced for 2016 (top left) and 2017 (top right), as well as to the virtual W/Z signal MC samples ($m(\tilde{\chi}^2_0)$ = 300 GeV, Δm = 5 GeV) for 2016 (bottom left) and 2017 (bottom right).

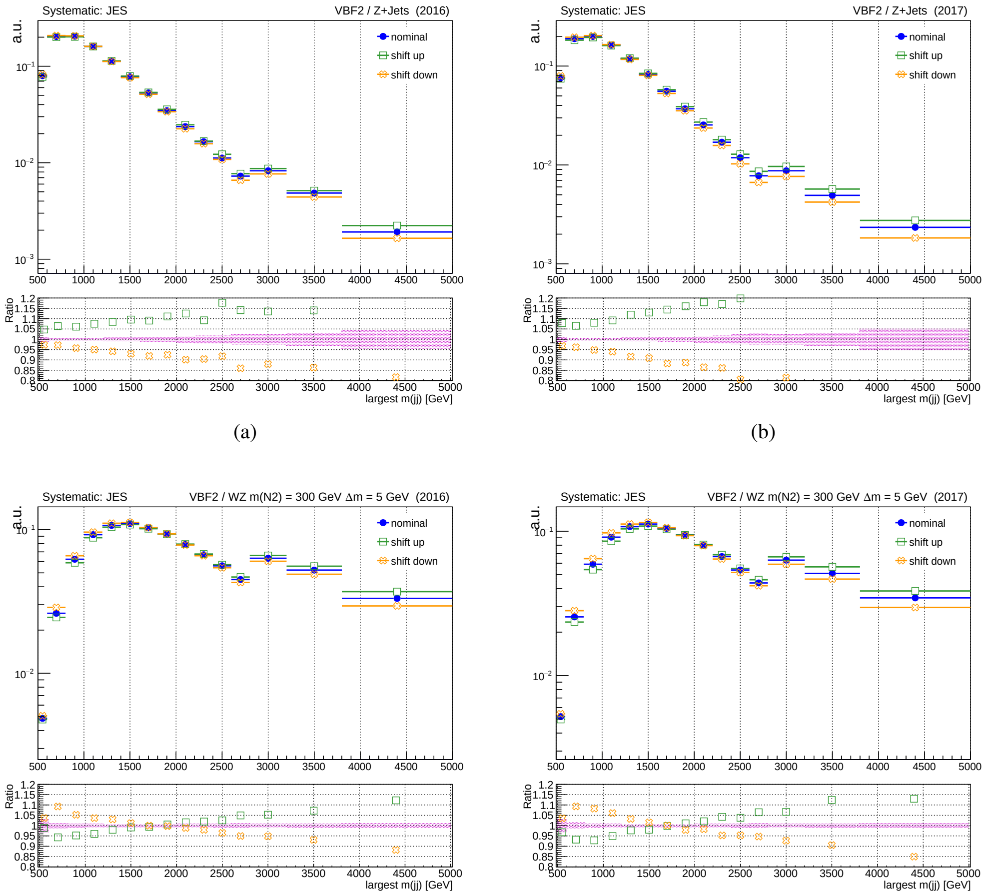

(a)

(b)

(c)

(d)

Figure 8.5: Largest dijet mass distribution after applying all selection cuts (including VBF2 selections) in the 0ℓ channels to Z+jets MC samples produced for 2016 (top left) and 2017 (top right) and to virtual W/Z signal MC samples ($m(\tilde{\chi}^2_0)$ = 300 GeV, Δm = 5 GeV) produced for 2016 (bottom left) and 2017 (bottom right). The nominal and $\pm 1\sigma$ variations to JES are shown in the top plot, where each distribution has been normalized to unity in order to compare the shapes. The bottom plot shows the ratio of the $\pm 1\sigma$ variations to the nominal value, with the magenta indicating the statistical uncertainty in each bin.

8.4 L1-PreFiring

the L1-PreFiring issue is discussed in length in section 5.6.1. Systematic uncertainty studies for this effect were performed by applying ±1σ variations which were provided by CMS (see reference [66]). These results can be seen in figure 8.6, showing the largest dijet mass distribution after applying all selection cuts (including VBF2 selections) in the 0ℓ channels to Z+jets MC samples produced for 2016 (top left) and 2017 (top right), as well as to the virtual W/Z signal MC samples ($m(\tilde{\chi}_0^2)$ = 300 GeV, Δm = 5 GeV) for 2016 (bottom left) and 2017 (bottom right).

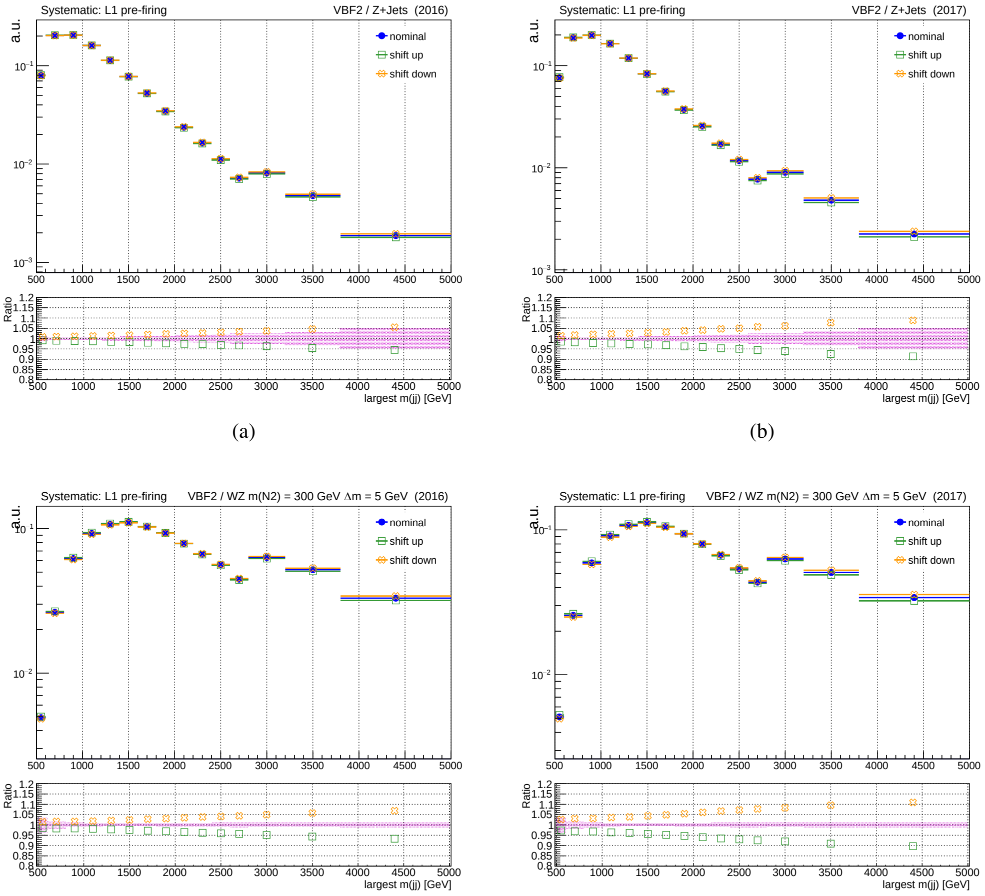

(a)

(b)

(c)

(d)

Figure 8.6: Largest dijet mass distribution after applying all selection cuts (including VBF2 selections) in the 0ℓ channels to Z+jets MC samples produced for 2016 (top left) and 2017 (top right) and to virtual W/Z signal MC ($m(\tilde{\chi}_0^2)$ = 300 GeV, Δm = 5 GeV) produced for 2016 (bottom left) and 2017 (bottom right). The nominal and ±1σ variations to L1-PreFiring weights are shown in the top plot, where each distribution has been normalized to unity in order to compare the shapes. The bottom plot shows the ratio of the ±1σ variations to the nominal value, with the magenta indicating the statistical uncertainty in each bin.

8.5 Miscellaneous

Various other systematic uncertainties were studied for this analysis, which include but are not limited to:

- **Luminosity**: We consider a 1.2% uncertainty for 2016, a 2.3% uncertainty for 2017, and a 2.5% uncertainty for 2018 [72, 73, 74]. Uncertainties within years are considered 100% correlated across MC samples and channels within a given year.
- **Electron Energy Scale**: We consider the effect on the signal acceptance efficiency of 1% (2.5%) shift on the electron energy scale in the barrel (endcap) region. The systematic effect is $<1\%$. These values follow from the EGamma POG recommendations [23].
- **Muon Momentum Scale**: We consider the effect on the signal acceptance efficiency of a 1% momentum scale uncertainty on the muon momentum. The resultant systematic uncertainty on signal and MC based backgrounds is $<1\%$.

CHAPTER 9

Results

Although the data remains blinded, it is possible to still make predictions regarding the signal region (SR), including the expected contributions from signal and background processes as well as the expected kinematics. Similarly, we can also make predictions regarding the exclusion limits which can be reached, assuming no signal is detected, and compare these results to the exclusion limits achieved by previous studies (as detailed in section 2.3). This chapter will discuss both of these results. As a reminder, this analysis is a search for compressed mass spectrum SUSY which will naturally produce soft decay products. Additionally, the work presented in this thesis, which searches for events resulting in two leptons (2ℓ), will be combined with similar studies looking for physics resulting in one lepton (1ℓ) and zero lepton (0ℓ) final states. As one begins to require more leptons in the final state, the expected yields will naturally decrease as soft leptons are difficult to efficiently reconstruct at CMS. This is reflected in figure 9.1 which shows the signal acceptance within the 0ℓ and 1ℓ channels (left), as well as the 2ℓ channels (right), for the virtual W/Z scenario across a range of Δm values (shown along the x-axis). The signal acceptance (A) is defined as the ratio of events passing all signal region selection cuts (N_{cuts}) to the total number of signal events present within the MC sample studied (N_{Tot}), in the following way:

$$A = \frac{N_{\text{cuts}}}{N_{\text{Tot}}} \tag{9.1}$$

Many interesting results can be interpreted from these plots. First, the 0ℓ channel has the largest signal acceptance across the entire range of Δm values studied. This is expected, given that the resulting soft leptons produced by these events are difficult to reconstruct. It is also the case that not all events will produce leptons, for instance in the fully hadronic decays of W or Z bosons. The branching fraction for $W \rightarrow$ jets or $Z \rightarrow$ jets is approximately 70%, so zero lepton events are expected to occur a large fraction of the time. Next in terms of largest signal acceptance is the 1ℓ channel, followed by the 2ℓ channel. This is again expected due to the combinatorics for producing one lepton being larger (more probable) than for producing two leptons when two vector bosons decay. It is also the case that the probability of reconstructing only one soft lepton when two are present is higher than fully reconstructing both, thus further reducing the signal acceptance.

It is also interesting to note that the signal acceptance of the 0ℓ channel decreases for increasing Δm value. This can be interpreted as events which actually do produce leptons are more likely to have those leptons be reconstructed for larger Δm scenarios, which implies they would no longer pass the 0ℓ SR cuts and instead pass the 1ℓ (or even 2ℓ) SR cuts. This is reflected in the 1ℓ signal acceptance distribution which generally increases for increasing Δm value. When studying the 1ℓ distribution, it is interesting to note the ordering. The μ channel generally has the highest signal acceptance, followed by the e channel, followed by the τ channel. This can be interpreted due to the different reconstruction and identification efficiencies, in which muons are the most efficiently reconstructed physics objects, followed by electrons, followed by taus. A similar effect is observed when studying the 2ℓ channel. The $\mu\mu$ channel produces the highest signal acceptance, followed by $e\mu$ and then ee, and then the τ channels which follow the same order of $\mu\tau$, $e\tau$, and finally $\tau\tau$. The small Δm behavior in the $\tau\tau$ channel is also interesting, in that it is difficult to reconstruct taus below p_{T} of 20 GeV (and in fact this is the lower bound of the p_{T} window for taus). This is reflected in the signal acceptance quickly going to zero for small Δm values.

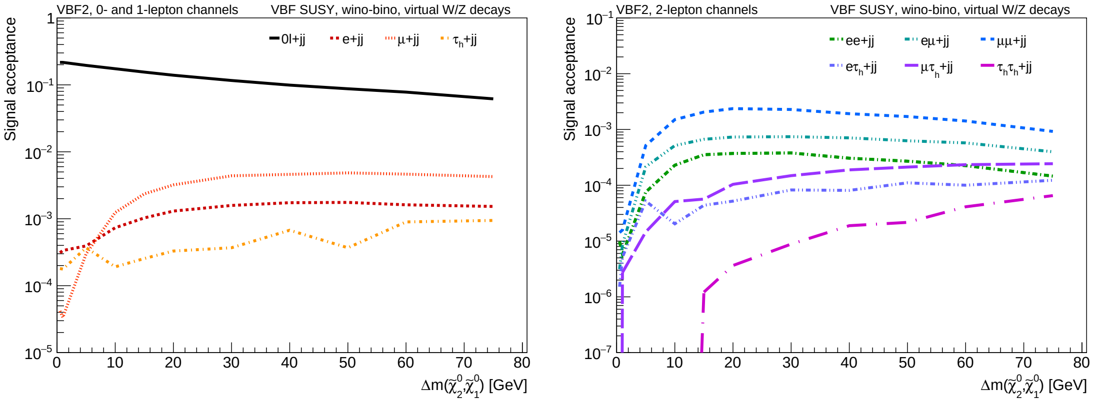

Figure 9.1: Signal acceptance within the 0ℓ and 1ℓ channels (left) and the 2ℓ channels (right) after applying all signal region selection cuts on the virtual W/Z scenario signal MC samples.

Figure 9.2 again shows the same signal acceptance results for the 0ℓ and 1ℓ channels (left) and 2ℓ channels (right) but for the $\tilde{\tau}$ dominated scenario instead. These results share many similarities with the virtual W/Z scenario results, but with a few key differences. Again, the ordering of the signal acceptance still goes from highest to lowest as 0ℓ, 1ℓ, and then 2ℓ, however within the individual channels the ordering of the objects is changed. For instance, in the 1ℓ channel, the highest signal acceptance is the τ channel and the lowest the e. This is due to the fact that within the $\tilde{\tau}$ dominated scenario, all electroweakinos besides the LSP will have a decay chain that eventually produces a τ. Therefore it is the higher production rate, and not a detector effect which produces the larger signal acceptance. Likewise in the 2ℓ channels, the three channels involving taus largely have higher signal acceptance than those without. These effects are important in order to properly be able to understand and interpret the predicted signal yields in the final results.

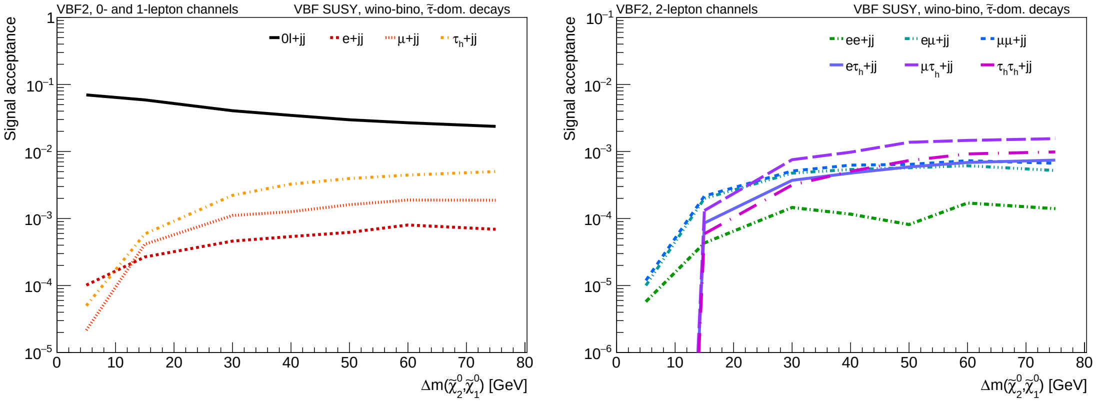

Figure 9.2: Signal acceptance within the 0ℓ and 1ℓ channels (left) and the 2ℓ channels (right) after applying all signal region selection cuts on the $\tilde{\tau}$ dominated scenario signal MC samples.

9.1 Signal Region Predictions

Presented here are the signal region event yield predictions for each individual background process, as well as a few select signal points from the virtual W/Z and $\tilde{\tau}$ dominated scenarios, showing different Δm values. Presented first are the dimuon channel results for all three years for both OS and LS channels, followed then by the dielectron channels, and finally the electron-muon channel. Kinematic plots showing the largest dijet mass distribution in each region are included as well, with a signal mass point overlaid accordingly. It is important to again note that the 2ℓ channels naturally expect low event production compared to the 0ℓ and 1ℓ channels. It is also important to point out that the event yields within each channel from the 2016, 2017, and 2018 runs will eventually be combined. Additionally, the results from all channels will be incorporated when creating exclusion plots, under the assumption that no excess or new physics is observed. This is mentioned to explain that low signal event yields within any single channel for a single year are not necessarily indicative of the overall sensitivity to that mass point.

9.1.1 Dimuon Channel (OS & LS)

The results for the OS and LS dimuon channels are shown in tables 9.1 through 9.6, with associated distributions for largest dijet mass in 2016, 2017, and 2018 shown in figures 9.3, 9.4, and 9.5, respectively. Within the dimuon OS channel, there is expected to be a large contribution from $t\bar{t}$, as well as processes that create Z bosons such as Z+jets, EWK V, and diboson. Indeed, $t\bar{t}$ is predicted to be the largest background present in this region. $t\bar{t}$ can easily produce two real muons of OS, as well as pass the large p_{T}^{miss} requirements when the system is produced with sufficient boost. Diboson can also readily pass the signal region selections, but has a comparatively smaller cross section than $t\bar{t}$, which reduces the overall yield. Z+jets does not produce any real p_{T}^{miss}, which greatly reduces the event yield in the SR, despite its very large cross section. EWK V suffers from both of these effects – small cross section and no real p_{T}^{miss} produced, which further reduces its presence in the SR. It is possible also for W+jets to enter this region if a jet present in the event fakes a muon, however muons have very low fake rates which greatly reduces the possibility of this occurring.

Within the dimuon LS channel, one does not expect many background processes to be present. There are few SM processes which can produce two LS muons, and those that can have extremely small cross sections (SM VBS or VBF for instance). It is therefore most likely that events which enter into this signal region are either muons whose charge have been mismeasured (which is rare) or jets which are faking muons (again rare). When examining the results it is observed that indeed yields in the LS region are approximately half of those in the OS region, which confirms this expectation as correct.

2016 VBF2 $\mu\mu$ (OS) channel				
Sample	$N_{\mathrm{Process}}^{\mathrm{MC/Data}}$(SR/CR)	SF^{CR1} or TF_1	SF^{CR2} or TF_2	$N_{\mathrm{Process}}^{\mathrm{Predicted}}$
Z+Jets	3.3 ± 0.6	0.95 ± 0.001	1.181 ± 0.008	3.7 ± 0.7
W+Jets	1.0 ± 0.4	0.992 ± 0.01	1.065 ± 0.042	1.0 ± 0.4
EWK V	0.3 ± 0.2	—	—	0.3 ± 0.2
Rares	0.8 ± 0.4	—	—	0.8 ± 0.4
Diboson	5.6 ± 0.9	0.821 ± 0.056	1.01 ± 0.16	4.6 ± 1.1
$t\bar{t}$	15.9 ± 1.1	0.66 ± 0.07	1.09 ± 0.22	11.4 ± 2.7
SingleTop	1.3 ± 0.4	—	—	1.3 ± 0.4
QCD	0.6 ± 0.6	—	—	0.6 ± 0.6
SR BG Prediction	28.8 ± 1.8	—	—	23.8 ± 3.2
$m(\tilde{\chi}_1^{\pm}), m(\tilde{\chi}_2^0), m(\tilde{\chi}_1^0) = 300, 300, 295$ GeV	—	—	—	0.0 ± 0.0
$m(\tilde{\chi}_1^{\pm}), m(\tilde{\chi}_2^0), m(\tilde{\chi}_1^0) = 300, 300, 270$ GeV	—	—	—	0.4 ± 0.0
$m(\tilde{\chi}_1^{\pm}), m(\tilde{\chi}_2^0), m(\tilde{\chi}_1^0) = 300, 300, 250$ GeV	—	—	—	0.5 ± 0.0
$m(\tilde{\chi}_1^{\pm}), m(\tilde{\tau}), m(\tilde{\chi}_1^0) = 300, 297.5, 295$ GeV	—	—	—	0.5 ± 0.0
$m(\tilde{\chi}_1^{\pm}), m(\tilde{\tau}), m(\tilde{\chi}_1^0) = 300, 285, 270$ GeV	—	—	—	1.1 ± 0.0
$m(\tilde{\chi}_1^{\pm}), m(\tilde{\tau}), m(\tilde{\chi}_1^0) = 300, 275, 250$ GeV	—	—	—	0.2 ± 0.0
Data	Unblinded	—	—	—

Table 9.1: Predicted and observed rates in the signal region for 2016 VBF2 $\mu\mu$ (OS) channel.

2016 VBF2 $\mu\mu$ (LS) channel				
Sample	$N^{\text{MC/Data}}_{\text{Process}}$(SR/CR)	SF^{CR1} or TF_1	SF^{CR2} or TF_2	$N^{\text{Predicted}}_{\text{Process}}$
Z+Jets	0.6 ± 0.1	0.95 ± 0.001	1.181 ± 0.008	0.7 ± 0.1
W+Jets	3.4 ± 0.8	0.992 ± 0.01	1.065 ± 0.042	3.6 ± 0.8
EWK V	0.4 ± 0.2	—	—	0.4 ± 0.2
Rares	0.9 ± 0.3	—	—	0.9 ± 0.3
Diboson	1.1 ± 0.1	0.821 ± 0.056	1.01 ± 0.16	0.9 ± 0.2
$t\bar{t}$	5.9 ± 0.4	0.66 ± 0.07	1.09 ± 0.22	4.3 ± 1.0
SingleTop	0.7 ± 0.2	—	—	0.7 ± 0.2
QCD	0.1 ± 0.1	—	—	0.1 ± 0.1
SR BG Prediction	13.1 ± 0.9	—	—	11.5 ± 1.4
$m(\tilde{\chi}_1^{\pm}), m(\tilde{\chi}_2^0), m(\tilde{\chi}_1^0) = 300, 300, 295$ GeV	—	—	—	0.0 ± 0.0
$m(\tilde{\chi}_1^{\pm}), m(\tilde{\chi}_2^0), m(\tilde{\chi}_1^0) = 300, 300, 270$ GeV	—	—	—	0.1 ± 0.0
$m(\tilde{\chi}_1^{\pm}), m(\tilde{\chi}_2^0), m(\tilde{\chi}_1^0) = 300, 300, 250$ GeV	—	—	—	0.1 ± 0.0
$m(\tilde{\chi}_1^{\pm}), m(\tilde{\tau}), m(\tilde{\chi}_1^0) = 300, 297.5, 295$ GeV	—	—	—	0.1 ± 0.0
$m(\tilde{\chi}_1^{\pm}), m(\tilde{\tau}), m(\tilde{\chi}_1^0) = 300, 285, 270$ GeV	—	—	—	0.3 ± 0.0
$m(\tilde{\chi}_1^{\pm}), m(\tilde{\tau}), m(\tilde{\chi}_1^0) = 300, 275, 250$ GeV	—	—	—	0.1 ± 0.0
Data	Unblinded	—	—	—

Table 9.2: Predicted and observed rates in the signal region for 2016 VBF2 $\mu\mu$ (LS) channel.

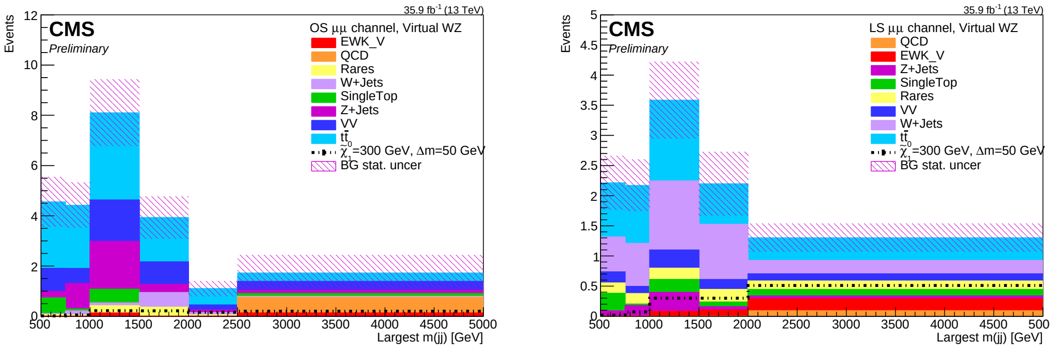

Figure 9.3: 2016 largest dijet mass for the $\mu\mu$ channel (left, OS; right, LS) with overlaid signal mass point of $m(\tilde{\chi}_2^0) = 300$ GeV, $\Delta M = 50$ GeV from the Wino-Bino Virtual WZ scenario.

2017 VBF2 $\mu\mu$ (OS) channel				
Sample	$N^{\text{MC/Data}}_{\text{Process}}$(SR/CR)	SF^{CR1} or TF_1	SF^{CR2} or TF_2	$N^{\text{Predicted}}_{\text{Process}}$
Z+Jets	2.8 ± 0.6	0.926 ± 0.001	1.025 ± 0.007	2.7 ± 0.6
W+Jets	2.5 ± 0.9	0.919 ± 0.009	1.004 ± 0.052	2.3 ± 0.9
EWK V	0.6 ± 0.3	—	—	0.6 ± 0.3
Rares	0.2 ± 0.1	—	—	0.2 ± 0.1
Diboson	7.7 ± 1.2	0.97 ± 0.064	1.17 ± 0.17	8.7 ± 1.9
$t\bar{t}$	17.9 ± 1.2	0.96 ± 0.08	0.71 ± 0.2	12.2 ± 3.7
SingleTop	1.5 ± 0.5	—	—	1.5 ± 0.5
QCD	0.1 ± 0.1	—	—	0.1 ± 0.1
SR BG Prediction	33.3 ± 2.1	—	—	28.3 ± 4.3
$m(\tilde{\chi}^{\pm}_1), m(\tilde{\chi}^0_2), m(\tilde{\chi}^0_1) = 300, 300, 295$ GeV	—	—	—	0.0 ± 0.0
$m(\tilde{\chi}^{\pm}_1), m(\tilde{\chi}^0_2), m(\tilde{\chi}^0_1) = 300, 300, 270$ GeV	—	—	—	0.5 ± 0.0
$m(\tilde{\chi}^{\pm}_1), m(\tilde{\chi}^0_2), m(\tilde{\chi}^0_1) = 300, 300, 250$ GeV	—	—	—	0.6 ± 0.1
$m(\tilde{\chi}^{\pm}_1), m(\tilde{\tau}), m(\tilde{\chi}^0_1) = 300, 297.5, 295$ GeV	—	—	—	0.6 ± 0.1
$m(\tilde{\chi}^{\pm}_1), m(\tilde{\tau}), m(\tilde{\chi}^0_1) = 300, 285, 270$ GeV	—	—	—	1.1 ± 0.0
$m(\tilde{\chi}^{\pm}_1), m(\tilde{\tau}), m(\tilde{\chi}^0_1) = 300, 275, 250$ GeV	—	—	—	0.2 ± 0.0
Data	Unblinded	—	—	—

Table 9.3: Predicted and observed rates in the signal region for 2017 VBF2 $\mu\mu$ (OS) channel.

2017 VBF2 $\mu\mu$ (LS) channel				
Sample	$N^{\text{MC/Data}}_{\text{Process}}$(SR/CR)	SF^{CR1} or TF_1	SF^{CR2} or TF_2	$N^{\text{Predicted}}_{\text{Process}}$
Z+Jets	0.2 ± 0.0	0.926 ± 0.001	1.025 ± 0.007	0.2 ± 0.0
W+Jets	4.3 ± 1.3	0.919 ± 0.009	1.004 ± 0.052	4.0 ± 1.2
EWK V	0.5 ± 0.2	—	—	0.5 ± 0.2
Rares	0.6 ± 0.3	—	—	0.6 ± 0.3
Diboson	0.6 ± 0.1	0.97 ± 0.064	1.17 ± 0.17	0.7 ± 0.1
$t\bar{t}$	5.3 ± 0.3	0.96 ± 0.08	0.71 ± 0.2	3.6 ± 1
SingleTop	1.1 ± 0.2	—	—	1.1 ± 0.2
QCD	0.1 ± 0.1	—	—	0.1 ± 0.1
SR BG Prediction	12.7 ± 1.4	—	—	10.8 ± 1.7
$m(\tilde{\chi}^{\pm}_1), m(\tilde{\chi}^0_2), m(\tilde{\chi}^0_1) = 300, 300, 295$ GeV	—	—	—	0.0 ± 0.0
$m(\tilde{\chi}^{\pm}_1), m(\tilde{\chi}^0_2), m(\tilde{\chi}^0_1) = 300, 300, 270$ GeV	—	—	—	0.0 ± 0.0
$m(\tilde{\chi}^{\pm}_1), m(\tilde{\chi}^0_2), m(\tilde{\chi}^0_1) = 300, 300, 250$ GeV	—	—	—	0.1 ± 0.0
$m(\tilde{\chi}^{\pm}_1), m(\tilde{\tau}), m(\tilde{\chi}^0_1) = 300, 297.5, 295$ GeV	—	—	—	0.1 ± 0.0
$m(\tilde{\chi}^{\pm}_1), m(\tilde{\tau}), m(\tilde{\chi}^0_1) = 300, 285, 270$ GeV	—	—	—	0.3 ± 0.0
$m(\tilde{\chi}^{\pm}_1), m(\tilde{\tau}), m(\tilde{\chi}^0_1) = 300, 275, 250$ GeV	—	—	—	0.1 ± 0.0
Data	Unblinded	—	—	—

Table 9.4: Predicted and observed rates in the signal region for 2017 VBF2 $\mu\mu$ (LS) channel.

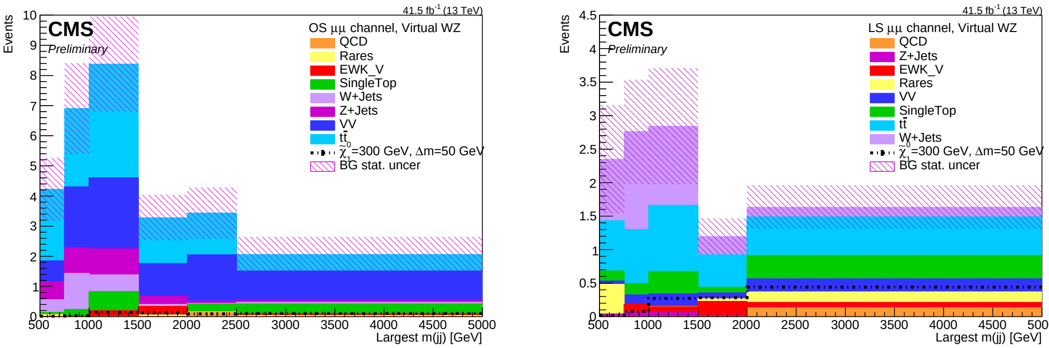

Figure 9.4: 2017 largest dijet mass for the $\mu\mu$ channel (left, OS; right, LS) with overlaid signal mass point of $m(\tilde{\chi}_2^0)$ = 300 GeV, ΔM = 50 GeV from the Wino-Bino Virtual WZ scenario.

2018 VBF2 $\mu\mu$ (OS) channel				
Sample	$N^{\mathrm{MC/Data}}_{\mathrm{Process}}$(SR/CR)	SF^{CR1} or TF_1	SF^{CR2} or TF_2	$N^{\mathrm{Predicted}}_{\mathrm{Process}}$
Z+Jets	5.8 ± 1.2	0.904 ± 0.001	0.966 ± 0.006	5.1 ± 1.0
W+Jets	1.5 ± 0.6	0.885 ± 0.007	0.982 ± 0.033	1.3 ± 0.5
EWK V	0.6 ± 0.4	—	—	0.6 ± 0.4
Rares	0.2 ± 0.1	—	—	0.2 ± 0.1
Diboson	9.1 ± 1.3	0.972 ± 0.056	1.19 ± 0.15	10.6 ± 2.1
$t\bar{t}$	22.9 ± 1.4	0.97 ± 0.06	0.73 ± 0.17	16.2 ± 4.0
SingleTop	1.7 ± 0.5	—	—	1.7 ± 0.5
QCD	0.0 ± 0.0	—	—	0.0 ± 0.0
SR BG Prediction	41.8 ± 2.4	—	—	35.7 ± 4.7
$m(\tilde{\chi}_1^{\pm}), m(\tilde{\chi}_2^0), m(\tilde{\chi}_1^0) = 300, 300, 295$ GeV	—	—	—	0.0 ± 0.0
$m(\tilde{\chi}_1^{\pm}), m(\tilde{\chi}_2^0), m(\tilde{\chi}_1^0) = 300, 300, 270$ GeV	—	—	—	0.5 ± 0.0
$m(\tilde{\chi}_1^{\pm}), m(\tilde{\chi}_2^0), m(\tilde{\chi}_1^0) = 300, 300, 250$ GeV	—	—	—	0.8 ± 0.1
$m(\tilde{\chi}_1^{\pm}), m(\tilde{\tau}), m(\tilde{\chi}_1^0) = 300, 297.5, 295$ GeV	—	—	—	0.8 ± 0.1
$m(\tilde{\chi}_1^{\pm}), m(\tilde{\tau}), m(\tilde{\chi}_1^0) = 300, 285, 270$ GeV	—	—	—	1.7 ± 0.0
$m(\tilde{\chi}_1^{\pm}), m(\tilde{\tau}), m(\tilde{\chi}_1^0) = 300, 275, 250$ GeV	—	—	—	0.3 ± 0.0
Data	Unblinded	—	—	—

Table 9.5: Predicted and observed rates in the signal region for 2018 VBF2 $\mu\mu$ (OS) channel.

2018 VBF2 $\mu\mu$ (LS) channel				
Sample	$N_{\text{Process}}^{\text{MC/Data}}$(SR/CR)	SF^{CR1} or TF_1	SF^{CR2} or TF_2	$N_{\text{Process}}^{\text{Predicted}}$
Z+Jets	0.9 ± 0.2	0.904 ± 0.001	0.966 ± 0.006	0.8 ± 0.1
W+Jets	7.0 ± 2.2	0.885 ± 0.007	0.982 ± 0.033	6.1 ± 1.9
EWK V	0.9 ± 0.4	—	—	0.9 ± 0.4
Rares	0.5 ± 0.3	—	—	0.5 ± 0.3
Diboson	1.9 ± 0.2	0.972 ± 0.056	1.19 ± 0.15	2.2 ± 0.4
$t\bar{t}$	8.7 ± 0.5	0.97 ± 0.06	0.73 ± 0.17	6.2 ± 1.5
SingleTop	1.7 ± 0.4	—	—	1.7 ± 0.4
QCD	1.6 ± 1.4	—	—	1.6 ± 1.4
SR BG Prediction	23.2 ± 2.7	—	—	19.9 ± 2.9
$m(\tilde{\chi}_1^\pm), m(\tilde{\chi}_2^0), m(\tilde{\chi}_1^0) =$ $300, 300, 295$ GeV	—	—	—	0.0 ± 0.0
$m(\tilde{\chi}_1^\pm), m(\tilde{\chi}_2^0), m(\tilde{\chi}_1^0) =$ $300, 300, 270$ GeV	—	—	—	0.1 ± 0.0
$m(\tilde{\chi}_1^\pm), m(\tilde{\chi}_2^0), m(\tilde{\chi}_1^0) =$ $300, 300, 250$ GeV	—	—	—	0.2 ± 0.0
$m(\tilde{\chi}_1^\pm), m(\tilde{\tau}), m(\tilde{\chi}_1^0) =$ $300, 297.5, 295$ GeV	—	—	—	0.2 ± 0.0
$m(\tilde{\chi}_1^\pm), m(\tilde{\tau}), m(\tilde{\chi}_1^0) =$ $300, 285, 270$ GeV	—	—	—	0.5 ± 0.0
$m(\tilde{\chi}_1^\pm), m(\tilde{\tau}), m(\tilde{\chi}_1^0) =$ $300, 275, 250$ GeV	—	—	—	0.2 ± 0.0
Data	Unblinded	—	—	—

Table 9.6: Predicted and observed rates in the signal region for 2018 VBF2 $\mu\mu$ (LS) channel.

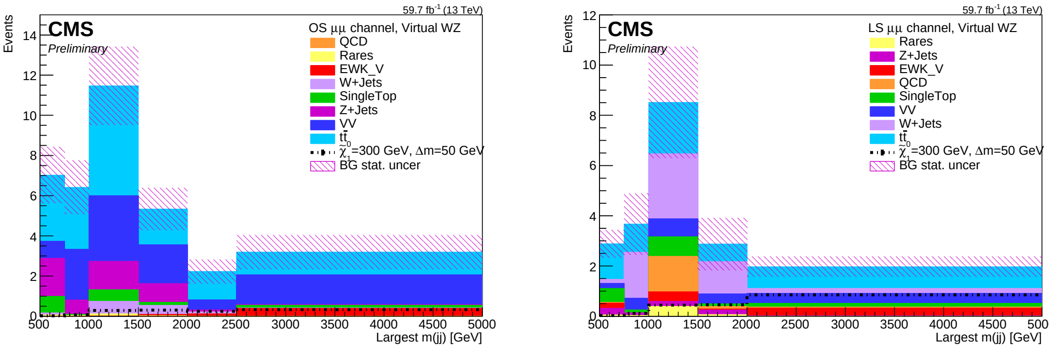

Figure 9.5: 2018 largest dijet mass for the $\mu\mu$ channel (left, OS; right, LS) with overlaid signal mass point of $m(\tilde{\chi}_2^0)$ = 300 GeV, ΔM = 50 GeV from the Wino-Bino Virtual WZ scenario.

9.1.2 Dielectron Channel (OS & LS)

The results for the OS and LS dielectron channels are shown in tables 9.7 through 9.12 with associated distributions for largest dijet mass in 2016, 2017, and 2018 shown in figures 9.6, 9.7, and 9.8, respectively. The expectations of these two channels largely mirror those of the dimuon channels, with the exception that the detector is more efficient at reconstructing muons than electrons, leading to lower comparative event yields in these regions. Indeed when inspecting the predicted event yield tables it is observed that $t\bar{t}$ is again a major background process present, but with slightly lower yields. A similar trend can be observed for diboson, as well as the predicted signal processes. W+jets has slightly larger yields, which can be explained given the larger fake rate of jet → electron as compared to jet → μ, making it more likely to pass the SR cuts.

2016 VBF2 *ee* (OS) channel				
Sample	$N^{\text{MC/Data}}_{\text{Process}}$(SR/CR)	SF^{CR1} or TF_1	SF^{CR2} or TF_2	$N^{\text{Predicted}}_{\text{Process}}$
Z+Jets	0.7 ± 0.3	0.95 ± 0.001	1.181 ± 0.008	0.8 ± 0.4
W+Jets	4.8 ± 1.2	0.992 ± 0.01	1.065 ± 0.042	5.1 ± 1.3
EWK V	0.7 ± 0.3	—	—	0.7 ± 0.3
Rares	0.2 ± 0.2	—	—	0.2 ± 0.2
Diboson	0.9 ± 0.4	0.821 ± 0.056	1.01 ± 0.16	0.8 ± 0.3
$t\bar{t}$	3.6 ± 0.5	0.66 ± 0.07	1.09 ± 0.22	2.6 ± 0.7
SingleTop	0.7 ± 0.3	—	—	0.7 ± 0.3
QCD	0.0 ± 0.0	—	—	0.0 ± 0.0
SR BG Prediction	11.7 ± 1.5	—	—	10.9 ± 1.6
$m(\tilde{\chi}^{\pm}_1), m(\tilde{\chi}^0_2), m(\tilde{\chi}^0_1) = 300, 300, 295$ GeV	—	—	—	0.0 ± 0.0
$m(\tilde{\chi}^{\pm}_1), m(\tilde{\chi}^0_2), m(\tilde{\chi}^0_1) = 300, 300, 270$ GeV	—	—	—	0.1 ± 0.0
$m(\tilde{\chi}^{\pm}_1), m(\tilde{\chi}^0_2), m(\tilde{\chi}^0_1) = 300, 300, 250$ GeV	—	—	—	0.1 ± 0.0
$m(\tilde{\chi}^{\pm}_1), m(\tilde{\tau}), m(\tilde{\chi}^0_1) = 300, 297.5, 295$ GeV	—	—	—	0.1 ± 0.0
$m(\tilde{\chi}^{\pm}_1), m(\tilde{\tau}), m(\tilde{\chi}^0_1) = 300, 285, 270$ GeV	—	—	—	0.2 ± 0.0
$m(\tilde{\chi}^{\pm}_1), m(\tilde{\tau}), m(\tilde{\chi}^0_1) = 300, 275, 250$ GeV	—	—	—	0.0 ± 0.0
Data	Unblinded	—	—	—

Table 9.7: Predicted and observed rates in the signal region for 2016 VBF2 *ee* (OS) channel.

2016 VBF2 *ee* (LS) channel				
Sample	$N^{\mathrm{MC/Data}}_{\mathrm{Process}}$(SR/CR)	SF^{CR1} or TF_1	SF^{CR2} or TF_2	$N^{\mathrm{Predicted}}_{\mathrm{Process}}$
Z+Jets	0.2 ± 0.1	0.95 ± 0.001	1.181 ± 0.008	0.2 ± 0.1
W+Jets	3.5 ± 0.7	0.992 ± 0.01	1.065 ± 0.042	3.7 ± 0.7
EWK V	0.4 ± 0.1	—	—	0.4 ± 0.1
Rares	0.8 ± 0.3	—	—	0.8 ± 0.3
Diboson	0.3 ± 0.1	0.821 ± 0.056	1.01 ± 0.16	0.3 ± 0.1
$t\bar{t}$	2.1 ± 0.3	0.66 ± 0.07	1.09 ± 0.22	1.5 ± 0.4
SingleTop	0.0 ± 0.0	—	—	0.0 ± 0.0
QCD	0.0 ± 0.0	—	—	0.0 ± 0.0
SR BG Prediction	7.3 ± 0.8	—	—	6.9 ± 0.9
$m(\tilde{\chi}_1^{\pm}), m(\tilde{\chi}_2^0), m(\tilde{\chi}_1^0) = 300, 300, 295$ GeV	—	—	—	0.0 ± 0.0
$m(\tilde{\chi}_1^{\pm}), m(\tilde{\chi}_2^0), m(\tilde{\chi}_1^0) = 300, 300, 270$ GeV	—	—	—	0.0 ± 0.0
$m(\tilde{\chi}_1^{\pm}), m(\tilde{\chi}_2^0), m(\tilde{\chi}_1^0) = 300, 300, 250$ GeV	—	—	—	0.0 ± 0.0
$m(\tilde{\chi}_1^{\pm}), m(\tilde{\tau}), m(\tilde{\chi}_1^0) = 300, 297.5, 295$ GeV	—	—	—	0.0 ± 0.0
$m(\tilde{\chi}_1^{\pm}), m(\tilde{\tau}), m(\tilde{\chi}_1^0) = 300, 285, 270$ GeV	—	—	—	0.0 ± 0.0
$m(\tilde{\chi}_1^{\pm}), m(\tilde{\tau}), m(\tilde{\chi}_1^0) = 300, 275, 250$ GeV	—	—	—	0.0 ± 0.0
Data	Unblinded	—	—	—

Table 9.8: Predicted and observed rates in the signal region for 2016 VBF2 *ee* (LS) channel.

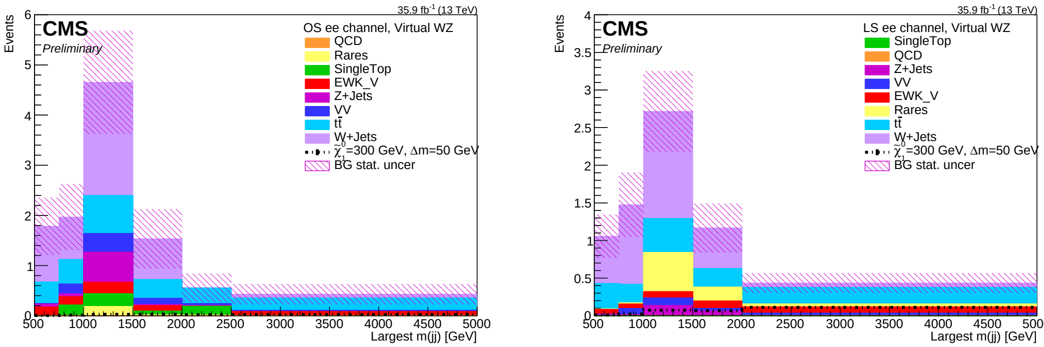

Figure 9.6: 2016 largest dijet mass for the *ee* channel (left, OS; right, LS) with overlaid signal mass point of $m(\tilde{\chi}_2^0) = 300$ GeV, $\Delta M = 50$ GeV from the Wino-Bino Virtual WZ scenario.

2017 VBF2 *ee* (OS) channel				
Sample	$N_{\text{Process}}^{\text{MC/Data}}$(SR/CR)	SF^{CR1} or TF_1	SF^{CR2} or TF_2	$N_{\text{Process}}^{\text{Predicted}}$
Z+Jets	0.1 ± 0.1	0.926 ± 0.001	1.025 ± 0.007	0.1 ± 0.1
W+Jets	3.1 ± 1.1	0.919 ± 0.009	1.004 ± 0.052	2.9 ± 1.1
EWK V	0.7 ± 0.4	—	—	0.7 ± 0.4
Rares	0.3 ± 0.2	—	—	0.3 ± 0.2
Diboson	0.7 ± 0.3	0.97 ± 0.064	1.17 ± 0.17	0.8 ± 0.3
$t\bar{t}$	2.0 ± 0.4	0.96 ± 0.08	0.71 ± 0.2	1.4 ± 0.5
SingleTop	0.3 ± 0.1	—	—	0.3 ± 0.1
QCD	0.0 ± 0.0	—	—	0.0 ± 0.0
SR BG Prediction	7.2 ± 1.3	—	—	6.4 ± 1.3
$m(\tilde{\chi}_1^{\pm}), m(\tilde{\chi}_2^0), m(\tilde{\chi}_1^0) = 300, 300, 295$ GeV	—	—	—	0.0 ± 0.0
$m(\tilde{\chi}_1^{\pm}), m(\tilde{\chi}_2^0), m(\tilde{\chi}_1^0) = 300, 300, 270$ GeV	—	—	—	0.0 ± 0.0
$m(\tilde{\chi}_1^{\pm}), m(\tilde{\chi}_2^0), m(\tilde{\chi}_1^0) = 300, 300, 250$ GeV	—	—	—	0.1 ± 0.0
$m(\tilde{\chi}_1^{\pm}), m(\tilde{\tau}), m(\tilde{\chi}_1^0) = 300, 297.5, 295$ GeV	—	—	—	0.1 ± 0.0
$m(\tilde{\chi}_1^{\pm}), m(\tilde{\tau}), m(\tilde{\chi}_1^0) = 300, 285, 270$ GeV	—	—	—	0.2 ± 0.0
$m(\tilde{\chi}_1^{\pm}), m(\tilde{\tau}), m(\tilde{\chi}_1^0) = 300, 275, 250$ GeV	—	—	—	0.0 ± 0.0
Data	Unblinded	—	—	—

Table 9.9: Predicted and observed rates in the signal region for 2017 VBF2 *ee* (OS) channel.

2017 VBF2 *ee* (LS) channel				
Sample	$N_{\text{Process}}^{\text{MC/Data}}$(SR/CR)	SF^{CR1} or TF_1	SF^{CR2} or TF_2	$N_{\text{Process}}^{\text{Predicted}}$
Z+Jets	0.2 ± 0.1	0.926 ± 0.001	1.025 ± 0.007	0.2 ± 0.1
W+Jets	5.8 ± 1.4	0.919 ± 0.009	1.004 ± 0.052	5.3 ± 1.3
EWK V	0.6 ± 0.2	—	—	0.6 ± 0.2
Rares	0.5 ± 0.2	—	—	0.5 ± 0.2
Diboson	0.2 ± 0.1	0.97 ± 0.064	1.17 ± 0.17	0.2 ± 0.1
$t\bar{t}$	1.8 ± 0.3	0.96 ± 0.08	0.71 ± 0.2	1.2 ± 0.4
SingleTop	0.1 ± 0.0	—	—	0.1 ± 0.0
QCD	0.1 ± 0.1	—	—	0.1 ± 0.1
SR BG Prediction	9.3 ± 1.5	—	—	8.3 ± 1.4
$m(\tilde{\chi}_1^{\pm}), m(\tilde{\chi}_2^0), m(\tilde{\chi}_1^0) = 300, 300, 295$ GeV	—	—	—	0.0 ± 0.0
$m(\tilde{\chi}_1^{\pm}), m(\tilde{\chi}_2^0), m(\tilde{\chi}_1^0) = 300, 300, 270$ GeV	—	—	—	0.1 ± 0.0
$m(\tilde{\chi}_1^{\pm}), m(\tilde{\chi}_2^0), m(\tilde{\chi}_1^0) = 300, 300, 250$ GeV	—	—	—	0.0 ± 0.0
$m(\tilde{\chi}_1^{\pm}), m(\tilde{\tau}), m(\tilde{\chi}_1^0) = 300, 297.5, 295$ GeV	—	—	—	0.0 ± 0.0
$m(\tilde{\chi}_1^{\pm}), m(\tilde{\tau}), m(\tilde{\chi}_1^0) = 300, 285, 270$ GeV	—	—	—	0.0 ± 0.0
$m(\tilde{\chi}_1^{\pm}), m(\tilde{\tau}), m(\tilde{\chi}_1^0) = 300, 275, 250$ GeV	—	—	—	0.1 ± 0.0
Data	Unblinded	—	—	—

Table 9.10: Predicted and observed rates in the signal region for 2017 VBF2 *ee* (LS) channel.

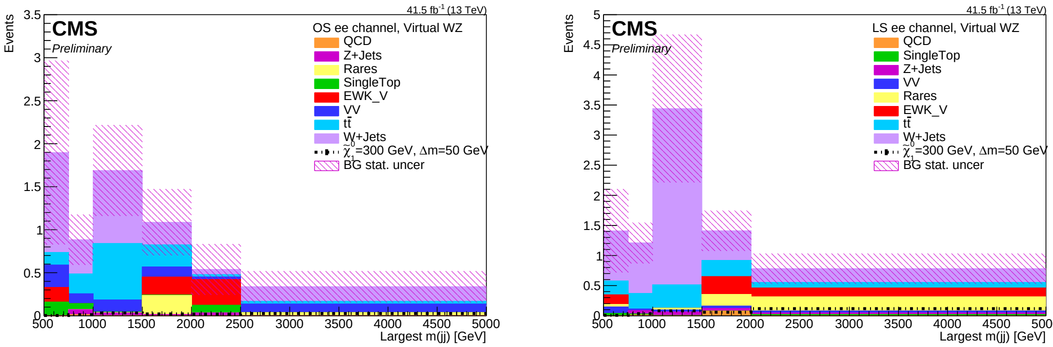

Figure 9.7: 2017 largest dijet mass for the *ee* channel (left, OS; right, LS) with overlaid signal mass point of $m(\tilde{\chi}_2^0)$ = 300 GeV, ΔM = 50 GeV from the Wino-Bino Virtual WZ scenario.

2018 VBF2 ee (OS) channel				
Sample	$N^{\text{MC/Data}}_{\text{Process}}$(SR/CR)	SF^{CR1} or TF_1	SF^{CR2} or TF_2	$N^{\text{Predicted}}_{\text{Process}}$
Z+Jets	0.7 ± 0.3	0.904 ± 0.001	0.966 ± 0.006	0.6 ± 0.3
W+Jets	5.8 ± 1.9	0.885 ± 0.007	0.982 ± 0.033	5.0 ± 1.7
EWK V	1.4 ± 0.8	—	—	1.4 ± 0.8
Rares	0.1 ± 0.1	—	—	0.1 ± 0.1
Diboson	1.5 ± 0.5	0.972 ± 0.056	1.19 ± 0.15	1.7 ± 0.6
$t\bar{t}$	4.6 ± 0.6	0.97 ± 0.06	0.73 ± 0.17	3.3 ± 0.9
SingleTop	0.2 ± 0.1	—	—	0.2 ± 0.1
QCD	0.0 ± 0.0	—	—	0.0 ± 0.0
SR BG Prediction	14.3 ± 2.3	—	—	12.3 ± 2.2
$m(\tilde{\chi}_1^{\pm}), m(\tilde{\chi}_2^0), m(\tilde{\chi}_1^0) = 300, 300, 295$ GeV	—	—	—	0.0 ± 0.0
$m(\tilde{\chi}_1^{\pm}), m(\tilde{\chi}_2^0), m(\tilde{\chi}_1^0) = 300, 300, 270$ GeV	—	—	—	0.1 ± 0.0
$m(\tilde{\chi}_1^{\pm}), m(\tilde{\chi}_2^0), m(\tilde{\chi}_1^0) = 300, 300, 250$ GeV	—	—	—	0.1 ± 0.0
$m(\tilde{\chi}_1^{\pm}), m(\tilde{\tau}), m(\tilde{\chi}_1^0) = 300, 297.5, 295$ GeV	—	—	—	0.1 ± 0.0
$m(\tilde{\chi}_1^{\pm}), m(\tilde{\tau}), m(\tilde{\chi}_1^0) = 300, 285, 270$ GeV	—	—	—	0.2 ± 0.0
$m(\tilde{\chi}_1^{\pm}), m(\tilde{\tau}), m(\tilde{\chi}_1^0) = 300, 275, 250$ GeV	—	—	—	0.0 ± 0.0
Data	Unblinded	—	—	—

Table 9.11: Predicted and observed rates in the signal region for 2018 VBF2 *ee* (OS) channel.

2018 VBF2 ee (LS) channel				
Sample	$N^{\text{MC/Data}}_{\text{Process}}$(SR/CR)	SF^{CR1} or TF_1	SF^{CR2} or TF_2	$N^{\text{Predicted}}_{\text{Process}}$
Z+Jets	0.2 ± 0.1	0.904 ± 0.001	0.966 ± 0.006	0.2 ± 0.1
W+Jets	6.0 ± 1.4	0.885 ± 0.007	0.982 ± 0.033	5.2 ± 1.2
EWK V	0.5 ± 0.2	—	—	0.5 ± 0.2
Rares	0.5 ± 0.3	—	—	0.5 ± 0.3
Diboson	0.2 ± 0.1	0.972 ± 0.056	1.19 ± 0.15	0.2 ± 0.1
$t\bar{t}$	2.6 ± 0.3	0.97 ± 0.06	0.73 ± 0.17	1.8 ± 0.5
SingleTop	0.2 ± 0.1	—	—	0.2 ± 0.1
QCD	0.1 ± 0.0	—	—	0.1 ± 0.0
SR BG Prediction	10.2 ± 1.4	—	—	8.7 ± 1.3
$m(\tilde{\chi}_1^{\pm}), m(\tilde{\chi}_2^0), m(\tilde{\chi}_1^0) = 300, 300, 295$ GeV	—	—	—	0.0 ± 0.0
$m(\tilde{\chi}_1^{\pm}), m(\tilde{\chi}_2^0), m(\tilde{\chi}_1^0) = 300, 300, 270$ GeV	—	—	—	0.0 ± 0.0
$m(\tilde{\chi}_1^{\pm}), m(\tilde{\chi}_2^0), m(\tilde{\chi}_1^0) = 300, 300, 250$ GeV	—	—	—	0.1 ± 0.0
$m(\tilde{\chi}_1^{\pm}), m(\tilde{\tau}), m(\tilde{\chi}_1^0) = 300, 297.5, 295$ GeV	—	—	—	0.1 ± 0.0
$m(\tilde{\chi}_1^{\pm}), m(\tilde{\tau}), m(\tilde{\chi}_1^0) = 300, 285, 270$ GeV	—	—	—	0.1 ± 0.0
$m(\tilde{\chi}_1^{\pm}), m(\tilde{\tau}), m(\tilde{\chi}_1^0) = 300, 275, 250$ GeV	—	—	—	0.1 ± 0.0
Data	Unblinded	—	—	—

Table 9.12: Predicted and observed rates in the signal region for 2018 VBF2 *ee* (LS) channel.

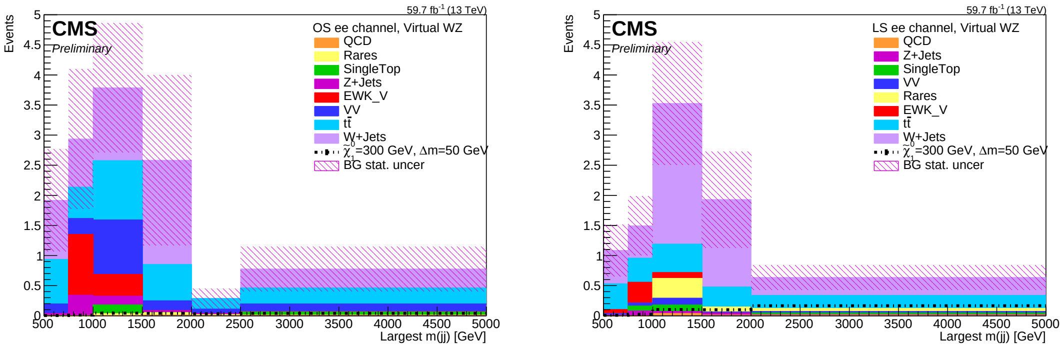

Figure 9.8: 2018 largest dijet mass for the *ee* channel (left, OS; right, LS) with overlaid signal mass point of $m(\tilde{\chi}_2^0)$ = 300 GeV, ΔM = 50 GeV from the Wino-Bino Virtual WZ scenario.

9.1.3 Muon-Electron Channel (OS & LS)

The results for the OS and LS electron-muon channels are shown in tables 9.13 through 9.18 with associated distributions for largest dijet mass in 2016, 2017, and 2018 shown in figures 9.9, 9.10, and 9.11, respectively. The expected yields within the electron-muon OS channel will be similar to the dimuon OS channel, with the exception that the Z+jets yield will be suppressed, and the W+jets yield may be slightly increased. This is due to the fact that Z+jets cannot create leptons of different flavor (thus suppressing it), and that a W+jets event which creates a real muon along with a jet which fakes an electron can pass the SR selections. An exception to this however is if a Z boson decays to two taus, which subsequently decay to an OS electron and muon. This process is also suppressed, as taus primarily decay hadronically, and when they do decay leptonically one must considered the combinatorics required to produce an $e\mu$ pair. These conclusions are further confirmed when inspecting the LS channels, which see a significant increase in the W+jets yields compared to the dimuon LS channel. This can be attributed to the "charge blindness" of jets faking leptons, meaning they can fake both positive charged leptons and negative charged leptons at equal rates. If a W+jets event produces a real muon, then a jet faking a lepton will just as readily be LS as OS.

2016 VBF2 $e\mu$ (OS) channel				
Sample	$N^{\text{MC/Data}}_{\text{Process}}$(SR/CR)	SF^{CR1} or TF_1	SF^{CR2} or TF_2	$N^{\text{Predicted}}_{\text{Process}}$
Z+Jets	2.2 ± 0.5	0.95 ± 0.001	1.181 ± 0.008	2.5 ± 0.6
W+Jets	7.9 ± 1.5	0.992 ± 0.01	1.065 ± 0.042	8.4 ± 1.6
EWK V	1.5 ± 0.5	—	—	1.5 ± 0.5
Rares	0.9 ± 0.4	—	—	0.9 ± 0.4
Diboson	6.3 ± 1.0	0.821 ± 0.056	1.01 ± 0.16	5.2 ± 1.2
$t\bar{t}$	15.7 ± 1.1	0.66 ± 0.07	1.09 ± 0.22	11.3 ± 2.7
SingleTop	2.0 ± 0.6	—	—	2.0 ± 0.6
QCD	0.0 ± 0.0	—	—	0.0 ± 0.0
SR BG Prediction	36.6 ± 2.3	—	—	31.8 ± 3.5
$m(\tilde{\chi}^{\pm}_1), m(\tilde{\chi}^0_2), m(\tilde{\chi}^0_1) = 300, 300, 295$ GeV	—	—	—	0.0 ± 0.0
$m(\tilde{\chi}^{\pm}_1), m(\tilde{\chi}^0_2), m(\tilde{\chi}^0_1) = 300, 300, 270$ GeV	—	—	—	0.3 ± 0.0
$m(\tilde{\chi}^{\pm}_1), m(\tilde{\chi}^0_2), m(\tilde{\chi}^0_1) = 300, 300, 250$ GeV	—	—	—	0.4 ± 0.0
$m(\tilde{\chi}^{\pm}_1), m(\tilde{\tau}), m(\tilde{\chi}^0_1) = 300, 297.5, 295$ GeV	—	—	—	0.4 ± 0.0
$m(\tilde{\chi}^{\pm}_1), m(\tilde{\tau}), m(\tilde{\chi}^0_1) = 300, 285, 270$ GeV	—	—	—	0.3 ± 0.0
$m(\tilde{\chi}^{\pm}_1), m(\tilde{\tau}), m(\tilde{\chi}^0_1) = 300, 275, 250$ GeV	—	—	—	0.1 ± 0.0
Data	Unblinded	—	—	—

Table 9.13: Predicted and observed rates in the signal region for 2016 VBF2 $e\mu$ (OS) channel.

2016 VBF2 $e\mu$ (LS) channel				
Sample	$N_{\text{Process}}^{\text{MC/Data}}$(SR/CR)	SF^{CR1} or TF_1	SF^{CR2} or TF_2	$N_{\text{Process}}^{\text{Predicted}}$
Z+Jets	0.3 ± 0.1	0.95 ± 0.001	1.181 ± 0.008	0.3 ± 0.1
W+Jets	12.5 ± 1.5	0.992 ± 0.01	1.065 ± 0.042	13.2 ± 1.7
EWK V	2.2 ± 0.4	—	—	2.2 ± 0.4
Rares	1.5 ± 0.4	—	—	1.5 ± 0.4
Diboson	1.3 ± 0.2	0.821 ± 0.056	1.01 ± 0.16	1.1 ± 0.2
$t\bar{t}$	7.0 ± 0.4	0.66 ± 0.07	1.09 ± 0.22	5.0 ± 1.2
SingleTop	1.2 ± 0.3	—	—	1.2 ± 0.3
QCD	0.1 ± 0.1	—	—	0.1 ± 0.1
SR BG Prediction	26.1 ± 1.7	—	—	24.6 ± 2.2
$m(\tilde{\chi}_1^{\pm}), m(\tilde{\chi}_2^0), m(\tilde{\chi}_1^0) =$ 300, 300, 295 GeV	—	—	—	0.0 ± 0.0
$m(\tilde{\chi}_1^{\pm}), m(\tilde{\chi}_2^0), m(\tilde{\chi}_1^0) =$ 300, 300, 270 GeV	—	—	—	0.2 ± 0.0
$m(\tilde{\chi}_1^{\pm}), m(\tilde{\chi}_2^0), m(\tilde{\chi}_1^0) =$ 300, 300, 250 GeV	—	—	—	0.2 ± 0.0
$m(\tilde{\chi}_1^{\pm}), m(\tilde{\tau}), m(\tilde{\chi}_1^0) =$ 300, 297.5, 295 GeV	—	—	—	0.2 ± 0.0
$m(\tilde{\chi}_1^{\pm}), m(\tilde{\tau}), m(\tilde{\chi}_1^0) =$ 300, 285, 270 GeV	—	—	—	0.2 ± 0.0
$m(\tilde{\chi}_1^{\pm}), m(\tilde{\tau}), m(\tilde{\chi}_1^0) =$ 300, 275, 250 GeV	—	—	—	0.0 ± 0.0
Data	Unblinded	—	—	—

Table 9.14: Predicted and observed rates in the signal region for 2016 VBF2 $e\mu$ (LS) channel.

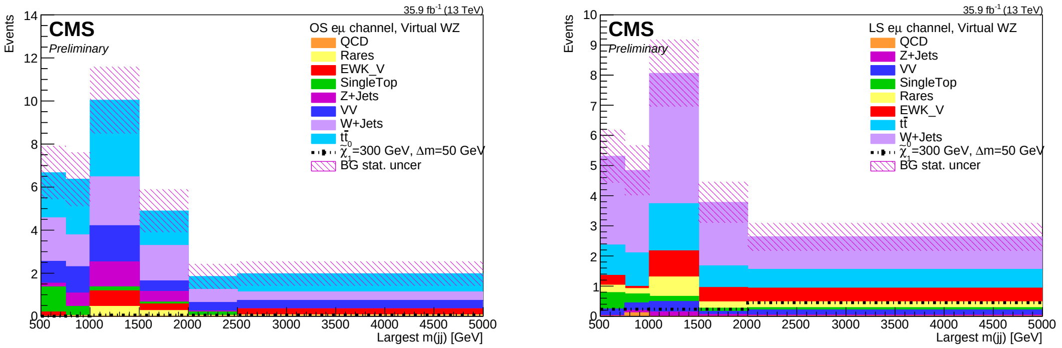

Figure 9.9: 2016 largest dijet mass for the $e\mu$ channel (left, OS; right, LS) with overlaid signal mass point of $m(\tilde{\chi}_2^0)$ = 300 GeV, ΔM = 50 GeV from the Wino-Bino Virtual WZ scenario.

2017 VBF2 $e\mu$ (OS) channel				
Sample	$N_{\text{Process}}^{\text{MC/Data}}$(SR/CR)	SF^{CR1} or TF_1	SF^{CR2} or TF_2	$N_{\text{Process}}^{\text{Predicted}}$
Z+Jets	2.6 ± 0.6	0.926 ± 0.001	1.025 ± 0.007	2.5 ± 0.5
W+Jets	12.1 ± 2.2	0.919 ± 0.009	1.004 ± 0.052	11.2 ± 2.1
EWK V	2.5 ± 0.8	—	—	2.5 ± 0.8
Rares	0.8 ± 0.3	—	—	0.8 ± 0.3
Diboson	3.5 ± 0.7	0.97 ± 0.064	1.17 ± 0.17	4.0 ± 1.0
$t\bar{t}$	14.8 ± 1.2	0.96 ± 0.08	0.71 ± 0.2	10.1 ± 3.1
SingleTop	0.6 ± 0.3	—	—	0.6 ± 0.3
QCD	0.0 ± 0.0	—	—	0.0 ± 0.0
SR BG Prediction	37.0 ± 2.8	—	—	31.7 ± 4.0
$m(\tilde{\chi}_1^\pm), m(\tilde{\chi}_2^0), m(\tilde{\chi}_1^0) = 300, 300, 295$ GeV	—	—	—	0.0 ± 0.0
$m(\tilde{\chi}_1^\pm), m(\tilde{\chi}_2^0), m(\tilde{\chi}_1^0) = 300, 300, 270$ GeV	—	—	—	0.3 ± 0.0
$m(\tilde{\chi}_1^\pm), m(\tilde{\chi}_2^0), m(\tilde{\chi}_1^0) = 300, 300, 250$ GeV	—	—	—	0.5 ± 0.0
$m(\tilde{\chi}_1^\pm), m(\tilde{\tau}), m(\tilde{\chi}_1^0) = 300, 297.5, 295$ GeV	—	—	—	0.5 ± 0.0
$m(\tilde{\chi}_1^\pm), m(\tilde{\tau}), m(\tilde{\chi}_1^0) = 300, 285, 270$ GeV	—	—	—	0.3 ± 0.0
$m(\tilde{\chi}_1^\pm), m(\tilde{\tau}), m(\tilde{\chi}_1^0) = 300, 275, 250$ GeV	—	—	—	0.1 ± 0.0
Data	Unblinded	—	—	—

Table 9.15: Predicted and observed rates in the signal region for 2017 VBF2 $e\mu$ (OS) channel.

2017 VBF2 $e\mu$ (LS) channel				
Sample	$N_{\text{Process}}^{\text{MC/Data}}$(SR/CR)	SF^{CR1} or TF_1	SF^{CR2} or TF_2	$N_{\text{Process}}^{\text{Predicted}}$
Z+Jets	0.7 ± 0.1	0.926 ± 0.001	1.025 ± 0.007	0.7 ± 0.1
W+Jets	14.4 ± 2.1	0.919 ± 0.009	1.004 ± 0.052	13.3 ± 2.0
EWK V	2.0 ± 0.5	—	—	2.0 ± 0.5
Rares	1.4 ± 0.4	—	—	1.4 ± 0.4
Diboson	1.5 ± 0.2	0.97 ± 0.064	1.17 ± 0.17	1.7 ± 0.4
$t\bar{t}$	6.0 ± 0.4	0.96 ± 0.08	0.71 ± 0.2	4.1 ± 1.2
SingleTop	0.6 ± 0.2	—	—	0.6 ± 0.2
QCD	0.2 ± 0.2	—	—	0.2 ± 0.2
SR BG Prediction	26.8 ± 2.2	—	—	23.9 ± 2.5
$m(\tilde{\chi}_1^\pm), m(\tilde{\chi}_2^0), m(\tilde{\chi}_1^0) = 300, 300, 295$ GeV	—	—	—	0.0 ± 0.0
$m(\tilde{\chi}_1^\pm), m(\tilde{\chi}_2^0), m(\tilde{\chi}_1^0) = 300, 300, 270$ GeV	—	—	—	0.1 ± 0.0
$m(\tilde{\chi}_1^\pm), m(\tilde{\chi}_2^0), m(\tilde{\chi}_1^0) = 300, 300, 250$ GeV	—	—	—	0.1 ± 0.0
$m(\tilde{\chi}_1^\pm), m(\tilde{\tau}), m(\tilde{\chi}_1^0) = 300, 297.5, 295$ GeV	—	—	—	0.1 ± 0.0
$m(\tilde{\chi}_1^\pm), m(\tilde{\tau}), m(\tilde{\chi}_1^0) = 300, 285, 270$ GeV	—	—	—	0.2 ± 0.0
$m(\tilde{\chi}_1^\pm), m(\tilde{\tau}), m(\tilde{\chi}_1^0) = 300, 275, 250$ GeV	—	—	—	0.0 ± 0.0
Data	Unblinded	—	—	—

Table 9.16: Predicted and observed rates in the signal region for 2017 VBF2 $e\mu$ (LS) channel.

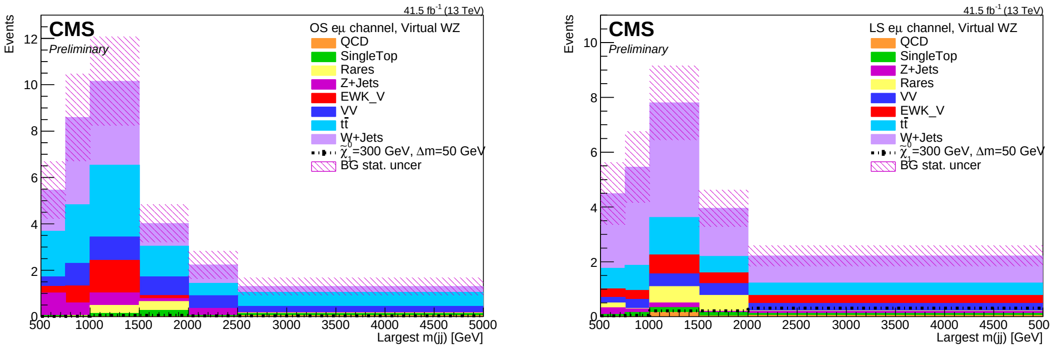

Figure 9.10: 2017 largest dijet mass for the $e\mu$ channel (left, OS; right, LS) with overlaid signal mass point of $m(\tilde{\chi}_2^0) = 300$ GeV, $\Delta M = 50$ GeV from the Wino-Bino Virtual WZ scenario.

2018 VBF2 $e\mu$ (OS) channel				
Sample	$N_{\text{Process}}^{\text{MC/Data}}$(SR/CR)	SF^{CR1} or TF_1	SF^{CR2} or TF_2	$N_{\text{Process}}^{\text{Predicted}}$
Z+Jets	3.8 ± 0.8	0.904 ± 0.001	0.966 ± 0.006	3.3 ± 0.7
W+Jets	15.5 ± 3.5	0.885 ± 0.007	0.982 ± 0.033	13.5 ± 3.0
EWK V	2.2 ± 0.9	—	—	2.2 ± 0.9
Rares	2.4 ± 0.8	—	—	2.4 ± 0.8
Diboson	4.9 ± 0.8	0.972 ± 0.056	1.19 ± 0.15	5.7 ± 1.2
$t\bar{t}$	19.3 ± 1.3	0.97 ± 0.06	0.73 ± 0.17	13.7 ± 3.4
SingleTop	2.0 ± 0.6	—	—	2.0 ± 0.6
QCD	0.3 ± 0.3	—	—	0.3 ± 0.3
SR BG Prediction	50.5 ± 4.1	—	—	43.1 ± 5.0
$m(\tilde{\chi}_1^{\pm}), m(\tilde{\chi}_2^0), m(\tilde{\chi}_1^0) = 300, 300, 295$ GeV	—	—	—	0.0 ± 0.0
$m(\tilde{\chi}_1^{\pm}), m(\tilde{\chi}_2^0), m(\tilde{\chi}_1^0) = 300, 300, 270$ GeV	—	—	—	0.5 ± 0.0
$m(\tilde{\chi}_1^{\pm}), m(\tilde{\chi}_2^0), m(\tilde{\chi}_1^0) = 300, 300, 250$ GeV	—	—	—	0.6 ± 0.1
$m(\tilde{\chi}_1^{\pm}), m(\tilde{\tau}), m(\tilde{\chi}_1^0) = 300, 297.5, 295$ GeV	—	—	—	0.6 ± 0.1
$m(\tilde{\chi}_1^{\pm}), m(\tilde{\tau}), m(\tilde{\chi}_1^0) = 300, 285, 270$ GeV	—	—	—	0.4 ± 0.0
$m(\tilde{\chi}_1^{\pm}), m(\tilde{\tau}), m(\tilde{\chi}_1^0) = 300, 275, 250$ GeV	—	—	—	0.1 ± 0.0
Data	Unblinded	—	—	—

Table 9.17: Predicted and observed rates in the signal region for 2018 VBF2 $e\mu$ (OS) channel.

2018 VBF2 $e\mu$ (LS) channel				
Sample	$N_{\text{Process}}^{\text{MC/Data}}$(SR/CR)	SF^{CR1} or TF_1	SF^{CR2} or TF_2	$N_{\text{Process}}^{\text{Predicted}}$
Z+Jets	1.6 ± 0.4	0.904 ± 0.001	0.966 ± 0.006	1.4 ± 0.4
W+Jets	21.7 ± 3.2	0.885 ± 0.007	0.982 ± 0.033	18.9 ± 2.9
EWK V	2.1 ± 0.6	—	—	2.1 ± 0.6
Rares	1.1 ± 0.3	—	—	1.1 ± 0.3
Diboson	2.7 ± 0.4	0.972 ± 0.056	1.19 ± 0.15	3.1 ± 0.6
$t\bar{t}$	9.0 ± 0.5	0.97 ± 0.06	0.73 ± 0.17	6.4 ± 1.6
SingleTop	0.9 ± 0.2	—	—	0.9 ± 0.2
QCD	1.3 ± 0.8	—	—	1.3 ± 0.8
SR BG Prediction	40.4 ± 3.5	—	—	35.2 ± 3.5
$m(\tilde{\chi}_1^{\pm}), m(\tilde{\chi}_2^0), m(\tilde{\chi}_1^0) = 300, 300, 295$ GeV	—	—	—	0.0 ± 0.0
$m(\tilde{\chi}_1^{\pm}), m(\tilde{\chi}_2^0), m(\tilde{\chi}_1^0) = 300, 300, 270$ GeV	—	—	—	0.2 ± 0.0
$m(\tilde{\chi}_1^{\pm}), m(\tilde{\chi}_2^0), m(\tilde{\chi}_1^0) = 300, 300, 250$ GeV	—	—	—	0.2 ± 0.0
$m(\tilde{\chi}_1^{\pm}), m(\tilde{\tau}), m(\tilde{\chi}_1^0) = 300, 297.5, 295$ GeV	—	—	—	0.2 ± 0.0
$m(\tilde{\chi}_1^{\pm}), m(\tilde{\tau}), m(\tilde{\chi}_1^0) = 300, 285, 270$ GeV	—	—	—	0.4 ± 0.0
$m(\tilde{\chi}_1^{\pm}), m(\tilde{\tau}), m(\tilde{\chi}_1^0) = 300, 275, 250$ GeV	—	—	—	0.1 ± 0.0
Data	Unblinded	—	—	—

Table 9.18: Predicted and observed rates in the signal region for 2018 VBF2 $e\mu$ (LS) channel.

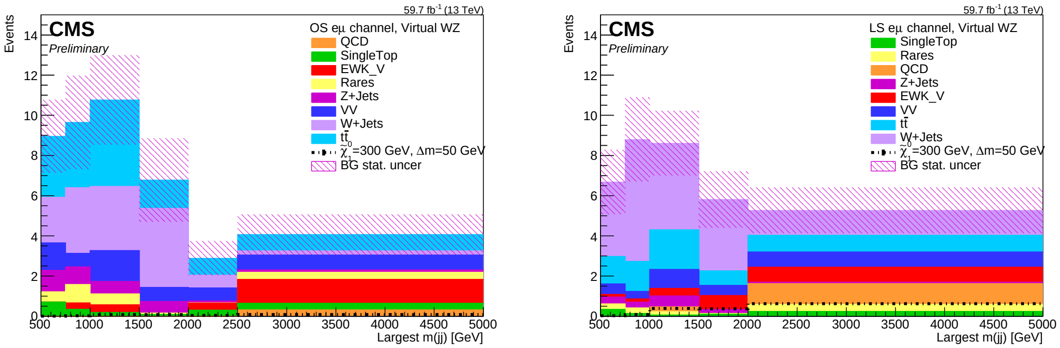

Figure 9.11: 2018 largest dijet mass for the $e\mu$ channel (left, OS; right, LS) with overlaid signal mass point of $m(\tilde{\chi}_2^0)$ = 300 GeV, ΔM = 50 GeV from the Wino-Bino Virtual WZ scenario.

9.2 Expected Upper Limits

The results presented here are 95% CL upper limits on the signal production cross section. This estimation was performed using the Modified Frequentist construction CL$_s$ method (see references [75, 76, 77]). Under this method, one defines the confidence level for excluding the possibility of both signal production and background production ($s+b$) as:

$$CL_{s+b} = P_{s+b}(X \leq X_{obs}). \tag{9.2}$$

In this case, $P_{s+b}(X \leq X_{obs})$ is a probability defined as:

$$P_{s+b}(X \leq X_{obs}) = \sum_{X(\{d_i'\}) \leq X(\{d_i\})} \prod_{i=1}^{n} \frac{e^{-(s_i+b_i)}(s_i+b_i)^{d_i'}}{d_i'!} \tag{9.3}$$

where i corresponds to individual channels (i.e. bins within a histogram, although these results can be, and will be, extended to combine actual final state channels), $X(\{d_i\})$ is a statistic corresponding to the actual observed data, or pseudo-data, in a bin, and the sum runs over all outcomes ($X(\{d_i'\})$) with yields less than $X(\{d_i\})$. This probability can then be seen to correspond to summing the likelihoods of observing specific outcomes, over all possible outcomes with events fewer than the number observed. One could simply define the confidence level then to be (1-CL_{s+b}), however this can lead to unphysical conclusions, such as excluding the background itself to high confidence levels. What is done to avoid this is to similarly define the confidence for the background alone as:

$$CL_b = P_b(X \leq X_{obs}). \tag{9.4}$$

Under the Modified Frequentist confidence level, CL_s is then ultimately computed as the ratio of these two values, such that:

$$CL_s = CL_{s+b}/CL_b. \tag{9.5}$$

The number of signal events is ultimately a function of the cross section (in addition to other factors such as luminosity and efficiency, however those are not relevant for this discussion). The upper limit on the production cross section is therefore the smallest cross section which can still be ruled out at 95% confidence level, given the null-hypothesis is true (i.e. no signal events are observed). As a reminder, in this study it is the largest dijet mass which is used as the discrimination variable, used to derive such expected upper limits. Systematic uncertainties are treated as nuisance parameters and are modeled with log normal distributions in the likelihood function.

Presented here are select plots for individual channels within the two main SUSY interpretations in this analysis, which are the $\tilde{\tau}$-dominated and virtual W/Z scenarios. This is followed by results combining the 0ℓ, 1ℓ, and 2ℓ channels. As a reminder, these scenarios are simplified models in which the branching fractions are set by hand. In the $\tilde{\tau}$-dominated model, these are set so that the branching fractions for $\tilde{\chi}_1^\pm \to \tilde{\tau}\nu_\tau$, $\tilde{\tau} \to \tilde{\chi}_1^0\tau$, and $\tilde{\chi}_2^0 \to \tilde{\tau}\tau$ are all 100%. In the virtual W/Z scenario, the branching fractions for $\tilde{\chi}_1^\pm \to \tilde{\chi}_1^0 W^\pm$ and $\tilde{\chi}_2^0 \to \tilde{\chi}_1^0 Z^0$ are each set to 100%.

9.2.1 Limits for Individual Channels

Figure 9.12 shows the expected upper limits on the cross section for the $\tilde{\tau}$-dominated scenario with Δm = 50 GeV for each individual channel (with OS and LS channels combined) as well as the three light lepton channels combined. It is observed that of the three light lepton channels, it is the dimuon channel which achieves the greatest sensitivity. This is due to the expected larger background and signal yields in this region, which increase at approximately equal rates. Not surprisingly however, it is the combination of the $1\ell + 2\ell$ channels, as seen in figure 9.13 which produces a better sensitivity. This is due to the previously mentioned branching fraction in this scenario which produces real taus in each event. Even a small cross section will produce many taus. Therefore by adding in the hadronic tau channels, the sensitivity is improved.

Figure 9.14 shows similar results for the virtual W/Z scenario with Δm = 30 GeV, when combining the 1ℓ channels (top left), the 2ℓ channels (top right), and then both of these channels together (bottom). It is interesting to note that the 2ℓ channels appear to perform better for this Δm value as compared to the 1ℓ channel. This is perhaps due to their comparable signal acceptance values, but larger number of channels being combined in total (twelve total for OS and LS in the 2ℓ channel, versus three in the 1ℓ channel). Figure 9.15 shows similar results but for the Δm = 5 GeV scenario, with results for the 0ℓ channel (left) and $1\ell + 2\ell$ channels combined (right). As expected, the 0ℓ channel performs significantly better, due to the very low reconstruction efficiencies for leptons of any flavor in this scenario.

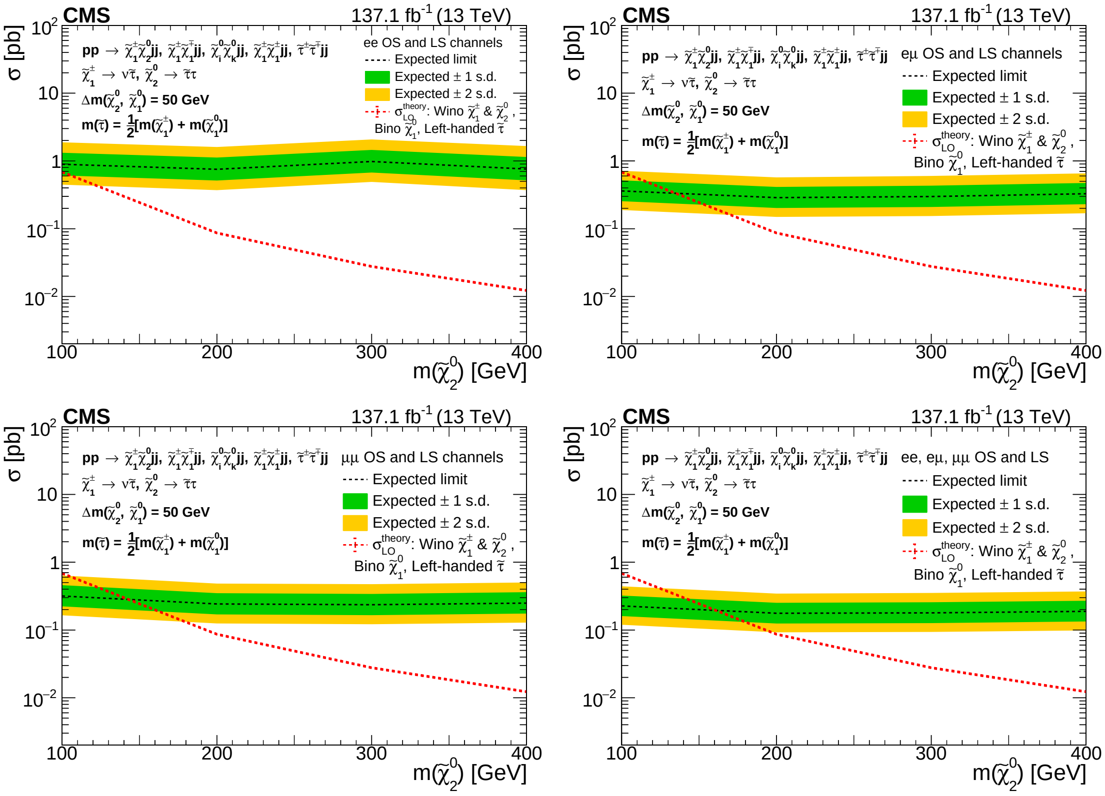

Figure 9.12: Predicted cross section upper limits for the $\tilde{\tau}$-dominated scenario with Δm = 50 GeV, showing the combined OS and LS ee channel (top left), combined OS and LS $e\mu$ channel (top right), combined OS and LS $\mu\mu$ channel (bottom left), and the three channels combined (bottom right).

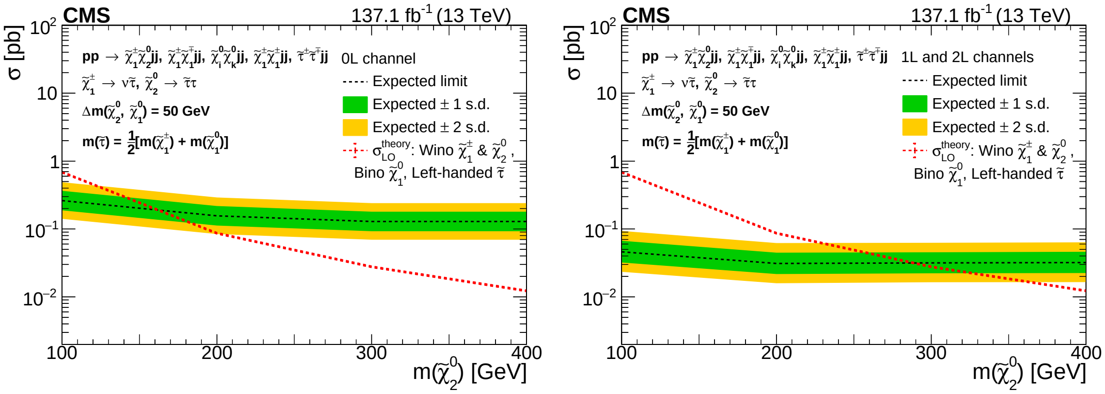

Figure 9.13: Predicted cross section upper limits for the $\tilde{\tau}$-dominated scenario with Δm = 50 GeV, showing the 0ℓ channel (left), and combined $1\ell + 2\ell$ channel (right).

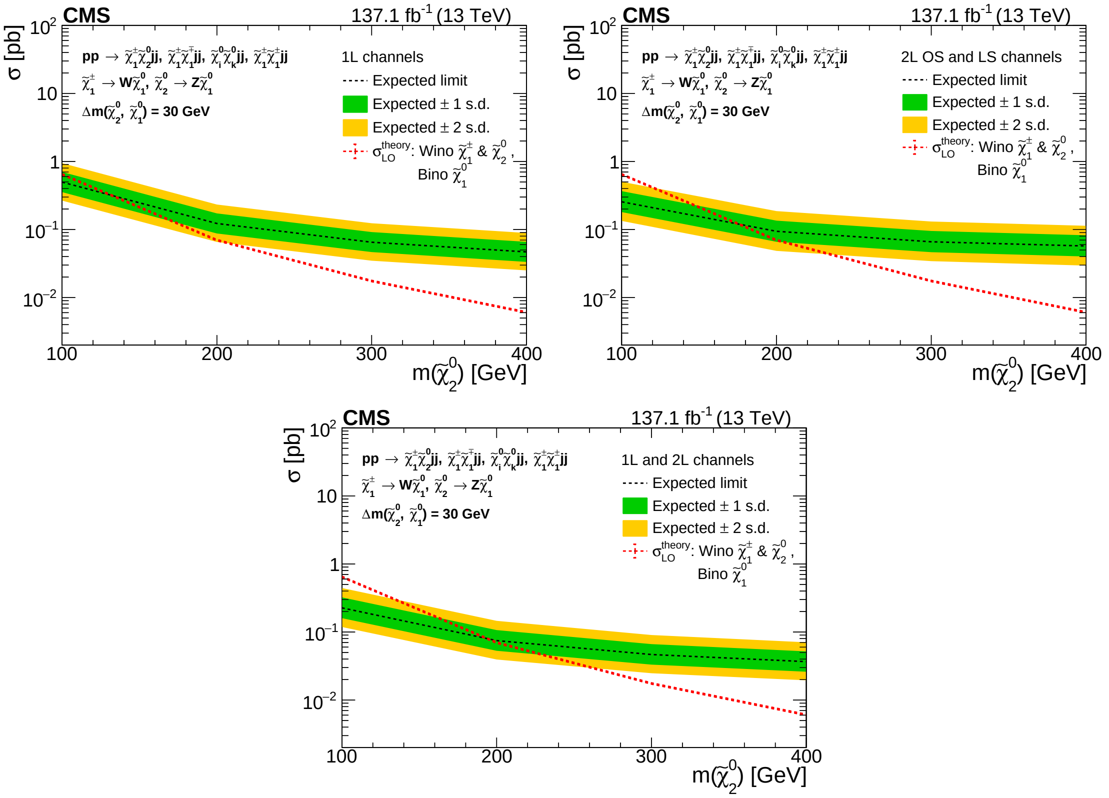

Figure 9.14: Predicted cross section upper limits for the virtual W/Z scenario with Δm = 30 GeV, showing the 1ℓ channel (top left), combined 2ℓ channels top (right), and combined $1\ell + 2\ell$ channels (bottom).

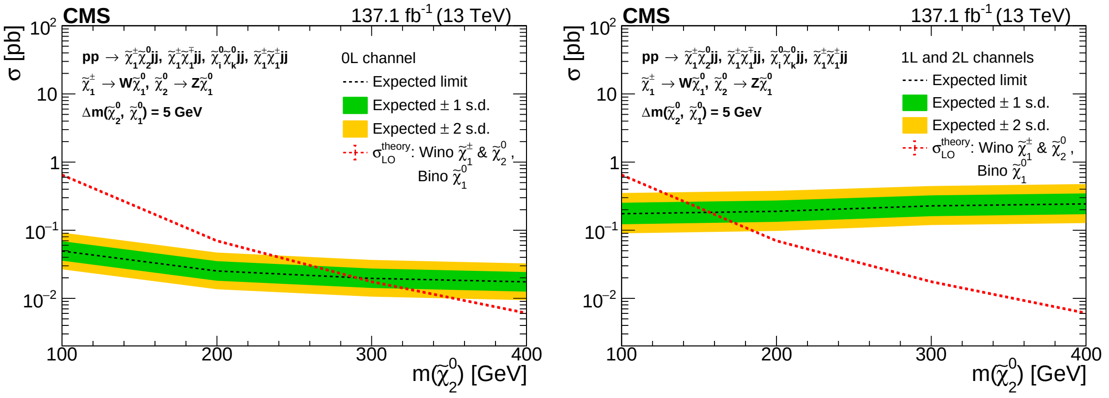

Figure 9.15: Predicted cross section upper limits for the virtual W/Z scenario with Δm = 5 GeV, showing the 0ℓ channel (left), and combined $1\ell + 2\ell$ channels (right).

9.2.2 Limits for Combined Channels

Figure 9.16 shows the expected upper limits results within the virtual W/Z scenario for two different mass gaps, Δm = 5 GeV (top left) and Δm = 30 GeV (top right), after combining the 0ℓ, 1ℓ, and 2ℓ channels together. These results are compared to the previous results of the ATLAS Collaboration (bottom left), and CMS Collaboration (bottom right). It is observed that this analysis expects to have sensitivity in the Δm = 5 GeV scenario to $\tilde{\chi}_2^0$ masses of approximately 300 GeV, which is a significant improvement over the current exclusion bounds of 250 GeV for both ATLAS and CMS. Likewise, in the Δm = 30 GeV scenario, this analysis expects sensitivity to $\tilde{\chi}_2^0$ masses of approximately 260 GeV, again a significant improvement over the current exclusion bounds of $\sim$ 160 GeV set by ATLAS, and $\sim$ 190 GeV set by CMS.

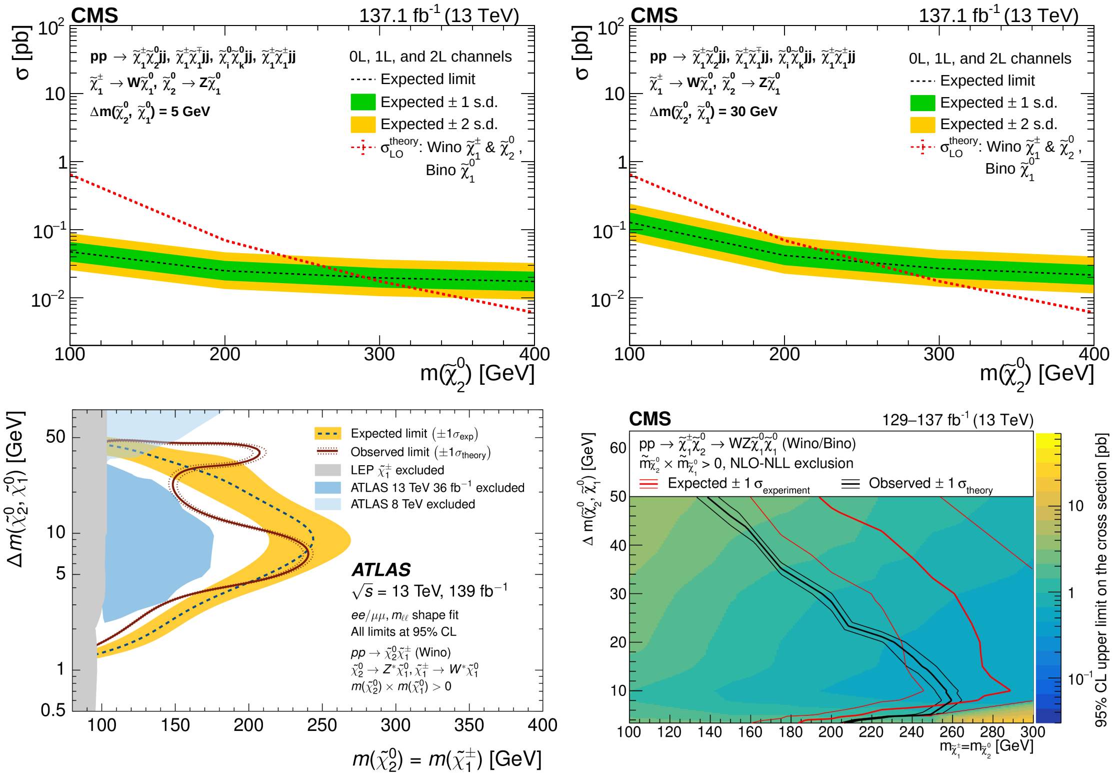

Figure 9.16: Predicted cross section upper limits for combined $0\ell + 1\ell + 2\ell$ channels in the virtual W/Z scenario with $\Delta m = 5$ GeV (top left), $\Delta m = 30$ GeV (top right). Similar results from the ATLAS Collaboration (bottom left) and CMS Collaboration (bottom right)[8, 9].

Figure 9.17 shows similar results for the $\tilde{\tau}$-dominated scenario for $\Delta m = 50$ GeV, again combining together the 0ℓ, 1ℓ, and 2ℓ channels (left). This is shown in comparison to the current exclusion bounds set by CMS for this same scenario and Δm value (right). It is observed that the expected $\tilde{\chi}_2^0$ mass bound for this study, 300 GeV, is slightly improved over the previous bound of 295 GeV. The cross section itself is significantly lowered, given that the previous study explored a different production mechanism [32].

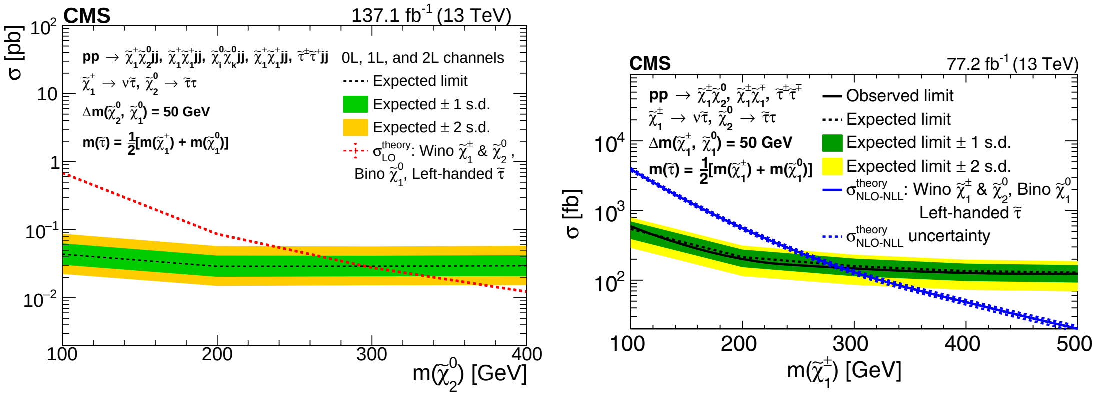

Figure 9.17: Predicted cross section upper limits for combined $0\ell + 1\ell + 2\ell$ channels in the $\tilde{\tau}$-dominated scenario with $\Delta m = 50$ GeV. [32].

9.3 Conclusions & Future Outlook

In conclusion, a search for new physics has been presented, using 137.1 fb^{-1} of proton-proton collision data recorded by the Compact Muon Solenoid (CMS) detector. This analysis seeks to probe compressed mass spectrum supersymmetry (SUSY), which is cosmologically motivated if one would like SUSY to account for the dark matter (DM) anomaly currently observed in the universe, which is believed to account for 85% of all matter. This search differs from traditional searches in that it attempts to use vector boson fusion (VBF) as a production mechanism. VBF is characterized by two high-p_T jets which are located in far-forward, opposite hemispheres of the detector. VBF processes are significantly more rare than other production mechanisms but have a unique detector signature which can simultaneously suppress background yields, as well as offer an efficient triggering mechanism. Monte Carlo simulated samples consisting of background processes and signal processes were generated for this study. It was observed that the kinematics in these samples agreed with the recorded data, and scale factors were derived in order to correct for any discrepancies in the total yields. Signal optimization was performed on key kinematic variables in order to ensure the highest reduction of background processes in the signal region (SR) as possible. Although the data remains blinded, it has already been demonstrated that this analysis will produce impactful results, by either providing evidence of new physics, or by pushing the exclusion limits on the production of electroweakinos for compressed mass spectrum scenarios to new bounds.

Appendix A

Appendix A

A.1 Mathematical Treatment of the Lorentz Group and the Poincaré Group

The Lorentz group is defined as the group of transformations which leave the scalar product of Minkowski spacetime invariant [78]. These consist of spacetime rotations and boosts. Let us denote the generator of rotations as J_i and the generator of boosts as K_i. A general Lorentz transformation can then be written as:

$$\Lambda = e^{i\vec{J}\cdot\vec{\theta}+i\vec{K}\cdot\vec{\Phi}} \tag{A.1}$$

The corresponding Lie algebra of these generators is as follows, where $[,]$ denotes the commutator of two objects given by $[x,y] = xy - yx$, and ε_{ijk} is the Levi-Civita symbol:

$$\begin{aligned} [J_i, J_j] &= i\varepsilon_{ijk}J_k \\ [J_i, K_j] &= i\varepsilon_{ijk}K_k \\ [K_i, K_j] &= -i\varepsilon_{ijk}J_k \end{aligned} \tag{A.2}$$

We see that the rotation generators J_i are closed under commutation, meaning the commutator of two rotation generators returns another rotation generator. The boost generators however are not closed under commutation. If we instead define a new set of generators in the following way:

$$\begin{aligned} N_i^+ &= \frac{1}{2}(J_i + iK_i) \\ N_i^- &= \frac{1}{2}(J_i - iK_i) \end{aligned} \tag{A.3}$$

then we get the following new commutation relations:

$$\begin{aligned} [N_i^+, N_j^+] &= i\varepsilon_{ijk}N_k^+ \\ [N_i^-, N_j^-] &= i\varepsilon_{ijk}N_k^- \\ [N_i^+, N_j^-] &= 0 \end{aligned} \tag{A.4}$$

We see that these two new generators close under commutation and that they both obey the Lie algebra of $SU(2)$. Indeed, we have just demonstrated that the Lorentz group can be decomposed into two independent copies of $SU(2)$. This decomposition allows us to further label particles according to their representations under the Lorentz group, with (0,0) being referred to as the spin-0 or “scalar representation”, ($\frac{1}{2}$,0) and (0,$\frac{1}{2}$) both being referred to as the spin-$\frac{1}{2}$ or “spinor representation” (one left handed, the other right handed), and ($\frac{1}{2}$,$\frac{1}{2}$) being referred to as the spin-1 or “vector representation”.

Let us now consider the Poincaré group, which consists of the Lorentz group transformations with the addition of spacetime translations. The generator for these spacetime translations will be denoted P_μ. We can then work out the commutation relations of the Poncaré algebra:

$$\begin{aligned}
[J_i, J_j] &= i\varepsilon_{ijk}J_k \\
[J_i, K_j] &= i\varepsilon_{ijk}K_k \\
[K_i, K_j] &= -i\varepsilon_{ijk}J_k \\
[J_i, P_j] &= i\varepsilon_{ijk}P_k \\
[J_i, P_0] &= 0 \\
[K_i, P_j] &= i\delta_{ij}P_0 \\
[K_i, P_0] &= -iP_i
\end{aligned} \tag{A.5}$$

We can shorten this by defining a new object $M_{\mu\nu}$ such that:

$$\begin{aligned}
J_i &= \frac{1}{2}\varepsilon_{ijk}(M_{jk}) \\
K_i &= M_{0i}
\end{aligned} \tag{A.6}$$

The Poincaré algebra may then be written as:

$$\begin{aligned}
[P_\mu, P_\nu] &= 0 \\
[M_{\mu\nu}, P_\rho] &= i(\eta_{\mu\rho}P_\nu - \eta_{\nu\rho}P_\mu) \\
[M_{\mu\nu}, M_{\rho\sigma}] &= i(\eta_{\mu\rho}M_{\nu\sigma} - \eta_{\mu\sigma}M_{\nu\rho} - \eta_{\nu\rho}M_{\mu\sigma} + \eta_{\nu\sigma}M_{\mu\rho})
\end{aligned} \tag{A.7}$$

where $\eta_{\mu\nu}$ is the Minkowski metric. From here we can form two Casimir elements which allow us to label the representations of the Poincaré group. The first is:

$$P_\mu P^\mu = m^2 \tag{A.8}$$

which is a continuous variable that we use to label the mass of the particle, and the second is $W_\mu W^\mu$ which is referred to as the “Pauli-Lubanksi four-vector” and is defined as:

$$W^{\mu} = \frac{1}{2}\varepsilon^{\mu\nu\rho\sigma}P_{\nu}M_{\rho\sigma} \tag{A.9}$$

which provides us with a discrete variable that we use to label the spin of the particle. This discussion is especially useful when looking to understand theories beyond the SM such as supersymmetry which attempts to expand the generators of the Poincaré group.

A.2 Mathematical Treatment of the SuperSymmetric Extension of the Poincaré Group

The supersymmetric extension of the Poincaré algebra, also known as the *Super-Poincaré* algebra, is as follows, where [,] again denotes the commutator, and {,} denots the anti-commutator:

$$\begin{aligned} [P_{\mu}, P_{\nu}] &= 0 \\ [M_{\mu\nu}, P_{\lambda}] &= i(g_{\nu\lambda}P_{\mu} - g_{\mu\lambda}P_{\nu}) \\ [M_{\mu\nu}, M_{\rho\sigma}] &= i(g_{\mu\rho}M_{\nu\sigma} - g_{\mu\sigma}M_{\nu\rho} - g_{\nu\rho}M_{\mu\sigma} + g_{\nu\sigma}M_{\mu\rho}) \\ [P_{\mu}, Q_a] &= 0 \\ [M_{\mu\nu}, Q_a] &= 1(\frac{1}{2}\sigma_{\mu\nu})_{ab}Q_b \\ \{Q_a, \bar{Q}_b\} &= 2(\gamma^{\mu})_{ab}P_{\mu} \end{aligned} \tag{A.10}$$

A.3 Mathematical Treatment of Vector Bosons

Mathematically, the vector bosons enter into the SM in a peculiar way. It was previously mentioned that each gauge group of the SM produces a conserved quantity, which is desirable given that conserved charges are readily observed in nature. Consider a “toy” Lagrangian of the form (which is sometimes referred to as “scalar QED”):

$$\mathscr{L} = \partial_{\mu}\phi^{\dagger}\partial^{\mu}\phi - m^2\phi^{\dagger}\phi \tag{A.11}$$

where ϕ is a complex scalar field. Now observe when one introduces a gauge transformation (for this example, a $U(1)$ gauge) of the form $e^{iq\alpha}$, where i is the imaginary number, q is a constant, and α is an arbitrary function that is local (i.e. α is a function of spacetime that is allowed to vary from point to point). ϕ now transforms as $\phi(x) \to \phi'(x) = e^{-iq\alpha(x)}\phi(x)$. Let us vary the Lagrangian in this way and observe what happens:

$$\begin{aligned}
\mathscr{L}' &= \partial_\mu \phi'^\dagger \partial^\mu \phi' - m^2 \phi'^\dagger \phi' \\
&= \partial_\mu (e^{-iq\alpha}\phi^\dagger)\partial^\mu (e^{-iq\alpha}\phi) - m^2 e^{-iq\alpha}\phi^\dagger e^{-iq\alpha}\phi \\
&= (iq\partial_\mu \alpha e^{iq\alpha}\phi^\dagger + e^{iq\alpha}\partial_\mu \phi^\dagger)(-iq\partial^\mu \alpha e^{iq\alpha}\phi + e^{iq\alpha}\partial^\mu \phi) - m^2\phi^\dagger\phi \\
&= q^2 \partial_\mu \alpha \partial^\mu \alpha \phi^* \phi + iq\partial_\mu \alpha \phi^\dagger \partial^\mu \phi - iq\partial_\mu \phi^\dagger \partial^\mu \alpha + \partial_\mu \phi^\dagger \partial^\mu \phi - m^2 \phi^\dagger \phi \\
&\neq \mathscr{L}
\end{aligned} \tag{A.12}$$

It is obvious that the Lagrangian is not invariant under this transformation. Consider however if one is to add a new vector field A_μ to the theory via the covariant derivative and the so-called "minimum coupling" prescription: $\partial_\mu \to D_\mu = \partial_\mu - iqA_\mu$, where A_μ transforms as $A_\mu \to A'_\mu = A_\mu + \partial_\mu \alpha$. Let us first compute how the covariant derivative acts on the scalar field ϕ as $\phi \to \phi'$:

$$\begin{aligned}
D_\mu \phi' &= [\partial_\mu + iqA'_\mu]e^{-iq\alpha}\phi \\
&= [\partial_\mu + iq(A_\mu + \partial_\mu \alpha)]e^{-iq\alpha}\phi \\
&= -iq\partial_\mu \alpha e^{iq\alpha}\phi + e^{-iq\alpha}\partial_\mu \phi + iqA_\mu e^{-iq\alpha}\phi + iq\partial_\mu \alpha e^{-iq\alpha}\phi \\
&= e^{-iq\alpha}\partial_\mu \phi + iqA_\mu e^{iq\alpha}\phi \\
&= e^{-iq\alpha}D_\mu \phi
\end{aligned} \tag{A.13}$$

We see that the covariant derivative commutes with the transformation of ϕ. Now let us see how this affects the transformation $\mathscr{L} \to \mathscr{L}'$:

$$\begin{aligned}
\mathscr{L} \to \mathscr{L}' &= (D_\mu \phi')^\dagger (D^\mu \phi') - m^2 \phi'^\dagger \phi' \\
&= (e^{-iq\alpha}D_\mu \phi)^\dagger (e^{-iq\alpha}D^\mu \phi) - m^2 \phi^\dagger \phi \\
&= D_\mu \phi^\dagger D^\mu \phi - m^2 \phi^\dagger \phi \\
&= \mathscr{L}
\end{aligned} \tag{A.14}$$

We find that by introducing a new vector field, we were able to ensure the gauge transformation was indeed a good symmetry of the Lagrangian. The power of this method is that by simply starting out with a scalar field (in the case of the SM, we would also need to consider spinor fields) and requiring a local gauge transformation, one is able to derive a conserved charge as well as particle interactions between the two fields. Consider however if we were to introduce a mass term for this vector field, which would be proportional to $\frac{m^2}{2}A_\mu A^\mu$. This additional term would again spoil the symmetry, implying that any new vector field which we introduce must be, similarly to the chiral fermions, massless. This is again at odds with nature however as there are experimentally observed massive bosons. The Higgs mechanism is able to resolve this dilemma, as explained in section 1.5.

A.4 Background Samples List

List of background simulation samples for 2016 in the NanoAODv6 data format and its corresponding cross sections in pb, where [*] = RunIISummer16NanoAODv6-PUMoriond17_Nano25Oct2019_102X_mcRun2_asymptotic_v7-v1

Process	Official CMS dataset	Cross section [pb]
$t\bar{t}$	/TTTo2L2Nu_TuneCP5_PSweights_13TeV-powheg-pythia8/[*]/NANOAODSIM	88.29
	/TTToSemiLeptonic_TuneCP5_PSweights_13TeV-powheg-pythia8/[*]/NANOAODSIM	377.96
	/TTToHadronic_TuneCP5_PSweights_13TeV-powheg-pythia8/[*]/NANOAODSIM	365.34
Single top	/ST_s-channel_4f_leptonDecays_13TeV-amcatnlo-pythia8_TuneCUETP8M1/[*]/NANOAODSIM	3.68
	/ST_t-channel_antitop_4f_inclusiveDecays_13TeV-powhegV2-madspin-pythia8_TuneCUETP8M1/[*]/NANOAODSIM	80.95
	/ST_t-channel_top_4f_inclusiveDecays_13TeV-powhegV2-madspin-pythia8_TuneCUETP8M1/[*]/NANOAODSIM	136.02
	/ST_tW_antitop_5f_inclusiveDecays_13TeV-powheg-pythia8_TuneCUETP8M1/[*]/NANOAODSIM	38.06
	/ST_tW_top_5f_inclusiveDecays_13TeV-powheg-pythia8_TuneCUETP8M1/[*]/NANOAODSIM	38.06
Z+jets H_T-incl.	/DYJetsToLL_M-10to50_TuneCUETP8M1_13TeV-madgraphMLM-pythia8/[*]/NANOAODSIM	18610.0 (NNLO)
	/DYJetsToLL_M-50_TuneCUETP8M1_13TeV-madgraphMLM-pythia8/[*]/NANOAODSIM	6025.2 (NLO)
Z+jets H_T-binned (5< $m(\ell\ell) \leq$ 50 GeV)	/DYJetsToLL_M-5to50_HT-100to200_TuneCUETP8M1_13TeV-madgraphMLM-pythia8/[*]/NANOAODSIM	224.2
	/DYJetsToLL_M-5to50_HT-200to400_TuneCUETP8M1_13TeV-madgraphMLM-pythia8/[*]/NANOAODSIM	37.2
	/DYJetsToLL_M-5to50_HT-400to600_TuneCUETP8M1_13TeV-madgraphMLM-pythia8/[*]/NANOAODSIM	3.581
	/DYJetsToLL_M-5to50_HT-600toInf_TuneCUETP8M1_13TeV-madgraphMLM-pythia8/[*]/NANOAODSIM	1.124
Z+jets H_T-binned ($m(\ell\ell) \geq$50 GeV)	/DYJetsToLL_M-50_HT-100to200_TuneCUETP8M1_13TeV-madgraphMLM-pythia8/[*]/NANOAODSIM	213.4
	/DYJetsToLL_M-50_HT-200to400_TuneCUETP8M1_13TeV-madgraphMLM-pythia8/[*]/NANOAODSIM	65.42
	/DYJetsToLL_M-50_HT-400to600_TuneCUETP8M1_13TeV-madgraphMLM-pythia8/[*]/NANOAODSIM	7.31
	/DYJetsToLL_M-50_HT-600to800_TuneCUETP8M1_13TeV-madgraphMLM-pythia8/[*]/NANOAODSIM	1.49
	/DYJetsToLL_M-50_HT-800to1200_TuneCUETP8M1_13TeV-madgraphMLM-pythia8/[*]/NANOAODSIM	0.661
	/DYJetsToLL_M-50_HT-1200to2500_TuneCUETP8M1_13TeV-madgraphMLM-pythia8/[*]/NANOAODSIM	0.119
	/DYJetsToLL_M-50_HT-2500toInf_TuneCUETP8M1_13TeV-madgraphMLM-pythia8/[*]/NANOAODSIM	0.0028
Diboson	/WWToLNuQQ_13TeV-powheg/[*]/NANOAODSIM	43.53
	/WWTo2L2Nu_13TeV-powheg/[*]/NANOAODSIM	10.48
	/WWTo4Q_13TeV-powheg/[*]/NANOAODSIM	51.723
	/GluGluWWTo2L2Nu_MCFM_13TeV/[*]/NANOAODSIM	0.5906
	/WpWpJJ_QCD_TuneCUETP8M1_13TeV-madgraph-pythia8/[*]/NANOAODSIM	0.02612
	/WWJJToLNuLNu_EWK_QCD_noTop-noHiggs_13TeV-madgraph-pythia8/[*]/NANOAODSIM	2.616
	/WZTo1L1Nu2Q_13TeV_amcatnloFXFX_madspin_pythia8/[*]/NANOAODSIM	10.73
	/WZTo1L3Nu_13TeV_amcatnloFXFX_madspin_pythia8/[*]/NANOAODSIM	3.054
	/WZTo2L2Q_13TeV_amcatnloFXFX_madspin_pythia8/[*]/NANOAODSIM	5.606
	/WZTo3LNu_TuneCUETP8M1_13TeV-powheg-pythia8/[*]/NANOAODSIM	4.43
	/ZZTo2L2Nu_13TeV_powheg_pythia8_ext1/[*]/NANOAODSIM	0.5644
	/ZZTo2L2Q_13TeV_powheg_pythia8/[*]/NANOAODSIM	3.222
	/ZZTo2Q2Nu_13TeV_powheg_pythia8/[*]/NANOAODSIM	4.033
	/ZZTo4L_13TeV_powheg_pythia8/[*]/NANOAODSIM	1.256
	/ZZTo4Q_13TeV_amcatnloFXFX_madspin_pythia8/[*]/NANOAODSIM	6.842
W+jets (H_T-incl.)	/WJetsToLNu_TuneCUETP8M1_13TeV-madgraphMLM-pythia8/[*]/NANOAODSIM	61334.0
W+jets (H_T-binned)	/WJetsToLNu_HT-100To200_TuneCUETP8M1_13TeV-madgraphMLM-pythia8/[*]/NANOAODSIM	1695.0
	/WJetsToLNu_HT-200To400_TuneCUETP8M1_13TeV-madgraphMLM-pythia8/[*]/NANOAODSIM	532.4
	/WJetsToLNu_HT-400To600_TuneCUETP8M1_13TeV-madgraphMLM-pythia8/[*]/NANOAODSIM	61.6
	/WJetsToLNu_HT-600To800_TuneCUETP8M1_13TeV-madgraphMLM-pythia8/[*]/NANOAODSIM	12.4
	/WJetsToLNu_HT-800To1200_TuneCUETP8M1_13TeV-madgraphMLM-pythia8/[*]/NANOAODSIM	5.77
	/WJetsToLNu_HT-1200To2500_TuneCUETP8M1_13TeV-madgraphMLM-pythia8/[*]/NANOAODSIM	1.023
	/WJetsToLNu_HT-2500ToInf_TuneCUETP8M1_13TeV-madgraphMLM-pythia8/[*]/NANOAODSIM	0.248
QCD (H_T-binned)	/QCD_HT50to100_TuneCUETP8M1_13TeV-madgraphMLM-pythia8/[*]/NANOAODSIM	246300000.0
	/QCD_HT100to200_TuneCUETP8M1_13TeV-madgraphMLM-pythia8/[*]/NANOAODSIM	27990000.0
	/QCD_HT200to300_TuneCUETP8M1_13TeV-madgraphMLM-pythia8/[*]/NANOAODSIM	1559000.0
	/QCD_HT300to500_TuneCUETP8M1_13TeV-madgraphMLM-pythia8/[*]/NANOAODSIM	351900.0
	/QCD_HT500to700_TuneCUETP8M1_13TeV-madgraphMLM-pythia8/[*]/NANOAODSIM	29070.0
	/QCD_HT700to1000_TuneCUETP8M1_13TeV-madgraphMLM-pythia8/[*]/NANOAODSIM	5962.0
	/QCD_HT1000to1500_TuneCUETP8M1_13TeV-madgraphMLM-pythia8/[*]/NANOAODSIM	1005.0
	/QCD_HT1500to2000_TuneCUETP8M1_13TeV-madgraphMLM-pythia8/[*]/NANOAODSIM	101.0
	/QCD_HT2000toInf_TuneCUETP8M1_13TeV-madgraphMLM-pythia8/[*]/NANOAODSIM	20.54

Table A.1: List of background simulation samples for 2016 in the NanoAODv6 data format.

List of background simulation samples for 2016 in the NanoAODv6 data format and its corresponding cross sections in pb, where [*] = RunIISummer16NanoAODv6-PUMoriond17_Nano25Oct2019_102X_mcRun2_asymptotic_v7-v1.

Process	Official CMS dataset	Cross section [pb]
QCD (Muon-enriched)	/QCD_Pt-15to20_MuEnrichedPt5_TuneCUETP8M1_13TeV_pythia8/[*]/NANOAODSIM	3819570.0
	/QCD_Pt-20to30_MuEnrichedPt5_TuneCUETP8M1_13TeV_pythia8/[*]/NANOAODSIM	2960198.4
	/QCD_Pt-30to50_MuEnrichedPt5_TuneCUETP8M1_13TeV_pythia8/[*]/NANOAODSIM	1652471.5
	/QCD_Pt-50to80_MuEnrichedPt5_TuneCUETP8M1_13TeV_pythia8/[*]/NANOAODSIM	437504.5
	/QCD_Pt-80to120_MuEnrichedPt5_TuneCUETP8M1_13TeV_pythia8/[*]/NANOAODSIM	106033.7
	/QCD_Pt-120to170_MuEnrichedPt5_TuneCUETP8M1_13TeV_pythia8/[*]/NANOAODSIM	25190.5
	/QCD_Pt-170to300_MuEnrichedPt5_TuneCUETP8M1_13TeV_pythia8/[*]/NANOAODSIM	8654.5
	/QCD_Pt-300to470_MuEnrichedPt5_TuneCUETP8M1_13TeV_pythia8/[*]/NANOAODSIM	797.4
	/QCD_Pt-470to600_MuEnrichedPt5_TuneCUETP8M1_13TeV_pythia8/[*]/NANOAODSIM	79.0
	/QCD_Pt-600to800_MuEnrichedPt5_TuneCUETP8M1_13TeV_pythia8/[*]/NANOAODSIM	25.1
	/QCD_Pt-800to1000_MuEnrichedPt5_TuneCUETP8M1_13TeV_pythia8/[*]/NANOAODSIM	4.7
	/QCD_Pt-1000toInf_MuEnrichedPt5_TuneCUETP8M1_13TeV_pythia8/[*]/NANOAODSIM	1.6
QCD (EM-enriched)	/QCD_Pt-20to30_EMEnriched_TuneCUETP8M1_13TeV_pythia8/[*]/NANOAODSIM	5352960.0
	/QCD_Pt-30to50_EMEnriched_TuneCUETP8M1_13TeV_pythia8/[*]/NANOAODSIM	9928000.0
	/QCD_Pt-50to80_EMEnriched_TuneCUETP8M1_13TeV_pythia8/[*]/NANOAODSIM	2890800.0
	/QCD_Pt-80to120_EMEnriched_TuneCUETP8M1_13TeV_pythia8/[*]/NANOAODSIM	350000.0
	/QCD_Pt-120to170_EMEnriched_TuneCUETP8M1_13TeV_pythia8/[*]/NANOAODSIM	629664.0
	/QCD_Pt-170to300_EMEnriched_TuneCUETP8M1_13TeV_pythia8/[*]/NANOAODSIM	18810.0
	/QCD_Pt-300toInf_EMEnriched_TuneCUETP8M1_13TeV_pythia8/[*]/NANOAODSIM	1350.0
VBS/VBF diboson	/WpWpJJ_EWK_TuneCUETP8M1_13TeV-madgraph-pythia8/[*]/NANOAODSIM	0.02695
	/WWJJToLNuLNu_EWK_noTop_13TeV-madgraph-pythia8/[*]/NANOAODSIM	0.3439
	/WLLJJ_WToLNu_EWK_TuneCUETP8M1_13TeV_madgraph-madspin-pythia8/[*]/NANOAODSIM	0.01762
	/ZZJJTo4L_EWK_13TeV-madgraph-pythia8/[*]/NANOAODSIM	0.0004454
	/ZZJJ_ZZTo2L2Nu_EWK_13TeV-madgraph-pythia8/[*]/NANOAODSIM	0.002971
WW/ZZ Double Parton Scattering	/WWTo2L2Nu_DoubleScattering_13TeV-pythia8/[*]/NANOAODSIM	0.170300
	/ZZTo4L_DoubleScattering_13TeV-pythia8/[*]/NANOAODSIM	0.929108
VBS/VBF W/Z+Jets	/EWKWPlus2Jets_WToLNu_M-50_13TeV-madgraph-pythia8/[*]/NANOAODSIM	25.81
	/EWKWMinus2Jets_WToLNu_M-50_13TeV-madgraph-pythia8/[*]/NANOAODSIM	20.35
	/EWKZ2Jets_ZToLL_M-50_13TeV-madgraph-pythia8/[*]/NANOAODSIM	3.997
	/EWKZ2Jets_ZToNuNu_13TeV-madgraph-pythia8/[*]/NANOAODSIM	10.04
Higgs	/GluGluHToZZTo4L_M125_13TeV_powheg2_JHUgenV6_pythia8/[*]/NANOAODSIM	0.0129763
	/VBF_HToZZTo4L_M125_13TeV_powheg2_JHUgenV6_pythia8/[*]/NANOAODSIM	0.0010102
	/WPlusH_HToMuMu_M125_13TeV_powheg_pythia8/[*]/NANOAODSIM	0.0001828
	/WMinusH_HToMuMu_M125_13TeV_powheg_pythia8/[*]/NANOAODSIM	0.001159
	/ZH_HToZZ_4LFilter_M125_13TeV_powheg2-minlo-HZJ_JHUgenV6_pythia8/[*]/NANOAODSIM	0.002361
	/ttH_HToZZ_4LFilter_M125_13TeV_powheg2_JHUgenV6_pythia8/[*]/NANOAODSIM	0.0001355
	/VBFHToBB_M-125_13TeV_powheg_pythia8/[*]/NANOAODSIM	2.183
	/GluGluHToBB_M125_13TeV_powheg_pythia8/[*]/NANOAODSIM	25.34
	/WplusH_HToBB_WToQQ_M125_13TeV_powheg_pythia8/[*]/NANOAODSIM	0.339
	/WminusH_HToBB_WToQQ_M125_13TeV_powheg_pythia8/[*]/NANOAODSIM	0.199
	/ZH_HToBB_ZToQQ_M125_13TeV_powheg_pythia8/[*]/NANOAODSIM	0.311
	/ggZH_HToBB_ZToQQ_M125_13TeV_powheg_pythia8/[*]/NANOAODSIM	0.043
	/bbHToBB_M-125_4FS_yb2_13TeV_amcatnlo/[*]/NANOAODSIM	0.310
$t\bar{t}$+X	/TTWJetsToLNu_TuneCUETP8M1_13TeV-amcatnloFXFX-madspin-pythia8/[*]/NANOAODSIM	0.2043
	/TTWJetsToQQ_TuneCUETP8M1_13TeV-amcatnloFXFX-madspin-pythia8/[*]/NANOAODSIM	0.4062
	/TTZToLLNuNu_M-10_TuneCUETP8M1_13TeV-amcatnlo-pythia8/[*]/NANOAODSIM	0.2529
	/TTZToQQ_TuneCUETP8M1_13TeV-amcatnlo-pythia8/[*]/NANOAODSIM	0.5297
	/TTGJets_TuneCUETP8M1_13TeV-amcatnloFXFX-madspin-pythia8/[*]/NANOAODSIM	3.697
	/TTTT_TuneCUETP8M1_13TeV-amcatnlo-pythia8/[*]/NANOAODSIM	0.009
Vγ+jets	/WGJJToLNu_EWK_QCD_TuneCUETP8M1_13TeV-madgraph-pythia8/[*]/NANOAODSIM	5.664
	/LLAJJ_EWK_MLL-50_MJJ-120_13TeV-madgraph-pythia8/[*]/NANOAODSIM	0.1084
	/LNuAJJ_EWK_MJJ-120_TuneCUETP8M1_13TeV-madgraph-pythia8/[*]/NANOAODSIM	0.776
	/ZGTo2LG_TuneCUETP8M1_13TeV-amcatnloFXFX-pythia8/[*]/NANOAODSIM	123.8
Triboson	/WWW_4F_TuneCUETP8M1_13TeV-amcatnlo-pythia8/[*]/NANOAODSIM	0.2086
	/WWZ_TuneCUETP8M1_13TeV-amcatnlo-pythia8/[*]/NANOAODSIM	0.16510
	/WZZ_TuneCUETP8M1_13TeV-amcatnlo-pythia8/[*]/NANOAODSIM	0.05565
	/ZZZ_TuneCUETP8M1_13TeV-amcatnlo-pythia8/[*]/NANOAODSIM	0.1398

Table A.2: List of background simulation samples for 2016 in the NanoAODv6 data format (cont.).

List of background simulation samples for 2017 in the NanoAODv6 data format and its corresponding cross sections in pb, where [*] = RunIIFall17NanoAODv6-PU2017_12Apr2018_Nano25Oct2019_new_pmx_102X_mc2017_realistic_v7-v1, [**] = RunIIFall17NanoAODv6-PU2017_12Apr2018_Nano25Oct2019_102X_mc2017_realistic_v7-v1, [***] = RunIIFall17NanoAODv6-PU2017RECOSIMstep_12Apr2018_Nano25Oct2019_102X_mc2017_realistic_v7-v1, [4*] = RunIIFall17NanoAODv6-PU2017_12Apr2018_Nano25Oct2019_ext_102X_mc2017_realistic_v7-v1, [5*] = RunIIFall17NanoAODv6-PU2017_12Apr2018_Nano25Oct2019_102X_mc2017_realistic_v7-v2 and [6*] = RunIIFall17NanoAODv6-PU2017_12Apr2018_Nano25Oct2019_new_pmx_102X_mc2017_realistic_v7-v2.

Process	Official CMS dataset	Cross section [pb]
$t\bar{t}$	/TTTo2L2Nu_TuneCP5_PSweights_13TeV-powheg-pythia8/[*]/NANOAODSIM	88.29
	/TTToHadronic_TuneCP5_PSweights_13TeV-powheg-pythia8/[*]/NANOAODSIM	377.96
	/TTToSemiLeptonic_TuneCP5_PSweights_13TeV-powheg-pythia8/[**]/NANOAODSIM	365.34
Single top	/ST_t-channel_top_4f_InclusiveDecays_TuneCP5_PSweights_13TeV-powheg-pythia8/[**]/NANOAODSIM	3.68
	/ST_t-channel_antitop_4f_InclusiveDecays_TuneCP5_PSweights_13TeV-powheg-pythia8/[**]/NANOAODSIM	80.95
	/ST_tW_top_5f_inclusiveDecays_TuneCP5_13TeV-powheg-pythia8/[**]/NANOAODSIM	136.02
	/ST_tW_antitop_5f_inclusiveDecays_TuneCP5_13TeV-powheg-pythia8/[**]/NANOAODSIM	38.06
	/ST_s-channel_4f_leptonDecays_TuneCP5_PSweights_13TeV-amcatnlo-pythia8/[*]/NANOAODSIM	38.06
Z+Jets H$_T$-incl.	/DYJetsToLL_M-10to50_TuneCP5_13TeV-madgraphMLM-pythia8/[*]/NANOAODSIM	18610.0 (NNLO)
	/DYJetsToLL_M-50_TuneCP5_13TeV-madgraphMLM-pythia8/[***]/NANOAODSIM	6025.6 (NLO)
Z+jets M-4To50 H$_T$-binned	/DYJetsToLL_M-4to50_HT-100to200_TuneCP5_13TeV-madgraphMLM-pythia8/[*]/NANOAODSIM	224.2
	/DYJetsToLL_M-4to50_HT-200to400_TuneCP5_13TeV-madgraphMLM-pythia8/[*]/NANOAODSIM	37.2
	/DYJetsToLL_M-4to50_HT-400to600_TuneCP5_13TeV-madgraphMLM-pythia8/[**]/NANOAODSIM	3.581
	/DYJetsToLL_M-4to50_HT-600toInf_TuneCP5_13TeV-madgraphMLM-pythia8/[**]/NANOAODSIM	1.124
Z+jets M-50 H$_T$-binned	/DYJetsToLL_M-50_HT-100to200_TuneCP5_13TeV-madgraphMLM-pythia8/[*]/NANOAODSIM	213.4
	/DYJetsToLL_M-50_HT-200to400_TuneCP5_13TeV-madgraphMLM-pythia8/[**]/NANOAODSIM	65.42
	/DYJetsToLL_M-50_HT-400to600_TuneCP5_13TeV-madgraphMLM-pythia8/[*]/NANOAODSIM	7.31
	/DYJetsToLL_M-50_HT-600to800_TuneCP5_13TeV-madgraphMLM-pythia8/[*]/NANOAODSIM	1.49
	/DYJetsToLL_M-50_HT-800to1200_TuneCP5_13TeV-madgraphMLM-pythia8/[*]/NANOAODSIM	0.661
	/DYJetsToLL_M-50_HT-1200to2500_TuneCP5_13TeV-madgraphMLM-pythia8/[**]/NANOAODSIM	0.119
	/DYJetsToLL_M-50_HT-2500toInf_TuneCP5_13TeV-madgraphMLM-pythia8/[*]/NANOAODSIM	0.0028
Diboson	/WWTo2L2Nu_NNPDF31_TuneCP5_PSweights_13TeV-powheg-pythia8/[**]/NANOAODSIM	10.48
	/WWTo4Q_NNPDF31_TuneCP5_PSweights_13TeV-powheg-pythia8/[**]/NANOAODSIM	51.723
	/WWToLNuQQ_NNPDF31_TuneCP5_PSweights_13TeV-powheg-pythia8/[**]/NANOAODSIM	43.53
	/GluGluToWWToENEN_13TeV_MCFM701_pythia8/[5*]/NANOAODSIM	0.0457
	/GluGluToWWToENMN_13TeV_MCFM701_pythia8/[**]/NANOAODSIM	0.0457
	/GluGluToWWToENTN_13TeV_MCFM701_pythia8/[**]/NANOAODSIM	0.0457
	/GluGluToWWToMNEN_13TeV_MCFM701_pythia8/[5*]/NANOAODSIM	0.0457
	/GluGluToWWToMNMN_13TeV_MCFM701_pythia8/[**]/NANOAODSIM	0.0457
	/GluGluToWWToMNTN_13TeV_MCFM701_pythia8/[**]/NANOAODSIM	0.0457
	/GluGluToWWToTNEN_13TeV_MCFM701_pythia8/[**]/NANOAODSIM	0.0457
	/GluGluToWWToTNMN_13TeV_MCFM701_pythia8/[**]/NANOAODSIM	0.0457
	/GluGluToWWToTNTN_13TeV_MCFM701_pythia8/[**]/NANOAODSIM	0.0457
	/WpWpJJ_QCD_TuneCP5_13TeV-madgraph-pythia8/[**]/NANOAODSIM	0.02615
	/WWJJToLNuLNu_EWK_QCD_noTop-noHiggs_TuneCP5_13TeV-madgraph-pythia8/[5*]/NANOAODSIM	2.616
	/WZTo1L1Nu2Q_13TeV_amcatnloFXFX_madspin_pythia8/[**]/NANOAODSIM	10.73
	/WZTo1L3Nu_13TeV_amcatnloFXFX_madspin_pythia8_v2/[**]/NANOAODSIM	3.054
	/WZTo2L2Q_13TeV_amcatnloFXFX_madspin_pythia8/[**]/NANOAODSIM	5.606
	/WZTo3LNu_13TeV-powheg-pythia8/[**]/NANOAODSIM	4.43
	/ZZTo2L2Nu_13TeV_powheg_pythia8/[**]/NANOAODSIM	0.5644
	/ZZTo2L2Q_13TeV_amcatnloFXFX_madspin_pythia8/[**]/NANOAODSIM	3.222
	/ZZTo2Q2Nu_TuneCP5_13TeV_amcatnloFXFX_madspin_pythia8/[**]/NANOAODSIM	4.033
	/ZZTo4L_13TeV_powheg_pythia8/[*]/NANOAODSIM	1.256
W+Jets H$_T$-incl.	/WJetsToLNu_TuneCP5_13TeV-madgraphMLM-pythia8/[**]/NANOAODSIM	61334.0 (NLO)
	/WJetsToLNu_TuneCP5_13TeV-madgraphMLM-pythia8/[4*]/NANOAODSIM	61334.0 (NLO)
W+Jets H$_T$-binned	/WJetsToLNu_HT-100To200_TuneCP5_13TeV-madgraphMLM-pythia8/[**]/NANOAODSIM	1695.0
	/WJetsToLNu_HT-200To400_TuneCP5_13TeV-madgraphMLM-pythia8/[**]/NANOAODSIM	532.4
	/WJetsToLNu_HT-400To600_TuneCP5_13TeV-madgraphMLM-pythia8/[**]/NANOAODSIM	61.6
	/WJetsToLNu_HT-600To800_TuneCP5_13TeV-madgraphMLM-pythia8/[**]/NANOAODSIM	12.4
	/WJetsToLNu_HT-800To1200_TuneCP5_13TeV-madgraphMLM-pythia8/[**]/NANOAODSIM	5.77
	/WJetsToLNu_HT-1200To2500_TuneCP5_13TeV-madgraphMLM-pythia8/[**]/NANOAODSIM	1.023
	/WJetsToLNu_HT-2500ToInf_TuneCP5_13TeV-madgraphMLM-pythia8/[**]/NANOAODSIM	0.0248
QCD H$_T$-binned	/QCD_HT50to100_TuneCP5_13TeV-madgraphMLM-pythia8/[**]/NANOAODSIM	246300000.0
	/QCD_HT100to200_TuneCP5_13TeV-madgraph-pythia8/[**]/NANOAODSIM	27990000.0
	/QCD_HT200to300_TuneCP5_13TeV-madgraph-pythia8/[*]/NANOAODSIM	1559000.0
	/QCD_HT300to500_TuneCP5_13TeV-madgraph-pythia8/[*]/NANOAODSIM	351900.0
	/QCD_HT500to700_TuneCP5_13TeV-madgraph-pythia8/[**]/NANOAODSIM	29070.0
	/QCD_HT700to1000_TuneCP5_13TeV-madgraph-pythia8/[*]/NANOAODSIM	5962.0
	/QCD_HT1000to1500_TuneCP5_13TeV-madgraph-pythia8/[*]/NANOAODSIM	1005.0
	/QCD_HT1500to2000_TuneCP5_13TeV-madgraph-pythia8/[**]/NANOAODSIM	101.8
	/QCD_HT2000toInf_TuneCP5_13TeV-madgraph-pythia8/[**]/NANOAODSIM	20.54

Table A.3: List of background simulation samples for 2017 in the NanoAODv6 data format.

List of background simulation samples for 2017 in the NanoAODv6 data format and its corresponding cross sections in pb, where [*] = RunIIFall17NanoAODv6-PU2017_12Apr2018_Nano25Oct2019_new_pmx_102X_mc2017_realistic_v7-v1, [**] = RunIIFall17NanoAODv6-PU2017_12Apr2018_Nano25Oct2019_102X_mc2017_realistic_v7-v1, [***] = RunIIFall17NanoAODv6-PU2017RECOSIMstep_12Apr2018_Nano25Oct2019_102X_mc2017_realistic_v7-v1, [4*] = RunIIFall17NanoAODv6-PU2017_12Apr2018_Nano25Oct2019_ext_102X_mc2017_realistic_v7-v1, [5*] = RunIIFall17NanoAODv6-PU2017_12Apr2018_Nano25Oct2019_102X_mc2017_realistic_v7-v2 and [6*] = RunIIFall17NanoAODv6-PU2017_12Apr2018_Nano25Oct2019_new_pmx_102X_mc2017_realistic_v7-v2.

Process	Official CMS dataset	Cross section [pb]
QCD Muon enriched	/QCD_Pt-15to20_MuEnrichedPt5_TuneCP5_13TeV_pythia8/[**]/NANOAODSIM	3819570.0
	/QCD_Pt-20to30_MuEnrichedPt5_TuneCP5_13TeV_pythia8/[**]/NANOAODSIM	2960198.4
	/QCD_Pt-30to50_MuEnrichedPt5_TuneCP5_13TeV_pythia8/[**]/NANOAODSIM	1652471.5
	/QCD_Pt-50to80_MuEnrichedPt5_TuneCP5_13TeV_pythia8/[**]/NANOAODSIM	437504.5
	/QCD_Pt-80to120_MuEnrichedPt5_TuneCP5_13TeV_pythia8/[**]/NANOAODSIM	106033.7
	/QCD_Pt-120to170_MuEnrichedPt5_TuneCP5_13TeV_pythia8/[**]/NANOAODSIM	25190.5
	/QCD_Pt-170to300_MuEnrichedPt5_TuneCP5_13TeV_pythia8/[**]/NANOAODSIM	8654.5
	/QCD_Pt-300to470_MuEnrichedPt5_TuneCP5_13TeV_pythia8/[**]/NANOAODSIM	797.4
	/QCD_Pt-470to600_MuEnrichedPt5_TuneCP5_13TeV_pythia8/[**]/NANOAODSIM	79.0
	/QCD_Pt-600to800_MuEnrichedPt5_TuneCP5_13TeV_pythia8/[**]/NANOAODSIM	25.1
	/QCD_Pt-800to1000_MuEnrichedPt5_TuneCP5_13TeV_pythia8/[**]/NANOAODSIM	4.7
	/QCD_Pt-1000toInf_MuEnrichedPt5_TuneCP5_13TeV_pythia8/[**]/NANOAODSIM	1.6
QCD EM Enriched	/QCD_Pt-15to20_EMEnriched_TuneCP5_13TeV_pythia8/[**]/NANOAODSIM	1327000.0
	/QCD_Pt-20to30_EMEnriched_TuneCP5_13TeV_pythia8/[**]/NANOAODSIM	5352960.0
	/QCD_Pt-30to50_EMEnriched_TuneCP5_13TeV_pythia8/[**]/NANOAODSIM	9928000.0
	/QCD_Pt-50to80_EMEnriched_TuneCP5_13TeV_pythia8/[**]/NANOAODSIM	2890800.0
	/QCD_Pt-80to120_EMEnriched_TuneCP5_13TeV_pythia8/[**]/NANOAODSIM	350000.0
	/QCD_Pt-120to170_EMEnriched_TuneCP5_13TeV_pythia8/[**]/NANOAODSIM	62964.0
	/QCD_Pt-170to300_EMEnriched_TuneCP5_13TeV_pythia8/[**]/NANOAODSIM	18810.0
	/QCD_Pt-300toInf_EMEnriched_TuneCP5_13TeV_pythia8/[**]/NANOAODSIM	1350.0
VBS/VBF Diboson	/WpWpJJ_EWK_TuneCP5_13TeV-madgraph-pythia8/[**]/NANOAODSIM	0.02696
	/WWJJToLNuLNu_EWK_noTop_TuneCP5_13TeV-madgraph-pythia8/[**]/NANOAODSIM	0.3452
	/WLLJJ_WToLNu_EWK_TuneCP5_13TeV_madgraph-madspin-pythia8/[**]/NANOAODSIM	0.01628
	/ZZJJTo4L_EWK_TuneCP5_13TeV-madgraph-pythia8/[**]/NANOAODSIM	0.00044
WW/ZZ Double Parton Scattering	/WWTo2L2Nu_DoubleScattering_13TeV-pythia8/[**]/NANOAODSIM	0.1703
	/ZZTo4L_TuneCP5_DoubleScattering_13TeV-pythia8/[**]/NANOAODSIM	0.929108
VBS/VBF W/Z+jets	/EWKWMinus2Jets_WToLNu_M-50_TuneCP5_13TeV-madgraph-pythia8/[*]/NANOAODSIM	23.24
	/EWKWPlus2Jets_WToLNu_M-50_TuneCP5_13TeV-madgraph-pythia8/[*]/NANOAODSIM	29.59
	/EWKZ2Jets_ZToLL_M-50_TuneCP5_13TeV-madgraph-pythia8/[*]/NANOAODSIM	4.321
	/EWKZ2Jets_ZToNuNu_TuneCP5_13TeV-madgraph-pythia8/[6*]/NANOAODSIM	10.66
Vγ+jets	/LLAJJ_EWK_MLL-50_MJJ-120_TuneCP5_13TeV-madgraph-pythia8/[**]/NANOAODSIM	0.1097
	/LNuAJJ_EWK_MJJ-120_TuneCP5_13TeV-madgraph-pythia8/[**]/NANOAODSIM	0.5345
	/WGJJToLNu_EWK_QCD_TuneCP5_13TeV-madgraph-pythia8/[**]/NANOAODSIM	5.05
	/ZGToLLG_01J_5f_TuneCP5_13TeV-amcatnloFXFX-pythia8/[**]/NANOAODSIM	50.43
Higgs	/VBF_HToZZTo4L_M125_13TeV_powheg2_JHUGenV7011_pythia8/[**]/NANOAODSIM	0.0010102
	/VBFHToBB_M-125_13TeV_powheg_pythia8_weightfix/[**]/NANOAODSIM	2.183
	/GluGluHToBB_M125_TuneCP5_13TeV-powheg-pythia8/[**]/NANOAODSIM	25.340
	/GluGluHToZZTo2L2Q_M125_13TeV_powheg2_JHUGenV7011_pythia8/[**]/NANOAODSIM	0.1618
	/GluGluHToZZTo4L_M125_13TeV_powheg2_JHUGenV7011_pythia8/[**]/NANOAODSIM	0.0129763
	/ZH_HToZZ_4LFilter_M125_13TeV_powheg2-minlo-HZJ_JHUGenV7011_pythia8/[**]/NANOAODSIM	0.0002361
	/ZH_HToBB_ZToLL_M125_13TeV_powheg_pythia8/[**]/NANOAODSIM	0.07523
	/ttH_HToZZ_4LFilter_M125_13TeV_powheg2_JHUGenV7011_pythia8/[**]/NANOAODSIM	0.0001355
$t\bar{t}$+X	/TTWJetsToLNu_TuneCP5_PSweights_13TeV-amcatnloFXFX-madspin-pythia8/[6*]/NANOAODSIM	0.2043
	/TTWJetsToQQ_TuneCP5_13TeV-amcatnloFXFX-madspin-pythia8/[**]/NANOAODSIM	0.4062
	/TTZToLLNuNu_M-10_TuneCP5_13TeV-amcatnlo-pythia8/[**]/NANOAODSIM	0.2529
	/TTZToQQ_TuneCP5_13TeV-amcatnlo-pythia8/[**]/NANOAODSIM	0.5297
	/TTGJets_TuneCP5_13TeV-amcatnloFXFX-madspin-pythia8/[*]/NANOAODSIM	3.697
	/TTTT_TuneCP5_13TeV-amcatnlo-pythia8/[**]/NANOAODSIM	0.009
Triboson	/WWW_4F_TuneCP5_13TeV-amcatnlo-pythia8/[**]/NANOAODSIM	0.2086
	/WWZ_4F_TuneCP5_13TeV-amcatnlo-pythia8/[**]/NANOAODSIM	0.1651
	/WZZ_TuneCP5_13TeV-amcatnlo-pythia8/[4*]/NANOAODSIM	0.05565
	/ZZZ_TuneCP5_13TeV-amcatnlo-pythia8/[4*]/NANOAODSIM	0.0139

Table A.4: List of background simulation samples for 2017 in the NanoAODv6 data format (cont.).

List of background simulation samples for 2018 in the NanoAODv6 data format and its corresponding cross sections in pb, where [*] = RunIIAutumn18NanoAODv6-Nano25Oct2019_102X_upgrade2018_realistic_v20-v1, [**] = RunIIAutumn18NanoAODv6-Nano25Oct2019_102X_upgrade2018_realistic_v20-v2, [***] = RunIIAutumn18NanoAODv6-Nano25Oct2019_102X_upgrade2018_realistic_v20-v3.

Process	Official CMS dataset	Cross section [pb]
$t\bar{t}$	/TTTo2L2Nu_TuneCP5_13TeV-powheg-pythia8/[*]/NANOAODSIM	88.29
	/TTToHadronic_TuneCP5_13TeV-powheg-pythia8/[***]/NANOAODSIM	377.96
	/TTToSemiLeptonic_TuneCP5_13TeV-powheg-pythia8/[*]/NANOAODSIM	365.34
Single top	/ST_s-channel_4f_leptonDecays_TuneCP5_13TeV-madgraph-pythia8/[*]/NANOAODSIM	3.68
	/ST_t-channel_antitop_4f_InclusiveDecays_TuneCP5_13TeV-powheg-madspin-pythia8/[*]/NANOAODSIM	80.95
	/ST_t-channel_top_4f_InclusiveDecays_TuneCP5_13TeV-powheg-madspin-pythia8/[*]/NANOAODSIM	136.02
	/ST_tW_antitop_5f_inclusiveDecays_TuneCP5_13TeV-powheg-pythia8/[*]/NANOAODSIM	38.06
	/ST_tW_top_5f_inclusiveDecays_TuneCP5_13TeV-powheg-pythia8/[*]/NANOAODSIM	38.06
Z+jets H_T-incl.	/DYJetsToLL_M-50_TuneCP5_13TeV-madgraphMLM-pythia8/[*]/NANOAODSIM	18610.0
	/DYJetsToLL_M-10to50_TuneCP5_13TeV-madgraphMLM-pythia8/[*]/NANOAODSIM	6025.2
Z+jets M-4to50 H_T-binned	/DYJetsToLL_M-4to50_HT-100to200_TuneCP5_PSweights_13TeV-madgraphMLM-pythia8/[*]/NANOAODSIM	224.2
	/DYJetsToLL_M-4to50_HT-200to400_TuneCP5_PSweights_13TeV-madgraphMLM-pythia8/[*]/NANOAODSIM	37.2
	/DYJetsToLL_M-4to50_HT-400to600_TuneCP5_PSweights_13TeV-madgraphMLM-pythia8/[*]/NANOAODSIM	3.581
	/DYJetsToLL_M-4to50_HT-600toInf_TuneCP5_PSWeights_13TeV-madgraphMLM-pythia8/[*]/NANOAODSIM	1.124
Z+jets M-50 H_T-binned	/DYJetsToLL_M-50_HT-100to200_TuneCP5_PSweights_13TeV-madgraphMLM-pythia8/[*]/NANOAODSIM	213.4
	/DYJetsToLL_M-50_HT-200to400_TuneCP5_PSweights_13TeV-madgraphMLM-pythia8/[*]/NANOAODSIM	65.42
	/DYJetsToLL_M-50_HT-400to600_TuneCP5_PSweights_13TeV-madgraphMLM-pythia8/[*]/NANOAODSIM	7.31
	/DYJetsToLL_M-50_HT-600to800_TuneCP5_PSweights_13TeV-madgraphMLM-pythia8/[*]/NANOAODSIM	1.49
	/DYJetsToLL_M-50_HT-800to1200_TuneCP5_PSweights_13TeV-madgraphMLM-pythia8/[*]/NANOAODSIM	0.661
	/DYJetsToLL_M-50_HT-1200to2500_TuneCP5_PSweights_13TeV-madgraphMLM-pythia8/[*]/NANOAODSIM	0.119
	/DYJetsToLL_M-50_HT-2500toInf_TuneCP5_PSweights_13TeV-madgraphMLM-pythia8/[*]/NANOAODSIM	0.0028
Diboson	/WWTo2L2Nu_NNPDF31_TuneCP5_13TeV-powheg-pythia8/[*]/NANOAODSIM	10.48
	/WWTo4Q_NNPDF31_TuneCP5_13TeV-powheg-pythia8/[*]/NANOAODSIM	51.723
	/WWToLNuQQ_NNPDF31_TuneCP5_13TeV-powheg-pythia8/[*]/NANOAODSIM	43.53
	/GluGluToWWToENEN_TuneCP5_13TeV_MCFM701_pythia8/[*]/NANOAODSIM	0.0457
	/GluGluToWWToENMN_TuneCP5_13TeV_MCFM701_pythia8/[*]/NANOAODSIM	0.0457
	/GluGluToWWToENTN_TuneCP5_13TeV_MCFM701_pythia8/[*]/NANOAODSIM	0.0457
	/GluGluToWWToMNEN_TuneCP5_13TeV_MCFM701_pythia8/[*]/NANOAODSIM	0.0457
	/GluGluToWWToMNMN_TuneCP5_13TeV_MCFM701_pythia8/[*]/NANOAODSIM	0.0457
	/GluGluToWWToMNTN_TuneCP5_13TeV_MCFM701_pythia8/[*]/NANOAODSIM	0.0457
	/GluGluToWWToTNEN_TuneCP5_13TeV_MCFM701_pythia8/[*]/NANOAODSIM	0.0457
	/GluGluToWWToTNMN_TuneCP5_13TeV_MCFM701_pythia8/[*]/NANOAODSIM	0.0457
	/GluGluToWWToTNTN_TuneCP5_13TeV_MCFM701_pythia8/[*]/NANOAODSIM	0.0457
	/WpWpJJ_QCD_TuneCP5_13TeV-madgraph-pythia8/[*]/NANOAODSIM	0.02615
	/WWJJToLNuLNu_QCD_noTop_13TeV-madgraph-pythia8/[*]/NANOAODSIM	0.02615
	/WWJJToLNuLNu_EWK_QCD_noTop-noHiggs_13TeV-madgraph-pythia8/[*]/NANOAODSIM	2.616
	/WZTo1L1Nu2Q_13TeV_amcatnloFXFX_madspin_pythia8/[*]/NANOAODSIM	10.73
	/WZTo1L3Nu_13TeV_amcatnloFXFX_madspin_pythia8/[*]/NANOAODSIM	3.054
	/WZTo2L2Q_13TeV_amcatnloFXFX_madspin_pythia8/[*]/NANOAODSIM	5.606
	/WZTo3LNu_TuneCP5_13TeV-powheg-pythia8/[*]/NANOAODSIM	4.43
	/ZZTo2L2Nu_TuneCP5_13TeV_powheg_pythia8/[*]/NANOAODSIM	0.5644
	/ZZTo2L2Q_13TeV_amcatnloFXFX_madspin_pythia8/[*]/NANOAODSIM	3.222
	/ZZTo2Q2Nu_TuneCP5_13TeV_amcatnloFXFX_madspin_pythia8/[*]/NANOAODSIM	4.033
	/ZZTo4L_13TeV_powheg_pythia8_TuneCP5/[*]/NANOAODSIM	1.256
	/ZZTo4L_TuneCP5_13TeV_powheg_pythia8/[*]/NANOAODSIM	1.256
W+jets H_T-incl.	/WJetsToLNu_TuneCP5_13TeV-madgraphMLM-pythia8/[*]/NANOAODSIM	61334.90
W+Jets H_T-binned	/WJetsToLNu_HT-100To200_TuneCP5_13TeV-madgraphMLM-pythia8/[*]/NANOAODSIM	1695.0
	/WJetsToLNu_HT-200To400_TuneCP5_13TeV-madgraphMLM-pythia8/[*]/NANOAODSIM	532.4
	/WJetsToLNu_HT-400To600_TuneCP5_13TeV-madgraphMLM-pythia8/[*]/NANOAODSIM	61.6
	/WJetsToLNu_HT-600To800_TuneCP5_13TeV-madgraphMLM-pythia8/[*]/NANOAODSIM	12.4
	/WJetsToLNu_HT-800To1200_TuneCP5_13TeV-madgraphMLM-pythia8/[*]/NANOAODSIM	5.77
	/WJetsToLNu_HT-1200To2500_TuneCP5_13TeV-madgraphMLM-pythia8/[*]/NANOAODSIM	1.023
	/WJetsToLNu_HT-2500ToInf_TuneCP5_13TeV-madgraphMLM-pythia8/[*]/NANOAODSIM	0.0248
QCD H_T-binned	/QCD_HT50to100_TuneCP5_13TeV-madgraphMLM-pythia8/[*]/NANOAODSIM	246300000.0
	/QCD_HT100to200_TuneCP5_13TeV-madgraphMLM-pythia8/[*]/NANOAODSIM	27990000.0
	/QCD_HT200to300_TuneCP5_13TeV-madgraphMLM-pythia8/[*]/NANOAODSIM	1559000.0
	/QCD_HT300to500_TuneCP5_13TeV-madgraphMLM-pythia8/[*]/NANOAODSIM	351900.0
	/QCD_HT500to700_TuneCP5_13TeV-madgraphMLM-pythia8/[*]/NANOAODSIM	29070.0
	/QCD_HT700to1000_TuneCP5_13TeV-madgraphMLM-pythia8/[*]/NANOAODSIM	5962.0
	/QCD_HT1000to1500_TuneCP5_13TeV-madgraphMLM-pythia8/[*]/NANOAODSIM	1005.0
	/QCD_HT1500to2000_TuneCP5_13TeV-madgraphMLM-pythia8/[*]/NANOAODSIM	101.0
	/QCD_HT2000toInf_TuneCP5_13TeV-madgraphMLM-pythia8/[*]/NANOAODSIM	20.54

Table A.5: List of background simulation samples for 2018 in the NanoAODv6 data format.

List of background simulation samples for 2018 in the NanoAODv6 data format and its corresponding cross sections in pb, where [*] = RunIIAutumn18NanoAODv6-Nano25Oct2019_102X_upgrade2018_realistic_v20-v1, [**] = RunIIAutumn18NanoAODv6-Nano25Oct2019_102X_upgrade2018_realistic_v20-v2, [***] = RunIIAutumn18NanoAODv6-Nano25Oct2019_102X_upgrade2018_realistic_v20-v3.

Process	Official CMS dataset	Cross section [pb]
QCD Muon enriched	/QCD_Pt-15to20_MuEnrichedPt5_TuneCP5_13TeV_pythia8/[*]/NANOAODSIM	3819570.0
	/QCD_Pt-20to30_MuEnrichedPt5_TuneCP5_13TeV_pythia8/[*]/NANOAODSIM	2960198.4
	/QCD_Pt-30to50_MuEnrichedPt5_TuneCP5_13TeV_pythia8/[*]/NANOAODSIM	1652471.5
	/QCD_Pt-50to80_MuEnrichedPt5_TuneCP5_13TeV_pythia8/[*]/NANOAODSIM	437504.5
	/QCD_Pt-80to120_MuEnrichedPt5_TuneCP5_13TeV_pythia8/[*]/NANOAODSIM	106033.7
	/QCD_Pt-120to170_MuEnrichedPt5_TuneCP5_13TeV_pythia8/[*]/NANOAODSIM	25190.5
	/QCD_Pt-170to300_MuEnrichedPt5_TuneCP5_13TeV_pythia8/[*]/NANOAODSIM	8654.5
	/QCD_Pt-300to470_MuEnrichedPt5_TuneCP5_13TeV_pythia8/[*]/NANOAODSIM	797.4
	/QCD_Pt-470to600_MuEnrichedPt5_TuneCP5_13TeV_pythia8/[*]/NANOAODSIM	79.0
	/QCD_Pt-600to800_MuEnrichedPt5_TuneCP5_13TeV_pythia8/[*]/NANOAODSIM	25.1
	/QCD_Pt-800to1000_MuEnrichedPt5_TuneCP5_13TeV_pythia8/[*]/NANOAODSIM	4.7
	/QCD_Pt-1000toInf_MuEnrichedPt5_TuneCP5_13TeV_pythia8/[*]/NANOAODSIM	1.6
QCD EM Enriched	/QCD_Pt-15to20_EMEnriched_TuneCP5_13TeV_pythia8/[*]/NANOAODSIM	1327000.0
	/QCD_Pt-20to30_EMEnriched_TuneCP5_13TeV_pythia8/[*]/NANOAODSIM	5352960.0
	/QCD_Pt-30to50_EMEnriched_TuneCP5_13TeV_pythia8/[*]/NANOAODSIM	99280000.0
	/QCD_Pt-50to80_EMEnriched_TuneCP5_13TeV_pythia8/[*]/NANOAODSIM	2890800.0
	/QCD_Pt-80to120_EMEnriched_TuneCP5_13TeV_pythia8/[*]/NANOAODSIM	350000.0
	/QCD_Pt-120to170_EMEnriched_TuneCP5_13TeV_pythia8/[*]/NANOAODSIM	62964.0
	/QCD_Pt-170to300_EMEnriched_TuneCP5_13TeV_pythia8/[*]/NANOAODSIM	18810.0
	/QCD_Pt-300toInf_EMEnriched_TuneCP5_13TeV_pythia8/[*]/NANOAODSIM	1350.0
VBS/VBF Diboson	/WpWpJJ_EWK_TuneCP5_13TeV-madgraph-pythia8/[*]/NANOAODSIM	0.02696
	/WWJJToLNuLNu_EWK_noTop_13TeV-madgraph-pythia8/[*]/NANOAODSIM	0.3452
	/WLLJJ_WToLNu_EWK_TuneCP5_13TeV_madgraph-madspin-pythia8/[*]/NANOAODSIM	0.01628
	/ZZJJTo4L_EWK_TuneCP5_13TeV-madgraph-pythia8/[*]/NANOAODSIM	0.00044
WW/ZZ Double Parton Scattering	/WWTo2L2Nu_DoubleScattering_13TeV-pythia8/[*]/NANOAODSIM	0.1703
	/ZZTo4L_TuneCP5_DoubleScattering_13TeV-pythia8/[**]/NANOAODSIM	0.929108
Vγ+jets	/LLAJJ_EWK_MLL-50_MJJ-120_TuneCP5_13TeV-madgraph-pythia8/[*]/NANOAODSIM	0.1097
	/LNuAJJ_EWK_MJJ-120_TuneCP5_13TeV-madgraph-pythia8/[*]/NANOAODSIM	0.5345
	/ZGToLLG_01J_5f_TuneCP5_13TeV-amcatnloFXFX-pythia8/[*]/NANOAODSIM	50.43
	/WGJJToLNu_EWK_QCD_TuneCP5_13TeV-madgraph-pythia8/[*]/NANOAODSIM	5.05
VBS/VBF W/Z+jets	/EWKWMinus2Jets_WToLNu_M-50_TuneCP5_13TeV-madgraph-pythia8/[*]/NANOAODSIM	23.24
	/EWKWPlus2Jets_WToLNu_M-50_TuneCP5_13TeV-madgraph-pythia8/[*]/NANOAODSIM	29.59
	/EWKZ2Jets_ZToLL_M-50_TuneCP5_PSweights_13TeV-madgraph-pythia8/[*]/NANOAODSIM	4.321
	/EWKZ2Jets_ZToNuNu_TuneCP5_PSweights_13TeV-madgraph-pythia8/[*]/NANOAODSIM	10.66
Higgs	/GluGluHToZZTo4L_M125_13TeV_powheg2_JHUGenV7011_pythia8/[*]/NANOAODSIM	0.0129763
	/VBF_HToZZTo4L_M125_13TeV_powheg2_JHUGenV7011_pythia8/[*]/NANOAODSIM	0.0010102
	/VBFHToBB_M-125_13TeV_powheg_pythia8_weightfix/[*]/NANOAODSIM	2.183
	/GluGluHToBB_M-125_13TeV_powheg_MINLO_NNLOPS_pythia8/[*]/NANOAODSIM	25.340
	/ZH_HToBB_ZToLL_M125_13TeV_powheg_pythia8/[*]/NANOAODSIM	0.311
	/ZH_HToBB_ZToQQ_M125_13TeV_powheg_pythia8/[*]/NANOAODSIM	0.311
	/ggZH_HToBB_ZToBB_M125_TuneCP5_13TeV_powheg_pythia8/[*]/NANOAODSIM	0.07784
	/ggZH_HToBB_ZToLL_M125_13TeV_powheg_pythia8/[*]/NANOAODSIM	0.006954
	/ggZH_HToBB_ZToQQ_M125_13TeV_powheg_pythia8/[*]/NANOAODSIM	0.04884
	/ttH_HToZZ_4LFilter_M125_13TeV_powheg2_JHUGenV7011_pythia8/[*]/NANOAODSIM	0.0001355
	/GluGluHToZZTo2L2Q_M125_13TeV_powheg2_JHUGenV7011_pythia8/[*]/NANOAODSIM	0.1618
	/ZH_HToZZ_4LFilter_M125_13TeV_powheg2-minlo-HZJ_JHUGenV7011_pythia8/[*]/NANOAODSIM	0.0002361
$t\bar{t}$+X	/TTWJetsToLNu_TuneCP5_13TeV-amcatnloFXFX-madspin-pythia8/[*]/NANOAODSIM	0.2043
	/TTWJetsToQQ_TuneCP5_13TeV-amcatnloFXFX-madspin-pythia8/[*]/NANOAODSIM	0.4062
	/TTZToLLNuNu_M-10_TuneCP5_13TeV-amcatnlo-pythia8/[*]/NANOAODSIM	0.2529
	/TTZToQQ_TuneCP5_13TeV-amcatnlo-pythia8/[*]/NANOAODSIM	0.5297
	/TTGJets_TuneCP5_13TeV-amcatnloFXFX-madspin-pythia8/[*]/NANOAODSIM	3.697
	/TTTT_TuneCP5_13TeV-amcatnlo-pythia8/[*]/NANOAODSIM	0.009
Triboson	/WWW_4F_TuneCP5_13TeV-amcatnlo-pythia8/[*]/NANOAODSIM	0.2086
	/WWZ_TuneCP5_13TeV-amcatnlo-pythia8/[*]/NANOAODSIM	0.1651
	/WZZ_TuneCP5_13TeV-amcatnlo-pythia8/[*]/NANOAODSIM	0.05565
	/ZZZ_TuneCP5_13TeV-amcatnlo-pythia8/[*]/NANOAODSIM	0.01398

Table A.6: List of background simulation samples for 2018 in the NanoAODv6 data format (cont.).

A.5 Z+jets Full Event Tables

Sample	2016	2017	2018
DPS VV	889.9 ± 1.9	1068.9 ± 2.2	1255.9 ± 0.8
DY+Jets	14833626.6 ± 4465.6	18455293.7 ± 6511.4	25675036.2 ± 9107.0
EWK V	14152.4 ± 42.8	18766.0 ± 56.2	25465.9 ± 79.9
EWK VV	78.1 ± 0.7	93.9 ± 1.2	135.7 ± 1.8
Higgs	36.8 ± 0.1	372.4 ± 1.3	741.9 ± 2.5
QCD	0.6 ± 0.6	54.4 ± 48.0	3087.3 ± 2096.2
SingleTop	633.4 ± 11.0	749.2 ± 11.7	961.3 ± 15.4
$V\gamma$	39387.5 ± 101.8	21394.0 ± 38.0	29514.9 ± 79.1
VV	20672.6 ± 44.2	18947.6 ± 35.2	25449.1 ± 34.0
VVV	79.0 ± 1.2	92.2 ± 1.3	128.2 ± 1.9
W+Jets	153.3 ± 47.9	248.8 ± 67.5	423.7 ± 119.0
$t\bar{t}$	33.7 ± 0.3	34.1 ± 0.4	45.1 ± 0.7
$t\bar{t}$+X	3265.1 ± 12.9	3525.5 ± 14.4	4632.4 ± 19.4
Total MC	14913009 ± 4467.5	18520640.7 ± 6512.4	25766877.6 ± 9346.7
Data	14174710	17146880	23298593
Purity	99.5%	99.6%	99.6%
Central Selection Scale Factor	0.95 ± 0.001	0.93 ± 0.001	0.90 ± 0.001

Table A.7: Event yields for Z+Jets (referred to as DY+jets in the table) after central selection cuts have been applied.

Sample	2016	2017	2018
DPS VV	0.6 ± 0.1	0.7 ± 0.1	1.0 ± 0.0
DY+Jets	2984.7 ± 31.4	4216.0 ± 43.9	5838.6 ± 59.8
EWK V	667.3 ± 9.8	744.1 ± 11.8	1139.5 ± 17.8
EWK VV	14.7 ± 0.2	14.7 ± 0.5	22.5 ± 0.7
Higgs	0.2 ± 0.0	0.8 ± 0.1	1.9 ± 0.1
QCD	0.0 ± 0.0	0.0 ± 0.0	0.0 ± 0.0
SingleTop	2.0 ± 0.6	1.3 ± 0.4	2.7 ± 0.8
$V\gamma$	78.4 ± 3.2	53.6 ± 1.3	82.0 ± 2.7
VV	60.7 ± 2.1	54.6 ± 1.8	76.0 ± 2.1
VVV	1.5 ± 0.2	1.3 ± 0.2	1.6 ± 0.2
W+Jets	0.0 ± 0.0	0.1 ± 0.1	0.0 ± 0.0
$t\bar{t}$	29.9 ± 1.2	28.3 ± 1.3	37.3 ± 1.7
$t\bar{t}$+X	1.1 ± 0.0	0.9 ± 0.1	1.2 ± 0.1
Total MC	3841.1 ± 33.1	5116.4 ± 45.5	7204.3 ± 62.5
Data	3900.0	5145.0	6663.0
Purity	77.7 %	82.4 %	81.0 %
VBF1 Scale Factor	1.07 ± 0.02	1.09 ± 0.02	1.00 ± 0.02
VBF1 Combined Scale Factor	1.02 ± 0.02	1.01 ± 0.02	0.91 ± 0.02

Table A.8: Event yields after VBF I selections are applied in the Z+Jets CR.

Sample	2016	2017	2018
DPS VV	7.4 ± 0.2	5.9 ± 0.2	10.0 ± 0.1
DY+Jets	34092.9 ± 159.9	37564.6 ± 189.2	61969.5 ± 299.0
EWK V	1755.1 ± 15.8	1794.2 ± 18.3	2835.5 ± 27.9
EWK VV	29.4 ± 0.4	28.7 ± 0.6	45.7 ± 1.0
Higgs	1.0 ± 0.0	4.3 ± 0.1	13.3 ± 0.3
QCD	0.0 ± 0.0	0.0 ± 0.0	0.0 ± 0.0
SingleTop	17.5 ± 1.8	12.6 ± 1.5	21.7 ± 2.2
$V\gamma$	480.6 ± 10.3	203.7 ± 3.2	335.0 ± 7.1
VV	486.8 ± 6.4	343.9 ± 4.5	555.8 ± 5.6
VVV	6.5 ± 0.3	6.1 ± 0.4	7.9 ± 0.5
W+Jets	0.5 ± 0.5	1.8 ± 1.3	0.9 ± 0.7
$t\bar{t}$	206.5 ± 3.2	170.4 ± 3.2	256.8 ± 4.6
$t\bar{t}$+X	4.9 ± 0.1	3.5 ± 0.1	5.1 ± 0.2
Total MC	37089.1 ± 161.2	40139.7 ± 190.2	66057.2 ± 300.5
Data	41287.0	38165.0	58172.0
Purity	91.9 %	93.4 %	93.8 %
VBF2 Scale Factor	1.18 ± 0.01	1.03 ± 0.01	0.97 ± 0.01
VBF2 Combined Scale Factor	1.12 ± 0.01	0.95 ± 0.01	0.87 ± 0.01

Table A.9: Event yields after VBF II selections are applied in the Z+Jets CR.

Sample	2016	2017	2018
DPS VV	1.4 ± 0.1	0.9 ± 0.1	1.6 ± 0.0
DY+Jets	6917.2 ± 87.1	5102.5 ± 88.3	10760.5 ± 156.5
EWK V	298.8 ± 6.5	260.3 ± 7.0	427.0 ± 10.9
EWK VV	6.1 ± 0.2	4.7 ± 0.3	8.1 ± 0.4
Higgs	0.3 ± 0.0	0.7 ± 0.1	2.3 ± 0.1
QCD	0.0 ± 0.0	0.0 ± 0.0	0.0 ± 0.0
SingleTop	3.2 ± 0.8	1.7 ± 0.5	4.5 ± 1.0
$V\gamma$	65.7 ± 3.7	21.8 ± 1.0	33.5 ± 2.0
VV	84.6 ± 2.8	37.6 ± 1.4	74.0 ± 2.0
VVV	0.7 ± 0.1	0.5 ± 0.1	0.8 ± 0.1
W+Jets	0.5 ± 0.5	0.0 ± 0.0	0.0 ± 0.0
$t\bar{t}$	35.6 ± 1.4	22.2 ± 1.2	36.5 ± 1.7
$t\bar{t}$+X	0.7 ± 0.1	0.4 ± 0.1	0.5 ± 0.1
Total MC	7414.8 ± 87.5	5453.3 ± 88.6	11349.3 ± 156.9
Data	7872.0	5142.0	9416.0
Purity	93.3 %	93.6 %	94.8 %
VBF3 Scale Factor	1.12 ± 0.02	1.02 ± 0.02	0.91 ± 0.01
VBF3 Combined Scale Factor	1.07 ± 0.02	0.94 ± 0.02	0.82 ± 0.01

Table A.10: Event yields after VBF III selections are applied in the Z+Jets CR.

A.6 W+jets Full Event Tables

Sample	2016	2017	2018
DPS VV	0.2 ± 0.0	0.1 ± 0.0	0.2 ± 0.0
DY+Jets	68.2 ± 4.4	114.7 ± 10.1	111.2 ± 7.6
EWK V	740.6 ± 11.4	1351.8 ± 18.6	1828.9 ± 26.1
EWK VV	70.4 ± 1.3	39.3 ± 1.0	59.0 ± 1.5
Higgs	0.0 ± 0.0	0.0 ± 0.0	0.0 ± 0.0
QCD	7.4 ± 1.4	21.5 ± 3.5	27.8 ± 5.2
SingleTop	347.5 ± 7.4	322.0 ± 7.0	429.7 ± 9.4
$V\gamma$	176.6 ± 5.4	171.4 ± 5.8	225.8 ± 7.7
VV	762.2 ± 10.7	779.2 ± 11.9	1102.5 ± 13.1
VVV	14.1 ± 0.6	15.5 ± 0.7	18.8 ± 0.9
W+Jets	16767.1 ± 74.4	20525.2 ± 120.6	28328.7 ± 148.8
$t\bar{t}$	11.0 ± 0.3	13.0 ± 0.5	13.9 ± 0.7
$t\bar{t}$+X	1342.7 ± 12.1	1319.3 ± 12.7	1728.0 ± 11.3
Total MC	20308.0 ± 77.67	24673.0 ± 124.06	33874.5 ± 152.84
Data	20171	23003	30620
Purity	82.6 %	83.2 %	83.6 %
Central Selection Scale Factor	0.99 ± 0.010	0.92 ± 0.009	0.89 ± 0.008

Table A.11: Event yields for W+Jets after central selection cuts and vetoes have been applied.

Sample	2016	2017	2018
DPS VV	0.0 ± 0.0	0.0 ± 0.0	0.0 ± 0.0
DY+Jets	1.2 ± 0.2	6.7 ± 3.4	2.8 ± 0.6
EWK V	112.0 ± 4.5	135.3 ± 5.9	199.6 ± 8.7
EWK VV	5.3 ± 0.3	7.1 ± 0.4	13.1 ± 0.7
Higgs	0.0 ± 0.0	0.0 ± 0.0	0.0 ± 0.0
QCD	0.6 ± 0.3	1.2 ± 1.0	4.3 ± 2.4
SingleTop	13.1 ± 1.3	11.8 ± 1.2	19.2 ± 1.8
$V\gamma$	24.8 ± 1.9	20.2 ± 1.9	35.8 ± 2.9
VV	25.6 ± 2.0	22.5 ± 2.0	32.9 ± 2.5
VVV	0.5 ± 0.1	0.5 ± 0.1	0.5 ± 0.2
W+Jets	337.5 ± 8.9	439.4 ± 45.0	539.1 ± 16.8
$t\bar{t}$	68.5 ± 2.7	61.7 ± 2.7	85.4 ± 2.5
$t\bar{t}$+X	0.8 ± 0.1	0.3 ± 0.1	0.5 ± 0.1
Total MC	589.9 ± 10.8	706.7 ± 45.7	933.2 ± 19.7
Data	587.0	685.0	923.0
Purity	57.2%	62.2%	57.8%
VBF1 Scale Factor	1.00 ± 0.08	1.03 ± 0.12	1.11 ± 0.07
VBF1 Combined Scale Factor	0.99 ± 0.08	0.95 ± 0.12	0.98 ± 0.07

Table A.12: Event yields for VBF I selections applied, W+Jets.

Sample	2016	2017	2018
DPS VV	0.0 ± 0.0	0.0 ± 0.0	0.0 ± 0.0
DY+Jets	5.1 ± 0.7	13.3 ± 4.8	8.4 ± 1.0
EWK V	187.0 ± 5.8	237.9 ± 7.9	353.5 ± 11.6
EWK VV	11.1 ± 0.5	11.0 ± 0.5	18.8 ± 0.8
Higgs	0.0 ± 0.0	0.0 ± 0.0	0.0 ± 0.0
QCD	1.0 ± 0.3	2.0 ± 1.0	6.2 ± 2.6
SingleTop	48.1 ± 2.7	33.9 ± 2.2	55.3 ± 3.2
$V\gamma$	51.2 ± 2.8	36.9 ± 2.6	65.4 ± 4.1
VV	81.4 ± 3.5	60.9 ± 3.3	99.6 ± 4.4
VVV	1.6 ± 0.2	1.3 ± 0.2	1.5 ± 0.2
W+Jets	1098.8 ± 17.3	1177.9 ± 48.3	1784.9 ± 33.4
$t\bar{t}$ 198.6 ± 4.6	160.4 ± 4.4	235.0 ± 4.2	
$t\bar{t}$+X	2.1 ± 0.1	1.5 ± 0.2	1.8 ± 0.2
Total MC	1686.0 ± 19.6	1737.0 ± 49.6	2630.4 ± 36.4
Data	1748.0	1639.0	2397.0
Purity	65.2 %	67.8 %	67.8 %
VBF2 Scale Factor	1.07 ± 0.04	1.00 ± 0.05	0.98 ± 0.03
VBF2 Combined Scale Factor	1.06 ± 0.04	0.92 ± 0.05	0.87 ± 0.03

Table A.13: Event yields for VBF II selections applied, W+Jets.

Sample	2016	2017	2018
DPS VV	0.0 ± 0.0	0.0 ± 0.0	0.0 ± 0.0
DY+Jets	0.2 ± 0.1	1.4 ± 1.0	1.1 ± 0.5
EWK V	17.7 ± 1.8	21.5 ± 2.4	30.6 ± 3.4
EWK VV	1.8 ± 0.2	1.0 ± 0.2	1.4 ± 0.2
Higgs	0.0 ± 0.0	0.0 ± 0.0	0.0 ± 0.0
QCD	0.1 ± 0.1	0.0 ± 0.0	0.4 ± 0.3
SingleTop	6.4 ± 1.0	3.0 ± 0.6	5.1 ± 0.9
$V\gamma$	4.6 ± 0.8	1.2 ± 0.4	4.0 ± 1.0
VV	9.2 ± 1.2	3.8 ± 0.8	5.5 ± 0.9
VVV	0.1 ± 0.0	0.1 ± 0.1	0.1 ± 0.1
W+Jets	75.7 ± 4.6	64.5 ± 4.6	135.0 ± 9.4
$t\bar{t}$	21.6 ± 1.5	15.3 ± 1.4	21.8 ± 1.3
$t\bar{t}$+X	0.4 ± 0.1	0.1 ± 0.1	0.1 ± 0.1
Total MC	137.8 ± 5.5	111.9 ± 5.6	205.1 ± 10.2
Data	180.0	101.0	169.0
Purity	54.9 %	57.6 %	65.8 %
VBF3 Scale Factor	1.57 ± 0.20	0.91 ± 0.17	0.83 ± 0.11
VBF3 Combined Scale Factor	1.56 ± 0.20	0.83 ± 0.17	0.73 ± 0.11

Table A.14: Event yields for VBF III selections applied, W+Jets.

A.7 $t\bar{t}$ Full Event Tables

Sample	2016	2017	2018
EWK V	0.0 ± 0.0	0.0 ± 0.0	0.0 ± 0.0
QCD	0.0 ± 0.0	0.0 ± 0.0	0.0 ± 0.0
Rares	0.0 ± 0.0	0.1 ± 0.0	0.1 ± 0.1
SingleTop	31.1 ± 2.5	23.1 ± 2.2	33.8 ± 3.0
VV	2.0 ± 0.6	2.2 ± 0.7	2.4 ± 0.7
W+Jets	0.0 ± 0.0	0.0 ± 0.0	0.0 ± 0.0
Z+Jets	0.3 ± 0.1	1.4 ± 0.8	0.6 ± 0.1
$t\bar{t}$	190.7 ± 3.0	204.0 ± 3.3	300.9 ± 4.9
Total MC	224.1 ± 4.0	230.8 ± 4.1	337.8 ± 5.8
Data	160.0	223.0	330.0
Central Selection Purity	85.1 %	88.4 %	89.1%
Central Selection Scale Factor	0.66 ± 0.07	0.96 ± 0.08	0.97 ± 0.06

Table A.15: Event yields for $t\bar{t}$ in the dimuon channel after central selection cuts and vetoes have been applied.

Sample	2016	2017	2018
EWK V	0.1 ± 0.1	0.1 ± 0.1	0.0 ± 0.0
QCD	0.0 ± 0.0	0.0 ± 0.0	0.0 ± 0.0
Rares	0.0 ± 0.0	0.0 ± 0.0	0.0 ± 0.0
SingleTop	2.2 ± 0.7	1.3 ± 0.5	3.2 ± 0.9
VV	0.6 ± 0.3	0.1 ± 0.0	0.3 ± 0.3
W+Jets	0.0 ± 0.0	0.0 ± 0.0	0.0 ± 0.0
Z+Jets	0.6 ± 0.2	0.6 ± 0.1	0.8 ± 0.1
$t\bar{t}$	89.2 ± 2.1	88.2 ± 2.2	127.8 ± 3.2
Total MC	92.7 ± 2.2	90.3 ± 2.3	132.1 ± 3.3
Data	76.0	68.0	106.0
Purity [%]	96.2 %	97.7 %	96.7 %
VBF1 Scale Factor	0.94 ± 0.10	0.76 ± 0.10	0.82 ± 0.08
Combined VBF1 & CS Sale Factor	0.62 ± 0.10	0.73 ± 0.10	0.80 ± 0.08

Table A.16: Event yields for $t\bar{t}$ in the dimuon channel after VBF1 selection cuts with modified $p_{\mathrm{T}}^{miss} > 100$ GeV have been applied.

Sample	2016	2017	2018
EWK V	0.0 ± 0.0	0.0 ± 0.0	0.0 ± 0.0
QCD	0.0 ± 0.0	0.0 ± 0.0	0.0 ± 0.0
Rares	0.0 ± 0.0	0.0 ± 0.0	0.0 ± 0.0
SingleTop	0.6 ± 0.4	0.0 ± 0.0	1.0 ± 0.5
VV	0.2 ± 0.1	0.0 ± 0.0	0.0 ± 0.0
W+Jets	0.0 ± 0.0	0.0 ± 0.0	0.0 ± 0.0
Z+Jets	0.0 ± 0.0	0.8 ± 0.4	0.0 ± 0.0
$t\bar{t}$	9.8 ± 0.7	0.0 ± 0.0	12.5 ± 1.0
Total MC	10.6 ± 0.8	15.5 ± 1.0	13.5 ± 1.1
Data	8.0	8.0	8.0
VBF1 Purity	92.4 %	94.8 %	92.6 %
VBF1 Scale Factor	1.00 ± 0.30	0.51 ± 0.20	0.58 ± 0.23
VBF1 Combined Sale Factor	0.66 ± 0.30	0.49 ± 0.20	0.56 ± 0.23

Table A.17: Event yields for $t\bar{t}$ in the dimuon channel after VBF1 selection cuts have been applied (including $p_{\mathrm{T}}^{miss} > 250$ GeV requirement).

Sample	2016	2017	2018
EWK V	0.0 ± 0.0	0.0 ± 0.0	0.0 ± 0.0
QCD	0.0 ± 0.0	0.0 ± 0.0	0.0 ± 0.0
Rares	0.0 ± 0.0	0.0 ± 0.0	0.0 ± 0.0
SingleTop	2.2 ± 0.7	0.8 ± 0.4	2.8 ± 0.9
VV	0.2 ± 0.1	0.1 ± 0.0	0.0 ± 0.0
W+Jets	0.0 ± 0.0	0.0 ± 0.0	0.0 ± 0.0
Z+Jets	0.0 ± 0.0	0.0 ± 0.0	0.0 ± 0.0
$t\bar{t}$	18.8 ± 0.9	19.2 ± 1.0	31.1 ± 1.6
Total MC	21.2 ± 1.1	20.1 ± 1.1	33.9 ± 1.8
Data	16.0	14.0	25.0
VBF2 Purity	88.7 %	95.5 %	91.7 %
VBF2 Sale Factor	1.09 ± 0.22	0.71 ± 0.20	0.73 ± 0.17
VBF2 Combined Scale Factor	0.72 ± 0.22	0.68 ± 0.20	0.71 ± 0.17

Table A.18: Event yields for $t\bar{t}$ in the dimuon channel after VBF2 selection cuts have been applied.

A.8 Diboson Full Event Tables

Sample	2016	2017	2018
EWK V	1.2 ± 0.4	3.2 ± 0.8	3.5 ± 1.0
QCD	0.0 ± 0.0	1.3 ± 0.0	0.0 ± 0.0
Rares	46.7 ± 2.2	70.4 ± 1.8	81.4 ± 2.7
Single top	3.5 ± 0.8	8.0 ± 1.2	14.4 ± 1.9
Diboson	459.2 ± 1.9	516.5 ± 9.1	675.9 ± 8.8
W+Jets	5.4 ± 1.8	10.9 ± 3.8	16.7 ± 5.6
Z+Jets	76.5 ± 8.2	131.0 ± 11.3	154.4 ± 15.9
$t\bar{t}$	71.6 ± 1.8	122.0 ± 2.6	146.6 ± 3.4
Total MC	664.0 ± 9.1	863.3 ± 15.4	1092.9 ± 19.6
Data	582	848	1074
Purity [%]	69.2	59.8	61.8
Central Selection Scale Factor	0.821 ± 0.056	0.970 ± 0.064	0.972 ± 0.056

Table A.19: Event yields for diboson after central selection cuts and vetoes have been applied.

Sample	2016	2017	2018
EWK V	0.2 ± 0.0	0.4 ± 0.3	1.0 ± 0.5
QCD	0.0 ± 0.0	0.0 ± 0.0	0.0 ± 0.0
Rares	6.5 ± 0.8	8.5 ± 0.6	9.0 ± 0.9
Single top	0.7 ± 0.4	1.7 ± 0.6	0.6 ± 0.3
Diboson	69.5 ± 0.7	77.2 ± 3.5	86.9 ± 3.1
W+Jets	0.8 ± 0.5	1.5 ± 0.4	3.3 ± 1.9
Z+Jets	4.5 ± 1.1	9.6 ± 1.6	8.2 ± 1.4
$t\bar{t}$	14.2 ± 0.8	22.2 ± 1.1	26.6 ± 1.4
Total MC	96.5 ± 1.8	121.1 ± 4.1	135.6 ± 4.3
Data	108	130	100
Purity [%]	72.1	63.7	64.1
VBF1 Scale Factor	1.42 ± 0.24	1.15 ± 0.20	1.26 ± 0.19

Table A.20: Event yields for diboson after VBF1 cuts and vetoes have been applied.

Sample	2016	2017	2018
EWK V	0.7 ± 0.3	1.2 ± 0.5	1.8 ± 0.7
QCD	0.0 ± 0.0	0.0 ± 0.0	0.0 ± 0.0
Rares	18.0 ± 1.4	21.3 ± 1.0	22.8 ± 1.4
Single top	1.2 ± 0.5	3.4 ± 0.8	4.4 ± 1.0
Diboson	164.8 ± 1.1	168.9 ± 5.2	204.0 ± 4.8
W+Jets	3.3 ± 1.3	6.5 ± 2.9	7.4 ± 3.0
Z+Jets	19.7 ± 3.6	27.0 ± 3.2	35.1 ± 4.1
$t\bar{t}$	33.2 ± 1.3	53.9 ± 1.8	67.3 ± 2.2
Total MC	241.0 ± 4.4	281.6 ± 7.1	342.9 ± 7.6
Data	213	305	375
Purity [%]	68.4	60.0	59.5
SF	1.01 ± 0.16	1.17 ± 0.17	1.19 ± 0.15

Table A.21: Event yields for diboson after VBF2 cuts and vetoes have been applied.

References

[1] Geraldine Servant. Concepts in HEP (Fundamental Concepts in Particle Physics).

[2] Matthew Robinson. *Symmetry and the Standard Model*. Springer, 1st edition, 2011.

[3] Stephen P. Martin. A Supersymmetry Primer. In *Perspectives on Supersymmetry*, pages 1–98. World Scientific, jul 1998.

[4] Ivan Melo. Higgs potential and fundamental physics. *European Journal of Physics*, 38(6):065404, oct 2017.

[5] Kolb E.W. & Turner M.S. (Eds.). *The Early Universe*. CRC Press, 1st edition, 1990.

[6] A. M. Sirunyan et al. Search for supersymmetry in proton-proton collisions at 13 TeV in final states with jets and missing transverse momentum. *Journal of High Energy Physics*, 2019(10), oct 2019.

[7] P.A. Zyla et al. Review of Particle Physics. *PTEP*, 2020(8):083C01, 2020. and 2021 update.

[8] G. Aad et al. Searches for electroweak production of supersymmetric particles with compressed mass spectra in $\sqrt(s) = 13$ tev in pp collisions with the ATLAS detector. *Physical Review D*, 101(5), mar 2020.

[9] Armen Tumasyan et al. Search for supersymmetry in final states with two or three soft leptons and missing transverse momentum in proton-proton collisions at $\sqrt{s} = 13$ TeV. *JHEP*, 04:091, 2022.

[10] Sarah Charley. The LHC does a dry run.

[11] James Stirling. Parton Distribution Functions.

[12] Saranya Samik Ghosh and on behalf of the CMS Collaboration. Highlights from the compact muon solenoid (CMS) experiment. *Universe*, 5(1), 2019.

[13] Isobel Ojalvo. Overview of Triggering and Realtime Systems, 2019.

[14] David Barney and Sergio Cittolin. CMS Detector Drawings, Jan 2000.

[15] Izaak Neutelings. CMS coordinate system.

[16] Izaak Neutelings. Pseudorapidity.

[17] G. L. Bayatian et al. CMS Physics: Technical Design Report Volume 1: Detector Performance and Software, 2006.

[18] Cristina Biino. The CMS electromagnetic calorimeter: overview, lessons learned during run 1 and future projections. *Journal of Physics: Conference Series*, 587:012001, feb 2015.

[19] S Chatrchyan et al. Precise Mapping of the Magnetic Field in the CMS Barrel Yoke using Cosmic Rays. *JINST*, 5:T03021, 2010.

[20] Pierluigi Paolucci. The CMS Muon system, Apr 2005.

[21] CMS Collaboration. The CMS trigger system. *Journal of Instrumentation*, 12(01):P01020–P01020, jan 2017.

[22] CMS Collaboration. Particle-flow reconstruction and global event description with the CMS detector. *Journal of Instrumentation*, 12(10):P10003–P10003, oct 2017.

[23] A.M. Sirunyan et. al. Electron and photon reconstruction and identification with the CMS experiment at the CERN LHC. *Journal of Instrumentation*, 16(05):P05014, may 2021.

[24] A.M. Sirunyan et al. Performance of the CMS muon detector and muon reconstruction with proton-proton collisions at $\sqrt{S}$=13 TeV. *Journal of Instrumentation*, 13(06):P06015–P06015, jun 2018.

[25] Eric M. Metodiev. The Fractal Lives of Jets.

[26] Viola Sordini. Jets and MET at CMS.

[27] Andrea Malara. Reconstruction of jets and missing transverse momentum at the CMS experiment: Run 2 and perspective for Run 3. *PoS*, ICHEP2020:752. 6 p, Dec 2020. 6 pages, 11 figures, Contribution to 40th International Conference on High Energy physics - ICHEP2020, Accepted for publication on POS https://pos.sissa.it/390/752/pdf.

[28] Henning Kirschenmann, Alexx Perloff, David Yu. Pileup and Jet Energy Corrections in CMS.

[29] CMS Collaboration. Reconstruction and identification of τ lepton decays to hadrons and ν_τ at CMS. *Journal of Instrumentation*, 11(01):P01019–P01019, jan 2016.

[30] Jet Types and Algorithms.

[31] A. M. Sirunyan et al. Search for supersymmetry with a compressed mass spectrum in the vector boson fusion topology with 1-lepton and 0-lepton final states in proton-proton collisions at $\sqrt{s}$ = 13 TeV. *Journal of High Energy Physics*, 2019(8), aug 2019.

[32] A. M. et al. Sirunyan. Search for supersymmetry with a compressed mass spectrum in events with a soft τ lepton, a highly energetic jet, and large missing transverse momentum in proton-proton collisions at $\sqrt{s} = 13$ tev. *Phys. Rev. Lett.*, 124:041803, Jan 2020.

[33] H. Baer and X. Tata. *Weak Scale Supersymmetry From Fields to Scattering Events*. Cambridge University Press, 1st edition, 2006.

[34] G. McCabe. *The Structure and Interpretation of the Standard Model*. Elsevier, 1st edition, 2007.

[35] G. Arnison et al. Experimental observation of isolated large transverse energy electrons with associated missing energy at s=540 gev. *Physics Letters B*, 122(1):103–116, 1983.

[36] G. Arnison et al. Experimental Observation of Lepton Pairs of Invariant Mass Around 95-GeV/c^2 at the CERN SPS Collider. *Phys. Lett. B*, 126:398–410, 1983.

[37] S. Abachi et al. Observation of the Top Quark. *Physical Review Letters*, 74(14):2632–2637, apr 1995.

[38] K. Kodama et al. Observation of tau neutrino interactions. *Physics Letters B*, 504(3):218–224, apr 2001.

[39] G. Aad et al. Observation of a new particle in the search for the Standard Model Higgs boson with the ATLAS detector at the LHC. *Physics Letters B*, 716(1):1–29, 2012.

[40] Vincent Mathieu, Nikolai Kochelev, and Vicente Vento. The Physics of Glueballs. *Int. J. Mod. Phys. E*, 18:1–49, 2009.

[41] Hitoshi Murayama. The origin of neutrino mass. *Physics World*, 15(5):35–39, may 2002.

[42] Gerard Jungman, Marc Kamionkowski, and Kim Griest. Supersymmetric dark matter. *Physics Reports*, 267(5):195–373, 1996.

[43] Neta A. Bahcall. Dark matter universe. *Proceedings of the National Academy of Sciences*, 112(40):12243–12245, 2015.

[44] Ruth Durrer. What do we really know about dark energy? *Philosophical Transactions of the Royal Society A: Mathematical, Physical and Engineering Sciences*, 369(1957):5102–5114, 2011.

[45] B. et al Abi. Measurement of the positive muon anomalous magnetic moment to 0.46 ppm. *Phys. Rev. Lett.*, 126:141801, Apr 2021.

[46] Andreas Crivellin and Martin Hoferichter. Hints of lepton flavor universality violations. *Science*, 374(6571):1051–1052, nov 2021.

[47] T. Aaltonen et al. High-precision measurement of the w boson mass with the cdf ii detector. *Science*, 376(6589):170–176, 2022.

[48] N. Aghanim et al. Planck 2018 results. *Astronomy & Astrophysics*, 641:A6, sep 2020.

[49] Howard Baer, Tadas Krupovnickas, Azar Mustafayev, Eun-Kyung Park, Stefano Profumo, and Xerxes Tata. Exploring the BWCA (bino-wino co-annihilation) scenario for neutralino dark matter. *Journal of High Energy Physics*, 2005(12), dec 2005.

[50] Kim Griest and David Seckel. Three exceptions in the calculation of relic abundances. *Phys. Rev. D*, 43:3191–3203, May 1991.

[51] Carlos Avila, Andrés Flórez, Alfredo Gurrola, Dale Julson, and Savanna Starko. Connecting particle physics and cosmology: Measuring the dark matter relic density in compressed supersymmetry models at the lhc. *Physics of the Dark Universe*, 27:100430, 2020.

[52] Lyndon Evans and Philip Bryant. LHC machine. *Journal of Instrumentation*, 3(08):S08001–S08001, aug 2008.

[53] The CMS Collaboration. The CMS experiment at the CERN LHC. *Journal of Instrumentation*, 3(08):S08004–S08004, aug 2008.

[54] Sarah Charley. When was the Higgs actuakly discovered?

[55] Deepak Kar. *Experimental Particle Physics*. 2053-2563. IOP Publishing, 2019.

[56] T Carli, A Cooper-Sarkar, J Feltesse, A Glazov, C Gwenlan, M Klein, T Lastoviicka, G Lastoviicka-Medin, S Moch, B Reisert, Gavin P Salam, and F Siegert. Experimental determination of parton distributions, 2005.

[57] Ramon Cid Manzano Xabier Cid Vidal. LHC p collisions: Taking a closer look at LHC.

[58] CMS Collaboration. *The CMS magnet project: Technical Design Report*. Technical design report. CMS. CERN, Geneva, 1997.

[59] The CMS Collaboration. Description and performance of track and primary-vertex reconstruction with the CMS tracker. *Journal of Instrumentation*, 9(10):P10009–P10009, oct 2014.

[60] Andrea Malara. Jet Energy Resolution.

[61] Izaak Neutelings. Hadronic tau reconstruction and identification performance in ATLAS and CMS. *PoS*, LHCP2020:045, 2021.

[62] CMS Collaboration. Performance of missing transverse momentum reconstruction in proton-proton collisions at $\sqrt{s} = 13$ TeV using the CMS detector. *Journal of Instrumentation*, 14(07):P07004–P07004, jul 2019.

[63] Dordevic, Milos. The cms particle flow algorithm. *EPJ Web Conf.*, 191:02016, 2018.

[64] Debajyoti Choudhury, Anindya Datta, Katri Huitu, Partha Konar, Stefano Moretti, and Biswarup Mukhopadhyaya. Slepton production from gauge boson fusion. *Phys. Rev. D*, 68:075007, Oct 2003.

[65] Ehatäht, Karl. Nanoaod: a new compact event data format in cms. *EPJ Web Conf.*, 245:06002, 2020.

[66] Laurent Thomas. Reweighting recipe to emulate Level 1 ECAL prefiring.

[67] Laurent Thomas, Jordan Damgov. MET report.

[68] A. M. Sirunyan et al. Measurements of differential z boson production cross sections in proton-proton collisions at $\sqrt{s} = 13$ TeV. *Journal of High Energy Physics*, 2019(12), dec 2019.

[69] Mauro Verzetti . Jet classification techniques in CMS.

[70] A. M. Sirunyan et al. Measurement of the top quark pair production cross section in dilepton final states containing one τ lepton in pp collisions at $\sqrt{s}$ = 13 TeV. *Journal of High Energy Physics*, 2020(2), feb 2020.

[71] Joscha Knolle. Utilities for Accessing Pileup Information for Data.

[72] CMS Collaboration. Precision luminosity measurement in proton-proton collisions at $\sqrt{s}$= 13 tev in 2015 and 2016 at cms. *European Physical Journal C*, 81, 2021.

[73] CMS Collaboration. CMS luminosity measurement for the 2017 data-taking period at $\sqrt{s}$ = 13 TeV. CMS Physics Analysis Summary CMS-PAS-LUM-17-004, 2018.

[74] CMS Collaboration. CMS luminosity measurement for the 2018 data-taking period at $\sqrt{s}$ = 13 TeV. CMS Physics Analysis Summary CMS-PAS-LUM-18-002, 2019.

[75] Thomas Junk. Confidence level computation for combining searches with small statistics. *Nuclear Instruments and Methods in Physics Research Section A: Accelerators, Spectrometers, Detectors and Associated Equipment*, 434(2):435–443, 1999.

[76] A L Read. Presentation of search results: the cl_s technique. *Journal of Physics G: Nuclear and Particle Physics*, 28(10):2693–2704, sep 2002.

[77] Procedure for the LHC Higgs boson search combination in Summer 2011, Aug 2011.

[78] Jakob Schwichtenberg. *Physics from Symmetry*. Springer, 2nd edition, 2018.